SUPERCONDUCTIVITY, HIGH-TEMPERATURE SUPERCONDUCTIVITY

Fields and currents of Abrikosov–Josephson vortices in a thin film

A. S. Malishevskiĭ

P. Lebedev Institute of Physics, Russian Academy of Sciences, 117924 Moscow, Russia*

Fields and currents induced by vortex structures in a Josephson junction in a thin superconducting film are considered. Simple asymptotic regularities describing fields and currents induced by solitary Abrikosov–Josephson vortices and periodic chains of such vortices are obtained. These regularities are applied to some nonlinear small-scale states. © *1997 American Institute of Physics.* [S1063-777X(97)00107-2]

1. INTRODUCTION

In 1975, Likharev *et al.*[1] formulated important statements and obtained first results in the field of nonlocal Josephson electrodynamics of structures of the type of variable-thickness bridge arranged over a superconducting screen. In 1990, Ivanchenko and Soboleva[2] laid the basis of nonlocal electrodynamics of a Josephson junction in a thin superconducting film whose thickness D is much smaller than the London depth λ of magnetic field penetration in a superconductor. On the other hand, a systematic development of the nonlocal Josephson electrodynamics of junctions between bulk superconductors was started in 1992 in Refs. 3 and 4. In this case, a nonlocal description is essential when the critical Josephson current density j_c is large:

$$j_c > j_0 \equiv c\,\phi_0/(16\pi^2\lambda^3), \tag{1}$$

where $\phi_0 \equiv \pi\hbar c/|e| = 2.05 \times 10^{-7}\,\text{Oe}\cdot\text{cm}^2$ is the magnetic flux quantum. A set of exact solutions describing vortex structures was obtained for junctions between bulk superconductors under the condition (1).[1,4–11] It is clear now that the results obtained in Refs. 1, 4–11 can be used in the Ivanchenko–Soboleva electrodynamics for junctions in which the critical Josephson current density satisfies the condition

$$j_c > \frac{D}{\lambda}\,j_0, \tag{2}$$

since in this case the basic electrodynamic equation in Ref. 2 assumes an analytic form coinciding with the basic equation in the one-dimensional nonlocal electrodynamics of Josephson junctions between bulk superconductors under conditions (1).[1,4,12–15] The solutions of a nonlocal integro-differential equation obtained in Refs. 1, 4–11 for a phase difference φ of Cooper pairs on different sides of a Josephson junction make it possible to determine magnetic and electric fields and currents. The magnetic field distribution in junctions between bulk superconductors is analyzed in Refs. 4–11, while similar analysis for the electrodynamics of a Josephson junction in a thin film can be found only in Refs. 12, 13, in which the magnetic field structure was considered on the basis of Refs. 1, 4 (in these publications, a solution of

the form of a stationary 2π-kink was obtained for the phase difference of Cooper pairs) as well as in our preliminary research[14] in which the results for static periodic structures are considered. In the present communication, we investigate (on the basis of a large number of solutions obtained in Refs. 1, 4, 6–10), the electromagnetic field structure for the phase difference φ for various vortex states of a tunnel junction in a thin superconducting film under conditions (2).

In Sec. 2 of this communication, we shall obtain the kernels of nonlocal operators connecting the magnetic and electric fields with the derivative of phase difference. In Sec. 3, all the available plane-wave solutions of the sin-Hilbert equation will be listed.

Section 4 is devoted to an analysis of fields and currents of solitary vortices. The characteristics of periodic states (with the mean magnetic field and without it) will be considered in Sec. 5. The main results are summarized in the Conclusion.

2. MAGNETIC AND ELECTRIC FIELDS. SURFACE CURRENT

We shall derive expressions for the current as well as vortex magnetic and electric fields created by the phase difference in a Josephson junction in a thin superconducting film ($D \ll \lambda$) lying in the plane $y = 0$. We proceed from the expression for the superconducting current density

$$j_s(x,z,t) = -\frac{c}{4\pi\lambda^2}\left[\frac{\phi_0}{2\pi}\,\nabla\phi(x,z,t) + \mathbf{A}(x,0,z,t)\right] \tag{3}$$

and from Maxwell's equations in the entire space

$$-\Delta\mathbf{A}(\mathbf{r},t) = \frac{4\pi}{c}\,\mathbf{j}(\mathbf{r},t) - \frac{1}{c^2}\frac{\partial^2\mathbf{A}}{\partial t^2} - \frac{1}{c}\,\nabla\frac{\partial V(\mathbf{r},t)}{\partial t}, \tag{4}$$

$$\Delta V(\mathbf{r},t) = 0, \tag{5}$$

where V and $\mathbf{A}$ are the scalar and vector potentials, respectively (we choose the gauge $\text{div}\,\mathbf{A} = 0$), $\phi(x,z,t) = \theta(-x-d)\phi_1(x,z,t) + \theta(x-d)\phi_2(x,z,t)$; ϕ_1 and ϕ_2 are the phases of the wave functions of Cooper pairs on the left and right of the tunnel junction, which is symmetric about the straight line $x = 0$ and has the width $2d$.

Assuming that the junction is infinitely thin, following Abrikosov,[16] and using (3), we can write the following expression for current density in the entire space:

$$j(\mathbf{r},t)=\mathbf{I}(x,z,t)\,\delta(y)=\mathbf{j}_s(x,z,t)D\,\delta(y)$$

$$=-\frac{c\,\delta(y)}{4\pi\lambda_e}[\mathbf{S}(x,z,t)+\mathbf{A}(x,0,z,t)], \qquad (6)$$

where $\mathbf{I}$ is the current in the superconducting film, and $\mathbf{S}(x,z,t)=(\phi_0/2\pi)\nabla\phi(x,z,t)$; $\lambda_e=\lambda^2/D$ is the effective London penetration depth. Substituting (6) into Maxwell's equation (4), we obtain

$$\Delta\mathbf{A}=\frac{1}{\lambda_e}[\mathbf{S}+\mathbf{A}(x,0,z,t)]\delta(y)+\frac{1}{c^2}\frac{\partial^2\mathbf{A}}{\partial t^2}+\frac{1}{c}\nabla\frac{\partial V}{\partial t}. \quad (7)$$

Let us find the conditions under which we can neglect the displacement current in this equation. It can be seen from (7) that the displacement current in vacuum is small in comparison with the superconducting current if the characteristic frequencies ω are quite low ($\omega^2/c^2\ll\lambda^{-2}$). On the other hand, it will be shown below that the displacement current density in the dielectric gap can be estimated as $\omega^2\omega_j^{-2}j_c\varphi$, where $\omega_j=4\pi[dcj_c/(\varepsilon\phi_0)]^{1/2}$ is the Josephson frequency and ε is the permittivity of the junction. Since the Josephson current density is estimated as $j_c\varphi$, it can be stated that the displacement current in the gap is significant for $\omega\sim\omega_j$ (vortex emission in vacuum can occur at such frequencies. This effect is weak in view of the smallness of the ratio of vortex velocity to the velocity of light). Hence the displacement current in vacuum can be neglected if $\omega_j^2/c^2\ll\lambda^{-2}$, i.e. if the junction width is quite small:

$$2d\ll\frac{\varepsilon c\phi_0}{8\pi^2j_c\lambda^2}.$$

In this case, Eq. (7) assumes the form

$$\Delta\mathbf{A}=\lambda_e^{-1}[\mathbf{S}+\mathbf{A}(x,0,z,t)]\delta(y).$$

Going over to Fourier transforms, we obtain

$$\mathbf{A}(\mathbf{q},t)=-\frac{2\sqrt{q_x^2+q_z^2}}{q^2(1+2\lambda_e\sqrt{q_x^2+q_z^2})}\mathbf{S}(q_x,q_z,t). \qquad (8)$$

It follows from formula (3) that $\nabla\mathbf{S}(x,z,t)=0$. This means that $\mathbf{S}(q_x,q_z,t)$ can be presented in the form

$$\mathbf{S}(q_x,q_z,t)=\frac{q_zS_x-q_xS_z}{q_z^2+q_z^2}[\mathbf{e}_y\times\mathbf{q}].$$

Using this formula, we can present vector potential (8) in the form

$$\mathbf{A}(\mathbf{q},t)=2i\frac{i(q_zS_x-q_xS_z)}{q^2\sqrt{q_x^2+q_z^2}(1+2\lambda_e\sqrt{q_x^2+q_z^2})}[\mathbf{e}_y\times\mathbf{q}]. \quad (9)$$

The combination $i(q_zS_x-q_xS_z)$ appearing in this equation is the Fourier transform of $\mathrm{curl}_y\mathbf{S}(x,z,t)=(\phi_0/2\pi)\mathrm{curl}_y\nabla\varphi$. Since the function $\phi(x,z,t)$ suffers a discontinuity at $x=0$, $\mathrm{curl}\nabla\phi\neq0$. It will be shown in Appendix I (cf. Ref. 17) that

$$q_zS_x-q_xS_z=\frac{\phi_0}{2\pi}q_z\varphi(q_z,t), \qquad (10)$$

where $\varphi(q_z,t)$ is the Fourier transform of the phase difference: $\varphi(z,t)=\phi_1(-0,z,t)-\phi_2(+0,z,t)$. Substituting (10) into (9), we obtain a relation between the Fourier transforms of the vector potential and the phase difference:

$$\mathbf{A}(\mathbf{q},t)=-\frac{\phi_0}{\pi}\frac{q_z\varphi(q_z,t)}{q^2\sqrt{q_x^2+q_z^2}(1+2\lambda_e\sqrt{q_x^2+q_z^2})}[\mathbf{e}_y\times\mathbf{q}].$$

Reverting to the coordinate representation, we obtain the vector potential

$$\mathbf{A}(\mathbf{r},t)=-\frac{\phi_0}{8\pi^2\lambda_e}\int_{-\infty}^{+\infty}dz'$$

$$\times\frac{\partial\varphi(z',t)}{\partial z'}\frac{(z-z')\mathbf{e}_x-x\mathbf{e}_z}{\sqrt{x^2+(z-z')^2}}P(|y|,$$

$$\sqrt{x^2+(z-z')^2}), \qquad (11)$$

where

$$P(|y|,\rho)=\int_0^{+\infty}\frac{dQ}{1+Q}\exp\left(-\frac{|y|Q}{2\lambda_e}\right)J_1\left(\frac{Q\rho}{2\lambda_e}\right).$$

Evaluating the curl in the potential (11), we obtain the following equation for the magnetic field:

$$\mathbf{H}(\mathbf{r},t)=\frac{\phi_0}{8\pi^2\lambda_e}\,\mathrm{sgn}\,y\,\nabla\int_{-\infty}^{+\infty}dz'\,\frac{\partial\varphi(z',t)}{\partial z'}R(|y|,$$

$$\sqrt{x^2+(z-z')^2}, \qquad (12)$$

where

$$R(|y|,\rho)=\int_0^{+\infty}\frac{dQ}{1+Q}\exp\left(-\frac{|y|Q}{2\lambda_e}\right)J_0\left(\frac{Q\rho}{2\lambda_e}\right).$$

While deriving (11) and (12), we assumed that the tunnel junction is infinitely thin. If, however, the junction width $2d$ is small but finite, the vector-potential and the magnetic field are defined for $|x|>d$ by the same formulas, since we can disregard for small d the variation of the kernels P and R associated with d (cf. the case of bulk superconductors in Ref. 7). For $|x|<d$, the vector-potential $\mathbf{A}(\mathbf{r},t)$ and the field $\mathbf{H}(\mathbf{r},t)$ are obtained approximately from (11) and (12) in which we put $x=0$.

In order to obtain the electric field $\mathbf{E}=c^{-1}\partial\mathbf{A}/\partial t-\nabla V$, we must know the vector potential $\mathbf{A}$ as well as the scalar potential V. The latter quantity is obtained from the Josephson relation: for $y=0$, $|x|<d$, we have

$$E_x\approx\frac{\phi_0}{4\pi cd}\frac{\partial\varphi(z,t)}{\partial t}. \qquad (13)$$

It was mentioned above that the characteristic frequencies $\sim\omega_j\propto d^{1/2}$. This means that $E_x\propto d^{-1/2}$ inside the junction. On the other hand, it follows from (12) that $\partial A_x/\partial t\propto\omega_j\propto d^{1/2}$. Hence, in view of the assumption concerning a small junction width, it can be assumed that the electric field inside the junction is determined only by the scalar potential which is obtained from (13):

$$V(x,0,z,t) \approx -\frac{\phi_0 x}{4\pi cd}\frac{\partial\varphi(z,t)}{\partial t}, \quad -d<x<d.$$

The distribution of scalar potential in superconducting fields is obtained by solving the Laplace equation (5) under the boundary conditions

$$V(\pm d,0,z,t)=\mp(\phi_0/4\pi c)\partial\varphi(z,t)/\partial t;$$

$$V(x,0,z,t)=-\frac{\phi_0}{4\pi^2 c}\,\text{sgn}\,x(|x|-d)$$

$$\times\frac{\partial}{\partial t}\int_{-\infty}^{+\infty}dz'\,\frac{\varphi(z',t)}{(z-z')^2+(|x|-d)^2},$$

$$|x|>d. \tag{14}$$

Using these boundary conditions, we obtain from the Laplace equation (5) the following expression for the scalar potential in vacuum for $y \neq 0$:

$$V(\mathbf{r},t)=\frac{i\phi_0}{8\pi^3 c}\frac{\partial}{\partial t}\int_{-\infty}^{+\infty}dz'dq_xdq_z\varphi(z',t)\exp(iq_x x$$

$$+iq_z(z-z')-\sqrt{q_x^2+q_z^2}|y|)$$

$$\times\left[\frac{|q_z|\sin(dq_x)+q_x\cos(dq_x)}{q_x^2+q_z^2}\right.$$

$$\left.-\frac{dq_x\cos(dq_x)-\sin(dq_x)}{dq_x^2}\right].$$

This leads to the following relatively simple asymptotic representations for the scalar potential:

$$V(\mathbf{r},t)=\frac{\phi_0 x}{8\pi^3 cd}\frac{\partial}{\partial t}\int_{-\infty}^{+\infty}dz'dq_xdq_z\exp(iq_z(z-z')$$

$$-\sqrt{q_x^2+q_z^2}|y|\varphi(z',t)q_x\frac{d}{dq_x}\frac{\sin(dq_x)}{q_x}, \quad |x|\lesssim d;$$

$$V(\mathbf{r},t)\approx-\frac{\phi_0 x}{4\pi^2 c}\frac{\partial}{\partial t}\int_{-\infty}^{+\infty}dz'$$

$$\times\frac{\varphi(z',t)}{\sqrt{x^2+y^2+(z-z')^2}(|y|+\sqrt{x^2+y^2+(z-z')^2})},$$

$$|x|\gg d.$$

Knowing the expressions for $\mathbf{A}(\mathbf{r},t)$ and $V(\mathbf{r},t)$, we can determine the electric field. If $-d\lesssim x\lesssim d$, we obtain

$$\mathbf{E}\approx\frac{\phi_0}{8\pi^3 c}\frac{\partial}{\partial t}\left\{-\nabla\left[\frac{x}{d}\int_{-\infty}^{+\infty}dz'\varphi(z',t)\int_{-\infty}^{+\infty}dq_xdq_z\right.\right.$$

$$\times\exp[iq_z(z-z')-\sqrt{q_x^2+q_z^2}|y|]q_x\frac{d}{dq_x}\frac{\sin(dq_x)}{q_x}\Big]$$

$$\left.+\lambda_e^{-1}\int_{-\infty}^{+\infty}dz'\frac{\partial\varphi(z',t)}{\partial z'}\sin(z-z')P(|y|,|z-z'|)\right\}.$$

$$\tag{15}$$

It can easily be verified that, for $y=0$, the x-component of the last formula is transformed into formula (13). For $|x|\gg d$, we can write

$$E_x\approx\frac{2\lambda_e}{c}\,\text{sgn}\,y\,\frac{\partial H_z}{\partial t}+\frac{\phi_0|y|}{4\pi^2 c}\frac{\partial}{\partial t}$$

$$\times\int_{-\infty}^{+\infty}\frac{dz'\,\varphi(z',t)}{[x^2+y^2+(z-z')^2]^{3/2}},$$

$$E_y\approx-\frac{\phi_0 x\,\text{sgn}\,y}{4\pi^2 c}\frac{\partial}{\partial t}\int_{-\infty}^{+\infty}\frac{dz'\,\varphi(z',t)}{[x^2+y^2+(z-z')^2]^{3/2}},$$

$$E_z\approx-\frac{2\lambda_e}{c}\,\text{sgn}\,y\,\frac{\partial H_x}{\partial t}. \tag{16}$$

Finally, we obtain an expression for the surface current $\mathbf{I}(x,z,t)$ passing over the film. For this purpose, we use the boundary condition imposed on the Maxwell equation $\mathbf{I}(x,z,t)=(c/4\pi)\mathbf{e}_y$, $\mathbf{H}(x,+0,z,t)=\mathbf{H}(x,-0,z,t)$. It follows from Eq. (12) that

$$H_\alpha(x,+0,z,t)-H_\alpha(x,-0,z,t)=2[\text{sgn}\,yH_\alpha(\mathbf{r},t)]_{y=0},$$

$\alpha=x$ or z. This leads to a connection between $\mathbf{I}(x,z,t)$ and the magnetic field components parallel to the film for $y=\pm 0$[14]:

$$I_x(x,z,t)=\frac{c}{2\pi}[\text{sgn}\,yH_z(\mathbf{r},t)]_{y=0},$$

$$\tag{17}$$

$$H_z(x,z,t)=-\frac{c}{2\pi}[\text{sgn}\,yH_x(\mathbf{r},t)]_{y=0}.$$

Thus, we obtain general expressions which enable us to determine the fields and current from the known phase difference. We shall apply these expressions to specific nonlinear states in Secs. 4 and 5.

3. SIN-HILBERT EQUATION AND ITS SOLUTIONS

It was shown in Refs. 2, 17 that the phase difference of Cooper pairs satisfies the equation

$$\frac{l}{\pi}\int_{-\infty}^{+\infty}dz'\,\frac{\partial\varphi(z',t)}{\partial z'}R(0,|z-z'|)$$

$$=\sin\,\varphi(z,t)+\frac{\beta}{\omega_j^2}\frac{\partial\varphi(z,t)}{\partial t}+\frac{1}{\omega_j^2}\frac{\partial^2\varphi(z,t)}{\partial t^2}, \tag{18}$$

where $l=c\phi_0/(16\pi^2 j_c\lambda^2); \beta=4\pi\sigma/\varepsilon; \sigma$ is the conductivity of the tunnel junction. In the following analysis, we shall focus our attention on the case when a significant variation of the phase difference occurs over lengths smaller than λ_e. In this case, we can use the approximation

$$\frac{dR(0,|z|)}{dz}=\frac{\mathscr{P}}{z},$$

where $\mathscr{P}$ is the symbol for Cauchy's principal value, and Eq. 18 then assumes the form[12-14,17]:

$$\frac{l}{\pi}\int_{-\infty}^{+\infty}\frac{dz'}{z'-z}\frac{\partial\varphi(z',t)}{\partial z'}$$

$$=\sin\varphi(z,t)+\frac{\beta}{\omega_j^2}\frac{\partial\varphi(z,t)}{\partial t}+\frac{1}{\omega_j^2}\frac{\partial^2\varphi(z,t)}{\partial t^2}. \qquad (19)$$

At present, there are no general techniques available for solving the sin-Hilbert equation (19). So far, twelve exact solutions have been obtained for Eq. (19).[1,4–11] We shall confine ourselves only to plane-wave solutions:

1. a stationary 2π-kink[1,4]

$$\varphi=\pi+2\arctan\frac{z}{l}; \qquad (20)$$

2. a strongly dissipative traveling 2π-kink in a junction carrying a constant current[8]:

$$\varphi=\pi+\arcsin i+2\arctan\frac{z-v_1t}{l(1-i^2)^{-1/2}}, \qquad (21)$$

where i is the current density distributed uniformly over the junction and normalized to j_c, $v_1=\omega_j^2l/(\beta\sqrt{i^{-2}-1})$ is the wave velocity;

3. a travelling nondissipative 4π-kink[6,7]:

$$\varphi=4\arctan\frac{z-l\omega_jt}{l}; \qquad (22)$$

4. a stationary periodic chain with a nonzero mean magnetic field[9]

$$\varphi=\pi+2\arctan\left[(\sqrt{(L/l)^2+1}+L/l)\tan\frac{z}{2L}\right]; \qquad (23)$$

5. a nondissipative traveling periodic chain with a mean field[9]

$$\varphi=4\arctan\left[\left(\frac{l\omega_j+v_2}{l\omega_j-v_2}\right)^{1/2}\tan\frac{z-v_2t}{2L}\right]. \qquad (24)$$

The wave velocity is connected with L through the relation $v_2^2=\omega_j^2L(\sqrt{L^2+4l^2}-L)/2$;

6. a strongly dissipative travelling periodic vortex structure in a junction with current[10]:

$$\varphi=\pi+\theta+2\arctan\left[\frac{1}{\tanh(\alpha/2)}\tan\frac{z-v_3t}{2L}\right], \qquad (25)$$

where θ and α are defined by the formula $\sin\theta\cosh\alpha=i$, $\cos\theta\sinh\alpha=l/L$, while the vortex velocity is defined by the relation $v_3=-\omega_j^2Li\tanh\alpha/\beta$;

7. a stationary periodic chain with a mean field equal to zero[9]:

$$\varphi=\pi+2\arctan\left[\sqrt{(L/l)^2-1}\sin\frac{z}{L}\right]; \qquad (26)$$

8. a nondissipative travelling periodic vortex structure without the mean field[9]:

$$\varphi=4\arctan\left[\frac{1}{\sqrt{v_4/(\omega_jl)-1}}\sin\frac{z-v_4t}{L}\right], \qquad (27)$$

where

$$L=\omega_j^{-1}v_4\sqrt{1-(l\omega_j/v_4)}.$$

The above set of solutions of the sin-Hilbert equation (19) will be used for determining magnetic and electric fields and currents corresponding to known vortex solutions of Eq. (19). It should be emphasized that all these solutions were obtained in the theory of Josephson junctions formed by bulk superconductors. These solutions will be used below for studying the vortex structures in a Josephson junction formed in a thin film.

4. FIELDS AND CURRENTS IN ISOLATED VORTICES

Proceeding from general formulas (12), (15)–(17) connecting the fields with the phase difference and current with the magnetic field, we obtain asymptotic expressions for fields and currents in the case when the source of the electromagnetic field is an arbitrary small-scale vortex. We shall use these expressions for solving Eqs. (20)–(22).

A common feature of all these states is the existence of a characteristic scale $l_*\ll\lambda_e$ such that for $|z-vt|\gg l_*$, the derivative of the phase difference decreases rapidly: $\partial\varphi/\partial z\propto l_*(z-vt)^{-2}$. Considering further that $\varphi(z,t)$ for these states is an odd function of $(z-vt)$, it can be stated that the magnetic flux across a superconducting film exists and is nonzero: $\Phi=(\phi_0/2\pi)\int_{-\infty}^{+\infty}dz\,\partial\varphi/\partial z$

Using the asymptotic representations[14]

$$R(|y|,\rho)\approx\begin{cases}\ln\dfrac{4\lambda_e}{\gamma\rho}, & y=0, \quad \rho\ll2\lambda_e \quad (\gamma=1.78...), \\[2mm] \dfrac{2\lambda}{\sqrt{y^2+\rho^2}}, & \sqrt{y^2+\rho^2}\gg2\lambda_e,\end{cases}$$

$$\frac{\partial R(0,\rho)}{\partial|y|}\approx-\frac{1}{\rho}, \quad \rho\ll2\lambda_e,$$

we obtain an expression for the magnetic field for an arbitrary phase difference $\varphi(z,t)=\psi(\zeta)(\zeta=z-vt)$ whose derivative $d\psi/d\zeta$ decreases rapidly for $|\zeta|\gg l_*$:

(a) If $\psi(\zeta)$ varies significantly over scales smaller than λ_e (i.e., $l_*\ll\lambda_e$), we can write in the plane of the junction ($y=0$) in the vicinity of the vortex ($\sqrt{x^2+\zeta^2}\ll2\lambda_e$)

$$H_x(x,\pm0,\zeta)=\mp\frac{\phi_0x}{8\pi^2\lambda_e}\psi_x(|x|,\zeta),$$

$$H_y(x,0,\zeta)=-\frac{\phi_0}{8\pi^2\lambda_e}\psi_y(|x|,\zeta), \qquad (28)$$

$$H_z(x,\pm0,\zeta)=\mp\frac{\phi_0}{8\pi^2\lambda_e}\psi_z(|x|,\zeta),$$

where we have introduced the magnetic form factors of the vortex

$$\psi_x(|x|,\zeta)\equiv\int_{-\infty}^{+\infty}dz'\frac{\psi'(z')}{x^2+(\zeta-z')^2},$$

$$\psi_y(|x|,\zeta)\equiv\int_{-\infty}^{+\infty}dz'\frac{\psi'(z')}{\sqrt{x^2+(\zeta-z')^2}},$$

500   Low Temp. Phys. **23** (7), July 1997

A. S. Malishevskiĭ   500

$$\psi_z(|x|,\zeta) \equiv \int_{-\infty}^{+\infty} dz' \, \frac{(\zeta-z')\,\psi'(z')}{x^2+(\zeta-z')^2}, \quad \psi'(z) \equiv d\psi/dz;$$

(b) at large distances from the vortex ($\sqrt{x^2+y^2+\zeta^2} \gg 2\lambda_e$ and $|\zeta| \gg l_*$), we can write

$$\mathbf{H} \approx \frac{\Phi}{2\pi} \, \mathrm{sgn} \, y \, \frac{\mathbf{r}'}{r'^3}, \tag{29}$$

where $\mathbf{r}' \equiv \{x,y,\zeta\}$. The last formula was obtained for states in which $\Phi \neq 0$. This is just the case in which we are interested.

Let us now derive asymptotic formulas for the electric field produced by an isolated vortex. ?We assume that d is the smallest scale, i.e., $d \ll l_*$, λ_e, and confine ourselves to states with a nonzero magnetic flux. Let us first consider the field inside a tunnel layer as well as in vacuum just above and below the junction. Taking into account the asymptotic form of the kernel

$$P(|y|,\rho) \approx \begin{cases} 1, & y=0, \quad \rho \ll 2\lambda_e, \\ \dfrac{2\lambda_e}{\rho}\left(1-\dfrac{|y|}{\sqrt{y^2+\rho^2}}\right), & \sqrt{y^2+\rho^2} \gg 2\lambda_e \end{cases}$$

we obtain from (15) the following expressions for small-scale states ($l_* \ll \lambda_e$) in this region of space:
(a) inside the tunnel layer ($-d<x<d$, $y=0$):

$$E_x \approx -\frac{\phi_0 v}{4\pi cd} \, \psi'(z), \quad E_y \approx \frac{\phi_0 vx}{\pi^2 cd^2} \, \mathrm{sgn} \, y \, \psi'(\zeta),$$

$$E_z \approx -\frac{\phi_0 vx}{4\pi cd} \, \psi''(\zeta); \tag{30}$$

(b) away from the vortex ($|\zeta| \gg l_*$) and the junction plane ($|y| \gg \lambda_e$):

$$E_x = \frac{\Phi v}{2\pi c} \frac{\partial}{\partial \zeta}\left[\frac{\zeta}{\sqrt{y^2+\zeta^2}(|y|+\sqrt{y^2+\zeta^2})}\right],$$

$$E_y = \frac{\phi_0 vxd^2}{\pi^2 cy^4} \, \mathrm{sgn} \, y \, \psi'(\zeta), \quad E_z = -\frac{\phi_0 vxd^2}{3\pi^2 cy^3} \, \psi''(\zeta). \tag{31}$$

Finally, the electric field away from the junction ($|x| \gg d$) is obtained from (16):
(a) in the junction plane ($y=0$) for $\sqrt{x^2+\zeta^2}$, $l_* \ll \lambda_e$

$$E_x \approx \frac{\phi_0 v}{4\pi^2 c} \frac{\partial \psi_z(|x|,\zeta)}{\partial \zeta},$$

$$E_y \approx \frac{\phi_0 vx}{4\pi^2 c} \, \mathrm{sgn} \, y \, \frac{\partial \psi_E(|x|,\zeta)}{\partial \zeta},$$

$$E_z \approx -\frac{\phi_0 vx}{4\pi^2 c} \frac{\partial \psi_x(|x|,\zeta)}{\partial \zeta}, \tag{32}$$

where the electric form factor ψ_E is defined as

$$\psi_E(|x|,\zeta) \equiv \int_{-\infty}^{+\infty} dz' \, \frac{\psi'(z')}{[x^2+(\zeta-z')^2]^{3/2}};$$

(b) if, however, $\sqrt{x^2+y^2+\zeta^2} \gg 2\lambda_e$ and $|\zeta| \gg l_*$, we can write

$$E_x \approx \frac{\Phi v}{2\pi cr'^3}\left[|y|-2\lambda_e(1-3\zeta^2(r')^{-2})\right],$$

$$E_y \approx -\frac{\Phi v}{2\pi c} \, \mathrm{sgn} \, y \, \frac{x}{r'^3},$$

$$E_z \approx -\frac{3\Phi v\lambda_e x}{\pi c} \, \mathrm{sgn} \, y \, \frac{\zeta}{r'^5}. \tag{33}$$

It follows from formulas (29) and (32) that away from the vortex $E \sim vH/c$, which corresponds to the case of slow motion considered by us.

In order to apply formulas (28)–(32) to the specific non-linear states (20)–(22), we observe that these states may be obtained from the function

$$\psi(\zeta) = \psi_0 + 2n \, \arctan\frac{\zeta}{l_*} \tag{34}$$

through an appropriate choice of parameters ψ_0, n and l_*. The form factors for the function (34) have the form

$$\psi_x(|x|,\zeta) = \frac{2\pi n}{(|x|+l_*)^2+\zeta^2} \frac{|x|+l_*}{|x|},$$

$$\psi_z(|x|,\zeta) = \frac{2\pi n\zeta}{(|x|+l_*)^2+\zeta^2},$$

$$\psi_y(|x|,\zeta) \approx \begin{cases} \dfrac{4n}{l_*}\left(1-\dfrac{\zeta^2}{l_*^2}\right)\ln\dfrac{2l_*}{|x|}, & \sqrt{x^2+\zeta^2} \ll l_*, \\ \dfrac{2\pi n}{\sqrt{x^2+\zeta^2}}, & |x|, \quad |\zeta| \gg l_*, \end{cases}$$

$$\psi_E(|x|,\zeta) \approx \begin{cases} \dfrac{4n}{l_*x^2}, & \sqrt{x^2+\zeta^2} \ll l_*, \\ \dfrac{2\pi n}{(x^2+\zeta^2)^{3/2}}, & |x|, \quad |\zeta| \gg l_*. \end{cases} \tag{35}$$

The exact expressions for the form factors ψ_y and ψ_E, which are valid for any relation between $|x|$, ζ, and l_*, are given in Appendix 2.

In order to obtain magnetic and electric fields for solutions (20)–(22), we must substitute form factors (35) into (28)–(33), and take into account the fact that the following relations hold for function (34):

$$\Phi = -n\phi_0, \quad \psi'(\zeta) = \frac{2nl_*}{\zeta^2+l_*^2}, \quad \psi''(\zeta) = -\frac{4nl_*\zeta}{(\zeta^2+l_*^2)^2}.$$

The values of the parameters n, l_*, and v can be found by comparing formulas (20)–(22) with (34): $n=1$, $l_*=l$, $v=0$ for a 2π-kink (20), $n=1$, $l_*=l/\sqrt{1-i^2}$, $v=\omega_j^2 l/(\beta\sqrt{i^2-1})$ for solution (21), and finally $n=2$, $l_*=l$, $v=\omega_j l$ for a 4π-kink. The surface current can be determined from relation (17).

In the vicinity of the small-scale $2\pi n$-kink ($\sqrt{x^2+\zeta^2}$, $l_* \ll \lambda_e$), for example, we can write

$$\mathbf{I} \approx \frac{n\phi_0 c}{8\pi^2\lambda_e} \frac{-\zeta\mathbf{l}_x+\mathrm{sgn}\,x(l_*+|x|)\mathbf{l}_z}{(|x|+l_*)^2+\zeta^2}. \tag{36}$$

This formula generalizes the expression obtained in Ref. 13 for the current in a 2π-kink for $l\ll|x|$, $|z|\ll\lambda_e$. It follows from (6) and (36) that the maximum density of the current passing through the junction is $n\phi_0 c/(8\pi^2\lambda^2 l_*)$. We require that this current density must not exceed the depairing current density $j_d=c\phi_0/(12\sqrt{3}\pi^2\lambda^2\xi)$, where ξ is the correlation length. In this case, we obtain the following constraint on the Ginzburg–Landau parameter $\kappa=\lambda/\xi$:

$$\kappa>\frac{3\sqrt{3}n}{2}\frac{\lambda}{l_*}.$$

The magnetic field in the plane of the junction ($y=0$) at the smallest distances from the vortex is obtained by substituting (35) into (28):

$$H_y(x,0,\zeta)\approx\frac{n\phi_0}{2\pi^2\lambda_e l_*}\ln\frac{|x|}{2l_*},\quad \sqrt{x^2+\zeta^2}\ll l_*. \tag{37}$$

This formula shows that for any of the Abrikosov–Josephson vortices (20)–(22), the magnetic field in the junction plane diverges logarithmically for $\sqrt{x^2+\zeta^2}\to0$. Such a divergence also occurs in the theory of regular Abrikosov vortices. It is eliminated by truncation at the correlation length ξ, which physically indicates the presence of a normal *core* of size $\sim\xi$ (it should be recalled that such a violation of superconductivity does not arise in the nonlocal theory of junctions formed by bulk superconductors[4–7]). We carry out such a regularization in our case also. In this case, formula (37) is valid for $|x|>\xi$, and the field inside the normal core can be presented with logarithmic accuracy in the form

$$H_y\approx\frac{n\phi_0}{2\pi^2 l_*\lambda_e}\ln\frac{\xi}{l_*}.$$

Before concluding this section, let us compare the electric field in the states (21) and (22). For this purpose, we first determine the values of the dimensionless current density i and parameter β characterizing dissipation for which both these states can be realized (for a fixed value of the Josephson frequency ω_j). The condition for the applicability of the solution (21) is a large dissipation ($\beta\gg v l_*^{-1}$) or, if we take into account the values of v and l_*,

$$\beta\gg i^{1/2}\omega_j. \tag{38}$$

On the contrary, solution (22) is nondissipative, i.e., applicable for $\beta\ll v l_*^{-1}$. Substituting v and l_* into this expression, we obtain

$$\beta\ll\omega_j. \tag{39}$$

Conditions (38) and (39) can be realized simultaneously for $i^{1/2}\ll1$. In this case, we obtain for the state (21) $v\approx il\omega_j^2/\beta\ll l\omega_j$, $l_*\approx l$. In other words, the vortex velocity (21) is smaller than (22), even as the characteristic scales of these vortices are identical. Among other things, this means that, in accordance with (30)–(33) and (35), the electric field in state (22) is larger than in state (21).

5. FIELDS AND CURRENTS IN PERIODIC VORTEX CHAINS

Proceeding from formulas (12), (15)–(17), we shall obtain expressions for fields and currents in the case when

$[\psi(\zeta)-2\pi L]$ is a periodic function of ζ. The expressions obtained in this way will be applied for specific nonlinear states (23)–(27).

While analyzing the $2\pi L$-periodic chains, it is convenient to present the derivative of the phase difference in the form[14]

$$\psi'(\zeta)=\frac{1}{L}\sum_{n=0}^{+\infty}A_n\cos\frac{n\zeta}{L}. \tag{40}$$

In particular, if

$$\psi(\zeta)=\psi_0+2m\arctan\left(\gamma\tan\frac{\zeta}{2L}\right), \tag{41}$$

we obtain (in accordance with Ref. 18) $A_0=m$, $A_n=2m(\gamma-1)^n(\gamma+1)^{-n}$, $n\geq1$. Solutions (23)–(25) are obtained from function (41) through an appropriate choice of parameters ψ_0, m, γ. If, however,

$$\psi(\zeta)=\psi_0+2m\arctan\left(\delta\sin\frac{\zeta}{L}\right), \tag{42}$$

then $A_n=0$ for $n=2k\geq0$, and the coefficients of expansion of ψ' with odd numbers are defined by formula $A_{2k+1}=4m[\delta/(1+\sqrt{1+\delta^{-2}})]^{2k+1}$, $k\geq0$.[18] The nonlinear states (26), (27) can be obtained from the function (42) through an appropriate choice of parameters ψ_0, m and δ.

Substituting the expansion (40) into expression (12) for the magnetic field, we obtain $\mathbf{H}=\bar{\mathbf{H}}(x,y)+\delta\mathbf{H}(x,y,\zeta)$, where the bar indicates averaging over the period $2\pi L$ of spatial oscillations, and $\delta\mathbf{H}$ denotes the oscillating correction to the mean value. The quantities $\bar{\mathbf{H}}$ and $\delta\mathbf{H}$ are defined as follows[14]:

$$\bar{H}_x=-\frac{\phi_0}{4\pi^2\lambda_e}\,\mathrm{sgn}\,y\,\bar{\psi}'\int_0^{+\infty}\frac{dQ}{1+Q}$$
$$\times\exp\left(-\frac{|y|Q}{2\lambda_e}\right)\sin\frac{xQ}{2\lambda_e},$$

$$\bar{H}_y=-\frac{\phi_0}{4\pi^2\lambda_e}\,\bar{\psi}'\int_0^{+\infty}\frac{dQ}{1+Q}\exp\left(-\frac{|y|Q}{2\lambda_e}\right)\cos\frac{xQ}{2\lambda_e},$$

$$\bar{H}_z=0, \tag{43}$$

$$\delta H_x=-\frac{\phi_0}{4\pi^2\lambda_e L}\,\mathrm{sgn}\,y\sum_{n=1}^{+\infty}A_n F_x\left(\frac{n|y|}{L},\frac{nx}{L}\right)\cos\frac{n\zeta}{L},$$

$$\delta H_y=-\frac{\phi_0}{4\pi^2\lambda_e L}\sum_{n=1}^{+\infty}A_n F_y\left(\frac{n|y|}{L},\frac{nx}{L}\right)\cos\frac{n\zeta}{L},$$

$$\delta H_z=-\frac{\phi_0}{4\pi^2\lambda_e L}\,\mathrm{sgn}\,y\sum_{n=1}^{+\infty}A_n F_z\left(\frac{n|y|}{L},\frac{nx}{L}\right)\sin\frac{n\zeta}{L},$$

where $\bar{\psi}'=A_0/L$ is the derivative of the phase difference averaged over the period (if the phase difference is defined by (41), then $\bar{\psi}'=m/L$. For the state (42), the mean value of ψ' is equal to zero.) The values of the functions F_x, F_y, F_z are presented in Appendix C.

The expansion of the electric field in harmonics for $-d<x<d$ is obtained from formula (15):

$$\bar{E}_x = -\frac{\phi_0 v}{2\pi^2 cd} f(y)\bar{\psi}',$$

$$\bar{E}_y = \frac{\phi_0 v d^2 x}{\pi^2 c}\bar{\psi}'\frac{\operatorname{sgn} y}{(d^2+y^2)^2}, \quad \bar{E}_z = 0,$$

$$\delta E_x = -\frac{\phi_0 v}{2\pi^2 cd} f(y)\sum_{n=1}^{+\infty}\frac{A_n}{L}\cos\frac{n\zeta}{L}$$
$$-\frac{\phi_0 v}{4\pi^2 c\lambda_e}\sum_{n=1}^{+\infty}\frac{A_n}{L}\cos\frac{n\zeta}{L}F_z\left(\frac{n|y|}{L},0\right),$$

$$\delta E_y = \frac{\phi_0 v x d^2}{\pi^2 c}\frac{\operatorname{sgn} y}{(d^2+y^2)^2}\sum_{n=1}^{+\infty}\frac{A_n}{L}\cos\frac{n\zeta}{L},$$

$$\delta E_z = \frac{\phi_0 v x}{2\pi^2 cd}f(y)\sum_{n=1}^{+\infty}\frac{nA_n}{L}\sin\frac{n\zeta}{L}, \quad (44)$$

where $f(y)\equiv\arctan(d|y|^{-1})-d|y|(d^2+y^2)^{-1}$.

Formulas (44) were obtained under the assumption that $d\ll L$. Away from the junction ($|x|\gg d$), the electric field is obtained from (16):

$$\mathbf{\bar{E}} = -\frac{\phi_0 v}{2\pi^2 c}\bar{\psi}'\frac{|y|\mathbf{l}_x-x\operatorname{sgn}y\mathbf{l}_y}{x^2+y^2},$$

$$\delta E_x = \frac{\phi_0 v}{2\pi^2 cL^2}\sum_{n=1}^{+\infty}nA_n\left[F_z\left(\frac{n|y|}{L},\frac{nx}{L}\right)\right.$$
$$\left.-\frac{|y|}{\sqrt{x^2+y^2}}K_1\left(\frac{n\sqrt{x^2+y^2}}{L}\right)\right]\cos\frac{n\zeta}{L},$$

$$\delta E_y = \frac{\phi_0 v x\operatorname{sgn}y}{2\pi^2 cL^2\sqrt{x^2+y^2}}\sum_{n=1}^{+\infty}nA_nK_1\left(\frac{n\sqrt{x^2+y^2}}{L}\right)\cos\frac{n\zeta}{L},$$

$$\delta E_z = \frac{\phi_0 v}{2\pi^2 cL^2}\sum_{n=1}^{+\infty}nA_nF_x\left(\frac{n|y|}{L},\frac{nx}{L}\right)\sin\frac{n\zeta}{L}. \quad (45)$$

The subsequent discussion is based on the following remark[14]: periodic dependences of fields and currents on ζ may appear against the background of their mean values only near the tunnel layer, i.e., for $(x^2+y^2)^{1/2}\lesssim L$. Accordingly, if the mean value of ψ' is nonzero, the quantities H_x, H_y, E_x, E_y, I_z are defined by their mean values for $(x^2+y^2)^{1/2}\gg L$. In the opposite case, when $\bar{\psi}'=0$, the dependences of H_x, H_y, E_x, E_y, I_z on ζ are significant at all distances from the junction in view of the fact that the mean values of all field and current components are proportional to $\bar{\psi}'$. On the other hand, the periodic dependence on ζ must be taken into account for arbitrary $\bar{\psi}'$ and $(x^2+y^2)^{1/2}$ for finding H_z, E_z and I_x, since the mean values of these quantities are always equal to zero. Taking this into consideration, we obtain the following expressions for magnetic fields and currents for the case when $\bar{\psi}'\neq0$:

(a) for $\sqrt{x^2+y^2}\ll L$, the quantities

$$H_x\approx-\frac{\phi_0}{4\pi^2\lambda_e}\arctan\frac{x}{y}\psi'(\zeta),$$

$$H_y\approx-\frac{\varphi_0}{4\pi^2\lambda_e}\left(\bar{\psi}'\ln\frac{\lambda_e}{L}+\psi'\ln\frac{2L}{\gamma\sqrt{x^2+y^2}}\right),$$

$$H_z\approx-\frac{\phi_0}{8\pi\lambda_e L}\operatorname{sgn}y\sum_{n=1}^{+\infty}A_n\sin\frac{n\zeta}{L}, \quad (46)$$

$$I_x\approx\frac{c\phi_0}{16\pi\lambda_e L}\sum_{n=1}^{+\infty}A_n\sin\frac{n\zeta}{L},$$

$$I_z\approx\frac{c\phi_0}{16\pi^2\lambda_e}\operatorname{sgn}x\psi'(\zeta).$$

If A_n are the coefficients in the Fourier series of the derivative of the function (41), we can calculate the sum appearing in the expressions for H_z and I_x:

$$\sum_{n=1}^{+\infty}A_n\sin\frac{n\zeta}{L}=\frac{m\sin(\zeta/L)}{(\gamma^2+1)(\gamma^2-1)^{-1}-\cos(\zeta/L)};$$

(b) for $L\ll\sqrt{x^2+y^2}\ll\lambda_e$, we have

$$H_x\approx-\frac{\phi_0\bar{\psi}'}{4\pi^2\lambda_e}\arctan\frac{x}{y},$$

$$H_y\approx-\frac{\varphi_0\bar{\psi}'}{4\pi^2\lambda_e}\ln\frac{2\lambda_e}{\gamma\sqrt{x^2+y^2}},$$

$$I_z\approx\frac{c\varphi_0}{16\pi^2\lambda_e}\bar{\psi}'\operatorname{sgn}x.$$

If $y^2\gg L^2$ and $L|x|$, the first term becomes dominant in the sum (43) determining δH_z since $F_z\propto n^{-1/2}\exp(-n|y|/L)$. Consequently, $H_z\propto A_1\exp(-|y|/L)$. If, however, $|y|\ll L\ll|x|$, then, in view of the fact that $F_z\propto\exp(-n|x|/L)$, we can retain only the term with $n=1$ in the sum over n determining δH_z. Consequently, H_z, $I_x\propto A_1\exp(-|x|/L)$;

(c) for $\sqrt{x^2+y^2}\gg\lambda e$, we have

$$H_x\approx-\frac{\phi_0 x\operatorname{sgn}y}{2\pi^2(x^2+y^2)}\bar{\psi}',$$

$$H_y\approx-\frac{\phi_0|y|}{2\pi^2(x^2+y^2)}\bar{\psi}',$$

$$I_z\approx\frac{c\phi_0}{4\pi^3 x}\bar{\psi}'.$$

The components H_z and I_x attenuate in the same way as in case (b).

Let us now consider the magnetic fields and currents in the case when the mean value of the derivative of the phase difference is equal to zero:

(a) for $\sqrt{x^2+y^2}\ll L$, the values of $\mathbf{H}$ and $\mathbf{I}$ are obtained from formulas (46), in which we must put $\bar{\psi}'=0$. If A_n are Fourier coefficients for the derivative of the function (42), the sum of the series appearing in the expressions for H_z and I_x can be presented in the form

503   Low Temp. Phys. **23** (7), July 1997

A. S. Malishevskiĭ   503

$$\sum_{n=1}^{+\infty} A_n \sin \frac{n\zeta}{L} = 4m \sqrt{1+\delta^{-2}} \frac{\sin(\zeta/L)}{2\delta^{-2}+1-\cos(2\zeta/L)},$$

(b) If $y^2 \gg L^2$ and $L|x|$, we have F_x, $F_y \propto n^{-1/2} \exp(-n|y|/L)$. Hence, in analogy with the case $\bar{\psi}' \neq 0$ mentioned above, it can be stated that all magnetic field components attenuate as $\exp(-|y|/L)$ and are proportional to A_1;

(c) If $|y| \ll L \ll |x|$, we have $F_x \propto \exp(-n|x|/L)$, $F_y \propto n^{-1/2} \exp(-n|x|/L)$. Hence all components of magnetic fields and currents in this range are proportional to $A_1 \exp(-|x|/L)$.

Using (45), we obtain the following expression for the electric field for $-d < x < d$:

$$E_x \approx -\frac{\phi_0 v}{2\pi^2 dc} f(y)\psi'(\zeta) + g(y,\zeta),$$

$$E_y \approx \frac{\phi_0 v d^2 x}{\pi^2 c} \frac{\psi'(\zeta)}{(d^2+y^2)^2},$$

$$E_z \approx -\frac{\phi_0 xv}{2\pi^2 cd} f(y)\psi''(\zeta),$$

where $g \approx -\phi_0 v[\psi'(\zeta)-\bar{\psi}'] \times (8\pi^2\lambda_e c)^{-1}$, for $|y| \ll L$. For large values of $y(|y| \gg L)$, $g(y)$ attenuates exponentially and is defined by the first term in the expansion of the derivative of the phase difference: $g \propto A_1 \exp(-|y|/L)$. The electric field at large distances from the junction ($|x| \gg d$) is obtained from (45):

(a) for $\sqrt{x^2+y^2} \ll L$, we obtain

$$E_x \approx -\frac{\phi_0 v}{2\pi^2 c} \frac{|y|\psi'(\zeta)}{x^2+y^2} + \frac{\phi_0 v}{4\pi cL} \sum_{n=1}^{+\infty} \frac{nA_n}{L} \cos \frac{n\zeta}{L},$$

$$E_y \approx \frac{\phi_0 v}{2\pi^2 c} \frac{x \operatorname{sgn} y}{x^2+y^2} \psi'(\zeta),$$

$$E_z \approx -\frac{\phi_0 v}{4\pi Lc} \psi''(\zeta). \tag{47}$$

For the function (41), the sum over n appearing in (47) is defined as

$$\sum_{n=1}^{+\infty} \frac{nA_n}{L} \cos \frac{n\zeta}{L} = \frac{m}{L} \frac{(\gamma^2+1)(\gamma^2-1)^{-1}\cos(\zeta/L)-1}{[(\gamma^2+1)(\gamma^2-1)^{-1}-\cos(\zeta/L)]^2}.$$

If, however, the coefficients A_n determine the function (42), we can write

$$\sum_{n=1}^{+\infty} \frac{nA_n}{L} \cos \frac{n\zeta}{L}$$

$$= \frac{8m}{L} \sqrt{1+\delta^{-2}} \cos \frac{\zeta}{L} \times \frac{\delta^{-2}-\sin^2(\zeta/L)}{[1+2\delta^{-2}-\cos(2\zeta/L)]^2};$$

(b) If $y^2 \gg L^2$ and $L|x|$, we have

$$\mathbf{E} \approx -\frac{\phi_0 v}{2\pi^2 c} \bar{\psi}' \frac{|y|\mathbf{1}_x - x\operatorname{sgn} y\mathbf{l}_y}{x^2+y^2} + O[\exp(-|y|/L)];$$

(c) For $|y| \ll L \ll |x|$, the following expression is obtained:

$$\mathbf{E} \approx \frac{\phi_0 v}{2\pi^2 c} \frac{\operatorname{sgn} y}{x} \bar{\psi}'\mathbf{l}_y + O[\exp(-|x|/L)].$$

The asymptotic expressions obtained for fields and currents in this section lead to a number of conclusions about the structure of fields for periodic states of the junction:

(a) the z-components of magnetic and electric fields averaged over the period $2\pi L$ of spatial oscillations are equal to zero, while the x- and y-projections of mean fields vanish only for solutions for which $\bar{\psi}'=0$;

(b) it follows from (46) that in the vicinity of a junction, the magnetic field has a logarithmic singularity which, as in the case of isolated vortices, should be associated with the violation of superconductivity in the vicinity of the junction. The electric field is finite everywhere;

(c) for states (20)–(22), the magnetic field in films ($y=0$) averaged over the oscillation period

$$\bar{H}_y \approx \frac{m\phi_0}{4\pi\lambda_e L} \ln \frac{\gamma|x|}{2\lambda_e}, \quad |x| \ll \lambda_e$$

differs qualitatively from the mean field in bulk superconductors[9]:

$$\bar{H}_y \approx \frac{m\phi_0}{4\pi\lambda L}, \quad |x| \ll \lambda.$$

This is associated with the fact that, in contrast to thin films, Abrikosov–Josephson vortices in bulk superconductors have a regular core.

6. CONCLUSION

In this work, we have presented a theoretical analysis of fields and currents in a Josephson junction in a thin superconducting film. The maximum attention is paid to the case of a large critical Josephson current, when the phase difference satisfies the sin-Hilbert equation. The general results obtained here are applicable to eight specific nonlinear solutions of spatially nonlocal sin-Hilbert equation, which were obtained in the theory of bulk superconductors.

It is shown that Abrikosov–Josephson vortices in a thin film differ from vortices in the nonlocal electrodynamics of bulk superconductors having a regular core (i.e., a magnetic field without singularities). On the other hand, vortices in a film have a singularity like normal Abrikosov vortices. This singularity must be regularized at distances of the order of correlation length.

APPENDIX A

We shall show that the quantity $q_z S_x - q_x S_z$ appearing in formula (9) is connected with the phase jump for $x=0$. For this purpose, we first express $\phi(x,z)$ in terms of $\phi_1(-0, z)$ and $\phi_2(+0, z)$. It follows from (3) that ϕ_1 and ϕ_2 satisfy the Laplace equation in half-plane:

$$\Delta \phi_1(x,z)=0 \quad \text{for } x<0,$$

$$\Delta \phi_2(x,z)=0 \quad \text{for } x>0. \tag{A1}$$

Solving this equation, we obtain

$$\phi_1(x,z) = -\frac{x}{\pi} \int_{-\infty}^{+\infty} dz' \frac{\phi_1(-0,z')}{x^2+(z-z')^2},$$

$$\phi_2(x,z) = \frac{x}{\pi} \int_{-\infty}^{+\infty} dz' \frac{\phi_2(+0,z')}{x^2+(z-z')^2}. \tag{A2}$$

Calculating $\partial\phi/\partial x$ and $\partial\phi/\partial z$ on the basis of (A2) and going over to Fourier representation, we obtain

$$\left(\frac{\partial\phi}{\partial x}\right)_{q_x q_z} = -|q_z|\left[\frac{\phi_2(+0,q_z)}{|q_z|+iq_x} - \frac{\phi_1(-0,q_z)}{|q_z|-iq_x}\right],$$

$$\left(\frac{\partial\phi}{\partial z}\right)_{q_x q_z} = iq_z\left[\frac{\phi_2(+0,q_z)}{|q_z|+iq_x} + \frac{\phi_1(-0,q_z)}{|q_z|-iq_x}\right].$$

This leads to the following expression for the required quantity:

$$q_z S_x - q_x S_z = \frac{\phi_0}{2\pi}\left[q_z\left(\frac{\partial\phi}{\partial x}\right)_{q_x q_z} - q_x\left(\frac{\partial\phi}{\partial z}\right)_{q_x q_z}\right]$$

$$= \frac{\phi_0 q_z}{2\pi}[\phi_1(-0,q_z) - \phi_2(+0,q_z)].$$

APPENDIX B

For the function (34), form factors ψ_y and ψ_E have the form

$$\psi_y(|x|,\zeta) = -\frac{2^{3/2}n}{R^2}\left[\frac{\sqrt{R^2-x^2-\zeta^2+l_*^2}}{2}\ln\frac{R^2+\zeta^2+l_*^2-\sqrt{2}(l_*\sqrt{R^2-x^2-\zeta^2+l_*^2}+|\zeta|\sqrt{R^2+x^2+\zeta^2-l_*^2})}{x^2}\right.$$

$$\left.+\sqrt{R^2+x^2+\zeta^2-l_*^2}\arctan\frac{\sqrt{R^2+x^2+\zeta^2-l_*^2}-\sqrt{2}|\zeta|}{\sqrt{R^2-x^2-\zeta^2+l_*^2}-\sqrt{2}l_*}\right],$$

$$\psi_E(|x|,\zeta) = \frac{2^{3/2}n}{x^2}\frac{\partial}{\partial l_*}\left\{\frac{l_*\psi_y(|x|,\zeta)}{2^{3/2}n} + \frac{|\zeta|}{R^2}\left[\frac{\sqrt{R^2+x^2+\zeta^2-l_*^2}}{2}\right.\right.$$

$$\times\ln\left(\frac{x^2}{R^2+\zeta^2+l_*^2-\sqrt{2}(l_*\sqrt{R^2-x^2-\zeta^2+l_*^2}+|\zeta|\sqrt{R^2+x^2+\zeta^2-l_*^2})}\right)$$

$$\left.\left.+\sqrt{R^2-x^2-\zeta^2+l_*^2}\arctan\frac{\sqrt{R^2+x^2+\zeta^2-l_*^2}-\sqrt{2}|\zeta|}{\sqrt{R^2-x^2-\zeta^2+l_*^2}-\sqrt{2}l_*}\right]\right\},$$

where $R \equiv [(x^2+\zeta^2-l_*^2)^2+4l_*^2\zeta^2]^{1/4}$.

APPENDIX C

The functions F_x, F_y, and F_z, which define the Fourier coefficients in the field expansion, are defined as follows:

$$F_x(a,b) = \int_0^{+\infty} \frac{du \, \sinh u}{\cosh u + L/(2n\lambda_e)}$$

$$\times\exp(-a \cosh u)\sin(b \sinh u),$$

$$F_y(a,b) = \int_0^{+\infty} \frac{du \, \cosh u}{\cosh u + L/(2n\lambda_e)}$$

$$\times\exp(-a \cosh u)\cos(b \sinh u),$$

$$F_z(a,b) = \int_0^{+\infty} \frac{du}{\cosh u + L/(2n\lambda_e)}$$

$$\times\exp(-a \cosh u)\cos(b \sinh u).$$

For small-scale periodic states ($L \ll \lambda_e$), in view of the fact that $n \geq 1$, we can disregard $L/(2n\lambda_e)$ in integrals with respect to u. In this case, we obtain the following asymptotic representations:

(a) if $\sqrt{a^2+b^2} \ll 1$, we obtain

$$F_x \approx \arctan\frac{b}{a}, \quad F_y \approx \ln\frac{2}{\gamma\sqrt{a^2+b^2}}, \quad F_z \approx \frac{\pi}{2};$$

(b) if $a^2 \gg 1, |b|$, we get

$$F_x \approx \sqrt{\pi/2a}\frac{b}{a}\exp(-a),$$

$$F_y \approx F_z \approx \sqrt{\pi/2a}\exp(-a);$$

(c) if $a \ll 1 \ll |b|$, we can write

$$F_{x'} \approx \frac{\pi}{2}\operatorname{sgn} b \exp(-|b|),$$

$$F_y \approx \sqrt{\pi/2|b|} \, \exp(-b),$$

$$F_z \approx \frac{\pi}{2} \exp(-|b|).$$

These asymptotic expressions can be used to obtain approximate formulas for fields and currents in periodic chains.

*E-mail: malish@sci.lpi.ac.ru

[1] G. M. Lapir, K. K. Likharev, L. A. Maslova, and V. K. Semenov, Fiz. Nizk. Temp. **1**, 1235 (1975) [Sov. J. Low Temp. Phys. **1**, 590 (1975)].

[2] Yu. M. Ivanchenko and T. K. Soboleva, Pis'ma Zh. Éksp. Teor. Fiz. **51**, 100 (1990) [JETP Lett. **51**, 114 (1990)]; Phys. Lett. **A147**, 65 (1990).

[3] Yu. M. Aliev, V. P. Silin, and S. A. Uryupin, Sverkhprovodimost': Fiz., Khim., Tekh. **5**, 228 (1992).

[4] A. Gurevich, Phys. Rev. **B46**, 3187 (1992).

[5] Yu. M. Aliev, V. P. Silin, and S. A. Uryupin, Pis'ma Zh. Éksp. Teor. Fiz. **57**, 187 (1993) [JETP Lett. **57**, 193 (1993)].

[6] Yu. M. Aliev and V. P. Silin, Phys. Lett. **A177**, 253 (1993).

[7] Yu. M. Aliev and V. P. Silin, Zh. Éksp. Teor. Fiz. **104**, 2526 (1993) [JETP **77**, 142 (1993)].

[8] A. Gurevich, Phys. Rev. **B48**, 12857 (1993).

[9] G. L. Alfimov and V. P. Silin, Zh. Éksp. Teor. Fiz. **106**, 671 (1994) [JETP **79**, 369 (1994)].

[10] V. P. Silin, Pis'ma Zh. Éksp. Teor. Fiz. **60**, 442 (1994) [JETP Lett. **60**, 460 (1994)].

[11] A. Gurevich, Physica **C243**, 191 (1995).

[12] R. G. Mints and I. B. Snapiro, Physica **A200**, 426 (1993).

[13] R. G. Mints and I. B. Snapiro, Phys. Rev. **B49**, 6188 (1994).

[14] A. S. Malishevskii and V. P. Silin, *Brief Communications in Physics, Physical Inst. Rus. Acad. Sci.* [in Russian], No. 1–2, 64 (1996).

[15] Yu. M. Aliev, G. L. Alfimov, K. N. Ovchinnikov *et al.*, Fiz. Nizk. Temp. **22**, 626 (1996) [Low Temp. Phys. **22**, 477 (1996)].

[16] A. A. Abrikosov, *Basic Principles of the Theory of Metals* [in Russian], Nauka, Moscow (1987)].

[17] R. G. Mints and I. B. Snapiro, Phys. Rev. **B51**, 3054 (1995).

[18] A. P. Prudnikov, Yu. A. Brychkov, and O. I. Marichev, *Integrals and Series. Elementary Functions* [in Russian], Nauka, Moscow (1981)].

Translated by R. S. Wadhwa

Quasiwaves in superconductors

E. V. Bezuglyi and A. V. Boichuk

*B. Verkin Institute for Low Temperature Physics and Engineering, National Academy of Sciences of the Ukraine, 310164 Kharkov, Ukraine**

Temperature dependence of the amplitude and ballistic velocity of a high-frequency signal (quasiwave) in a superconductor, associated with the energy dependence of the velocity of electron excitations, is studied theoretically. The spatial distribution of the quasiwave field and the transformation coefficient are calculated for quasiwave excitation by an electromagnetic wave as well as by longitudinal or transverse elastic deformation. The obtained results are in accord with the data on electron sound velocity measurements in the superconducting states of Ga, Mo, and Al. © *1997 American Institute of Physics.* [S1063-777X(97)00207-7]

1. INTRODUCTION

The effect of nonresonant transfer of a high-frequency excitation (quasiwave) by charge carriers with the Fermi velocity in metals were predicted theoretically by Kaganov, *et al.* [1–3] The physical nature of this effect is associated with the presence of a group of nonequilibrium electrons with the maximum component of the Fermi velocity along the direction of propagation of the exciting wave, which form a coherent signal of the quasiwave experiencing, apart from relaxation damping, a power damping due to divergence of the effective electron beam. As these electrons are out of resonance with the exciting wave, the efficiency of its transformation into a quasiwave is relatively low, and hence the first reliable quantitative results of its observation in a normal metal have been obtained only recently[4] in experiments with transverse as well as longitudinal polarization of the exciting acoustic signal.

The behavior of a quasiwave in a superconductor was studied even in the early research by Burma *et al.*[5] who were the first to report on the observation of a signal having a velocity of the order of the Fermi velocity and with a linear energy–momentum relation both in the normal metal and in the superconductor in which the velocity decreased significantly with temperature. Subsequent experiments with Ga and Mo[6,7] confirmed the existence of ''electron sound'' in superconductors, which was associated with the Fermi-liquid zeroth sound. It should be noted, however, that the theoretical model proposed in Refs. 6 and 7 was based on a stringent assumption concerning the absence of interband Cooper interaction between charge carriers forming zeroth sound. According to Leggett,[8] the spectrum of zeroth sound has an activation character with a gap of the order of Δ, and hence this signal must attenuate over distances of the order of coherence length ξ_0 under the given experimental conditions.[6,7]

In this communication, we propose an alternative interpretation of electron sound in superconductors as a manifestation of the ballistic (quasiwave) mechanism of high-frequency perturbation transfer by electron excitations of the superconductor. A decrease in the velocity of the signal for $T \rightarrow 0$ in this case is due to a decrease in the velocity of excitations $v = v_F \xi/\varepsilon$ ($\xi = (\varepsilon^2 - \Delta^2)^{1/2}$) upon a decrease in their energy ε.

2. SIMPLE MODEL

A complete analysis of excitation of a quasiwave in a superconductor includes the solution of the kinetic equation for the nonequilibrium correction χ to the distribution function $n_0(\varepsilon) = [1 + \tanh(\varepsilon/2T)]/2$ in the half-space $x > 0$, i.e.,

$$-i\omega\chi + \frac{\xi}{\varepsilon} v_x \frac{\partial \chi}{\partial x} + \nu \frac{\xi}{\varepsilon}(\chi - \langle\chi\rangle) = i\omega \frac{\partial n_0}{\partial \varepsilon}\left(\frac{\xi}{\varepsilon}(\Lambda_{ik} u_{ik}\right.$$
$$\left. + \widetilde{\varphi}) + \mathbf{v}\widetilde{\mathbf{p}}_s\right), \tag{1}$$

$$\Lambda_{ik} = \lambda_{ik} - \langle\lambda_{ik}\rangle, \quad \widetilde{\varphi} = \varphi + \langle\lambda_{ik}\rangle u_{ik}, $$

$$\widetilde{\mathbf{p}}_s = \mathbf{p}_s + i\omega m \mathbf{u} \tag{2}$$

(φ is the gradient-invariant electric potential, $\mathbf{p}_s$ the superfluid momentum, λ_{ik} the deformation potential, u_{ik} the strain tensor, and ν the relaxation frequency) together with Maxwell's equations

$$\delta N = 0, \quad \text{curl curl } \mathbf{E} = \frac{4\pi i\omega}{c^2} j, \tag{3}$$

where δN and $\mathbf{j}$ are the nonequilibrium charge and current densities, respectively:

$$\delta N = -e\nu_F\left(\widetilde{\varphi} + \int d\xi \frac{\xi}{\varepsilon}\langle\chi\rangle\right),$$

$$j_i = e\nu_F\left(\rho_s\langle v_i v_k\rangle \widetilde{p}_{sk} - \int d\xi(v_i\chi)\right) \tag{4}$$

(ρ_s is the density of superfluid condensate), and the equation in the theory of elasticity

$$\left(s_0^2 \frac{\partial^2}{\partial x^2} + \omega^2\right)u_i + \frac{1}{\rho} f_i = 0, \tag{5}$$

where

$$f_i = -\nu_F \frac{\partial}{\partial x_k}\int d\xi \frac{\xi}{\varepsilon}\langle\Lambda_{ik}\chi\rangle \tag{6}$$

is the force exerted by nonequilibrium electrons on the lattice, s_0 the velocity of sound, ρ the density of the metal, and ν_F the density of states; the angle brackets indicate averaging over the Fermi surface.

A complete self-consistent solution of the problem with the boundary condition on the metal surface $x = 0$ corresponding to the given way of quasiwave excitation is much more complicated than the corresponding problem for a normal metal in view of energy dispersion of the rate and frequency of relaxation of quasiparticles as well as the excitation of an additional degree of freedom, viz., the phase of the order parameter. This solution will be described in the following sections. In order to clarify the qualitative pattern of the temperature dependence of the phase and amplitude of a quasiwave, we first use a model approach, replacing the solution of the self-consistent equations (3) for electromagnetic fields by a perturbation of the form $i\omega A(\mu = v_x/v_F, z = \xi/\varepsilon)\delta(x)\partial n_0/\partial\varepsilon$ localized in the plane $x = 0$ into the right-hand side of Eq. (1) (the polynomial $A(\mu,z) = -A(-\mu,-z)$ reflects the symmetry of the right-hand side of the initial kinetic equation (1)). Confining our analysis to the collisionless limit and substituting the solution of the model equation into formulas (4) and (6), we obtain general expressions for the quasiparticle contribution to the response of the system at a distance x from the source of perturbation, which contain integrals of the form

$$C_n(x) = \frac{\Delta}{2T} \int_0^\infty \frac{d\xi}{\cosh^2(\varepsilon\Delta/2T)}$$
$$\times \int_0^1 \frac{d\mu}{i\mu} \left(\frac{\xi}{\varepsilon}\right)^n \exp\left(i\frac{\Phi(\varepsilon)}{\mu}\right),$$
$$\Phi(\varepsilon) = \Phi_0 \frac{\varepsilon}{\xi}, \tag{7}$$

where $\varepsilon = (\xi^2 + 1)^{1/2}$ is the excitation energy in the units of $\Delta(T)$ and $\Phi_0 = \omega x/v_F$ is the phase of a quasiwave in a normal metal.[1]

The physical meaning of expression (7) is the superposition of partial waves transferred to the point of observation by excitations with various velocities. An analysis of this expression can be carried out only for $\Phi \gg 1$, when mutual interference suppresses the contribution of a larger part of excitations and singles out a small region in the phase space (ε, μ) occupied by nearly synphase excitations forming a coherent signal of a quasiwave. The size and position of this region are determined by the combination of two factors: a rapid decrease in the number of excitations with high energies $\varepsilon > T/\Delta$, and the interference of partial contributions from low-energy excitations with a considerable spread in velocity, which increases for $\xi \to 0$, $\mu \to 0$.

In a normal metal without velocity dispersion $(\xi/\varepsilon \to 1)$, effective excitations are concentrated in a narrow region $1 - \mu \lesssim 1/\Phi_0$ near the reference point:

$$C_n^N = \int_0^1 \frac{d\mu}{i\mu} \exp\left(i\frac{\Phi_0}{\mu}\right) \approx \frac{\exp(i\Phi_0)}{\Phi_0}, \tag{8}$$

which leads to the familiar power dependence of the signal amplitude on the distance from the source, which is associated with a constriction of the effective electron beam. It should be noted that in the case of a transverse perturbation, the right-hand side of Eq. (1) and the model polynomial $A(\mu,z)$ corresponding to it vanish for $\mu \to 1$.[3] As a result, the expression for the amplitude of a transverse quasiwave contains an additional power Φ_0^{-1} [see also formulas (27) and (35)].

In a superconducting transition, effective excitations with $1 - \mu \lesssim 1/\Phi_0$ and characteristic energies of the order of temperature $(\varepsilon \lesssim T/\Delta)$ remain synphase in a small neighborhood of T_c, where variations of the partial phase $\Phi(\varepsilon)$ are small in this energy range:

$$\delta\Phi(\varepsilon) = \Phi(T/\Delta) - \Phi_0 \sim \Phi_0 \frac{\Delta^2}{T^2} \ll 1. \tag{9}$$

As in the case of the normal metal (8), asymptotic analysis of a quasiwave in region (9) is possible only for long distances $(\Phi_0 \gg 1)$ from the source, when the corrections $\delta\Phi_0$ and δU to the phase and to the amplitude of the quasiwave are formed in the region $1 \ll \varepsilon \lesssim \sqrt{\Phi_0}$:

$$C_n(x) = C_n^{(N)} F_1(T,\Phi_0), \quad F_1(T,\Phi_0) = 1$$
$$- \frac{\Delta\sqrt{\pi\Phi_0}}{2T\sqrt{2}} e^{-i\pi/4}, \tag{10}$$

$$\frac{\delta\Phi_0}{\Phi_0} = -\frac{\delta U}{U_0} = \frac{\Delta}{4T}\sqrt{\pi\Phi_0}, \quad \Phi_0\left(\frac{\Delta}{T}\right)^2 \ll 1, \quad \Phi_0 \gg 1. \tag{11}$$

As the temperature decreases $(\Phi_0(\Delta/T)^2 \gg 1)$, the synphase condition is satisfied only for a small number of high-energy excitations, and the main contribution to (7), in which we can replace the Fermi distribution by its Boltzmann limit and carry out integration with respect to the angular variable, i.e.,

$$C_n(x) = \frac{2\Delta}{T} \int_0^\infty d\xi \left(\frac{\xi}{\varepsilon}\right)^{n+1} \exp\left(-\frac{\Delta}{T}\varepsilon + i\Phi_0\frac{\varepsilon}{\xi}\right), \tag{12}$$

$$\Phi_0\left(\frac{\Delta}{T}\right)^2 \gg 1, \tag{13}$$

is determined by the position of the saddle point $\xi_* = \zeta \exp(-\pi i/6)$ in integral (12), where the quantity $\zeta(T,\Phi_0) = (\Phi_0 T/\Delta)^{1/3}$ has the meaning of the characteristic energy of effective excitations:

$$C_n(x) = C_n^{(N)} e^{-i\Phi_0} F_2^{(n)}(T,\Phi_0); \tag{14}$$

$$F_2^{(n)}(T,\Phi_0) = 2\left(\frac{2\pi\Delta\varepsilon_*}{3T}\right)^{1/2}\left(\frac{\xi_*}{\varepsilon_*}\right)^{n+1} \exp\left(-\frac{\Delta}{T}\varepsilon_*^3\right);$$

$$\varepsilon_*(T,\Phi_0) = \sqrt{1+\xi_*^2}, \quad \xi_* = \zeta\exp(-\pi i/6),$$

$$\zeta(T,\Phi_0) = (\Phi_0 T/\Delta)^{1/3}. \tag{15}$$

It can easily be proved that when condition (13) is satisfied, the phase of the exponent in (14) is large. This allows us to substantiate the above asymptotic estimate of the integral with respect to the angular variable and to use formula

(14) for evaluating the amplitude and phase of the quasiwave at an arbitrary distance from the source and at low temperatures.

The characteristic feature of the obtained results are the nonlinear dependence of the quasiwave phase on the distance from the source of perturbation and temperature, which is associated with a change in the effective quasiparticle energy $\zeta(T,\Phi_0)$, and a rapid decrease in the quasiwave amplitude upon cooling and upon an increase in the distance from the perturbation source, which are due to the displacement of effective (almost synphase) quasiparticles to the region of the distribution function ''tail''.

It will be shown below that formulas (10)–(15) reproduce with an exponential accuracy the main features of the complete solution. From the physical standpoint, the model approach describes the ''one-particle'' mechanism of formation of the temperature dependence and spatial distribution of the quasiwave signal without taking into account collective effects of screening of electromagnetic fields in a metal, which change significantly as a result of the superconducting transition and which determine the behavior of the pre-exponential factors. The inclusion of these effects requires a selfconsistent determination of electromagnetic and elastic fields accompanying the quasiwave propagation. This will be done in the following sections.

3. ELECTROMAGNETIC QUASIWAVE

In order to solve the problem on excitation of a quasiwave incident on the superconductor surface by an electromagnetic wave polarized along the y-axis, we consider the kinetic equation (1) and Maxwell's equations (3), retaining in them only the terms containing transverse electric fields and neglecting the contribution of the elastic component. Assuming that the electron reflection at the metal boundary is specular and that the Fermi surface is spherical, we can reduce the solution of the boundary-value problem in the half-space to the problem on the entire x-axis by continuing E, j, and p_s evenly to the semi-axis $x<0$. This leads to the emergence of a jump in the derivative of E at the metal boundary in the Fourier transform of Maxwell's equations:

$$2E'(0)+q^2E=\frac{4\pi i\omega}{c^2}j, \tag{16}$$

where j is the Fourier transform of current density in the infinite metal[9]:

$$j(q,\omega)=ev_Fb(q,\omega)p_s, \tag{17}$$

$$b(q,\omega)=\rho_s\langle v_y^2\rangle-2\int_0^\infty d\xi\,\frac{\partial n_0}{\partial\varepsilon}\left(\langle v_y^2K\rangle\right.$$

$$\left.-i\nu\,\frac{\xi}{\varepsilon}\,G\langle v_yK\rangle^2\right), \tag{18}$$

$$K=i\omega\left(qv_x\,\frac{\xi}{\varepsilon}-\omega-i\nu\,\frac{\xi}{\varepsilon}\right)^{-1},\quad G^{-1}=1+i\nu\,\frac{\xi}{\varepsilon}\,\langle K\rangle,$$

$$\langle K\rangle=-\frac{p}{2k}\ln\frac{p+i\beta+k}{p+i\beta-k};\quad p(\xi)=\frac{\varepsilon}{\xi},$$

$$k=\frac{qv_F}{\omega};\quad \beta=\frac{\nu}{\omega}. \tag{19}$$

It should be noted that, in view of the assumption that the Fermi surface is spherical, the last term in integral (17) vanishes.

Solving the system of equations (16)–(19) and returning to the coordinate representation, we obtain the general formula for the spatial distribution of transverse electric field in the superconductor:

$$E(x)=-\frac{E'(0)}{\pi q_0}\int_{-\infty}^\infty\frac{dk\,\exp(i\Phi_0k)}{\rho_sQ+k^2+3QJ_0(k)/2k},$$

$$Q=(q_L/q_0)^2,\quad q_0=\omega/v_F, \tag{20}$$

$$J_n(k)=2\int_0^\infty d\xi\,\frac{\partial n_0}{\partial\varepsilon}\,p\left(\frac{p+i\beta}{p}\right)^n f\left(\frac{p+i\beta}{k}\right),$$

$$f(z)=z+(1-z^2)\,\frac{1}{2}\ln\frac{z+1}{z-1},$$

$$J_n(k)\approx(1+i\beta)^nJ_0(k),\quad \frac{\Delta}{T}\ll1,$$

$$J_n(k)\approx J_0(k),\quad \frac{\Delta}{T}\gg1, \tag{21}$$

where q_L is the reciprocal London penetration depth.

In order to evaluate the integral in (20), we continue the integrand to the upper half-plane of the dimensionless wave number $k=q/q_0$ and displace the integration contour in the direction $\operatorname{Im}k>0$, bypassing the singularities of the integrand. The latter contains short-wave poles corresponding to conventional screening at the Meissner or skin depth as well as the branching point $k_0=1+i\beta$, corresponding to the contribution of the quasiwave to the spatial field distribution described by the formula

$$E_{QW}(x)=-\frac{2E'(0)}{3\pi q_0Q}\int_{(C)}\frac{kdk\,\exp(i\Phi_0k)}{2\rho_sk/3+J_0(k)}, \tag{22}$$

where the integration contour C in the complex plane k, which bypasses the cut of the integrand, is shown in Fig. 1a. In a normal metal, the branching point k_0 of the function $J_0(k)=f[(1+i\beta)/k]$ reflects directly the singularity of the logarithmic function in $f(z)$, while in a superconductor its origin is due to the fact that the branching point of the logarithm in the analytic continuation described above, i.e., $p(\xi)=p_0(k)=k-i\beta$, intersects the energy integration contour mapped on the semi-axis $(1,+\infty)$ in the complex plane $p(\xi)$ for $\operatorname{Re}k>1$.

The contour integral (22) can be represented as the sum of the integrals I_++I_- over the cut edges; in accordance with the analytical continuation rules, the energy integration contour on the right edge of the cut in $J_0(k)$ (21) must bypass the branching point $p_0(k)$ of the integrand in the complex plane $p(\xi)$ as shown in Fig. 1b. Substituting $k\to k+i\beta$ into I_+ and I_- and separating the contribution $J_0'(k)$ of the contour bypassing the branch point $p_0(k)$ in (21), we finally obtain
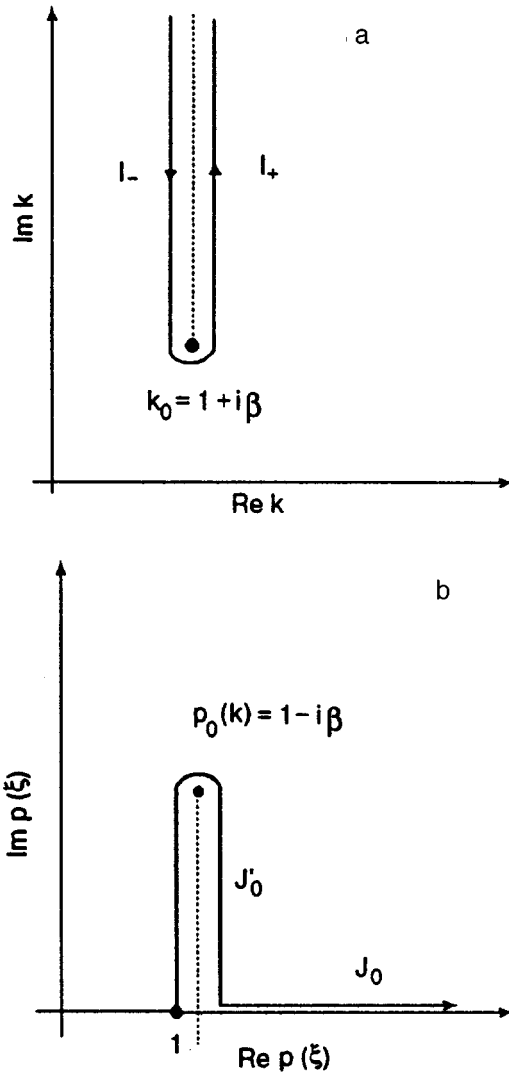
FIG. 1. Integration contours for calculating the coordinate dependence of the quasiwave field (a) and for analytic continuation of the response function (b).

$$E_{QW}(x) = -\frac{2E'(0)}{3\pi q_0 Q} \exp(-\beta\Phi_0)$$

$$\times \int_1^{1+i\infty} (k+i\beta)dk\, e^{i\Phi_0 k}\left(\frac{1}{Z(k+i\beta)+J_0'(k)}\right.$$

$$\left. -\frac{1}{Z(k+i\beta)}\right), \tag{23}$$

$$Z(k) = \frac{2}{3}k\rho_s + J_0(k),$$

$$J_0'(k) = -2i\pi\int_1^k dp\left|\frac{d\xi}{dp}\right|\frac{\partial n_0}{\partial\varepsilon}p\left(1-\left(\frac{p+i\beta}{k+i\beta}\right)^2\right). \tag{24}$$

It can easily be proved that the value of J_0' is small in the asymptotic region (11) and (13) under investigation: $|J_0'|\ll|Z|$. Indeed, for $(\Delta/T)(\Phi_0)^{1/2}\ll 1$, $\Phi_0\gg 1$ the characteristic values of k and p in (24) are close to unity in view of rapid attenuation of the exponential factor in (23), which

ensures the smallness of the integrand as well as of the integration interval in J_0'. In the opposite limit $(\Delta/T)\sqrt{\Phi_0}\gg 1$ the value of J_0' is exponentially small due to a rapid decrease in the distribution function of nonequilibrium excitations. This allows us to simplify the general formula (23) by retaining in it only the first nonvanishing term in J_0'. In the obtained expression, we direct the contour of integration with respect to k along the real axis and then interchange the order of integration with respect of k and p, carrying out the substitution $k\to kp$:

$$E_{QW}(x) = -\frac{2E'(0)}{3q_0 Q}\exp(-\beta\Phi_0)\int_1^\infty dk$$

$$\times \int_0^\infty \frac{\Delta}{2T}\frac{d\xi\,\exp(i\Phi_0 kp)}{\cosh^2(\varepsilon\Delta/2T)}\frac{p(kp+i\beta)}{Z^2(kp+i\beta)}$$

$$\times\left(1-\left|\frac{p+i\beta}{kp+i\beta}\right|^2\right). \tag{25}$$

Integrating with respect to the variable k playing the role of the angular variable $1/\mu$ in (25), we arrive at an expression which is close to the model formula (7), differing from it qualitatively only in the presence of the factor Z^{-2} describing the collective effect of the Meissner (ρ_s) and the skin (j_0) screening of the transverse field:

$$E_{QW}(x) = E_{QW}^N(x)\exp(-i\Phi_0)$$

$$\times\int_0^\infty \frac{\Delta}{2T}\frac{d\xi}{\cosh^2(\varepsilon\Delta/2T)}\exp\left(i\Phi_0\frac{\varepsilon}{\xi}\right)Z^{-2}$$

$$\times(p+i\beta), \tag{26}$$

where

$$E_{QW}^N(x) = \frac{4iE'(0)}{3q_0 Q\Phi_0^2}\exp(i\Phi_0[1+i\beta]) \tag{27}$$

is the distribution of the quasiwave field in the normal metal.[1)]

The calculation of asymptotic values of $E_{QW}(x)$ is analogous to the evaluation of the model result (7). In the vicinity of the superconducting transition temperature (11), the characteristic energies in (26) are large ($\sim T/\Delta\gg 1$, $p(\xi)\to 1$), and the factor $Z(p)\approx 1$, while, in the region (13) in which integral (26) is evaluated by the steepest decent method (see [(12)–(14)], the quantity $Z(p)$ is replaced by its value at the saddle point $Z(p_*)$, $p_*=\varepsilon_*/\xi_*$. Considering that $\rho_s\ll 1$, $p_*\approx 1$, and $J_0(p_*)\approx 1$ near T_c, and that the quasiparticle contribution $J_0(p_*)$ to the field screening is exponentially small at low temperatures, we obtain the final asymptotic form of the electromagnetic quasiwave field distribution in the superconductor:

$$E_{QW}(x) = E_{QW}^N(x)F_1(T,\Phi_0), \quad \frac{\Delta}{T}\sqrt{\Phi_0}\ll 1; \tag{28}$$

$$E_{QW}(x) = E_{QW}^N(x)e^{-i\Phi_0}z^{-2}(T,\beta)F_2^{(1)}(T,\Phi_0),$$

$$\frac{\Delta}{T}\sqrt{\Phi_0}\gg 1; \tag{29}$$

$$z(T,\beta) \approx \begin{cases} 1, & \Delta \ll T; \\ \dfrac{2}{3}\,(1+i\beta_*), & \Delta \gg T; \end{cases} \quad \beta_* = \frac{\nu}{\omega}\,\frac{\xi_*}{\varepsilon_*}, \qquad (30)$$

where β_* has the meaning of the frequency dispersion parameter for effective excitations. Thus, the obtained ratio of the quasiwave signal in the superconductor to its value in the normal state differs from the model ratio (10) and (14) only in the presence of the factor $z^{-2}(T,\beta)$ describing the change in the type of screening of the transverse field from the skin screening near T_c to the Meissner screening in the bulk of the superconductor.

It should be noted that, in view of the strong screening of the electromagnetic field in the metal, an electromagnetic quasiwave can be observed experimentally only in the microwave frequency range of the exciting wave. Indeed, substituting $E'(0) = \omega E/c$, $q_L = \omega_p/c$, into (27), where E is the incident wave amplitude and ω_p the plasma frequency, we obtain the following estimate for the coefficient of transformation of an exciting signal into a quasiwave for $\Phi_0 \sim 1$:

$$\frac{E_{QW}^{(N)}}{E} \sim \frac{c}{v_F}\left(\frac{\omega}{\omega_p}\right)^2 \sim 10^2 \left(\frac{\omega}{\omega_p}\right)^2,$$

which becomes equal to its typical value $m/M - (s_0/v_F)^2 \sim 10^{-4}$ for a longitudinal acoustic quasiwave (m and M are the masses of the electron and the ion, respectively; see Ref. 2 and also (40) and (41)) only for $\omega \sim 10^{12}$ s^{-1}. For a semimetal with a low value of ω_p, this estimate can be softened significantly. Apparently, the acoustic method of excitation of a quasiwave, which will be discussed in the following section, is most favorable from the experimental point of view.

4. ACOUSTIC QUASIWAVE

In this section, we consider the excitation of a quasiwave by transverse and longitudinal deformation of the metal surface, which is known to be accompanied by the emergence of electric fields. In this connections, we must use the general expressions for the Fourier components of the densities of charge, current, and electron force:

$$\delta N = -e\nu_F(c_k \widetilde{p}_{sk} + a\widetilde{\varphi} + c_k^{(d)} U_k),$$

$$j_i = e\nu_F(b_{ik}\widetilde{p}_{sk} - c_i\widetilde{\varphi} + b_{ik}^{(d)} U_k), \quad f_i = f_i^{(d)} + f_i^{(f)} + f_i^{(j)},$$

$$f_i^{(d)} = -i\omega m\nu_F D_{ik} U_k, \quad f_i^{(f)} = i\omega m\nu_F(b_{ik}^{(d)}\widetilde{p}_{sk} - c_i^{(d)}\widetilde{\varphi}),$$

$$f_i^{(j)} = -\frac{i\omega m c^2 q^2}{4\pi e^2}(\widetilde{p}_{s\alpha} - U_\alpha)\delta_{i\alpha},$$

$$\alpha = y, z, \quad \mathbf{U} = i\omega m\mathbf{u} \qquad (31)$$

with the kinetic coefficients $a, b, c, b^{(d)}, c^{(d)}$, and D as determined in Ref. 9. Omitting the simple but cumbersome calculations involved in the solution of the boundary value problem in the half-space in the model of free electrons ($\lambda_{ik} = -mv_i v_k$), we write the equation for the Fourier component of transverse strain excited in the metal by an external transverse perturbation (both of the deformation and the electromagnetic type):

$$u(q) = \frac{2s_0^2 u'(0) + (2e/M)E'(0)(\sigma + \sigma_d)/(q_L^2\sigma + q^2)}{\omega^2 - s_0^2 q^2 + \omega^2 m\widetilde{D}/M},$$

$$\widetilde{D} = D - \frac{1}{q_L^2}\left(q^2 - \frac{(q_L^2\sigma_d - q^2)^2}{q_L^2\sigma + q^2}\right), \qquad (32)$$

where σ and σ_d are the transverse and deformation conductivity and D is the coefficient of transverse deformation response:

$$\sigma(k) = \rho_s + \frac{3}{2k}J_0(k), \quad \sigma_d(k) = 1 - \rho_s - \frac{3}{2k}J_1(k),$$

$$D(k) = 2\int_0^\infty d\xi\,\frac{\partial n_0}{\partial\varepsilon}\,\frac{p+i\beta}{p} - \frac{3}{2k}J_2(k). \qquad (33)$$

Separating the contribution of the cut originating at the branch point k_0 in the coordinate representation $u(x)$ as was done in Sec. 3 and using the small parameter $m/M \ll 1$, we obtain the general expression for the spatial distribution of elastic field of a transverse quasiwave:

$$u_{QW}(x) = -\frac{mu'(0)}{\pi M}\left(\frac{s_0}{\omega}\right)^2 q_0 \int_{(C)} dk\,\exp(i\Phi_0 k)$$

$$\times\left(-\frac{3}{2k}J_2(k) + \frac{(1-\rho_s - 3J_1(k)/2k)^2}{\rho_s + 3J_0(k)/2k}\right)$$

$$+\frac{eE'(0)}{\pi M\omega^2 q_0 Q}\int_{(C)} dk\,e^{i\Phi_0 k}\,\frac{1-\rho_s - 3J_1(k)/2k}{\rho_s + 3J_0(k)/2k}. \tag{34}$$

It should be noted that, in the case of excitation of a transverse acoustic quasiwave by an electromagnetic wave incident on the free surface of a metal ($u'(0) = 0$), the first term in (34) is equal to zero. For acoustic excitation, the quantity $E'(0)$ should be determined self-consistently by solving the external problem for the electromagnetic field, but according to Iwanowski and Kaganov,[3] its contribution to the quasiwave amplitude is negligibly small.

Further procedure of evaluating the quasiwave component of transverse sound is similar to that used for calculating the field of an electromagnetic quasiwave (Sec. 3) and leads to the same temperature dependences of the signal (28)–(30) in which E_{QW}^N should be replaced by the field distribution for a transverse acoustic quasiwave in a normal metal[3]:

$$u_{QW}^N = \left(u'(0)\frac{4imq_0}{3M}\left(\frac{s_0}{\omega}\right)^2 - \frac{4ieE'(0)}{3M\omega^2 q_0 Q}\right)$$

$$\times\frac{\exp(i\Phi_0(1+i\beta))}{\Phi_0^2}. \tag{35}$$

The estimate of the coefficient of transformation of a transverse elastic perturbation to a quasiwave,

$$\frac{u_{QW}}{u(0)} \sim \frac{\omega}{s_0}\,\frac{m\omega}{Mv_F}\left(\frac{s_0}{\omega}\right)^2 \sim \left(\frac{s_0}{v_F}\right)^3 \sim 10^{-6}$$

contains an additional power of the small parameter s_0/v_F as compared to its value $(s_0/v_F)^2$ for a longitudinal acoustic

quasiwave. This factor, which complicates the experimental observation of a transverse acoustic quasiwave, is due to the vanishing of the transverse component of the model deformation potential at the reference point. It was mentioned in Ref. 3 that this factor can be absent in the general case of an arbitrary electron spectrum. This apparently explains why a transverse quasiwave could not be registered in recent experiments with Al whose Fermi surface is successfully described by the Harrison standard construction from spherical regions of the Fermi surface for free electrons, while the signals of transverse and longitudinal quasiwaves in Ga, which has a complex electron spectrum, have comparable amplitudes for the same excitation power.[4]

The calculation of the field distribution for a longitudinal quasiwave in a superconductor is much more complicated since the field component of the response cannot be expressed in terms of appropriate conductivities (it is well known that the concept of longitudinal conductivity cannot be introduced for the superconducting state even in the linear approximation since the contribution to the longitudinal current comes from the electric field as well as from the oscillations of the order parameter phase). In this connection, the nonanalytic part of the Fourier component of elastic strain, which has a branching point in the complex plane q and generates the quasiwave component of the signal, has a rather cumbersome structure:

$$u_{QW}(x) = \frac{imu(0)}{\pi M} \int_{(C)} \frac{dk}{k} e^{i\Phi_0 k} W(k),$$

$$W(k) = -3\left(D + \frac{ab_d^2 + 2cc_d b_d - bc_d^2}{k^2(ab + c^2)} \right), \tag{36}$$

where all the kinetic coefficients contain the branch point $k_0 = 1 + i\beta$. In contrast to the transverse field, the variation of the integrand upon a transition through the cut is significant, and the expansion in this quantity is impossible in the general case. Asymptotic analysis shows, however, that the structure of the response (30) can be simplified considerably in limiting cases. Indeed, at low temperatures $T \ll \Delta$, the quasiparticle contributions to kinetic coefficients containing the branching point are exponentially small, and their contribution to W can be separated in the perturbation theory. In the vicinity of the critical temperature, we can derive the following relation by using exact expressions for kinetic coefficients:

$$W(k) = 1 + i\beta - \frac{k^2}{3}[1 - a^{-1}(k)] + O(\Delta/T). \tag{37}$$

At the same time, nonanalytic corrections appearing due to the branch point of the function

$$a(k) \approx 1 - \frac{1}{2T} \int_0^\infty \frac{d\xi}{\cosh^2(\xi/2T)} g\left(\ln \frac{p + i\beta + k}{p + i\beta - k} \right),$$

$$g(z) = \frac{z/2}{1 + i\beta(1 - z/2)}, \tag{38}$$

are of the order of $(\Delta/T)\sqrt{\Phi_0}$, and the values of these corrections in the wave region $\Phi_0 \gg 1$ are large as compared to the last term in (37), which can consequently be neglected:

$$u_{QW}(x) = \frac{imu(0)}{3\pi M} \int_{1+i\beta}^{1+i\infty} dk e^{i\Phi_0 k} [a_+^{-1}(k) - a_-^{-1}(k)],$$

$$\Delta \ll T. \tag{39}$$

Here a_+ and a_- are the values of the function $a(k)$ at the edges of the cut.

Carrying out asymptotic calculations on the basis of formulas (38) and (39), we obtain for $\Delta\sqrt{\Phi_0} \ll T$, $\Phi_0 \gg 1$

$$u_{QW}(x) = \frac{4imu(0)}{3M\Phi_0} \exp[i\Phi_0(1 + i\beta)]\left(\int_0^\infty \frac{dk e^{-k}}{\Lambda^2(k) + \pi^2} \right.$$

$$\left. - \frac{\Delta\sqrt{\Phi_0}}{2T\sqrt{2}} \exp(-i\pi/4) \int_0^\infty \frac{dk}{\sqrt{k}} e^{-k} A(k) \right),$$

$$A(k) = \frac{\Lambda^2(k) - \pi^2}{[\Lambda^2(k) + \pi^2]^2}$$

$$- \frac{\beta}{4\pi} \int_0^\infty d\xi \left(\frac{l_+^2(\xi)}{\Lambda_+^2(k)} \frac{1}{1 - i\beta(\Lambda_+(k) + l_+(\xi))/2} \right.$$

$$\left. - \frac{l_-^2(\xi)}{\Lambda_-^2(k)} \frac{1}{1 - i\beta(\Lambda_-(k) + l_-(\xi))/2} \right),$$

$$\Lambda(k) = \ln \frac{2\Phi_0(1 + i\beta)}{ie^2 k}, \quad \Lambda_\pm(k) = \Lambda(k) \pm i\pi,$$

$$l_\pm(\xi) = \ln \frac{\xi^2}{\xi^2 - 1}, \ \xi > 1; \quad l_\pm(\xi) = \ln \frac{\xi^2}{1 - \xi^2} \mp i\pi,$$

$$\xi < 1; \quad A(k) \approx \frac{\Lambda^2(k) - \pi^2}{[\Lambda^2(k) + \pi^2]^2}(1 - 2i\beta \ln 2),$$

$$\beta \ll 1. \tag{40}$$

The first term in (40) corresponds to the quasiwave signal in a normal metal and coincides with the expression obtained by Gokhfeld and Kaganov[2] if we neglect the logarithmic dependence $\Lambda(k)$. Retaining in (40) only the large term $\ln \Phi_0$ according to the main logarithmic approximation, we can easily see that the obtained temperature dependence of the phase and amplitude of the quasiwave coincides with the model dependence (10) and (11) corresponding to a decrease in the velocity and amplitude of the quasiwave upon a transition through T_c. However, real experimental values of the signal phase are such that we must take into account the numerical factors in formula (40). This necessitated a numerical analysis which shows that the velocity and the amplitude of the quasiwave, which decrease rapidly in the superconducting state, can first pass through a maximum for not very large values of the phase Φ_0. It should be noted that in order to obtain a simplified numerical estimate, we can neglect the logarithmic dependence $\Lambda(k)$ in (40):

$$u_{QW}(x) = \frac{4imu(0)}{3M\Phi_0} \exp[i\Phi_0(1 + i\beta)]\left(\frac{1}{\Lambda^2(1) + \pi^2} \right.$$

$$\left. - \frac{\Delta\sqrt{\pi\Phi_0}}{2T\sqrt{2}} e^{-i\pi/4} A(1) \right). \tag{41}$$

For $\Delta\sqrt{\Phi_0}\gg T$, $\Delta\ll T$, the nonanalytic contribution to the function $a(k)$ (38) is exponentially small and can be separated in the perturbation theory [see comments to formula (24)]. In this case, the amplitude and velocity of a ballistic signal always decrease with temperature:

$$u_{QW}(x)=\frac{imu(0)}{3Mz^2\Phi_0}\exp(-\beta\Phi_0)$$

$$\times F_2^{(0)}(T,\Phi_0)\int_0^\infty \frac{dk\,\mathrm{e}^{-k}}{(1-i\beta\Lambda_+/2)(1-i\beta\Lambda_-/2)},$$

(42)

$$z=\int_0^\infty \frac{d\xi}{\cosh^2\xi}\frac{Z}{1-i\beta Z}, \quad Z=\ln\frac{4T}{e\Delta}\xi\sqrt{1+i\beta},$$

$$\Delta\sqrt{\Phi_0}\gg T, \quad \Delta\ll T;$$

$$u_{QW}(x)\approx\frac{4imu(0)}{3M\Phi_0}\exp(-\beta\Phi_0)F_2^{(0)}(T,\Phi_0)$$

$$\times\left(\begin{array}{ll}\ln^{-2}\left(\dfrac{\pi T}{e\gamma\Delta}\right)^2, & \beta\ll 1;\\[3mm] \displaystyle\int_0^\infty \dfrac{dk\,\mathrm{e}^{-k}}{\Lambda^2(k)+\pi^2}, & \beta\gg 1;\end{array}\right.$$

(43)

where $\ln\gamma=C=0.577\ldots$ is the Euler constant.

At low temperatures $T\ll\Delta$, the function $W(k)$ (36) can be linearized in the exponentially small quasiparticle contribution to the kinetic coefficients:

$$u_{QW}(x)=\frac{imu(0)}{\pi M}\int_{1+i\beta}^{1+i\infty}\frac{dk}{k}\,\mathrm{e}^{i\Phi_0 k}(W_+-W_-)(k),\quad (44)$$

$$(W_+-W_-)(k)=-\frac{2\Delta}{3T}\int_0^\infty d\xi\,\exp\left(-\frac{\Delta}{T}\varepsilon\right)\left(\frac{3}{k}(p+i\beta)\right.$$

$$\left.-\left(\frac{k}{p}\right)^2(G\langle K\rangle_+ - G\langle K\rangle_-)\right),\qquad (45)$$

where the functions G and $\langle K\rangle$ are defined in (18) and (19). Carrying out asymptotic expansions similar to (25)–(30), we finally get

$$u_{QW}(x)=\frac{4imu(0)}{3M\Phi_0}\left(1-\frac{i\beta_*}{2}\right)^2\mathrm{e}^{-\beta\Phi_0}$$

$$\times F_2^{(0)}(T,\Phi_0)\int_0^\infty$$

$$\times\frac{dk\,\mathrm{e}^{-k}}{(1-i\beta_*\Lambda_+^*(k)/2)(1-i\beta_*\Lambda_-^*(k)/2)},$$

$$\Delta\gg T,\qquad (46)$$

$$\Lambda_\pm^*(k)=\Lambda^*(k)\pm\pi i,\quad \Lambda^*(k)=\ln\left(\frac{2\Phi_0(1+i\beta_*)}{ie^2k}\frac{\varepsilon_*}{\xi_*}\right),$$

$$u_{QW}(x)\approx\frac{4imu(0)}{3M\Phi_0}\mathrm{e}^{-\beta\Phi_0}F_2^{(0)}(T,\Phi_0)$$

$$\times\left(\begin{array}{ll}1, & |\beta_*(\beta,T,\Phi_0)|\ll 1;\\[3mm] \displaystyle\int_0^\infty \dfrac{dk\,\mathrm{e}^{-k}}{\Lambda^{*2}(k)+\pi^2} & |\beta_*(\beta,T,\Phi_0)|\gg 1.\end{array}\right.$$

(47)

According to (46) and (47), the changes in the amplitude and phase of a longitudinal acoustic quasiwave referred to their values in the normal state exhibit at low temperatures a behavior similar to that following from the model calculations (14) and (15).

The obtained results describe qualitatively the experimental results[5-7] in which an increase in the phase of an electron sound signal was observed for $T\to 0$. In the vicinity of T_c, these variations are proportional to $\Delta(T)$, which is in accord with formula (10). It should also be noted that the amplitude of electron sound in Ga and Mo decreases abruptly upon a transition through T_c, which can be an indication of vanishing of the zeroth sound component of the signal in the superconducting state and of a transition to the purely ballistic transfer mode (quasiwave). A detailed analysis of the behavior of the signal of a longitudinal quasiwave in a superconductor supported by numerical calculations will be published in a separate article together with corresponding experimental data.

*E-mail: bezugly@ilt.kharkov.ua
[1)]It should be noted that, in the adopted approximation, the phase E_{QW}^N does not depend on the mean free path. At the same time, a numerical analysis of the exact formula reveals a weak increase in the ballistic transport velocity upon an increase in relaxation frequency. This circumstance has a simple physical meaning: as the mean free path decreases, the contribution from electrons arriving at the point of observation along slanting (longer) trajectories becomes smaller, which leads to narrowing of the effective electron beam and to an increase in the transport velocity.

[1] M. I. Kaganov, Usp. Fiz. Nauk **145**, 507 (1985) [Sov. Phys. Uspekhi **28**, 257 (1985)].
[2] V. M. Gokhfeld and M. I. Kaganov, Fiz. Nizk. Temp. **10**, 864 (1984) [Sov. J. Low Temp. Phys. **10**, 453() (1984)].
[3] G. I. Iwanowski and M. I. Kaganov, Zh. Éksp. Teor. Fiz. **83**, 2320 (1982) [Sov. Phys. JETP **56**, 1345 (1982)].
[4] E. V. Bezuglyi, A. V. Boichuk, N. G. Burma, and V. D. Fil', Fiz. Nizk. Temp. **21**, 633 (1995) [Low Temp. Phys. **21**, 493 (1995)].
[5] N. G. Burma, E. Yu. Deineka, and V. D. Fil', Pis'ma Zh. Éksp. Teor. Fiz. **50**, 18 (1989) [JETP Lett. **50**, 20 (1989)].
[6] E. V. Bezuglyi, N. G. Burma, E. Yu. Deineka, and V. D. Fil', Sverkhprovodimost': Fiz. Khim. Tekhn. **4**, 661 (1991).
[7] E. V. Bezuglyi, N. G. Burma, E. Yu. Deineka et al., J. Phys.: Cond. Matter **3**, 7687 (1991).
[8] A. J. Leggett, Progr. Theor. Phys. **36**, 901 (1966).
[9] E. V. Bezuglyi, Fiz. Nizk. Temp. **9**, 15 (1983) [Sov. J. Low Temp. Phys. **9**, 6 (1983)].

Translated by R. S. Wadhwa

513   Low Temp. Phys. 23 (7), July 1997

E. V. Bezuglyi and A. V. Boichuk   513

Simulation of resistive state of a granular superconductor

V. K. Ignatjev

Volgograd State University, 400062 Volgograd, Russia*

The equation for hypervortex in a slightly granular superconductor is obtained, and the vortex lattice is numerically simulated. The dissipation associated with the formation, collapse, and movement of hypervortices is considered. The equations describing the dynamics of magnetic field distribution, nonlinear susceptibility, and current–voltage characteristics in the resistive state are obtained. The numerically simulated equations give results that are in good agreement with those obtained experimentally. © *1997 American Institute of Physics.*
[S1063-777X(97)00307-1]

INTRODUCTION

Various models of high-temperature superconductors (Bean's, spin-glass, Josephson medium, percolation, etc.) treat a superconducting ceramic as a nonlinear medium (system with distributed parameters) with considerable time and spatial dispersions. No general approach has been worked out for simulating and studying such systems, and hence it is impossible to compare theoretical and experimental results or to analyze the operation of electrical and radioengineering units made of high-temperature superconductors and to optimize their characteristics.

The construction of a consistent phenomenological model of the electrodynamics of a medium requires the solution of three problems: (a) analysis, i.e., the construction of the response of the medium to an arbitrary external action with the help of the system function of the medium that depends only on its parameters and not on the action; (b) synthesis, i.e., using the experimental data for construction of the system function of an arbitrary medium satisfying the requirement of the analysis; and (c) simulation, i.e., connecting the integral parameters of the system function of the medium with the processes occurring in it to facilitate a comparison of the theoretical and experimental results. In modern theoretical electrical engineering, the problems of analysis and synthesis of linear chains have been solved completely with the help of uniquely connected pulse, transmission, and frequency characteristics. For nonlinear chains, the problem is solved in some particular cases only approximately, as a rule, by series expansion of the current-voltage characteristic for quasistationary processes, and by the method of harmonic balance and slowly varying amplitude for harmonic and narrow–band action. As a rule, we can isolate in the system under investigation a closed subsystem containing a superconducting sample and having two pairs of clamps for input and output. Such a system is treated as a passive nonlinear four-pole for which the work done by the external agency is equal to the change in the internal energy of the medium and losses in it. In turn, the internal energy and losses in a passive medium are nonlinear retarded potentials of the external agency and uniquely define the reaction of the medium to it, i.e., describe the system function of the medium. Such an approach makes it possible to characterize electromagnetic processes in a superconductor in terms of electrically measurable integral quantities (like total resistance, surface impedance, and nonlinear susceptibility) and to verify experimentally the results of theoretical analysis.

An analysis of vortex dynamics in a granular superconductors plays an important role in the construction of the phenomenological model of quasistationary nonlinear electrodynamics of high- temperature superconductors. The concept of Josephson hypervortices introduced by Sonin[1] proved to be quite useful for describing the mixed state in superconducting ceramics.[2,3] However, the models considered in Refs. 1–3 cannot be used for analytic description of magnetization curves and complex susceptibility. In Ref. 3, for example, it is assumed that there are no Abrikosov and Josephson vortices. An analysis of the motion of a solitary plane vortex was carried out in Ref. 4 for a regular Josephson medium with identical critical junction currents and in the absence of vortex penetration in granules, which does not permit a description of the critical state of real ceramic superconductors. A fairly complex system of equations was obtained in Ref. 5 for describing hypervortices in a granular superconductors for the general case taking into account the strongly stochastic and nonlocal nature of the medium.

It should be remarked that recently synthesized ceramic superconductors with a high current-carrying capacity have a comparatively high critical current of Josephson junctions between granules and hence the Josephson penetration depth becomes comparable with (or even smaller than) the granule size. Such superconductors can be called slightly granular. Numerical simulation of equations in Ref. 5 shows that the intergranular magnetic field at the center of a hypervortex becomes stronger than the lower critical field of a granule in a slightly granular superconductor even in an external magnetic field of the order of 10 Oe. In stronger external magnetic fields, Abrikosov vortices penetrate the granules practically everywhere in the bulk of the superconductor.

1. CONSTITUTIVE EQUATION

In order to generalize the constitutive equations obtained by the author earlier[5] to the case of a slightly granular superconductor taking into account the penetration of Abrikosov vortices into granules, let us assume that the superconductor

is in an external magnetic field that is uniform along the z-axis, and denote by $n(x,y)$ the concentration of Abrikosov vortices in granules, averaged over z. In external fields that are not too strong, vortices are located in the vicinity of the granule surfaces, and it can be assumed that there are no vortices at the center of granules. Following Ref. 5, we construct a smooth function $\chi(\mathbf{r})$ whose value at the center of each granule coincides with the phase of the order parameter. In this case, the following condition is satisfied for any closed contour C passing through the centers of granules and Josephson junctions:

$$\oint \nabla \chi(\mathbf{r})d\mathbf{r} = 2\pi\left(m + \oint \oint_s n(\mathbf{r})\mathbf{e}dS,\right), \qquad (1)$$

where $\mathbf{e}$ is a unit vector along the z-axis, S the surface stretched over the contour C is and m an integer.

This equation can be written in the form

$$\mathrm{curl}(\nabla\chi(\mathbf{r})) = 2\pi(n(\mathbf{r}) + m_i\delta(\mathbf{r}-\mathbf{r}_i)), \qquad (2)$$

where $\mathbf{r}_i$ is the hypervortex axis coordinate, m_i the number of magnetic flux quanta in the intergranular space of a hypervortex, and $\delta(\mathbf{r})$ is a twodimensional delta-function. We introduce the following notation: μ_1 is the average fraction of the normal phase in a superconductor or permeability of a superconductor in the absence of intergranular currents and Abrikosov vortices, $\mu_2(B_1)$ the permeability of a granule associated with the penetration of Abrikosov vortices, $\mathbf{B}$ the average magnetic induction in a superconductor, $\mathbf{B}_1$ the induction in the intergranular space, and μ_3 the averaged permeability of a superconductor in the absence of granular currents, when $\mathbf{B}_1$ is equal to the external field $\mathbf{H}$. In this case, we get

$$\mathbf{B}_1 = \mathbf{B}/\mu_3, \quad \mathbf{e}\Phi_0 n = \mu_2\mathbf{B}/\mu_3, \quad \mu_3 = \mu_1 + \mu_2 - \mu_1\mu_2. \qquad (3)$$

We introduce the dimensionless gradiently invariant vector $\mathbf{g} = a\pi\sqrt{\pi}\langle\mathbf{A}(\mathbf{r}) - \Phi_0\nabla\chi(\mathbf{r})/2\pi\rangle/2\Phi_0$, where $\mathbf{A}(\mathbf{r})$ is the magnetic field vector-potential, and a the mean separation between the centers of granules. Taking formula (2) into account, we can write

$$\mathbf{B} = \Phi_0(2\ \mathrm{curl}\ \mathbf{g}/(a\pi\sqrt{\pi}) + m_i\mathbf{e}\delta(\mathbf{r}-\mathbf{r}_i) + \mathbf{e}n),$$

which easily leads to the relation

$$\mathbf{B} = \Phi_0$$
$$\times\frac{[2\ \mathrm{curl}\ \mathbf{g}/(a\pi\sqrt{\pi}) + m_i\mathbf{e}\delta(\mathbf{r}-\mathbf{r}_i)](\mu_1+\mu_2-\mu_1\mu_2)}{\mu_1 - \mu_1\mu_2}. \qquad (4)$$

The total free energy of a superconductor measured from the zero level of magnetic field and currents assumes the form

$$W = \frac{1}{8\pi}\sum_{k=1}^N [\mu_1 V_k B_1^2(\mathbf{r}_k) + (1-\mu_1)V_k\Phi_0^2 n^2(\mathbf{r}_k)/\mu_2$$
$$+ 4\Phi_0 I_k(1-\cos(\varphi_k))]/c,$$

where $\mathbf{r}_k$ is the coordinate of the kth Josephson junction, V_k the volume of the region containing a part of the granule

and the intergranular space adjoining the junction, I_k the critical current in the junction, and φ_k the phase difference across the junction.

Averaging in accordance with the procedure described in Ref. 5, we obtain

$$\langle W\rangle = F_J\int\int\int (\lambda^2|\mathrm{curl}\ \mathbf{g} + \mathbf{e}m_i a\pi\sqrt{\pi}\delta(\mathbf{r}-\mathbf{r}_i)/2|^2$$
$$+ 1 - D^3\ \exp(-D^2 g^2))dV, \qquad (5)$$

where the following notation has been used: $F_J = \Phi_0\rho I_J/2\pi c$; $D = (1 + a^2|\nabla g|^2/40)^{-1}$; $\lambda = \lambda_J(\mu_3)^{1/2}/(\mu_1 - \mu_1\mu_2)$, $\lambda_J = (c\Phi_0/\pi^3 a^2\rho I_J)^{1/2}$ is the Josephson penetration depth, ρ the density of intergranular Josephson junctions, and I_J the average critical current in the junctions. In contrast to the exact expression obtained in Ref. 5, formula (3) here does not take into account fluctuations of the magnetic field vector potential. Numerical simulation shows that the contribution of the corresponding terms is small.

The time-independent constitutive equation for a slightly granular superconductor may be obtained in the conventional way by minimizing the free energy (5). Taking into account the resistive model of a Josephson junction,[6] we obtain the complete time-dependent equation:

$$\lambda^2\ \mathrm{curl}\ \mathrm{curl}\ \mathbf{g} = -\mathbf{g}D^3\ \exp(-D^2 g^2) - \tau\mathbf{g}' - \tau RC\mathbf{g}''$$
$$+ \beta m_i\ \mathrm{curl}\ (\mathbf{e}\delta(\mathbf{r}-\mathbf{r}_i)), \qquad (6)$$

where $\tau = \Phi_0/(2\pi I_J R_c)$, R is the mean normal resistance of the junctions, $\beta = a\lambda^2\pi\sqrt{\pi}/2$, and the prime indicates time derivative. Together with Eq. (4) which can be used to find the magnetic induction B in a superconductor from the known value of the vector $\mathbf{g}$ and Eq. (3) which expresses the intergranular magnetic field B_1 (and hence the permeability of granules $\mu_2(B_1)$ and the parameter $\lambda(\mu_2)$) in terms of B, Eq. (6) describes the dynamics of magnetic field distribution in a superconductor.

A stationary solitary vortex in an infinite superconductor is described by a one-dimensional time-independent equation in cylindrical coordinates

$$\lambda^2\left(r^2\frac{d^2 g}{dr^2} + r\frac{dg}{dr} - g\right) = r^2 D^3 g\ \exp(-g^2 D^2). \qquad (7)$$

The boundary conditions can be obtained from Eq. (1):

$$rg(r\to 0)\to -am\sqrt{\pi}/4, \quad g(r\to\infty)\to 0. \qquad (8)$$

Together with these boundary conditions, Eq. (7) can be easily solved numerically, and this leads to the following expression for magnetic induction $B(r)$ in a hypervortex:

$$B(r) = \left(\mu_1 + \mu_2 - \frac{\mu_1\mu_2}{\mu_1} - \mu_1\mu_2\right)\left(\frac{B_J\lambda_J}{r}\right)\frac{d(rg)}{dr},$$

$$B_J = 2\Phi_0/(a\lambda_J\pi\sqrt{\pi}) = (4\Phi_0 I_J\rho/c)^{1/2}.$$

The magnetic field distribution obtained in this way is qualitatively quite close to its distribution in an Abrikosov vortex, thus justifying the term ''hypervortex'' introduced in Ref. 1.

For the hypervortex boundary, we can naturally take a loop on which $\mathbf{j} = 0$. In this case, the energy of a vortex of
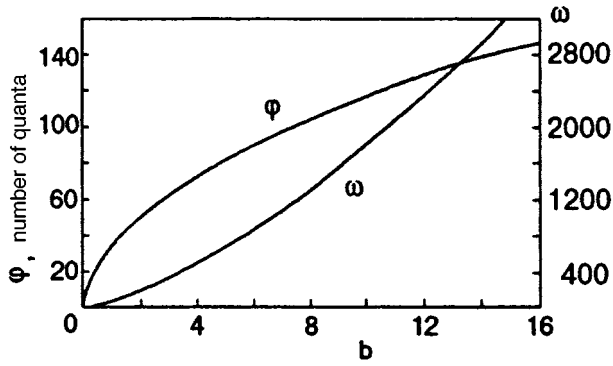
FIG. 1. Dependence of the energy ω and the flux φ in it as functions of the average magnetic field b.

unit length can be determined as the integral over the surface covered by this loop, of the energy density which, in accordance with Eq. (5), has the form

$$F = F_J(\lambda^2 |\mathrm{curl}\ \mathbf{g}|^2 + 1 - D^3 \exp(-g^2 D^2)),$$
$$F_J = B_J^2/8\pi. \tag{9}$$

Naturally, the total energy W of the hypervortex depends on the flux trapped by the vortex. It is borne out by numerical computations that as in the case of Abrikosov vortices, one-quantum hypervortices ($m=1$) are more advantageous than many-quantum hypervortices ($m>1$) from the energy point of view. Note that a hypervortex with $m=1$ can contain tens or even hundreds of magnetic flux quanta concentrated in Abrikosov vortices penetrating the granules. Hence it can be called a one-quantum hypervortex only in the sense that only one magnetic flux quantum is contained in the gaps between granules.

The dependence of the energy of two interacting vortices on the separation between them as well as the energy of hypervortices in square and triangular lattices can also be determined numerically. Like Abrikosov vortices, hypervortices moving in the same direction repel each other, while those moving in the opposite directions attract each other, and a triangular lattice is more advantageous (albeit slightly) than a square lattice from the energy point of view. Figure 1 shows the initial segments of the dependence of the energy W of a hypervortex and the magnetic flux Φ trapped by the hypervortex on the average magnetic induction $B = N\Phi$ in a superconductor in the normalized coordinates $\omega = W/(F_J\lambda_J^2)$, $b = B/(B_J\lambda_J^2)$. In our calculations, the dependence $\mu_2(B_1)$ was approximated by the function

$$\mu_2(|B_1| \geqslant H_{C1}) = \frac{(|B_1|)^{1/2} - (H_{C1})^{1/2}}{(|B_1|)^{1/2} + k(H_{C1})^{1/2}},$$

$$\mu_2(|B_1| < H_{C1}) = 0,$$

and it was assumed that $H_{C1} = B_J/3$; $k = 5$; $\mu_1 = 0.1$; $a/\lambda_J = 1$.

2. VORTEX LATTICE DYNAMICS

The study of vortex lattice dynamics requires the analysis of losses occurring during the hypervortex movement and associated with energy dissipation due to normal Josephson junction resistance. Averaging in the same way as during the derivation of constitutive equations in Ref. 5, we obtain the mean-square voltage across the junction: $\langle U_k^2 \rangle = \langle \varphi_k'^2 \rangle \Phi_0^2/(2\pi c)^2 = |\mathbf{g}'|^2 \Phi_0^2/(2\pi^2 c^2)$. From here we can easily obtain the mean density of dissipative power:

$$p = \rho \langle U_k^2 \rangle / R = \Phi_0^2 |\mathbf{g}'|^2 \rho/(2R\pi^2 c^2). \tag{10}$$

We shall assume that the attenuation of normal conduction currents is quite rapid, and a vortex moving along the x-axis with a constant velocity $\mathbf{v}$ in the coordinate system attached to the vortex center is described by a time-independent equation. In this case,

$$|\mathbf{g}'|^2 = |(\mathbf{v}\nabla)\mathbf{g}|^2 = v^2 \left(\left(\frac{\partial g_x}{\partial x}\right)^2 + \left(\frac{\partial g_y}{\partial x}\right)^2 \right) \approx \frac{v^2 B^2}{\mu_3 \lambda^2 B_J^2}.$$

Using formula (10) and considering that the magnetic energy in a vortex is equal to half the total energy W of the vortex, we determine the dissipative power: $P = v^2 \tau W/\lambda_J^2$. This formula enables us to determine the electromagnetic friction force acting on a unit length of a hypervortex moving in a granular superconductor:

$$\mathbf{f} = -\mathbf{v}\tau W/\lambda_J^2. \tag{11}$$

The problem of pinning of hypervortices remains largely unsolved at present. It was shown in Ref. 4 that under certain conditions, a considerable pinning force may act on a two-dimensional vortex in the regular lattice of Josephson junctions. Following Refs. 7 and 8, it can be shown that like an Abrikosov vortex, a hypervortex can be fixed at the boundary of a superconductor. However, if the size of the hypervortex considerably exceeds the granule size in a ceramic superconductor, averaging over the stochastic system of junctions makes the hypervortex energy practically independent of the position of its axes. In other words, the pinning disappears. However, if the vortex size is comparable with the granule size in a slightly granular superconductor, averaging does not occur, and the pinning remains. Moreover, Abrikosov vortices trapped by the hypervortex may be pinned at the boundaries of granules.[7,8] These vortices are also subjected to the Lorentz force exerted by the transport current. Hence it can be assumed that the pinning force $\mathbf{f}_P$ and the Lorentz force $\mathbf{f}_L$ acting on a hypervortex are proportional to the magnetic flux Φ trapped by it:

$$\mathbf{f}_L = \Phi\ \mathrm{sgn}(B)[\mathbf{j}\times\mathbf{e}]/c. \tag{12}$$

Taking into account the above assumptions and relations (11) and (12), we can use the modified Bean's model[9,10] to write the law of motion of a hypervortex:

$$\mathbf{v}(\mathbf{j}) = \Theta(|\mathbf{j}| - j_C)\mathrm{sgn}(B)[\mathbf{j}\times\mathbf{e}]\left(1 - \frac{j_C}{|\mathbf{j}|}\right)\frac{\lambda_J^2 \Phi}{W_{\tau c}}, \tag{13}$$

where $\Theta(x)$ is the Heaviside function, $\Theta(x \geqslant 0) = 0$, $\Theta(x < 0) = 0$, j_C is the critical current density, and $B = N\Phi$ is the average magnetic induction. Formulas (11) and (13) do not take into account the losses occurring during the motion of Abrikosov vortices in granules. Following Ref. 11, we can show that in magnetic fields that are much weaker than the

upper critical field of granules, these losses are negligible in comparison with the losses in intergranular junctions.

Several theoretical and experimental works[12] indicate that Bean's rigid model cannot be applied to real superconductors. In high-temperature superconductors, the thermal activation of vortex movement acquires a special significance. Taking into consideration the elastic model of interaction of a hypervortex with the pinning center,[7,8] we assume that the Lorentz force corresponding to the critical current density displaces the vortex lattice by a distance d, and this is followed by a free movement of the lattice. Taking formula (12) into consideration, we obtain $d = \Phi j_C/(kc)$, where k is the rigidity. This means that the potential barrier to be overcome for detaching a vortex from the pinning center is $U_0 = d\Phi j_C/(2c)$. The transport current having a density j displaces the vortex lattice by a distance $x = jd/j_C$, and the barrier for detaching a vortex is $\Delta U = U_0 - kx^2/2 = U_0(j_C^2 - j^2)/j_C^2$. Since the fraction of vortices overcoming the barrier as a result of thermal activation is equal to $\exp(-\Delta U/(k_B T))$, where k_B is the Boltzmann constant, and the Heaviside function $\Theta(|j| - j_C)$ in Eq. (13) should be replaced by the function $\Theta_1(j)$:

$$\Theta_1(|j| < j_C) = \exp\left(\frac{U_0(j^2 - j_C^2)}{j_C^2 k_B T}\right),$$

$$\Theta_1(|j| \geqslant j_C) = 1. \tag{14}$$

The motion of a hypervortex at a constant velocity is not the only dissipative process in a granular superconductor. Unlike Abrikosov vortices in a type II superconductor, the emergence and vanishing of hypervortices in granular superconductors is accompanied by losses in intergranular junctions. The vanishing of a solitary vortex in a slightly granular superconductor indicates that at the instant $t = 0$, the parameter m in Eq. (6) varies from 1 to 0. It should be noted that Eq. (6) is obtained as a result of averaging of the resistive model for a Josephson junction,[6] i.e., a model with lumped parameters which is valid only for quasistationary processes in which the wavelength of electromagnetic oscillations is considerably larger than the granule size. Hence Eq. (6) does not describe microwave oscillations emerging during the formation of a vortex, and we can speak of instantaneous variation of the parameter m in this model only when the period of microwave oscillations is much smaller than the time constant τ. Under these assumptions, the formation of a hypervortex is an adiabatic process, and the energy density at all points of the superconductor is a continuous function of time.

The energy loss Q associated with the vanishing of a hypervortex is obtained by taking into account Eqs. (6), (9), and (10) in analogy with losses occurring during vortex movement:

$$q = \rho \int_0^\infty dt \int\!\!\int\!\!\int_V d^3\mathbf{r} \langle u_k \rangle^2/R$$

$$= \frac{\Phi_0^2 \rho}{2\pi^2 c^2 R} \int_0^\infty dt \int\!\!\int\!\!\int_V |\mathbf{g}'|^2 d^3\mathbf{r}$$

$$= -2F_J \int\!\!\int\!\!\int_V d^3\mathbf{r} \int_0^\infty \mathbf{g}'(\mathbf{g}\exp(-g^2)$$

$$+ \lambda^2 \text{ curl curl } \mathbf{g} + \tau RC \mathbf{g}'')dt$$

$$= -F_J \int\!\!\int\!\!\int_V d^3\mathbf{r} \int_0^\infty \left(\frac{\partial}{\partial t}(1 - \exp(-g^2))\right.$$

$$\left. + \lambda^2 |\text{curl } \mathbf{g}|^2 + \tau RC |\mathbf{g}'|^2) - 2 \text{ div}[\mathbf{g}' \times \text{curl } \mathbf{g}]\right)dt$$

$$= U(0) - U(\infty) + \frac{\rho}{2} \int\!\!\int\!\!\int_V C\langle u_k(+0)\rangle^2 d^3\mathbf{r}$$

$$+ \oint\!\!\oint_S d^2\mathbf{r} \int_0^\infty [\mathbf{g}' \times \text{curl } \mathbf{g}]dt = W + W_C(+0).$$

Here S is the surface covering the volume V of the superconductor, $U(T)$ is the total energy of the superconductor, its variation due to the vanishing of a vortex is equal to the vortex energy W, and W_C is the energy of intergranular capacitors at the instant $t = +0$. Note that in view of formula (4), curl $g = \mathbf{H}_S a \pi \sqrt{\pi}/(2\Phi_0) = $ const on the surface S. On the other hand, the value of $\mathbf{g}$ on surface S in steady state is also determined by the external field only, i.e., $\mathbf{g}(0) = \mathbf{g}(\infty)$, and the surface integral is equal to zero.

Since the variation of parameter m in Eq. (6) is treated as an adiabatic process, the current distribution and the energy density do not change at any point at the instant of transition $t = 0$. On the other hand, the vanishing of a vortex is associated with a transition of intergranular Josephson junctions into resistive regime, i.e., $\varphi_k(+0) = 0$. In this case, nondissipative Josephson current is replaced by conduction and displacement currents, and the potential energy W_J of Josephson junctions is replaced by the energy W_C of charged intergranular capacitors. Subsequently, the energy W_C is scattered in microwave oscillations in Josephson junctions. Hence we can put $W_C(+0) = W_J(-0) = W/2$ and obtain an expression for the dissipation energy associated with the vanishing of a vortex:

$$q = 1.5W. \tag{15}$$

3. RESISTIVE STATE

Let a superconductor with hypervortex concentration $N(\mathbf{r})$ carry the transport current of density $\mathbf{j}$; hypervortices move at velocity $\mathbf{v}$, experience the action of the Lorentz force $\mathbf{f}_L$, and r vortices vanish per unit volume of the superconductor per unit time. In this case, the power balance equation for unit volume can be written in the form

$$\mathbf{Ej} = |N|\mathbf{f}_L\mathbf{v} + rq + W_J \partial(|N|)/\partial t. \tag{16}$$

Here we have taken into account the fact that the work done by the electric field to displace the charge is spent not only for heat losses, but also to change the potential energy of Josephson junctions. The force against which the work is done upon a change in the phase φ_k of a junction is of a nonelectromagnetic origin since the energy of the junction
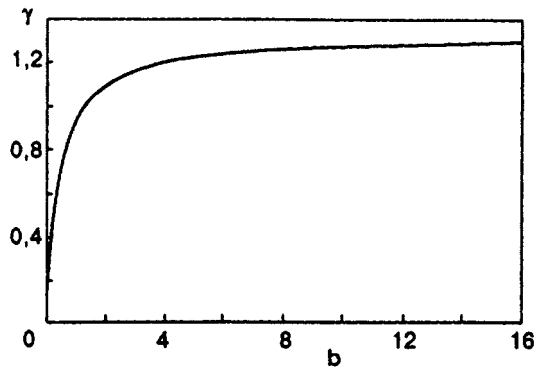
FIG. 2. Dependence of differential resistivity of a superconductor in the resistive state on magnetic field in normalized coordinates.

does not depend on the voltage applied to it, and hence it is an extraneous force. In a certain sense, the change in the junction energy is similar to the charge of a perfect storage cell. Taking into account relations (12) and (15) and the continuity equation

$$\partial|N|/\partial t = -\operatorname{div}(|N|\mathbf{v}) - r,$$

we can transform relation (16) to

$$\mathbf{E}\mathbf{j} = \frac{[\mathbf{B}\times\mathbf{v}]}{c}\mathbf{j} - \frac{W}{2}\left[2\frac{\partial(|B|/\Phi)}{\partial t} + 3\operatorname{div}\left(\frac{|B|}{\Phi}\mathbf{v}\right)\right]. \quad (17)$$

This relation is the constitutive equation for the critical and resistive states of weakly granular superconductor; together with the Maxwell's equations

$$\operatorname{curl}\ \mathbf{E} = -\frac{1}{c}\frac{\partial\mathbf{B}}{\partial t}; \quad (18)$$

$$\operatorname{curl}\ \mathbf{B} = \frac{4\pi}{c}\mathbf{j} \quad (19)$$

it describes the electrodynamics of the superconductor completely. If the magnetic field is directed along the z-axis, i.e., $\mathbf{B}(\mathbf{r}) = B(x,y)\mathbf{e} = N\Phi\mathbf{e}$, we have $\operatorname{grad} B = 4\pi[\mathbf{e}\times\mathbf{j}]/c$.

Let us consider steady-state conditions under which the transport current density is virtually constant, and the Laplacian of the magnetic induction B can be neglected. Taking relation (13) into account and carrying out simple vector transformations, we can write Eq. (17) in the form of the nonlinear Ohm's law:

$$\mathbf{E} = \gamma(|B|)\mathbf{j}\left(1 - \frac{j_C}{|\mathbf{j}|}\right)\Theta(|\mathbf{j}| - j_C), \quad (20)$$

where

$$\gamma(|B|) = \frac{\lambda_J^2}{\tau c^2}\left(\frac{\Phi|B|}{W} + 6\pi W\frac{d(|B|/W)}{d|B|}\right) \quad (21)$$

is the differential resistivity in the resistive state. Figure 2 shows the magnetic field dependence of the differential resistivity $\gamma(|B|)$ normalized to the characteristic resistance $\gamma_0 = Ra$ of the granular medium and calculated for the dependences of the vortex flux and its energy on the average magnetic field b, which are shown in Fig. 1. This dependence is successfully approximated by the formula

$$\gamma(|b|)/\gamma_0 = (2 + 40|b|)/(15 + 30|b|). \quad (22)$$

It should be noted that the approximation coefficients are different for different values of H_{C1} and $\mu_2(B_1)$ for granules and of the ratio a/λ_J, but the analytic form of approximating functions remains unchanged. For example, the flux resistivity γ for a certain value of mean field turns out to be larger than γ_0. The characteristic resistivity γ_0 is the resistivity of a three-dimensional matrix formed by resistors R with a period a, i.e., the resistivity of a granular superconductor with all the intergranular junctions in the resistive state. If the magnetic field created by the transport current at the superconductor surface is strong enough, and the condition $\gamma(B) > \gamma_0$ is satisfied in a certain cross section, the ceramic superconductor in the resistive state can be separated into two phases, viz., the internal "Josephson" phase in which the transport current flows through intergranular junctions in the superconducting state and is accompanied by the motion of hypervortices, and the external "Abrikosov" phase in which the junctions are in the resistive state, hypervortices are not formed, and the transport current is accompanied with the motion of Abrikosov vortices in the granules, which are formed and vanish at the boundaries of the granules.

The problem on phase equilibrium in dissipative systems has not been solved yet. Following the Zubarev method of nonequilibrium static operator,[13] and the matching principle of the minimum dissipative power for a given external effect whose role is played by the transport current, we can assume that the current density at the interface is continuous, and the following condition must be observed: $\gamma(j - j_C\operatorname{sgn}(j)) = \gamma_0 j$. It should be noted that the applicability of the Zubarev method to essentially nonstationary processes has not been analyzed so far.

Let us consider an plane-parallel plate of unit length cut from a granular superconductor of thickness d and carrying a direct transport current I passing along the y-axis, exceeding the critical value $I_C = dj_C$, and creating the magnetic field $H_I = 2\pi I/c$ at the plate surface. The condition $\mathbf{B}(t) = \operatorname{const}$ in this case leads to the condition $\mathbf{E}(t, \mathbf{r}) = \operatorname{const}$. Let us suppose that the plane $x = 0$ passes through the center of the plate, and $B(0) = 0$. If $H_I \gg H_{C1}$, we can assume that $B(d/2) = H_I$. Denoting by U the voltage drop over a unit length along the y-axis, we obtain from Eqs. (19) and (20)

$$I = \frac{c}{2\pi}B\left(\frac{d}{2}\right) = 2\int_0^{d/2}(U/\gamma + j_C)dx. \quad (23)$$

Let us find the differential resistance of the plate for $I = I_C$ and $U = 0$. Putting $E = 0$ in Eq. (20), we obtain $B(x) = 4\pi j_C x/c$. Then Eqs. (22) and (23) lead to

$$r = \frac{dU}{dI}\bigg|_{U=0} = \left(2\int_0^{d/2}\frac{dx}{\gamma(B(x))}\right)^{-1} = \frac{4Ra}{3d}\Bigg(1$$

$$+ \frac{9cB_J}{40\pi I_C}\ln\left(1 + \frac{49\pi I_C}{cB_J}\right)\Bigg)^{-1} > \frac{2Ra}{15d} > 0,$$

i.e., the current–voltage characteristic of a slightly granular superconductor has a kink at $U = 0$. Such a dependence was observed in Josephson structures experimentally.[14]

The kink on the current–voltage characteristic at the point $U=0$ is directly connected with the fact that according to Eq. (17), $E(B=0) \neq 0$ in view of the additional energy dissipation accompanying the vanishing of vortices. If we assume, as is usually done for type II superconductors, that $\mathbf{E}=[\mathbf{B}\times\mathbf{v}]/c$,[11] $E=0$ at the center of the plate, which contradicts the requirement that the electric field is constant over a cross section under steady-state conditions.

The general solution of the system of equations (17)–(19) is rather cumbersome. For a plane-parallel plate, it is convenient to reduce these equations to a system of one-dimensional first-order equations:

$$4\pi W \frac{d(|B|/\Phi)}{d|B|} \frac{\partial E}{\partial x} \operatorname{sgn}(B) + E \frac{\partial B}{\partial x} = -\frac{c}{4\pi}\left(\gamma(|B|) \right.$$

$$\times \left(\frac{\partial B}{\partial x}\right)^2 + \frac{6\pi\lambda_J^2 B}{\tau c^2} \frac{\partial^2 B}{\partial x^2}\right)\left(1 - \frac{4\pi j_C}{c|\partial B/\partial x|}\right)\Theta\left(\left|\frac{\partial B}{\partial x}\right|\right.$$

$$\left. \left. -\frac{4\pi j_C}{c}\right) \right) \tag{24}$$

$$\partial B/\partial t = -c\,\partial E/\partial x, \tag{25}$$

and to solve this system numerically. However, the distributions obtained as a result of numerical simulation can hardly be verified experimentally. In order to compare the results of calculations with experimental data, we must relate the dynamics of the magnetic induction distribution in the sample with the integral electrically measurable quantities, viz., current and voltage.

Let us consider a superconducting sample as a two-pole carrying the transport current $i(t)$. On one hand, the power of the external source is equal to the Poynting vector through the sample surface S, and on the other hand, it is spent for changing the internal energy W of the sample and the power loss P depending on the square of the instantaneous value of the current:

$$u(t)i(t) = \frac{4\pi}{c} \oint \oint_S [\mathbf{E}(\mathbf{r},t)\times\mathbf{H}(\mathbf{r},t)]d^2\mathbf{r} = P(i^2(t))$$

$$+ \frac{dW(i^2(t))}{dt},$$

where $u(t)$ is the voltage across the sample terminals. We denote by $u_D(t)=P(t)/i(t)$ the loss voltage and by $L=d(2W)/d(i^2)$ the differential inductance. Taking into account the fact that the vectors $\mathbf{E}$ and $\mathbf{H}$ on the surface of the superconducting sample are mutually orthogonal and directed along the tangent to the surface, and using Ampere's circuital law, we obtain

$$u(t) = \int_1^2 \mathbf{E}_S(\mathbf{r},t)d\mathbf{r} = u_D(i(t)) + L(i^2(t))\frac{di}{dt}. \tag{26}$$

The integral can be evaluated along the contour connecting the terminals over the shortest path on the conductor surface. The electric field strength $\mathbf{E}_S$ on the sample surface can be determined from Eq. (24).

Thus, the voltage $u(t)$ across the sample terminals for a given current $i(t)$ through the sample is a computable quan-
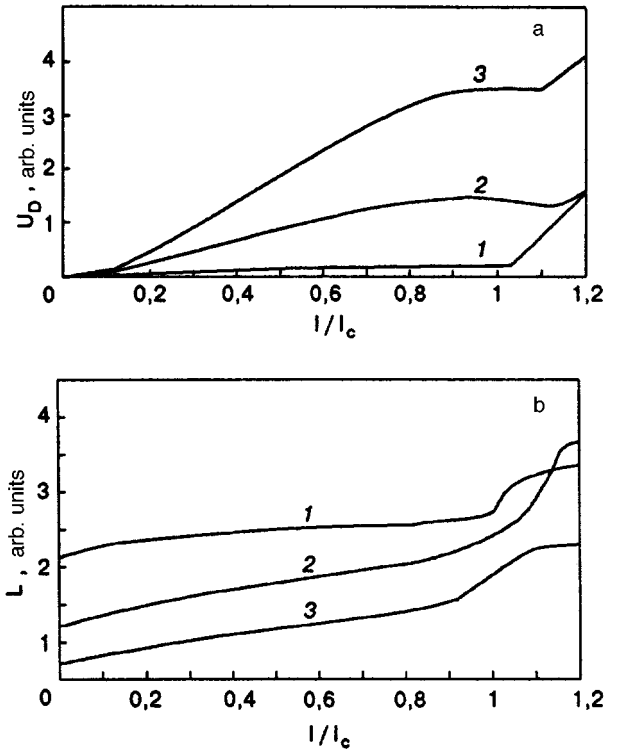

FIG. 3. Theoretical current–voltage characteristics (a) and the dependence of induction of a superconductor on transport current (b): $\omega = 10^{-5}\tau^{-1}$ (1); $\omega = 3\cdot10^{-5}\tau^{-1}$ (2); $\omega = 10^{-4}\tau^{-1}$ (3).

tity which can also be measured directly. In order to determine the loss voltage and differential inductance, we assume that the sample carries a sinusoidal current $i(t)=I_0 \sin(\omega t)$. For any value of the current I whose magnitude is smaller than I_0, we can find two instants of time t_1 and t_2 such that $i(t_1)=i(t_2)=I$ and $di(t_1)/dt=-di(t_2)/dt$. Denoting $u(t_1)=u_1$ and $u(t_2)=u_2$, we obtain from (26)

$$u_D(I) = \frac{u_1+u_2}{2}, \quad L(I^2) = \frac{u_1-u_2}{2\omega(I_0^2-I^2)^{1/2}}. \tag{27}$$

Figure 3 shows the results of numerical simulation of the current–voltage characteristics (dependences of the loss voltage u_D) and the dependences of the inductance of a granular superconductor on the transport current for a plate of thickness $d=100\lambda_J$ with a critical current density $j_C=5\cdot10^{-3}J_J$ at three different frequencies normalized to $1/\tau$. The current in Fig. 3 is normalized to the critical value $I_C=dj_C$, and the voltage and inductance are plotted in arbitrary units. Figure 4 shows for comparison the current–voltage characteristics and the dependence of inductance on transport current experimentally measured at frequencies 20, 60, and 300 Hz according to the technique proposed in Refs. 15 and 16. Measurements were made on a cylindrical sample made of an yttrium ceramic and having the height 30 mm, outer diameter 20 mm, and inner diameter 16 mm. It should be noted that an increase in the inductance of the sample upon its transition to the resistive state, which is sometimes considerably larger than its geometrical inductance, is a purely kinetic effect. It is due to the fact that the loss voltage in model (26) is assumed to be a function of the instanta-
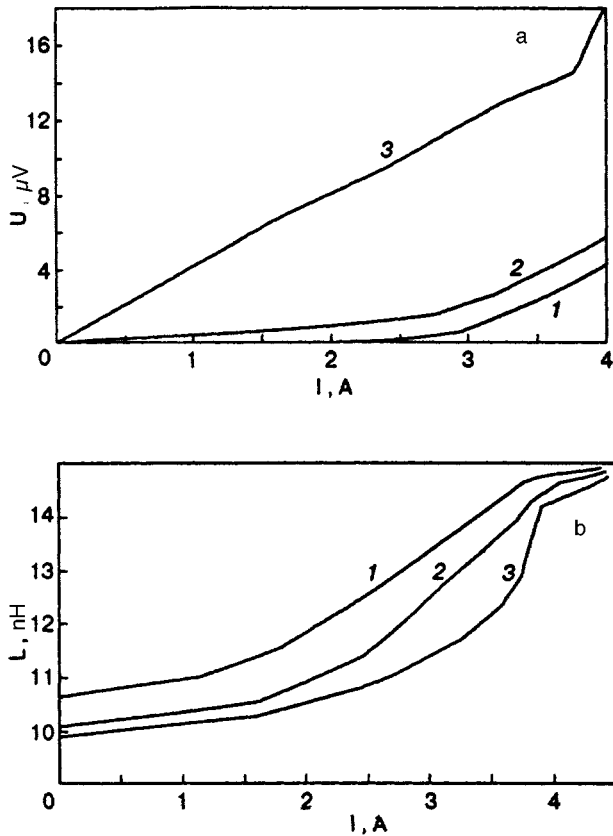
FIG. 4. Experimental current–voltage characteristics (a) and the dependence of induction of a superconductor on transport current (b) at various frequencies f (in Hz): 20 (curve 1), 60 (curve 2), and 300 (curve 3).

FIG. 5. Theoretical (a) and experimental (b) dependence of the real component of the second harmonic on constant magnetic field.

neous value of transport current. In actual practice, the power loss is a retarded potential of transport current in view of the finite velocity of vortices, which leads to a phase shift in the loss voltage $u_D(t)$ relative to the transport current $I(t)$. This phase shift is recorded by the measuring system as an increase in inductance.

Figure 5a shows the theoretical dependence of the real component of the second harmonic of the response of a weakly granular HTS material to a varying magnetic field on the strength of the applied constant magnetic field. The calculations were made for an infinitely long plane-parallel plate of thickness $2000\lambda_J$; the critical current density was assumed to be $j_C = 5 \cdot 10^{-3} J_J$, and the varying magnetic field was regarded as a sinusoidal field of frequency $\omega = 10^{-3}/\tau$ and amplitude $3.2B_J$. The strength H_0 of the constant magnetic field is laid along the abscissa axis in dimensionless units of $h_0 = H_0/B_J$, and the scale along the ordinate axis is arbitrary. Figure 5b shows for comparison the experimental dependence measured according to the technique described in Ref. 17. Measurements were made at 77 K on a yttrium ceramic sample of diameter 2.5 mm and length 15 mm in a varying magnetic field of frequency 10 kHz and amplitude 5 Oe. Similar experimental results are described in Ref. 18.

CONCLUSIONS

Good agreement between the theoretical and experimental dependences indicates that the models of hypervortices
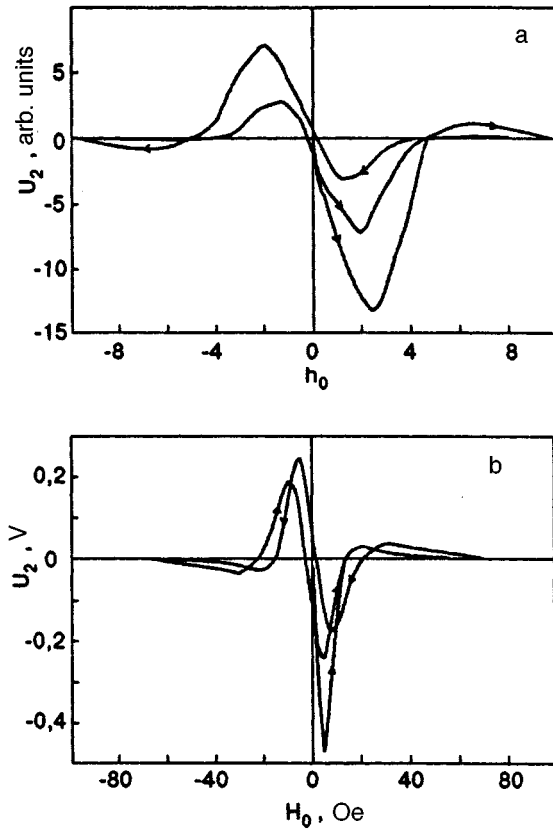
used for constructing the phenomenological electrodynamics of ceramic superconductors are fruitful. It would be interesting to establish the existence of hypervortices in actual practice and their observability in ceramic superconductors. A mathematically isolated hypervortex, which is a singular solution of the constituent equation (6), describes from the physical point of view a current loop connecting intergranular Josephson junctions, which plays the role of a link for Abrikosov vortices in granules. Numerical simulation demonstrates the advantage of such a structure from the energy point of view. The magnetic flux created by current loops in a vortex lattice can amount to a few thousandths of the flux of Abrikosov vortices, and the configuration of these currents is probably too complex for their direct observation. We can assume that the model of hypervortices describes analytically the nonlinear and nonlocal interaction between Abrikosov vortices in granules through the system of intergranular Josephson junctions as well as their interaction with the surface and transport currents. The experimentally observed complex nature of the nonlinear susceptibility of HTS materials,[17,18] which cannot be described quantitatively by using the Bean rigid model, the model of spin glass, or the percolation model, indicates the presence of such an interaction.

of the State Program ''High-Temperature Superconductivity.''

*E-mail: ivanov@physic.vgu.tsaritsyn.su

[1] È. B. Sonin, Pis'ma Zh. Éksp. Teor. Fiz. **47**, 415 (1988) [JETP Lett. **47**, 496 (1988)].

[2] E. Z. Meilikhov, and V. G. Shapiro, Sverkhprovodimost': Fiz., Khim., Tekh. **4**, 1437 (1991).

[3] A. S. Petrov and E. E. Slyadnikova, Sverkhprovodimost': Fiz., Khim., Tekh. **6**, 538 (1993).

[4] M. A. Zelikman, Sverkhprovodimost': Fiz., Khim., Tekh. **7**, 946 (1994).

[5] V. K. Ignatjev, Sverkhprovodimost': Fiz., Khim., Tekh. **7**, 215 (1994).

[6] K. K. Likharev and B. T. Ul'rikh, *Systems with Josephson Junctions* [in Russian], Moscow State Univ., Moscow (1978).

[7] G. S. Mkrtchan, F. R. Shakirzanova, E. A. Shapoval, and V. V. Shmidt, Zh. Éksp. Teor. Fiz. **63**, 667 (1972) [JETP **36**, 352 (1972)].

[8] G. S. Mkrtchan, Zh. Éksp. Teor. Fiz. **68**, 186 (1975) [JETP **41**, 90 (1975)].

[9] C. P. Bean, Phys. Rev. Lett. **8**, 250 (1962).

[10] C. P. Bean, Technical Report Grant 88f034-NYSIS 162 (1992).

[11] L. P. Gor'kov and N. B. Kopnin, Usp. Fiz. Nauk **116**, 413 (1975) [Sov. Phys. Uspekhi **18** 496 (1975)].

[12] A. V. Gurevich, R. G. Mints, and A. L. Rakhmanov, *Physics of Composite Superconductors* [in Russian], Nauka, Moscow (1987).

[13] D. N. Zubarev, *Nonequilibrium Statistical Thermodynamics* [in Russian], Nauka, Moscow (1971).

[14] I. Ya. Krasnopolin and I. Ya. Kislyanskiĭ, in *Abstracts of Papers to 24th All-Union Conf. on Low Temp. Phys.*, Tbilisi (1986).

[15] M. V. Belodedov and V. K. Ignatjev, Sverkhprovodimost': Fiz., Khim., Tekh. **3**, 953 (1990).

[16] V. K. Ignatjev and A. E. Konshin, Prib. Tekh. Éksp. [in press]

[17] V. K. Ignatjev and S. V. Chernykh, Sverkhprovodimost': Fiz., Khim., Tekh. **7**, 1411 (1994).

[18] V. F. Masterov *et al.*, Sverkhprovodimost': Fiz., Khim., Tekh. **4**, 470 (1991).

Translated by R. S. Wadhwa

LOW-TEMPERATURE MAGNETISM

Hydrodynamic theory of magnets with strong exchange interaction

A. A. Isayev, M. Yu. Kovalevsky, and S. V. Peletminsky

*National Scientific Center Institute of Physics and Technology, 310108, Kharkov, Academicheskaya 1, Ukraine**

A microscopic approach to the description of multisublattice magnets with strong exchange interaction is proposed. Low-frequency dynamics of such magnets is characterized by the appearance of an additional dynamical variable, i.e., the orthogonal matrix of rotation, which corresponds to the total breaking of spin invariance [broken $SO(3)$ symmetry]. The structure of the source that breaks the symmetry of the equilibrium Gibbs distribution is established. The quasiaverage representation is generalized to weakly anisotropic, locally equilibrium states. The thermodynamics of such states is constructed. The method of reduced description is formulated and in its framework the hydrodynamic equations for the density of total spin and the matrix of rotation are obtained. The spectra of spin waves are found and the number of Goldstone and activation modes is determined. Two-sublattice ferrimagnet is considered as a special case of the magnet with broken $SO(3)$ symmetry, which corresponds to the special dependence of thermodynamic functions from the matrix of rotation. © *1997 American Institute of Physics.* [S1063-777X(97)00407-6]

INTRODUCTION

In the present work we study the low-frequency dynamics of the multisublattice magnet with strong exchange interaction. It is known that high-frequency processes in magnets can be described on the basis of the Landau–Lifshitz equation.[1,2] The use of this equation in the low-frequency case (hydrodynamic limit) for the multisublattice magnets is not well justified since the sublattice spins are not approximate integrals of motion because of the strong intersublattice exchange interaction. In Ref. 3 it was shown that reduced description arises in the investigation of the low-frequency dynamics of the multisublattice magnet with exchange interaction. Reduced description parameters are the density of total spin $s_\alpha(\mathbf{x})$ and the orthogonal matrix of rotation $a_{\alpha\beta}(\mathbf{x})$, which characterizes the orientation of the rigid complex of the sublattice spins formed as a result of the exchange interaction. The appearance of the matrix of rotation as an additional dynamic variable corresponds to the total symmetry breaking relative to spin rotations [broken $SO(3)$ symmetry]. Thus, low-frequency dynamics of the multisublattice magnet with exchange interaction is accompanied by the appearance of the states with spontaneously broken spin invariance. This description needs the attraction of nontraditional reduced description parameters, which are connected with the matrix of rotation $a_{\alpha\beta}$. Effective method for the study of such states is a Hamiltonian approach.[4–7] In its framework the dynamics of the magnet with total symmetry breaking relative to spin rotations[8] and the dynamics of the ferrimagnet[9] were considered. The idea of spontaneous symmetry breaking of the statistical equilibrium state[10–12] has been also used for disordered magnetic systems of the ''spin glass'' type.[13–15] Note that in Ref. 16 on the basis of this concept and with the use of the analogy between the

''easy-plane'' magnetic systems and the superfluid systems the equations of motion have been formulated for uniaxial magnets with spontaneous symmetry breaking relative to the spin rotations around the anisotropy axis. This symmetry breaking is a special case of the total spontaneous symmetry breaking.

We shall consider in the microscopic approach the thermodynamics and hydrodynamics of the magnetic systems with strong exchange interaction in the presence of weak anisotropy on the basis of the quasiaverages[10] and the reduced description[17] methods. Standard quasiaverages, which apply for the description of equilibrium states, are generalized in the case of weakly anisotropic, locally equilibrium states. Locally equilibrium Gibbs distribution is constructed on the basis of consideration of the local unitary transformation which corresponds to the broken symmetry relative to the spin rotations [see Eq. (2.8)]. Performing this transformation on the source in Gibbs distribution, we introduce the matrix of rotation $a(\mathbf{x})$ for the locally equilibrium states. Weak anisotropy permits us to consider the total spin as an approximate integral of motion and in the sense of the main approximation of anisotropy (see the text for details) the corresponding term with the spin is included in the exponent of the Gibbs distribution.

To construct the hydrodynamic equations on the basis of reduced description method we introduce the matrix of rotation $b(\mathbf{x}, \hat\rho)$ as a functional of the nonequilibrium statistical operator $\hat\rho$, using the concept of the system order parameter operator. The connection between the matrix of rotation $a(\mathbf{x})$ in locally equilibrium Gibbs distribution and the matrix of rotation $b(\mathbf{x}, \hat\rho)$, which is the functional of the nonequilibrium statistical operator $\hat\rho$ is established. The equations of motion for the density of total spin, $s_\alpha(\mathbf{x})$ and the matrix of

rotation $a_{\alpha\beta}(\mathbf{x})$ [Eqs. (3.17) and (3.18)] are found. These equations describe the low-frequency dynamics of the multisublattice magnet with strong exchange interaction and weak anisotropy. The structure of the spectrum of spin waves is determined.

It is shown that weakly anisotropic ferrimagnet represents a special case of the magnet with total symmetry breaking, which corresponds to a special dependence of the matrix of rotation.

1. THE ORDER PARAMETER

In the microscopic approach to the magnetic systems the basic operators, from which all other operators are constructed, are the operators of site spins $s_n(l)$ of atoms (l is the number of the site, and n is the number of the crystal sublattice). The Hamiltonian H and the statistical operator $\hat{\rho}$ are constructed from these operators only, $H = H(\hat{s})$, $\hat{\rho} = \hat{\rho}(\hat{s})$. An arbitrary physical quantity $\hat{c}$ of the magnet is also the operator functional of the site spins $\hat{c} = \hat{c}(\hat{s})$. We switch from the site representation to the continuum representation: $v_0^{-1}\hat{s}_{n\alpha}(l) \xrightarrow[v_0 \to 0]{} \hat{s}_{n\alpha}(\mathbf{x})$. Here v_0 is the volume of the unit cell, and $\mathbf{x} \equiv \mathbf{R}_l$ is the position vector which defines the position of lth site. The spin-density operators $\hat{s}_{n\alpha}(\mathbf{x})$ satisfy the commutation relations

$$[\hat{s}_{n\alpha}(\mathbf{x}), \hat{s}_{m\beta}(\mathbf{x}')] = i\varepsilon_{\alpha\beta\gamma}\delta_{nm}\hat{s}_{m\gamma}(\mathbf{x})\delta(\mathbf{x} - \mathbf{x}'). \quad (1.1)$$

We introduce in the continuum limit the operation of the spatial shifts $[P_k, \ldots]$

$$[P_k, \rho(\hat{s}(\mathbf{x}'))] \equiv i\left.\frac{\partial\rho(\hat{s}(\mathbf{x}' + \mathbf{y}))}{\partial y_k}\right|_{y_k = 0},$$

$$[P_k, c(\mathbf{x}, \hat{s}(\mathbf{x}'))] \equiv i\left.\frac{\partial c(\mathbf{x}, \hat{s}(\mathbf{x}' + \mathbf{y}))}{\partial y_k}\right|_{y_k = 0}, \quad (1.2)$$

where $\rho(\hat{s}(\mathbf{x}'))$ and $c(\mathbf{x}, \hat{s}(\mathbf{x}'))$ are the functionals of $\hat{s}(\mathbf{x})$. In accordance with this definition

$$c(\mathbf{x}, \hat{s}(\mathbf{x}' + \mathbf{y})) = e^{-i\mathbf{Py}}c(\mathbf{x}, \hat{s}(\mathbf{x}'))e^{i\mathbf{Py}}. \quad (1.3)$$

Realization of the operator P_k in the classical case in terms of the spin densities in the framework of the Hamiltonian approach is given in Refs. 8 and 9. For our purposes satisfaction of the relationships (1.2) and (1.3) is sufficient in the quantum case and therefore we shall not solve the problem of concrete realization of the spatial shift operator P_k in terms of the spin density operators. Defining the translationally invariant operator $\hat{c}(\mathbf{x}) \equiv \hat{c}(\mathbf{x}, \hat{s}(\mathbf{x}'))$ by the relationship $\hat{c}(\mathbf{x} - \mathbf{y}, \hat{s}(\mathbf{x}' + \mathbf{y})) = \hat{c}(\mathbf{x}, \hat{s}(\mathbf{x}'))$, we have by virtue of Eq. (1.3)

$$i[P_k, \hat{c}(\mathbf{x})] = -\nabla_k \hat{c}(\mathbf{x}). \quad (1.4)$$

In the case of weakly anisotropic magnetic systems the main type of interactions are the exchange interactions. Anisotropic interactions are assumed to be small and can be taken into account by means of the perturbation theory. Disregarding the anisotropy, we can characterize the magnetic system by a set of additive motion integrals $\hat{\gamma}_a = \int d^3x\,\zeta_a(\mathbf{x})$ ($a = 0, \alpha$), where $\hat{\gamma}_0 \equiv H = \int d^3x\,\hat{\varepsilon}(\mathbf{x})$ is the Hamiltonian, and

$\hat{\gamma}_\alpha \equiv \hat{S}_\alpha = \int d^3x \Sigma_n \hat{s}_{n\alpha}(\mathbf{x})$ is the operator of the total spin. Taking into account the weak anisotropy, we see that the total spin $\hat{S}_\alpha$ is only the approximate integral of motion. Equations of motion for the densities $\hat{\zeta}_a(\mathbf{x})$ have the form

$$\dot{\hat{\zeta}}_a(\mathbf{x}) = i[H, \hat{\zeta}_a(\mathbf{x})], \quad (1.5)$$

and with allowance for the operator identity

$$i[\hat{A}, \hat{b}(\mathbf{x})] = -i[\hat{B}, \hat{a}(\mathbf{x})] - \nabla_k \hat{b}_k(\mathbf{x}) \quad (1.6)$$

for arbitrary quasilocal operators $\hat{a}(\mathbf{x})$, $\hat{b}(\mathbf{x})$, where

$$\hat{A} = \int d^3x\,\hat{a}(\mathbf{x}), \quad \hat{B} = \int d^3x\,\hat{b}(\mathbf{x}),$$

$$\hat{b}_k(\mathbf{x}) = i\int d^3x'\,x_k'\int_0^1 d\lambda[\hat{a}(\mathbf{x} - (1 - \lambda)\mathbf{x}'),$$

$$\hat{b}(\mathbf{x} + \lambda\mathbf{x}')]$$

can be represented in the form

$$\dot{\hat{\varepsilon}}(\mathbf{x}) = -\nabla_k \hat{q}_k(\mathbf{x}), \quad (1.7)$$

$$\dot{\hat{s}}_\alpha(\mathbf{x}) = -i[\hat{S}_\alpha, \hat{\varepsilon}(\mathbf{x})] - \nabla_k \hat{j}_{\alpha k}(\mathbf{x}).$$

Here $\{\hat{q}_k(\mathbf{x}), \hat{j}_{\alpha k}(\mathbf{x})\} \equiv \hat{\zeta}_{ak}(\mathbf{x})$ are the flux density operators of energy and momentum, for which, in accordance with (1.6), we have

$$\hat{q}_k(\mathbf{x}) = \frac{i}{2}\int d^3x'\,x_k'\int_0^1 d\lambda[\hat{\varepsilon}(\mathbf{x} - (1 - \lambda)\mathbf{x}'),$$

$$\hat{\varepsilon}(\mathbf{x} + \lambda\mathbf{x}')], \quad (1.8)$$

$$\hat{j}_{\alpha k}(\mathbf{x}) = i\int d^3x'\,x_k'\int_0^1 d\lambda[\hat{\varepsilon}(\mathbf{x} - (1 - \lambda)\mathbf{x}'),$$

$$\hat{s}_\alpha(\mathbf{x} + \lambda\mathbf{x}')].$$

In the case of the isotropic magnetic systems ($[\hat{S}_\alpha, \hat{\varepsilon}(\mathbf{x})] = 0$) equations of motion (1.7) have the form of differential conservation laws.

In macroscopic description of magnets the notion of the order parameter of the investigated system has an important role. We shall consider in what follows the magnet with total symmetry breaking relative to spin rotations. It is characterized by the three rotation angles φ_α, which realize a parametrization of the three-dimensional rotation group in spin space, or by the real rotation matrix associated with them, $a_{\alpha\beta}(\varphi)$ ($a\tilde{a} = 1$). Moreover, we shall study the two sublattice ferrimagnet with noncompensated sublattices characterized by the unit vector of antiferromagnetism l_α (or by the two rotation angles). In the case of total symmetry violation the order parameter is the complex spin vector $\Delta_\alpha(\mathbf{x}) = \mathrm{Tr}\,\rho\hat{\Delta}_\alpha(\mathbf{x}) = \Delta_{1\alpha}(\mathbf{x}) + i\Delta_{2\alpha}(\mathbf{x})$, where $\hat{\Delta}_\alpha(\mathbf{x}) = \hat{\Delta}_{1\alpha}(\mathbf{x}) + i\hat{\Delta}_{2\alpha}(\mathbf{x})$ is the order parameter operator ($\Delta_1^+ = \Delta_1$, $\Delta_2^+ = \Delta_2$). For the two sublattice ferrimagnet the order parameter is the real vector $\Delta_\alpha(\mathbf{x}) = \mathrm{Tr}\,\rho\hat{\Delta}_\alpha(\mathbf{x})$, where $\hat{\Delta}_\alpha(\mathbf{x})$ is the order parameter of the ferrimagnetic system ($\hat{\Delta}^+ = \hat{\Delta}$). The order parameter operator in each cases satisfies the symmetry properties

$$i[\hat{s}_\alpha(\mathbf{x}),\hat{\Delta}_\beta(\mathbf{x}')]=-\varepsilon_{\alpha\beta\gamma}\hat{\Delta}_\gamma(\mathbf{x})\,\delta(\mathbf{x}-\mathbf{x}'),$$

$$i[P_k,\hat{\Delta}_\alpha(\mathbf{x})]=-\nabla_k\hat{\Delta}_\alpha(\mathbf{x}). \tag{1.9}$$

Note that the order parameter operator is expressed in terms of the spin operators of the sublattices and it is usually chosen in such a way that the order parameter for the normal state is equal to zero. By virtue of relations (1.1) and (1.9) the operators $\hat{s}(\mathbf{x})$ and $\hat{\Delta}(\mathbf{x})$ are transformed under the local spin rotations as vectors

$$U_a^+\hat{s}_\alpha(\mathbf{x})U_a=a_{\alpha\beta}(\mathbf{x})\hat{s}_\beta(\mathbf{x}),$$

$$U_a^+\hat{\Delta}_\alpha(\mathbf{x})U_a=a_{\alpha\beta}(\mathbf{x})\hat{\Delta}_\beta(\mathbf{x}), \tag{1.10}$$

$$U_a=\exp\left(-i\int d^3x\,\varphi_\lambda(\mathbf{x})\hat{s}_\lambda(\mathbf{x})\right)$$

$[\varphi_\alpha(\mathbf{x})$ are the local rotation angles]. In accordance with (1.10), the orthogonal rotation matrix $a(\varphi)$ has the form

$$a_{\alpha\beta}(\varphi)=(\exp(-\varepsilon\varphi))_{\alpha\beta}=\delta_{\alpha\beta}\cos\,\varphi+n_\alpha n_\beta(1$$
$$-\cos\,\varphi)+\varepsilon_{\alpha\lambda\beta}n_\lambda\sin\,\varphi, \tag{1.11}$$

where

$$\varphi_\alpha=n_\alpha\varphi,\ \ n_\alpha^2=1,\ \ (\varepsilon\varphi)_{\alpha\beta}=\varepsilon_{\alpha\beta\gamma}\varphi_\gamma.$$

The infinitesimal characteristics of the unitary transformation U_a is the operator $U_a^+\delta U_a$, where δU_a is variation of the unitary transformation U_a due to variation δa of the orthogonal rotation matrix $(\delta a\cdot\tilde{a}=-a\cdot\delta\tilde{a})$. In accordance with (1.10),

$$U_a^+\delta U_a=i\int d^3x\,\delta R_\gamma(\mathbf{x})\hat{s}_\gamma(\mathbf{x}),$$

$$\delta R_\gamma=\frac{1}{2}\,\varepsilon_{\alpha\beta\gamma}(\tilde{a}\delta a)_{\alpha\beta}. \tag{1.12}$$

[The quantity δR_γ in (1.12) is not variation of some vector R_γ]. Note that in what follows it will be convenient for us to use the formalism of left and right Cartan forms[13,18]

$$\omega_{\alpha k}\equiv\frac{1}{2}\,\varepsilon_{\alpha\beta\gamma}(\tilde{a}\nabla_k a)_{\gamma\beta},$$

$$\underline{\omega}_{\alpha k}\equiv\frac{1}{2}\,\varepsilon_{\alpha\beta\gamma}(a\nabla_k\tilde{a})_{\beta\gamma}=a_{\alpha\beta}\omega_{\beta k}. \tag{1.13}$$

We define the translationally invariant states of the magnet by the relation $\hat{\rho}(s(\mathbf{x}'+\mathbf{y}))=\hat{\rho}(s(\mathbf{x}'))$ or by virtue of (1.2)

$$[P_k,\hat{\rho}]=0. \tag{1.14}$$

The statistical operators describing the equilibrium state of collinear magnet satisfy this relation. For spiral magnetic ordering the transformation of translations by the vector $\mathbf{x}$ and spin rotation around some axis n_α $(n_\alpha^2=1)$ by the angle $\mathbf{px}$ do not change the state of the system:

$$\exp[i\mathbf{x}(\hat{\mathbf{P}}-\mathbf{p}(n_\alpha\hat{S}_\alpha))]\hat{\rho}\,\exp[-i\mathbf{x}(\hat{\mathbf{P}}-\mathbf{p}(n_\alpha\hat{S}_\alpha))]=\hat{\rho}$$

or

$$[\hat{\rho},P_k-p_k(n_\alpha\hat{S}_\alpha)]=0. \tag{1.15}$$

The vector p_k is called the vector of the magnetic spiral.

2. WEAKLY ANISOTROPIC LOCALLY EQUILIBRIUM STATES

In the framework of thermodynamics and hydrodynamics of condensed media in the microscopic approach the concept of quasiaverages[10] plays an important role. In accordance with this concept, the equilibrium average of an arbitrary quasilocal operator $\hat{c}(\mathbf{x})$ of a magnetic system with spontaneously broken symmetry is defined by the formula

$$\langle\hat{c}(\mathbf{x})\rangle=\lim_{\nu\to 0}\ \lim_{V\to\infty}\ \mathrm{Tr}\ \omega_\nu\hat{c}(\mathbf{x})\equiv\mathrm{Tr}\ w\hat{c}(\mathbf{x}), \tag{2.1}$$

$$w_\nu=\exp\{\Omega_\nu-Y_a\hat{\gamma}_a-\nu\hat{G}\}.$$

Here $Y_a\equiv(Y_0,\ Y_\alpha)$ are the thermodynamic forces conjugate to the additive motion integrals $\hat{\gamma}_a$ $(Y_0^{-1}\equiv T$ is the temperature, and $-Y_\alpha Y_0^{-1}\equiv h_\alpha$ is the effective field). The source $\hat{G}$ in (2.1) lifts the degeneracy of the statistical equilibrium state and represents itself as a linear functional of the order parameter operator

$$\hat{G}=\int d^3x\mathbf{g}(\mathbf{x},t)\hat{\Delta}(\mathbf{x})+\text{h.c.}=\hat{G}(t). \tag{2.2}$$

The specific form of the function $g(\mathbf{x},t)$ (which can depend on time) is defined by the symmetry properties of the equilibrium state.

In the case of anisotropic magnetic systems the total spin $\hat{S}_\alpha$ stops to be the integral of motion so that in Eq. (2.1) one should set $Y_\alpha=0$. Allowance for anisotropy in the Hamiltonian H lifts the degeneracy relative to the uniform spin rotations. Therefore, the summand with the source in Eq. (2.1) should be put down. Nevertheless, in the investigation of weakly anisotropic magnetic systems we shall use the statistical operator of the form (2.1), which is ''main'' approximation of the weak isotropy. Here the next elucidations can be done. Since we consider the weak anisotropy, the total spin $\hat{S}_\alpha$ can be assumed to be the approximate motion integral and we include the corresponding summand with spin in the exponent of the Gibbs distribution (2.1).

The source $\hat{G}$ is introduced in Eq. (2.1) for the following purpose. If we take into account the weak anisotropy in the framework of perturbation theory, then as zero approximation we will have the statistical operator which corresponds to the magnetically ordered state with broken symmetry relative to the spin rotations. The source $\hat{G}$ in distribution (2.1) plays a role of the parameter that lifts the degeneracy.

This can be illustrated by using the following example. If we consider a ferromagnet with exchange interaction in the magnetic field, then the term describing the interaction with external field will play the role of the anisotropy and will fix the direction of the magnetic moment in space. When the field goes to zero (weak anisotropy), the source in the Gibbs distribution plays the role of the infinitesimally small anisotropy, which removes the degeneracy and fixes the direction of the moment. Thus, the statistical operator (2.1) describes the weakly anisotropic quasiequilibrium states of the magnetic system in the main approximation of the anisotropy and we shall use it in what follows for generalization of the case of locally equilibrium states.

In the given section we shall study the magnet with total symmetry breaking relative to spin rotations, for which the order parameter has the structure $\hat{\Delta}(\mathbf{x}) = \hat{\Delta}_1(\mathbf{x}) + i\hat{\Delta}_2(\mathbf{x})$ and $\hat{\Delta}_1^+ = \hat{\Delta}_1$, $\hat{\Delta}_2^+ = \hat{\Delta}_2$. We formulate the symmetry properties of the equilibrium state. For the spiral magnetic ordering in accordance with Eq. (1.15) we have

$$[w, P_k - p_k(n_\alpha \hat{S}_\alpha)] = 0,$$

$$[w, Y_0 H + Y_\alpha \hat{S}_\alpha] = 0. \tag{2.3}$$

From the Jacobi identity follows the condition of compatibility of Eqs. (2.3)

$$\varepsilon_{\alpha\beta\gamma} n_\alpha Y_\beta [w, \hat{S}_\gamma] = 0.$$

We thus obtain $n_\alpha = Y_\alpha / |\mathbf{Y}|$. The relations (2.3) allow us to find the function $\mathbf{g}(\mathbf{x}, t)$

$$g(\mathbf{x}, t) = \xi a(\varphi^0) a(\varphi(\mathbf{x}, t)) \equiv \xi a(\mathbf{x}, t),$$

$$\varphi_\alpha(\mathbf{x}, t) = n_\alpha(\mathbf{px} - ht), \tag{2.4}$$

where φ_α^0 is a uniform rotation; $h_\alpha = h n_\alpha$; and ξ_α is a constant complex vector which we can choose for convenience in the form $\xi = \xi_1 + i\xi_2$, $\xi_1^2 = \xi_2^2 = 1$, $\xi_1 \xi_2 = 0$. From here one can see that the statistical equilibrium state is characterized by the thermodynamic forces Y_a, the spiral vector p_k, and the rotation angles φ_α^0. The vector ξ_α fixes the reference frame for the rotation angles and is not a thermodynamic parameter. In accordance with definitions (1.13), the left and right forms corresponding to the rotation matrix $a(\mathbf{x}, t)$ in (2.4) are

$$\omega_{\alpha k} = p_k n_\alpha, \quad \underline{\omega}_{\alpha k} = p_k \underline{n}_\alpha, \tag{2.5}$$

where $\underline{n} = a(\varphi^0) n$.

Note that in the case of collinear magnets introduction of a source in the statistical operator (2.1) in the presence of thermodynamic forces Y_α has no meaning since the term $Y_\alpha \hat{S}_\alpha$ lifts the degeneracy of the statistical equilibrium state.

Let us examine the locally equilibrium states. It is well known[17] that the statistical operator

$$w(Y(\mathbf{x}')) = \exp\left\{\Omega_\nu - \int d^3x' Y_a(\mathbf{x}') \hat{\zeta}_a(\mathbf{x}')\right\} \tag{2.6}$$

generalizes the Gibbs statistical operator for the normal systems in the case of locally equilibrium states. For the systems with spontaneously broken symmetry the locally equilibrium states are described by the statistical operator

$$w_\nu(Y(\mathbf{x}'), \phi(\mathbf{x}')) = \exp\left\{\Omega_\nu - \int d^3x' Y_a(\mathbf{x}') \hat{\zeta}_a(\mathbf{x}')\right.$$
$$\left. - \nu U_\phi^+ \hat{G} U_\phi\right\} \equiv U_\phi^+ \underline{w}_\nu U_\phi, \tag{2.7}$$

where

$$\underline{w}_\nu = \exp\left\{\Omega_\nu - \int d^3x Y_a(\mathbf{x}) \hat{\zeta}_a(\mathbf{x}) - \nu \hat{G}\right\},$$

$$\hat{\zeta}_a(\mathbf{x}) = U_\phi \hat{\zeta}_a(\mathbf{x}) U_\phi^+$$

and U_ϕ is the local unitary operator which corresponds to the broken symmetry [see, for example, Eq. (1.10) for symmetry

breaking relative to spin rotations], and ϕ is the order parameter phase that enters into the source $\hat{G}$. Introducing the statistical operator (2.7) for the locally equilibrium states based on the calculation of the averages with the statistical operator $w_\nu(Y(\mathbf{x}'), \phi(\mathbf{x}'))$, we can go over to the averages with the statistical operator $\underline{w}_v$:

$$\text{Tr } w\hat{a}(\mathbf{x}) = \text{Tr } \underline{w} U_\phi \hat{a}(\mathbf{x}) U_\phi^+,$$

where the operator $U_\phi \hat{a}(\mathbf{x}) U_\phi^+ \equiv \hat{b}(\mathbf{x})$, as a rule, can be easily found. This operator is of the type $\hat{a}(\mathbf{x})$. In the statistical operator $\underline{w}_\nu$ the source $\hat{G}$ is space uniform and for calculation of the averages $\text{Tr } \underline{w}\hat{b}(\mathbf{x})$ the standard perturbation theory [on gradients of the parameters $Y_\alpha(\mathbf{x}), \phi(\mathbf{x})$], which leads to the ordinary quasiaverages, can be used.

Thus, in accordance with (2.1) and (2.7), the statistical operator of the weakly anisotropic, locally equilibrium states of the magnet with total symmetry breaking relative to spin rotations is written in the form

$$w_\nu(Y(\mathbf{x}'), a(\mathbf{x}')) = \exp\left\{\Omega_\nu - \int d^3x' [Y_0(\mathbf{x}') \hat{\varepsilon}(\mathbf{x}')\right.$$
$$\left. + Y_\alpha(\mathbf{x}') \hat{s}_\alpha(\mathbf{x}')] - \nu \hat{G}_a\right\}$$
$$\equiv U_a^+ \underline{w}_\nu U_a, \tag{2.8}$$

$$\hat{G}_a \equiv U_a^+ \hat{G} U_a = \int d^3x' (\xi a(\mathbf{x}') \hat{\Delta}(x') + \text{h.c.}),$$

where

$$\underline{w}_\nu = \exp\left\{\Omega_\nu - \int d^3x [Y_0(x) \hat{\underline{\varepsilon}}(x)\right.$$
$$\left. + \underline{Y}_\alpha(x) \hat{s}_\alpha(x)] - \nu \hat{G}\right\},$$

$$\hat{G} = \int d^3x \xi \Delta(\mathbf{x}) + \text{h.c.}, \tag{2.9}$$

and $\hat{\underline{\varepsilon}} = U_a \hat{\varepsilon} U_a^+$, $\underline{Y} = aY$. Here the thermodynamic forces $Y_a(\mathbf{x})$ and the orthogonal rotation matrix $a_{\alpha\beta}(\mathbf{x})$ are the arbitrary functions of coordinates. In the equilibrium state [see (2.1)] $Y_a(\mathbf{x}) = Y_a$ and the structure of the orthogonal rotation matrix $a_{\alpha\beta}(\mathbf{x})$ is determined by Eq. (2.4). The matrix of rotation $a_{\alpha\beta}(\mathbf{x})$ for the locally equilibrium states is introduced in the distribution (2.8) by the transformation of local spin rotation performed on the source $\hat{G}$.

We obtain now the main thermodynamic identity for the locally equilibrium states and show that the locally equilibrium averages of the densities of additive motion integrals and fluxes corresponding to them can be expressed in the approximation of small inhomogeneities in terms of the locally equilibrium thermodynamic potential. In this connection, it is worthwhile to go over to the statistical operator $\underline{w}_\nu$ which is defined by Eq. (2.9). From (2.9) it follows that the locally equilibrium thermodynamic potential Ω is the functional of the thermodynamic forces $\underline{Y}_a \equiv (Y_0, \underline{Y}_a)$ and the rotation matrix $a(x)$:

$$\Omega = \int d^3x \omega(\mathbf{x}, \underline{Y}(\mathbf{x}'), a(\mathbf{x}')). \tag{2.10}$$

525   Low Temp. Phys. **23** (7), July 1997

Isayev *et al.*   525

Here ω is the density of the thermodynamic potential. Varying the potential Ω with respect to the thermodynamic forces Y_0 and $\underline{Y}$, we obtain

$$\delta_{Y_0}\Omega = \int d^3x\, \delta Y_0(\mathbf{x})\mathrm{Tr}\, \underline{w}\hat{\underline{\varepsilon}}(\mathbf{x}) = \int d^3x\, \delta Y_0(\mathbf{x})\varepsilon(\mathbf{x}),$$

$$\delta_{\underline{Y}}\Omega = \int d^3x\, \delta\underline{Y}(\mathbf{x})\mathrm{Tr}\, \underline{w}\hat{s}(\mathbf{x}) = \int d^3x\, \delta\underline{Y}(\mathbf{x})\underline{s}(\mathbf{x}),$$

where $\underline{s}(\mathbf{x}) = \mathrm{Tr}\, \underline{w}\hat{s}(\mathbf{x}) = a(\mathbf{x})s(\mathbf{x})$. Varying the potential Ω with respect to the orthogonal matrix a, we have $\delta_a\Omega = \int d^3x\, Y_0(\mathbf{x})\mathrm{Tr}\, \underline{w}\, \delta\hat{\underline{\varepsilon}}(\mathbf{x})$. By virtue of the explicit form of the operator $\hat{\underline{\varepsilon}}(\mathbf{x})$ and the relation (1.12) we thus find

$$\delta_a\Omega = i\int d^3x\, d^3x'\, \delta R_\alpha(\mathbf{x})Y_0(\mathbf{x}')\mathrm{Tr}\, w\{Y,a\}$$
$$\times [\hat{s}_\alpha(\mathbf{x}),\hat{\varepsilon}(\mathbf{x}')]. \tag{2.11}$$

Under calculation of the trace in Eq. (2.11), by virtue of quasilocality of the operator $\hat{\varepsilon}(\mathbf{x}')$, the points $\mathbf{x}'$ placed near $\mathbf{x}$ give the main contribution. Therefore, expanding the quantity $Y_0(\mathbf{x}')$ near the point $\mathbf{x}$, $Y_0(\mathbf{x}') = Y_0(\mathbf{x}) + (\mathbf{x}' - \mathbf{x})_k\partial Y_0/\partial x_k + \ldots$, we obtain in the main approximation

$$\delta_a\Omega = i\int d^3x\, \delta R_\alpha(\mathbf{x})Y_0(\mathbf{x})\mathrm{Tr}\, w[\hat{s}_\alpha(\mathbf{x}),\, H] + O(\nabla Y_0). \tag{2.12}$$

We thus have

$$\left(\frac{\delta\Omega}{\delta a_{\rho\nu}(\mathbf{x})}\right)_{\underline{Y}} = \frac{i}{2}\,\varepsilon_{\alpha\mu\nu}a_{\rho\mu}(\mathbf{x})Y_0(\mathbf{x})\mathrm{Tr}\, w[\hat{s}_\alpha(\mathbf{x}),H]$$
$$+ O(\nabla Y_0). \tag{2.13}$$

Thus, the thermodynamic relationship for the locally equilibrium states takes the form

$$\delta\Omega = \int d^3x\bigg(\varepsilon(\mathbf{x})\delta Y_0(\mathbf{x}) + \underline{s}_\alpha(\mathbf{x})\delta\underline{Y}_\alpha(\mathbf{x})$$
$$+ \left(\frac{\delta\Omega}{\delta a_{\alpha\beta}(\mathbf{x})}\right)_{\underline{Y}}\delta a_{\alpha\beta}(\mathbf{x})\bigg), \tag{2.14}$$

where the variational derivative $(\delta\Omega/\delta a_{\alpha\beta}(\mathbf{x}))_{\underline{Y}}$ is determined by Eq. (2.13). If instead of the variables $\underline{Y}_\alpha$ we use the variables $Y_\alpha = \underline{Y}_\beta a_{\beta\alpha}$, then relation (2.14) can be rewritten in the form

$$\delta\Omega = \int d^3x\bigg(\varepsilon(\mathbf{x})\delta Y_0(\mathbf{x}) + s_\alpha(\mathbf{x})\delta Y_\alpha(\mathbf{x}) + \int$$
$$+ \left(\frac{\delta\Omega}{\delta a_{\alpha\beta}(\mathbf{x})}\right)_Y\delta a_{\alpha\beta}(\mathbf{x})\bigg),$$

where

$$\left(\frac{\delta\Omega}{\delta a_{\alpha\beta}}\right)_Y = \left(\frac{\delta\Omega}{\delta a_{\alpha\beta}}\right)_{\underline{Y}} + \left(\frac{\delta\Omega}{\delta\underline{Y}_\alpha}\right)_a Y_\beta.$$

We define the entropy density by the expression $\sigma = -\omega + Y_a\zeta_a$. We can then easily show that with an accuracy to ∇Y_0 the following equations are valid:

$$\frac{\delta H}{\delta\sigma} = \frac{1}{Y_0}, \quad \frac{\delta H}{\delta s_\alpha} = -\frac{Y_\alpha}{Y_0}, \quad \frac{\delta H}{\delta a_{\alpha\beta}} = \frac{1}{Y_0}\frac{\delta\Omega}{\delta a_{\alpha\beta}}. \tag{2.15}$$

Here $H = \int d^3x\varepsilon(\mathbf{x})$. If the density of the thermodynamic potential in the local limit allows expansion on gradients of the parameters $\underline{Y}, a$

$$\omega(\mathbf{x};\underline{Y}(\mathbf{x}'),a(\mathbf{x}')) = \omega(\underline{Y}(\mathbf{x}),a(\mathbf{x}),\underline{\omega}_k(\mathbf{x}))$$
$$+ O(\nabla\underline{Y},\nabla\underline{\omega}_k), \tag{2.16}$$

then Eq. (2.14) can be simplified. In the operator identity (1.6) setting $a(\mathbf{x}) = \hat{\varepsilon}(\mathbf{x})$, $\hat{b}(\mathbf{x}) = \hat{s}_\alpha(\mathbf{x})$ and taking into account that for the anisotropic magnetic systems $[\hat{S}_\alpha,\hat{\varepsilon}(\mathbf{x})] \neq 0$, from (2.12) we obtain

$$\delta_a\Omega = \int d^3x\, \delta R_\alpha(\mathbf{x})Y_0(\mathbf{x})\{i\, \mathrm{Tr}\, w[\hat{S}_\alpha,\hat{\varepsilon}(\mathbf{x})] + \nabla_k j_{\alpha k}\},$$

$$j_{\alpha k} \equiv \mathrm{Tr}\, w\hat{j}_{\alpha k},$$

where the operator of the spin flux density $\hat{j}_{\alpha k}$ is defined by Eq. (1.8). Since $\nabla_k\delta R_\alpha = -\delta\underline{\omega}_{\beta k}a_{\beta\alpha}$, the last relation can be rewritten in the form

$$\delta_a\Omega = i\int d^3x\, \delta R_\alpha(\mathbf{x})Y_0(\mathbf{x})\mathrm{Tr}\, w[\hat{S}_\alpha,\hat{\varepsilon}(\mathbf{x})]$$
$$+ \int d^3x Y_0(\mathbf{x})\underline{j}_{\alpha k}(\mathbf{x})\delta\underline{\omega}_{\alpha k}(\mathbf{x}), \quad \underline{j}_k = aj_k. \tag{2.17}$$

From it we find

$$\frac{\partial\omega}{\partial\underline{\omega}_{\alpha k}} = Y_0\underline{j}_{\alpha k}. \tag{2.18}$$

In addition,

$$\frac{\partial\omega}{\partial a_{\mu\gamma}} = \frac{iY_0}{2}\,\varepsilon_{\alpha\beta\gamma}a_{\mu\beta}\mathrm{Tr}\, w[\hat{S}_\alpha,\hat{\varepsilon}(\mathbf{x})]. \tag{2.19}$$

Therefore, the main thermodynamic identity can be represented in the form

$$d\omega = \varepsilon dY_0 + \underline{s}_\alpha d\underline{Y}_\alpha + \frac{\partial\omega}{\partial a_{\alpha\beta}}\, da_{\alpha\beta} + Y_0\underline{j}_{\alpha k}d\underline{\omega}_{\alpha k}, \tag{2.20}$$

or, taking into account the definition of the entropy density σ, we can write

$$d\varepsilon = T\, d\sigma + \underline{h}_\alpha d\underline{s}_\alpha + \frac{\partial\varepsilon}{\partial a_{\alpha\beta}}\, da_{\alpha\beta} + j_{\alpha k}d\underline{\omega}_{\alpha k}. \tag{2.21}$$

To find the energy flux density in the locally equilibrium state we use the relation

$$i\mathrm{Tr}\, w[\hat{A} + \hat{B},\hat{a}(\mathbf{x}) + \hat{b}(\mathbf{x})] = 0,$$

where $\hat{a}(\mathbf{x}) = Y_0(\mathbf{x})\hat{\varepsilon}(\mathbf{x})$ and $\hat{b}(\mathbf{x}) = Y_\alpha(\mathbf{x})\hat{s}_\alpha(\mathbf{x})$. Taking into account (1.6), we obtain

$$\nabla_k Q_k(\mathbf{x}) = 0,$$

$$Q_k(\mathbf{x}) = -\frac{i}{2}\int d^3x'\, x'_k\int_0^1 d\lambda Y_a(\mathbf{x} - (1$$
$$-\lambda)\mathbf{x}')\mathrm{Tr}\, w[\hat{\zeta}_a(\mathbf{x} - (1-\lambda)\mathbf{x}'),$$

$$\hat{\zeta}_b(\mathbf{x}+\lambda\mathbf{x}')]Y_b(\mathbf{x}+\lambda\mathbf{x}'). \qquad (2.22)$$

Ignoring in this expression the gradients ∇Y_0 and ∇Y_α, using (1.8), we find

$$Q_k = Y_0^2 q_k + Y_0 \underline{Y}_\alpha \underline{j}_{\alpha k} + O(\nabla \underline{Y}).$$

Because of the arbitrariness of the gradients of the parameters $\underline{Y}$ and $\underline{\omega}_k$, we have $Q_k = 0$. We thus obtain

$$q_k = \underline{h}_\alpha \underline{j}_{\alpha k},$$

and, therefore, in accordance with (2.21),

$$\underline{\zeta}_{ak} = \frac{\partial \varepsilon}{\partial \underline{\omega}_{\alpha k}} \frac{\partial \underline{\zeta}_a}{\partial \underline{s}_\alpha}, \quad a = (0, \alpha). \qquad (2.23)$$

3. REDUCED DESCRIPTION. HYDRODYNAMIC EQUATIONS

The reduced description method is used in describing the nonequilibrium states of macroscopic systems at the hydrodynamic stage of evolution (small inhomogeneities)[17]. For the weakly anisotropic magnetic systems with total symmetry breaking relative to spin rotations the reduced description parameters are the densities of the additive motion integrals $\zeta_a(\mathbf{x})$ (with respect to exchange Hamiltonian) and the rotation matrix $b_{\alpha\beta}(\mathbf{x})$ in spin space. To formulate the hydrodynamic equations, it is necessary to introduce the rotation matrix $b_{\alpha\beta}(\mathbf{x})$ as a functional of the nonequilibrium statistical operator $\hat{\rho}$, $b(\mathbf{x}) = b(\mathbf{x}, \hat{\rho})$. This matrix, which characterizes the orientation of the mean value of the order parameter operator $\Delta_\alpha(\mathbf{x}, \hat{\rho}) = \mathrm{Tr} \hat{\rho} \hat{\Delta}_\alpha(\mathbf{x})$ relative to some fixed frame $\mathbf{1}$, $\mathbf{m}$, $\mathbf{1} \times \mathbf{m}$ ($\mathbf{l}^2 = \mathbf{m}^2 = 1$, $\mathbf{1m} = 0$), does not coincide, in general, with the rotation matrix $a_{\alpha\beta}(\mathbf{x})$ that enters into the locally equilibrium Gibbs distribution and into the thermodynamic potential ω. We define the rotation matrix $b_{\alpha\beta}(\mathbf{x}, \hat{\rho})$ as a functional of the nonequilibrium statistical operator $\hat{\rho}$ by the relations[19]

$$\mathbf{l}b(\mathbf{x}, \hat{\rho})\Delta(\mathbf{x}, \hat{\rho}) = 0, \quad \mathbf{m}b(\mathbf{x}, \hat{\rho})\Delta_2(\mathbf{x}, \hat{\rho}) = 0. \qquad (3.1)$$

By virtue of (3.1) and (1.10) for the rotation matrix $b(\mathbf{x}, \hat{\rho})$ the following equation is valid:

$$b(\mathbf{x}, U_c^+ \rho U_c) = b(\mathbf{x}, \hat{\rho})c(\mathbf{x}), \qquad (3.2)$$

where $c(\mathbf{x})$ is the arbitrary matrix of local rotation. We take into account the variation of the orthogonal matrix of rotation $\delta b(\mathbf{x}, \hat{\rho})$, which is associated with the variation of the statistical operator $\delta \hat{\rho}$:

$$\delta b(\mathbf{x}, \hat{\rho}) = b(\mathbf{x}, \hat{\rho} + \delta\hat{\rho}) - b(\mathbf{x}, \hat{\rho}) = b(\mathbf{x}, \hat{\rho})\chi(\mathbf{x}, \hat{\rho}, \delta\hat{\rho}). \qquad (3.3)$$

Here the matrix $\chi(\mathbf{x}, \hat{\rho}, \delta\hat{\rho})$ is a linear functional of $\delta\hat{\rho}$ that can be represented in the form

$$\chi_{\alpha\beta}(\mathbf{x}, \hat{\rho}, \delta\hat{\rho}) = \mathrm{Tr}\, \delta\hat{\rho}\hat{\chi}_{\alpha\beta}(\mathbf{x}, \hat{\rho}).$$

The operator $\hat{\chi}_{\alpha\beta}(\mathbf{x}, \hat{\rho})$ which depends on the initial statistical operator $\hat{\rho}$ obeys, by virtue of the orthogonality condition $b\tilde{b} = 1$, the antisymmetry property $\hat{\chi}_{\alpha\beta}(\mathbf{x}, \hat{\rho}) = -\hat{\chi}_{\beta\alpha}(\mathbf{x}, \hat{\rho})$. Defining the dual quantity $\hat{\chi}_\gamma = 1/2\varepsilon_{\alpha\beta\gamma}\hat{\chi}_{\alpha\beta}$, we represent the variation of the rotation matrix $\delta b(\mathbf{x}, \hat{\rho})$ in the form

$$\delta b_{\alpha\beta}(\mathbf{x}, \hat{\rho}) = b_{\alpha\gamma}(\mathbf{x}, \hat{\rho})\varepsilon_{\gamma\beta\lambda}\mathrm{Tr}\, \delta\hat{\rho}\hat{\chi}_\lambda(\mathbf{x}, \hat{\rho}). \qquad (3.4)$$

We attribute the following properties to the operator $\hat{\chi}_\alpha(\mathbf{x}, \hat{\rho})$, whose proof one can find in Ref. 19:

1. The operator $\hat{\chi}_\alpha$ is determined to an accuracy of the transformation $\hat{\chi} \to \hat{\chi}' = \hat{\chi} + c(\hat{\rho})$, where $c(\hat{\rho})$ is an arbitrary c-number functional of the statistical operator $\hat{\rho}$, and is uniquely fixed by the condition $\mathrm{Tr}\, \hat{\rho}\hat{\chi}(\mathbf{x}, \hat{\rho}) = 0$.

2. For the operator $\hat{\chi}_\alpha$ the following equations are valid:

$$i\mathrm{Tr}\, \rho[\hat{s}_\alpha(\mathbf{x}), \hat{\chi}_\beta(\mathbf{x}', \hat{\rho})] = \delta_{\alpha\beta}\delta(\mathbf{x} - \mathbf{x}'),$$

$$i\mathrm{Tr}\, \rho[P_k, \hat{\chi}_\alpha(\mathbf{x}, \hat{\rho})] = \omega_{\alpha k}(\mathbf{x}, \hat{\rho}). \qquad (3.5)$$

The transformation laws relative to spin rotations and spatial translations for the operator $\hat{\chi}_\alpha$ are

$$U_c \hat{\chi}_\alpha(\mathbf{x}, U_c^+ \rho U_c)U_c^+ = \hat{\chi}_\lambda(\mathbf{x}, \hat{\rho})c_{\lambda\alpha}(\mathbf{x}),$$

$$e^{i\mathbf{Py}}\hat{\chi}_\alpha(\mathbf{x}, e^{-i\mathbf{Py}}\hat{\rho}\, e^{i\mathbf{Py}})e^{-i\mathbf{Py}} = \hat{\chi}_\alpha(\mathbf{x} - \mathbf{y}, \hat{\rho}),$$

where $c(\mathbf{x})$ is the arbitrary matrix of local rotation.

We formulate now the equation of motion for the orthogonal rotation matrix. Accordingly we choose the variation $\delta\rho$ in the form $\delta\rho = \dot{\rho}\delta t$ and assume that the statistical operator $\hat{\rho}(t)$ satisfies the Liouville equation

$$\dot{\hat{\rho}}(t) = i[\hat{\rho}(t), H]. \qquad (3.6)$$

As a result, by virtue of (3.4), we obtain the equation

$$\dot{b}_{\alpha\beta}(\mathbf{x}, \hat{\rho}) = ib_{\alpha\lambda}(\mathbf{x}, \hat{\rho})\varepsilon_{\lambda\beta\gamma}\mathrm{Tr}\, \hat{\rho}[H, \hat{\chi}_\gamma(\mathbf{x}, \hat{\rho})]. \qquad (3.7)$$

We consider the evolution of a nonequilibrium, spatially inhomogeneous state of the magnet with total symmetry breaking in the range $t \gg \tau_0$ (τ_0 is the relaxation time) at the hydrodynamic stage of evolution. In accordance with the reduced description hypothesis, at these times the nonequilibrium statistical operator is a functional of the reduced description parameters

$$\rho(t) \xrightarrow[t \gg \tau_0]{} \rho(\zeta(\mathbf{x},t), b(\mathbf{x},t)),$$

$$\zeta(\mathbf{x}) = \mathrm{Tr}\, \hat{\rho}(\zeta,b)\hat{\zeta}(\mathbf{x}), \quad b(\mathbf{x}) = b(\mathbf{x}, \hat{\rho}(\zeta,b)). \qquad (3.8)$$

In these relations the orthogonal rotation matrix $b(\mathbf{x}, \hat{\rho})$ as a functional of the nonequilibrium statistical operator is defined by Eqs. (3.1). In accordance with (1.7) and (3.7) and by virtue of the reduced description hypothesis (3.8), the equations of motion for the reduced description parameters, have the form

$$\dot{\varepsilon}(\mathbf{x}, \hat{\rho}) = -\nabla_k\, \mathrm{Tr}\, \hat{\rho}(\zeta,b)\hat{q}_k(\mathbf{x}),$$

$$\dot{s}_\alpha(\mathbf{x}, \hat{\rho}) = i\, \mathrm{Tr}\, \hat{\rho}(\zeta,b)[H, \hat{s}_\alpha(\mathbf{x})], \qquad (3.9)$$

$$\dot{b}_{\alpha\beta}(\mathbf{x}, \hat{\rho}) = ib_{\alpha\lambda}(\mathbf{x}, \hat{\rho})\varepsilon_{\lambda\beta\gamma}\, \mathrm{Tr}\, \hat{\rho}(\zeta,b)[H, \hat{\chi}_\gamma(\mathbf{x}, \hat{\rho})].$$

We represent the statistical operator $\hat{\rho}(\zeta,b)$ in the form

$$\hat{\rho}(\zeta,b) = w(Y,a) + \hat{\rho}'(\zeta,b). \qquad (3.10)$$

Here $w(Y,a)$ is the locally equilibrium statistical operator (2.8) and the operator $\hat{\rho}'(\zeta,b)$ determines the dissipative processes. Since we are interested in the main approximation of the spatial gradients, and since we disregard the dissipative processes, we can disregard the contribution of the operator $\hat{\rho}'(\zeta,b)$ in Eqs. (3.9). We can therefore assume that

the relation $\mathrm{Tr}\,\hat{\rho}(\zeta,b)\ldots\approx\mathrm{Tr}\,w(Y,a)\ldots$ is approximately satisfied. The relation between the densities of the additive motion integrals and the thermodynamic forces is defined by the relation (2.14). We recall that the orthogonal rotation matrix $a(\mathbf{x})$, which enters into the locally equilibrium Gibbs distribution and the thermodynamic potential ω, does not coincide with the rotation matrix $b(\mathbf{x},w)$.

To find the equation of motion for the spin density $s_\alpha(\mathbf{x})$, we make use of the expression (2.13) for the variational derivative $\delta\Omega/\delta a$ of the thermodynamic potential Ω with respect to the rotation matrix a. Comparing Eqs. (3.9) and (2.13), we represent the equation of motion for the spin density $s_\alpha(\mathbf{x})$ in the form

$$\dot{s}_\alpha=-\frac{1}{Y_0}\,\varepsilon_{\alpha\mu\nu}a_{\lambda\mu}\left(\frac{\delta\Omega}{\delta a_{\lambda\nu}}\right)_{\underline{Y}}. \tag{3.11}$$

In Eq. (3.11) the thermodynamic potential $\Omega=\int d^3x\,\omega(\mathbf{x})$ is considered to be a functional of the variables $\underline{Y}_\alpha(\mathbf{x}),a_{\alpha\beta}(\mathbf{x})$ under the local dependence of the inverse temperature $Y_0(\mathbf{x})$: $\omega(\mathbf{x})=\omega(\mathbf{x};Y_0(\mathbf{x}),\underline{Y}_\alpha(\mathbf{x}'),a_{\alpha\beta}(\mathbf{x}'))$. If the thermodynamic potential is a functional of the form

$$\Omega=\int d^3x\,\omega(\mathbf{x}),$$

$$\omega(\mathbf{x})=\omega(\mathbf{x};Y_0(\mathbf{x}),Y_\alpha(\mathbf{x}'),a_{\alpha\beta}(\mathbf{x}')),\quad Y_\alpha=\underline{Y}_\beta a_{\beta\alpha},$$

then in terms of the new set of variables we have

$$\dot{s}_\alpha=-\varepsilon_{\alpha\beta\gamma}\left(\frac{Y_\beta}{Y_0}\frac{\delta\Omega}{\delta Y_\gamma}+\frac{1}{Y_0}a_{\mu\beta}\left(\frac{\delta\Omega}{\delta a_{\mu\gamma}}\right)_Y\right). \tag{3.12}$$

In the local limit, when the density of the thermodynamic potential ω is represented as

$$\omega(\mathbf{x})=\omega(Y_0(\mathbf{x}),\underline{Y}_\alpha(\mathbf{x}),a(\mathbf{x}),\underline{\omega}_k(\mathbf{x})),$$

from (3.11) we obtain

$$\dot{s}_\alpha=-\frac{1}{Y_0}\varepsilon_{\alpha\beta\gamma}a_{\mu\beta}\frac{\partial\omega}{\partial a_{\mu\gamma}}-\nabla_k j_{\alpha k}, \tag{3.13}$$

$$j_{\alpha k}=\frac{1}{Y_0}\frac{\partial\omega}{\partial\underline{\omega}_{\beta k}}a_{\beta\alpha}.$$

The first term on the right side of Eq. (3.13) takes into account the anisotropy.

We obtain the equation of motion for the orthogonal rotation matrix. Substituting expression (3.10) in (3.7) and ignoring the influence of the dissipative processes, we find

$$\dot{b}_{\alpha\beta}(\mathbf{x},\hat{\omega})=ib_{\alpha\gamma}(\mathbf{x},\hat{w})\varepsilon_{\gamma\beta\lambda}\,\mathrm{Tr}\,\hat{w}[H,\hat{\chi}_\lambda(\mathbf{x},\hat{w})].$$

Noting further that in the main approximation for the statistical operator $w(Y,a)$ the stationary condition (2.3) holds, we can rewrite the last equation in the form

$$\dot{b}_{\alpha\beta}(\mathbf{x},\hat{w})=ib_{\alpha\gamma}(\mathbf{x},\hat{w})\varepsilon_{\gamma\beta\lambda}h_\sigma\,\mathrm{Tr}\,\hat{w}[\hat{s}_\sigma,\hat{\chi}_\lambda(\mathbf{x},\hat{w})]$$

$$=b_{\alpha\gamma}(\mathbf{x},\hat{w})\varepsilon_{\gamma\beta\lambda}h_\lambda,$$

where the relation (3.5) is taken into account. We note that the asymptotic relation (3.8) contains the rotation matrix $b(\mathbf{x},\hat{\rho})$, which is defined by the relations (3.1). On the other hand, Eqs. (2.23) for the flux densities of the additive motion

integrals contain the Cartan forms which are the functions of the rotation matrix $a(\mathbf{x})$ that enters into the locally equilibrium Gibbs distribution and, in general, is not identical to the matrix $b(\mathbf{x},\hat{w})$. Therefore, to close the equations of motion we must establish a connection between these two orthogonal matrices. Using the relations (3.1), (3.2), and (2.8), we have

$$\mathbf{l}b(\mathbf{x},w)\Delta(\mathbf{x},w)=\mathbf{l}b(\mathbf{x},w)\widetilde{a}(\mathbf{x})\Delta(\mathbf{x},\underline{w})=0,$$

$$\mathbf{m}b(\mathbf{x},w)\Delta_2(\mathbf{x},w)=\mathbf{m}b(\mathbf{x},w)\widetilde{a}(\mathbf{x})\Delta_2(\mathbf{x},\underline{w})=0.$$

We see, therefore, that the rotation matrix $b(\mathbf{x},w)\widetilde{a}(\mathbf{x})=b(\mathbf{x},\underline{w})$ is a function of the arguments $\underline{Y},a,\underline{\omega}_k$. The variables $\underline{Y}$ and $\underline{\omega}_k$ change slowly in space and the time and the dependence on the matrix a is weak because of the small anisotropy. Therefore, the equation of motion for the rotation matrix $a(\mathbf{x})$ in the main approximation with respect to the spatial gradients and small anisotropy can be represented in the form

$$\dot{a}_{\alpha\beta}(\mathbf{x})\approx b_{\alpha\gamma}^{-1}(\mathbf{x},\underline{w})\dot{b}_{\gamma\beta}(\mathbf{x},w)=a_{\alpha\gamma}(\mathbf{x})\varepsilon_{\gamma\beta\lambda}h_\lambda. \tag{3.14}$$

Thus, we obtain a closed system of equations for the magnets considered by us, without regard for the dissipative processes:

$$\dot{s}_\alpha=-\frac{1}{Y_0}\varepsilon_{\alpha\beta\gamma}\left(Y_\beta\frac{\delta\Omega}{\delta Y_\gamma}+a_{\mu\beta}\frac{\delta\Omega}{\delta a_{\mu\gamma}}\right),$$

$$\dot{a}_{\alpha\beta}=-a_{\alpha\gamma}\varepsilon_{\gamma\beta\lambda}\frac{Y_\lambda}{Y_0}. \tag{3.15}$$

The equation for the energy density is

$$\dot{\varepsilon}=-\nabla_k\frac{1}{Y_0^2}\frac{\partial\omega}{\partial s_\alpha}\frac{\partial\omega}{\partial\omega_{\alpha k}}. \tag{3.16}$$

By virtue of (2.15), Eqs. (3.15) can be written in the form

$$\dot{s}_\alpha=\varepsilon_{\alpha\beta\gamma}\left(\frac{\delta H}{\delta s_\beta}s_\gamma+\frac{\delta H}{\delta a_{\mu\beta}}a_{\mu\gamma}\right),\quad \dot{a}_{\alpha\beta}=\varepsilon_{\beta\rho\gamma}a_{\alpha\gamma}\frac{\delta H}{\delta s_\rho}. \tag{3.17}$$

Since the energy density ε is a function of the quantities σ, a, $\underline{s}$, and $\underline{\omega}_k$ [see Eq. (2.21)] and since the quantities σ, $\underline{s}$, and $\underline{\omega}_k$ for the weakly inhomogeneous and weakly anisotropic states vary slowly in space and time, it is useful to change to the variables ε, a, $\underline{s}$, and $\underline{\omega}_k$ in Eqs. (3.15) and (3.16). By virtue of (1.13) and (2.15), we obtain from (3.15) and (3.16) a closed system of equations

$$\dot{\varepsilon}=-\nabla_k\frac{\partial\varepsilon}{\partial\underline{s}_\alpha}\frac{\partial\varepsilon}{\partial\underline{\omega}_{\alpha k}},\quad \dot{a}_{\alpha\beta}=\varepsilon_{\alpha\rho\nu}a_{\rho\beta}\frac{\partial\varepsilon}{\partial\underline{s}_\nu},$$

$$\dot{s}_\alpha=-\nabla_k\frac{\partial\varepsilon}{\partial\underline{\omega}_{\alpha k}}+\varepsilon_{\alpha\xi\mu}\left(\underline{s}_\xi\frac{\partial\varepsilon}{\partial\underline{s}_\mu}+\underline{\omega}_{\xi k}\frac{\partial\varepsilon}{\partial\underline{\omega}_{\mu k}}\right.$$

$$\left.+a_{\xi\rho}\frac{\partial\varepsilon}{\partial a_{\mu\rho}}\right). \tag{3.18}$$

As a result of the equation of motion for the rotation matrix, we find the equation of motion for the Cartan form $\omega_{\alpha k}$

$$\dot{\underline{\omega}}_{\alpha k}=-\nabla_k\frac{\partial\varepsilon}{\partial\underline{s}_\alpha}+\varepsilon_{\alpha\beta\gamma}\underline{\omega}_{\beta k}\frac{\partial\varepsilon}{\partial\underline{s}_\gamma}. \tag{3.19}$$

From these equations and from the thermodynamic relation (2.21) follows the adiabaticity of the processes in the approximation considered by us, $\dot{\sigma}=0$.

4. FERRIMAGNET

In this section we consider the thermodynamics and hydrodynamics of the weakly anisotropic, two-sublattice ferrimagnet with noncompensated sublattices. We see that there is an essential simplifying circumstance which allows to consider the two-sublattice ferrimagnet (for brevity simply "ferrimagnet") as a special case of the magnet with total symmetry breaking relatively to spin rotations with a special kind of dependence of the thermodynamic quantities on the rotation matrix.

For the ferrimagnet the source $\hat{G}$ in the statistical operator (2.1) is defined by the formula

$$\hat{G}=\int d^3x \mathbf{l}(\mathbf{x},t)\hat{\Delta}(\mathbf{x})=\hat{G}(t), \quad \hat{\Delta}^+(\mathbf{x})=\hat{\Delta}(\mathbf{x}),$$

$$|\mathbf{l}(\mathbf{x})|=1. \tag{4.1}$$

The real vector l_α ($l_\alpha^* = l_\alpha$) has a sense of the antiferromagnetism vector. Assuming that the equilibrium state is the spiral ordering state [see Eq. (2.3)], we find the form of the function $l_\alpha(\mathbf{x},t)$

$$\mathbf{l}(\mathbf{x},t)=\xi a(\varphi^0)a(\varphi(\mathbf{x},t))\equiv \xi a(\mathbf{x},t),$$

$$\varphi_\alpha(\mathbf{x},t)=n_\alpha(p\mathbf{x}-ht), \quad |\xi|=1, \tag{4.2}$$

where ξ_α is a constant real unit vector, and φ_α^0 is a uniform rotation. Thus, the statistical equilibrium state of the ferrimagnet is characterized by the thermodynamic forces Y_0 and Y_α, by the rotation angles φ_α^0, and by the spiral vector p_k. The difference from the case of the total symmetry violation [see Eq. (2.4)] is that in Eq. (4.2) ξ_α is a constant real vector. Therefore, rotations around the vector ξ_α do not change the antiferromagnetism vector l_α and, hence, ferrimagnet is characterized by the two independent rotation angles φ_α^0.

In accordance with (2.1), (2.7), and (4.1), the locally equilibrium distribution of the ferrimagnet is defined by the formula

$$w_\nu(Y(\mathbf{x}'),l(\mathbf{x}'))=\exp\left\{\Omega_\nu-\int d^3x' Y_a(\mathbf{x}')\hat{\zeta}_a(\mathbf{x}')\right.$$

$$\left.-\nu\hat{G}_l\right\}\equiv U_a^+ \underline{w}_\nu U_a, \tag{4.3}$$

$$\hat{G}_l=U_a^+ G U_a=\int d^3x' \xi a(\mathbf{x}')\hat{\Delta}(\mathbf{x}')$$

$$\equiv \int d^3x' \mathbf{l}(\mathbf{x}')\hat{\Delta}(\mathbf{x}'),$$

where

$$\underline{w}_\nu=\exp\left\{\Omega_\nu-\int d^3x[Y_0(\mathbf{x})\underline{\hat{\varepsilon}}(\mathbf{x})+\underline{Y}_\alpha(\mathbf{x})\hat{s}_\alpha(\mathbf{x})]-\nu\hat{G}\right\},$$

$$\hat{G}=\int d^3x \xi\hat{\Delta}(\mathbf{x}).$$

Here the thermodynamic forces $Y_a(\mathbf{x})$ and the vector $l_\alpha(\mathbf{x})$ are the arbitrary functions of coordinates. In the state of the total equilibrium $Y_a(\mathbf{x})=Y_a$ and the structure of the antiferromagnetism vector l_α is defined by formula (4.2). From (4.3) and the normalization condition $\mathrm{Tr}\, w=1$ it follows that the locally equilibrium thermodynamic potential Ω is a functional of the quantities $Y_a(\mathbf{x}),l_\alpha(\mathbf{x})$:

$$\Omega=\Omega(Y(\mathbf{x}'),l(\mathbf{x}'))=\int d^3x\,\omega(\mathbf{x};Y(\mathbf{x}'),l(\mathbf{x}')). \tag{4.4}$$

Note the next important peculiarity. It follows from (4.3) that the antiferromagnetism vector l_α is related to the rotation matrix $a_{\alpha\beta}$ by the relation $l_\alpha=\xi_\beta a_{\beta\alpha}$. This allows us to consider the ferrimagnet as a particular case of the magnet with total symmetry breaking relative to spin rotations, for which the dependence of the thermodynamic potential Ω on the rotation matrix $a_{\alpha\beta}$ occurs only through the combination $\xi_\beta a_{\beta\alpha}\equiv l_\alpha$. Therefore, we can use the results obtained earlier with allowance for the indicated peculiarity without repeating the calculations of the second section.

We write the main thermodynamic identity for the locally equilibrium states. Variational derivatives of the thermodynamic potential $\Omega=\Omega(Y,l)$ with respect to the thermodynamic forces Y_a are defined by the equations

$$\left(\frac{\delta\Omega}{\delta Y_0}\right)_l=\varepsilon, \quad \left(\frac{\delta\Omega}{\delta Y_\alpha}\right)_l=s_\alpha. \tag{4.5}$$

We find the variational derivative $(\delta\Omega/\delta l)_Y$. Since in the case of the ferrimagnet

$$\left(\frac{\delta\Omega}{\delta a_{\rho\nu}}\right)_Y=\xi_\rho\left(\frac{\delta\Omega}{\delta l_\nu}\right)_Y,$$

then scalary multiplying both parts of the last relation on the vector ξ_ρ ($\xi_\rho^2=1$), we have

$$\left(\frac{\delta\Omega}{\delta l_\nu}\right)_Y=\left(\frac{\delta\Omega}{\delta a_{\rho\nu}}\right)_Y \xi_\rho. \tag{4.6}$$

The derivative $(\delta\Omega/\delta a)_{\underline{Y}}$ is defined by formula (2.13), and the derivative $(\delta\Omega/\delta a)_Y$ is related to the derivative $(\delta\Omega/\delta a)_{\underline{Y}}$ by the relation

$$\left(\frac{\delta\Omega}{\delta a_{\alpha\beta}}\right)_Y=\left(\frac{\delta\Omega}{\delta a_{\alpha\beta}}\right)_{\underline{Y}}-\left(\frac{\delta\Omega}{\delta Y_\beta}\right)_a a_{\alpha\mu}Y_\mu. \tag{4.7}$$

Using (4.6), (4.7), and (2.13) for the derivative $(\delta\Omega/\delta l)_Y$, we obtain

$$\left(\frac{\delta\Omega}{\delta l_\alpha(\mathbf{x})}\right)_Y=\frac{i}{2}\,\varepsilon_{\alpha\gamma\mu}l_\mu(\mathbf{x})Y_0(\mathbf{x})\mathrm{Tr}\,w[\hat{s}_\gamma(\mathbf{x}),H]$$

$$-\left(\frac{\delta\Omega}{\delta Y_\alpha(\mathbf{x})}\right)_l l_\mu(\mathbf{x})Y_\mu(\mathbf{x}). \tag{4.8}$$

Thus, the thermodynamic identity for the locally equilibrium states of the weakly anisotropic ferrimagnet has the form

$$\delta\Omega=\int d^3x\left(\varepsilon(\mathbf{x})\delta Y_0(\mathbf{x})+s_\alpha(\mathbf{x})\delta Y_\alpha(\mathbf{x})\right.$$

$$\left. +\left(\frac{\delta\Omega}{\delta l_\alpha}\right)_Y \delta l_\alpha(\mathbf{x})\right). \tag{4.9}$$

Taking into account the expression for the entropy density $\sigma = -\omega + Y_a\zeta_a$, we see that to an accuracy of ∇Y_0 the following equations are valid:

$$\frac{\delta H}{\delta\sigma} = \frac{1}{Y_0}, \quad \frac{\delta H}{\delta s_\alpha} = -\frac{Y_\alpha}{Y_0}, \quad \frac{\delta H}{\delta l_\alpha} = \frac{1}{Y_0}\frac{\delta\Omega}{\delta l_\alpha}. \tag{4.10}$$

Let us consider the local limit of the relations which we obtained when the density of the thermodynamic potential ω depends on the variables. Y, l, and $\nabla_k l$ (or, in the last case, on the quantity $v_{\alpha k} = -\varepsilon_{\alpha\beta\gamma} l_\beta \nabla_k l_\gamma$):

$$\omega(\mathbf{x}) = \omega(Y(\mathbf{x}), l(\mathbf{x}), v_k(\mathbf{x})). \tag{4.11}$$

The connection between the variables Y, l, and v_k, and the variables $\underline{Y}$, a, and $\underline{\omega}_k$ is given by

$$Y_\alpha = \underline{Y}_\beta a_{\beta\alpha}, \quad l_\alpha = \xi_\beta a_{\beta\alpha},$$

$$v_{\alpha k} = (\delta_{\rho\nu} - \xi_\rho\xi_\nu) a_{\rho\alpha}\underline{\omega}_{\nu k}. \tag{4.12}$$

The quantity j_k was obtained in the second section of Eq. (2.18) for the spin flux density. Taking it into account and also Eqs. (4.11) and (4.12) for the spin flux density in the case of the ferrimagnet, we find

$$\underline{j}_{\alpha k} = \frac{1}{Y_0}\frac{\partial\omega}{\partial v_{\alpha k}}\delta^\perp_{\alpha\beta}\widetilde{a}_{\beta\gamma}, \quad \delta^\perp_{\alpha\beta} \equiv \delta_{\alpha\beta} - l_\alpha l_\beta$$

or

$$j_{\alpha k} = \frac{1}{Y_0}\frac{\partial\omega}{\partial v_{\alpha k}}. \tag{4.13}$$

Here we took into account that since variations of the quantities l_α and $v_{\alpha k}$ are not independent (see Ref. 9), $l_\alpha\partial\omega/\partial v_{\alpha k} = 0$. Besides, it is easy to obtain the relation that connects the derivatives $(\partial\omega/\partial l)_{Y,v}$ and $(\partial\omega/\partial a)_{Y,\omega}$:

$$\left(\frac{\partial\omega}{\partial l_\nu}\right)_{Y,v} = \xi_\mu\left(\frac{\partial\omega}{\partial a_{\mu\nu}}\right)_{Y,\underline{\omega}} - \left(\frac{\partial\omega}{\partial Y_\nu}\right)_{l,v} l_\rho Y_\rho.$$

Using Eq. (2.19), we thus have

$$\left(\frac{\partial\omega}{\partial l_\nu}\right)_{Y,v} = i\frac{Y_0}{2}\varepsilon_{\alpha\beta\nu}l_\beta\,\text{Tr}\,w[\hat{S}_\alpha,\hat{\varepsilon}(\mathbf{x})] - \left(\frac{\partial\omega}{\partial Y_\nu}\right)_{l,v} l_\rho Y_\rho. \tag{4.14}$$

The second law of thermodynamics in the local limit can thus be written in the form

$$d\omega = \varepsilon dY_0 + sdY + \frac{\partial\omega}{\partial l}dl + Y_0 j_k dv_k, \tag{4.15}$$

where the derivative $(\partial\omega/\partial l)_{Y,v}$ is defined by Eq. (4.14). Using the entropy density σ, we can rewrite the last relation as follows:

$$d\varepsilon = T\,d\sigma + hds + \frac{\partial\varepsilon}{\partial l}dl + j_k dv_k. \tag{4.16}$$

Here we have taken into account that

$$\left(\frac{\partial\varepsilon}{\partial l}\right)_{\sigma,s,v_k} = \frac{1}{Y_0}\left(\frac{\partial\omega}{\partial l}\right)_{Y_0,Y,v_k}.$$

To find the energy flux density in the locally equilibrium state we use, by analogy with the case of the total symmetry violation, the relation (2.22). Within accuracy of ∇Y_0 we then obtain

$$q_k = h_\alpha j_{\alpha k}. \tag{4.17}$$

Therefore, in accordance with (4.16),

$$\zeta_{ak} = \frac{\partial\varepsilon}{\partial v_{\alpha k}}\frac{\partial\zeta_a}{\partial s_\alpha}.$$

Let us consider the hydrodynamic stage of evolution of a weakly anisotropic ferrimagnet at times $t \gg \tau_0$ (τ_0 is the relaxation time). To construct hydrodynamics we will use, by analogy with the case of a magnet with total symmetry breaking relative to spin rotations, the reduced description hypothesis. The reduced description parameters are the densities of the additive motion integrals $\zeta_a(\mathbf{x})$ and the antiferromagnetism vector $g_a(\mathbf{x}, \hat{\rho})$ considered as a functional of the nonequilibrium statistical operator $\hat{\rho}*$.[1] In such a scheme the equation of motion for the antiferromagnetism vector is obtained on the basis of the operator $\hat{g}_a(\mathbf{x}, \hat{\rho})$ of the antiferromagnetism vector. As in the case of the magnet with total symmetry breaking, we have used the operator $\hat{\chi}(\mathbf{x}, \hat{\rho})$ [see Eq. (3.4)] to derive the equation of motion for the rotation matrix. However, we can at once obtain the equation of motion for the vector l_α by using the connection between the antiferromagnetism vector l_α and the rotation matrix $a_{\alpha\beta}$, $l_\alpha = \xi_\beta a_{\beta\alpha}$, indicated above. After convolution of both sides of Eq. (3.14) with the constant vector ξ_ρ we have

$$\dot{l}_\alpha = \varepsilon_{\alpha\beta\gamma}h_\beta l_\gamma \tag{4.18}$$

or

$$\dot{l}_\alpha = -\varepsilon_{\alpha\beta\gamma}\frac{Y_\beta}{Y_0}l_\gamma.$$

Further, the equation for the spin density s_α in the general case was found earlier and is given by Eq. (3.12). Assuming that the density of the thermodynamic potential ω depends on the variables Y_0, Y_α, and l_α,

$$\omega(\mathbf{x}) = \omega(\mathbf{x}; Y_0(\mathbf{x}), Y_\alpha(\mathbf{x}'), l_\alpha(\mathbf{x}')), \quad l_\alpha = \xi_\beta a_{\beta\alpha},$$

[we recall that in the derivation of Eq. (3.12) the potential ω is considered under the local dependence on the inverse temperature Y_0], then, switching from Eq. (3.12) to the new variables, we obtain

$$\dot{s}_\alpha = -\frac{1}{Y_0}\varepsilon_{\alpha\beta\gamma}\left(Y_\beta\frac{\delta\Omega}{\delta Y_\gamma} + l_\beta\frac{\delta\Omega}{\delta l_\gamma}\right). \tag{4.19}$$

Thus, Eqs. (4.18) and (4.19) are the dissipation-free dynamic equations for the weakly anisotropic ferrimagnet. The equation for the energy density is

$$\dot{\varepsilon} = -\nabla_k\frac{1}{Y_0^2}\frac{\partial\omega}{\partial s_\alpha}\frac{\partial\omega}{\partial v_{\alpha k}} \tag{4.20}$$

[here we have used the expression (4.17) for the energy flux density q_k].

Using (4.10), we can write Eqs. (4.18) and (4.19) in the form

$$\dot{s}_\alpha = \varepsilon_{\alpha\beta\gamma}\left(\frac{\delta H}{\delta s_\beta}s_\gamma + \frac{\delta H}{\delta l_\beta}l_\gamma\right), \dot{l}_\alpha = \varepsilon_{\alpha\beta\gamma}\frac{\delta H}{\delta s_\beta}l_\gamma. \quad (4.21)$$

Equations (4.21) coincide with the corresponding equations obtained in the framework of the Hamiltonian approach in Ref. 9.

Since the energy density ε is a function of the quantities σ, s, l, and v_k [see Eq. (4.16)], for verification of the adiabaticity condition we switch in Eqs. (4.18) and (4.19) to the variables ε, s, l, and v_k. By virtue of (4.16), from (4.18) and (4.19) we obtain in the local limit the system of equations

$$\dot{s}_\alpha = \varepsilon_{\alpha\beta\gamma}\left(\frac{\partial\varepsilon}{\partial s_\beta}s_\gamma + \frac{\partial\varepsilon}{\partial l_\beta}l_\gamma + \frac{\partial\varepsilon}{\partial v_{\beta k}}v_{\gamma k}\right) - \nabla_k\frac{\partial\varepsilon}{\partial v_{\alpha k}},$$

$$\dot{l}_\alpha = \varepsilon_{\alpha\beta\gamma}\frac{\partial\varepsilon}{\partial s_\beta}l_\gamma, \dot{\varepsilon} = -\nabla_k\frac{\partial\varepsilon}{\partial s_\alpha}\frac{\partial\varepsilon}{\partial v_{\alpha k}}. \quad (4.22)$$

From the equation for the antiferromagnetism vector follows the equation for the quantity $v_{\alpha k}$:

$$\dot{v}_{\alpha k} = \varepsilon_{\alpha\beta\gamma}\frac{\partial\varepsilon}{\partial s_\beta}v_{\gamma k} - (\delta_{\alpha\beta} - l_\alpha l_\beta)\nabla_k\frac{\partial\varepsilon}{\partial s_\beta}.$$

Using (4.16) and (4.22), we have $\dot{\sigma} = 0$, which proves the adiabaticity of the processes in the approximation which we are considering.

5. SPECTRUM OF SPIN WAVES

To find the spectrum of spin waves for the multisublattice magnet with total symmetry breaking we linearize the system of equations (3.18) and choose as parameters, which describe the deviation from equilibrium, the quantities $\delta s_\alpha(\mathbf{x},t) = s_\alpha(\mathbf{x},t) - s_\alpha^{(0)}$ and $\delta a_{\alpha\beta}(\mathbf{x},t) = \varepsilon_{\alpha\gamma\rho}\delta\varphi_\gamma(\mathbf{x},t)a_{\rho\beta}^{(0)} \times(\mathbf{x},t)$, where $s^{(0)}$ and $a^{(0)}$ are the equilibrium values. The matrix of rotation $a_{\alpha\beta}^{(0)}(\mathbf{x},t)$ satisfies the equation $\dot{a}_{\alpha\beta}^{(0)} = \varepsilon_{\alpha\rho\gamma}(\partial\varepsilon/\partial s_\gamma)a_{\rho\beta}^{(0)}$. The variation of the right Cartan form is

$$\delta\omega_{\alpha k}(a) = \omega_{\alpha k}(ba) - \omega_{\alpha k}(a) = \nabla_k\delta\varphi_\alpha - \varepsilon_{\alpha\beta\gamma}\omega_{\beta k}\delta\varphi_\gamma,$$

$$b_{\alpha\beta} = \delta_{\alpha\beta} - \varepsilon_{\alpha\beta\gamma}\delta\varphi_\gamma.$$

Assuming δs, $\delta\varphi \propto \exp i(\mathbf{kx} - \omega t)$, we obtain the system of equations

$$(i\omega I - hN - if + f'N - T)_{\alpha\beta}\delta\varphi_\beta = \varepsilon_{\alpha\beta}\delta s_\beta, \quad (5.1)$$

$$(-i\omega I + i\tilde{f} + hN - M\varepsilon - N\tilde{f'} - \tilde{T})_{\alpha\beta}\delta s_\beta = (D - ND''N$$

$$- Mf'N + G'N + iD'N + iN\tilde{D'} + iMf - iG - iQ$$

$$+ i\tilde{Q} + NQ' - \tilde{Q}'N + H + MT)_{\alpha\beta}\delta\varphi_\beta,$$

where

$$\varepsilon_{\alpha\beta} = \frac{\partial^2\varepsilon}{\partial s_\alpha\partial s_\beta}, \quad f_{\alpha\beta} = k_i\frac{\partial^2\varepsilon}{\partial s_\alpha\partial\omega_{\beta i}},$$

$$f'_{\alpha\beta} = p_i\frac{\partial^2\varepsilon}{\partial s_\alpha\partial\omega_{\beta i}}, \quad D_{\alpha\beta} = k_ik_l\frac{\partial^2\varepsilon}{\partial\omega_{\alpha i}\partial\omega_{\beta l}},$$

$$D'_{\alpha\beta} = k_ip_l\frac{\partial^2\varepsilon}{\partial\omega_{\alpha i}\partial\omega_{\beta l}}, \quad D''_{\alpha\beta} = p_ip_l\frac{\partial^2\varepsilon}{\partial\omega_{\alpha i}\partial\omega_{\beta l}},$$

$$N_{\alpha\beta} = \varepsilon_{\alpha\gamma\beta}n_\gamma, \quad M_{\alpha\beta} = \varepsilon_{\alpha\gamma\beta}s_\gamma,$$

$$G_{\alpha\beta} = \varepsilon_{\alpha\gamma\beta}k_i\frac{\partial\varepsilon}{\partial\omega_{\gamma i}}, \quad G'_{\alpha\beta} = \varepsilon_{\alpha\gamma\beta}p_i\frac{\partial\varepsilon}{\partial\omega_{\gamma i}},$$

$$T_{\alpha\beta} = \frac{\partial^2\varepsilon}{\partial s_\alpha\partial\varphi_\beta}, \quad Q_{\alpha\beta} = k_i\frac{\partial^2\varepsilon}{\partial\omega_{\alpha i}\partial\varphi_\beta},$$

$$Q'_{\alpha\beta} = p_i\frac{\partial^2\varepsilon}{\partial\omega_{\alpha i}\partial\varphi_\beta}, \quad H_{\alpha\beta} = \frac{\partial^2\varepsilon}{\partial\varphi_\alpha\partial\varphi_\beta}.$$

The terms connected with the matrices T, Q, Q', and H take into account the anisotropy. Eliminating δs from Eqs. (5.1) and equating to zero the determinant of the equation for $\delta\varphi$, we find the next dispersion relation for determination of the spectrum of spin waves:

$$\det(\omega^2 a + \omega(ib_1 + b_2) + ic_1 + c_2) \equiv \det A = 0, \quad (5.2)$$

$$a = -\varepsilon^{-1}, \quad b_1 = M - aRN - N\tilde{R}a + aT - \tilde{T}a,$$

$$R = f' - Ih, \quad b_2 = -af - \tilde{f}a, \quad (5.3)$$

$$c_1 = -G + (D' + \tilde{f}aR)N + N(\tilde{D'} + \tilde{R}af) + \tilde{T}af - \tilde{f}aT$$

$$- Q + \tilde{Q},$$

$$c_2 = D - ND''N + \tilde{f}af - N\tilde{R}aRN + \tilde{T}aT + NQ' - \tilde{Q}'N$$

$$+ H + (G' - hM)N.$$

It is easy to see that the matrices a and b_2 are symmetrical and that the matrices b_1 and c_1 are antisymmetrical. In the matrix c_2 all terms are explicitly symmetrical, except the term $(G' - hM)N$. For the study of the symmetry of this matrix we note that equilibrium values s_α, p_k, and h_α, as follows from Eqs. (3.18), are related by the relation

$$N_{\alpha\beta}\left(s_\beta h - p_k\frac{\partial\varepsilon}{\partial\omega_{\beta k}}\right) = \frac{\partial\varepsilon}{\partial\varphi_\alpha}. \quad (5.4)$$

In the absence of anisotropy the right side of Eq. (5.4) is equal to zero. Using Eq. (5.4), it is not difficult to see that $((G' - hM)N)_{\alpha\beta} = ((G' - hM)N)_{\beta\alpha}$. Hence, in the absence of anisotropy the matrix A is a Hermitian that leads to real values of the spin wave frequencies[8]. In the presence of anisotropy we have

$$((G' - hM)N)_{\alpha\beta} - ((G' - hM)N)_{\beta\alpha} = (n_\alpha N_{\beta\gamma}$$

$$- n_\beta N_{\alpha\gamma})\frac{\partial\varepsilon}{\partial\varphi_\gamma}.$$

For the Hermitian character of the matrix A it follows that the relation

$$N_{\alpha\gamma}\frac{\partial\varepsilon}{\partial\varphi_\gamma} \equiv \varepsilon_{\alpha\beta\gamma}n_\beta\frac{\partial\varepsilon}{\partial\varphi_\gamma} = 0, \quad (5.5)$$

which means that the anisotropy should be such that the rotations around the direction $n_\alpha = \underline{h}_\alpha/\underline{h}$ do not change the energy functional ε. If the energy functional ε does not satisfy the relation (5.5), then the matrix A is not a Hermitian and complex frequencies, in general, arise in the spectrum. This means that the corresponding state is unstable. Therefore, when the matrix A is not a Hermitian, the exchange and anisotropy constants should satisfy certain inequalities for the spectrum of spin waves to be real. Further, we assume that Eq. (5.5) is satisfied.

We rewrite the dispersion relation (5.2) in the form

$$\sum_{n=0}^{6} A_n(\mathbf{k})\omega^n = 0, \tag{5.6}$$

where the coefficients A_n ($n=0,\ldots,6$) in terms of the convolution

$$|abc| = \frac{1}{6}\varepsilon_{\alpha\beta\gamma}\varepsilon_{uvt}a_{\alpha u}b_{\beta v}c_{\gamma t}$$

are defined by the formulas

$$A_0 = |c_2 c_2 c_2| - 3|c_1 c_2 c_1|,$$

$$A_1 = -6|b_1 c_1 c_2| - 3|b_2 c_1 c_1| - 3|b_2 c_2 c_2|,$$

$$A_2 = -3|ac_1 c_1| + 3|ac_2 c_2| + 3|b_2 b_2 c_2| - 6|b_1 b_2 c_1|$$
$$\quad - 3|b_1 b_1 c_2|,$$

$$A_3 = |b_2 b_2 b_2| + 6|ab_2 c_2| - 6|ab_1 c_1| - 3|b_1 b_1 b_2|,$$

$$A_4 = 3|aac_2| - 3|ab_1 b_1| + 3|ab_2 b_2|,$$

$$A_5 = 3|aab_2|,$$

$$A_6 = |aaa|.$$

We carry out the analysis of the possible spectra of spin waves in the limit of small wave vectors $\mathbf{k}$. Note that in the absence of anisotropy and at $\omega=0$, $k=0$ we have $\det A(0,0) = \det c_2$ and by virtue of the evident form of the matrix c_2 (5.3), $\det A(0,0) = 0$. This means that in the isotropic case the system has at least two Goldstone modes [since $A_{2l+1}(k=0)=0$]. In the presence of anisotropy the situation changes: $\det A(0,0) = \det c_2 \neq 0$ which means that all modes of the anisotropic magnet, in general, are activation modes. However, the order of the activation frequencies with respect to anisotropy may be different, and it changes from first to third. Since we are considering a small anisotropy, we take into account the anisotropy in the linear approximation. In the given approximation the modes, whose activation frequencies are quadratic and cubic in anisotropy, become activationless. Let us consider some special cases of equilibrium values of the quantities $\underline{s}$, $\underline{h}$, and p_k.

1. $\underline{s}=0$, $\underline{h}=0$, $p_k=0$.
The dispersion relation (5.6) has the form

$$A_6\omega^6 + (A_4' + A_4''k^2)\omega^4 + A_2''k^2\omega^2 + A_0'''k^4 = 0. \tag{5.7}$$

Here we have evidently given the dependence of the modulus $|\mathbf{k}|$ in the coefficients A_n in Eq. (5.6). Solution of Eq. (5.7) yields two pairs of Goldstone and one pair of activation modes

$$\omega_{1,2}^2 = F_{1,2}k^2, \quad \omega_3^2 = \omega_0^2 + F_3 k^2,$$

where

$$\omega_0^2 = -\frac{A_4'}{A_6},$$

$$F_{1,2} = \frac{1}{2A_4'}\{-A_2'' \pm \sqrt{(A_2'')^2 - 4A_0'''A_4'}\},$$

$$F_3 = \frac{A_6 A_2'' - A_4' A_4''}{A_6 A_4'}.$$

We present here for comparison the spectra of spin waves for the isotropic magnet[13,14] in the case under consideration

$$\omega_i^2 = \lambda_i^2 k^2, \quad i=1,2,3.$$

2. $\underline{s}\neq 0$, $\underline{h}=0$, $p_k=0$.
The dispersion relation has the form

$$A_6\omega^6 + (A_4' + A_4''k^2)\omega^4 + (A_2' + A_2''k^2)\omega^2 + A_0'''k^4 = 0. \tag{5.8}$$

At small k we have one pair of Goldstone and two pairs of activation modes

$$\omega_{1,2}^2 = \omega_\pm^2 + R_\pm k^2, \quad \omega_3^2 = R_3 k^4.$$

Here

$$\omega_\pm^2 = \frac{1}{2A_6}\{-A_4' \pm \sqrt{(A_4')^2 - 4A_2' A_6}\},$$

$$R_\pm = \mp\frac{A_2'' + A_4''\omega_\pm^2}{A_6(\omega_+^2 - \omega_-^2)}, \quad R_3 = -\frac{A_0'''}{A_2'}.$$

Similarly for the isotropic magnet[8] we have

$$\omega_1^2 = \nu_1 k^4, \quad \omega_2^2 = \nu_2 k^2, \quad \omega_3^2 = \omega_0^2 + \nu_3 k^2.$$

In connection with the appearance of the activation frequencies in the isotropic magnet, it should be noted that the quantities $\underline{s}_\alpha$ and $\underline{\omega}_{\alpha k}$ are invariant relative to the right uniform rotations with the matrix b:

$$s \to s' = bs, \quad a \to a' = a\tilde{b}.$$

The energy density in the isotropic case $\varepsilon = \varepsilon(\underline{s}, \underline{\omega}_k)$ is therefore also invariant relative to the right rotations. However, it need not necessarily be invariant relative to the left rotations

$$s \to s' = sb, \quad a \to a' = \tilde{b}a,$$

when, for example,[8] the quantities $\underline{s}_\alpha$ and $\underline{\omega}_{\alpha k}$ enter ε in convolution with some "foreign" vector, which characterizies the given magnet

$$\varepsilon = \varepsilon(l_\alpha \underline{s}_\alpha, l_\alpha \underline{\omega}_{\alpha k})$$

(l_α is the unit vector of anisotropy, which is connected with the left rotations). This is the reason for the occurrence of the activation branches in the spectrum. Such situation is characteristic of the considered exchange multisublattice magnets, whose state is described, jointly with the spin density, by the additional dynamic variable which is the matrix of rotation; if the state of the magnet is characterized only by the spin density, then the activation frequencies are absent.

We emphasize that in the equations of motion for the additive motion integrals the expansion in terms of spatial gradients begins with the linear terms on gradients and in the equation of motion for the rotation matrix the expansion begins with zero-order terms on gradients, which corresponds to the precession motion with the corresponding activation frequencies.

3. $s \neq 0$, $\underline{h} \neq 0$, $p_k = 0$.

Equation (5.6) has the form

$$A_6 \omega^6 + (A_4' + A_4'' k^2)\omega^4 + (A_2' + A_2'' k^2)\omega^2 + A_0' + A_0'' k^2 = 0. \tag{5.9}$$

In this case all branches are activation branches

$$\omega_i^2 = \omega_{0i}^2 + c_i^2 k^2, \quad i = 1,2,3,$$

where the activation frequencies ω_{0i}^2 are determined from the cubic equation, which is obtained from Eq. (5.9) at $k = 0$. For the isotropic magnet in this case[8] we have one pair of Goldstone branches and two pairs of activation branches

$$\omega_{1,2}^2 = \omega_{\pm}^2 + \mu_{\pm} k^2, \quad \omega_3^2 = \mu_3 k^2.$$

4. $\underline{s} \neq 0$, $\underline{h} \neq 0$, $p_k \neq 0$.

This is the most general case. Analysis of the dispersion relation shows that there are six activation branches whose spatial anisotropy is caused by the presence of the spiral structure

$$\omega_i = \omega_{0i} + \dot{c}_i(\mathbf{pk}) + d_i'(\mathbf{pk})^2 + c_i'' k^2.$$

For the isotropic magnet in the given case[8] we have

$$\omega_{1,2} = \alpha(\mathbf{pk}) \pm \sqrt{\beta k^2 + \gamma(\mathbf{pk})^2},$$

$$\omega_i = \omega_{0i} + \lambda_i'(\mathbf{pk}) + \mu_i'(\mathbf{pk})^2 + \mu_i'' k^2 \, (i = 3,\ldots,6).$$

6. CONCLUSIONS

Thus, on the basis of generalization the quasiaverages method for the weakly anisotropic, locally equilibrium states and with use of the reduced description method with the elements of the matrix of rotation as additional dynamic variables, we have built thermodynamics and have found the equations of low-frequency dynamics of the multisublattice magnets with strong exchange interaction. In some special cases the results are in agreement with the results of the phenomenological approach based on employment of the Hamiltonian formalism.[8,9] Except for the multisublattice magnets, the concept of total spontaneous symmetry breaking relative to spin rotations has been used in the Hamiltonian approach for the description of the low-frequency dynamics of the superfluid B-phase of ^{3}He (Ref. 19) and of the quantum spin crystals.[20]

[*]E-mail: kfti@rocket.kharkov.ua

[1)]As for the magnet with total symmetry breaking in the case of the antiferromagnet, it is necessary to differentiate between the antiferromagnetism vector l_α that enters into the Gibbs distribution and the antiferromagnetism vector $g_\alpha(\mathbf{x}, \hat{\rho})$ considered as a functional of the nonequilibrium statistical operator $\hat{\rho}$.

[1]L. D. Landau and E. M. Lifshitz, Phys. Zc. Sowjet. **8**, 153 (1935).

[2]A. I. Akhiezer, V. G. Bar'yakhtar, and S. V. Peletminsky, *Spin Waves*, North-Holland, Amsterdam (1960).

[3]A. A. Isayev and S. V. Peletminsky, Teor. Mat. Fiz. **102**, 470 (1995).

[4]H. Goldstein, *Classical Mechanics*, Addison-Wesley Press (1950).

[5]L. A. Takhtadzhyan and L. D. Faddeev, *Hamiltonian Approach in Theory of Solitons*, Nauka, Moscow (1986) (in Russian).

[6]I. E. Dzyaloshinskil and G. E. Volovick, Ann. Phys. **125**, 67 (1980).

[7]S. J. B. Einchcomb and A. J. McKane, Phys. Rev. **E51**, 2974 (1995).

[8]M. Yu. Kovalevsky, S. V. Peletminsky, and A. L. Shishkin, Ukr. Fiz. Zh. **36**, 245 (1991).

[9]A. A. Isayev, M. Yu. Kovalevsky, and S. V. Peletminsky, Teor. Mat. Fiz. **95**, 58 (1993).

[10]N. N. Bogolyubov, Physica **26**, 1 (1960).

[11]J. Goldstone, J. Nuovo cim. **19**, 154 (1961).

[12]D. Forster, *Hydrodynamic Fluctuations, Broken Symmetry and Correlation Functions*, Benjamin, Reading, MA (1975).

[13]D. V. Volkov and A. A. Gheltukhin, Izv. Akad. Nauk SSSR, Ser. Fiz. **14**, 1487 (1980).

[14]B. I. Halperin and W. M. Saslow, Phys. Rev. **B16**, 2154 (1977).

[15]A. F. Andreev and V. I. Marchenko, Usp. Fiz. Nauk **130**, 39 (1980).

[16]B. I. Halperin and P. C. Hohenberg, Phys. Rev. **188**, 898 (1969).

[17]A. I. Akhiezer and S. V. Peletminsky, *Methods of Statistical Physics*, Pergamon, Oxford (1981).

[18]V. G. Bar'yakhtar, V. G. Belykh, and T. K. Soboleva, Teor. Mat. Fiz. **77**, 311 (1988).

[19]M. Yu. Kovalevsky and A. A. Rozhkov, Fiz. Nizk. Temp. **21**, 1138 (1995).

[20]A. A. Isayev and M. Yu. Kovalevsky, Fiz. Nizk. Temp. **20**, 1125 (1994).

This article was published in English in the original Russian Journal. It was edited by S. J. Amoretty.

Classification of states and macroscopic degeneracy in an open *XY*-chain in transverse field

A. V. Loginov and Yu. V. Pereverzev

*B. I. Verkin Physicotechnical Institute of Low Temperatures, Ukrainian Academy of Sciences, 310164 Kharkov, Ukraine**

The spectral structure for an open $X-Y$ chain is determined rigorously, and one-fermion states are classified for all values of anisotropy and transverse field. Quasidegeneracy is interpreted as well as the general nature of ordering in a certain class of systems with a locally nondegenerate ground state. © *1997 American Institute of Physics.* [S1063-777X(97)00507-0]

1. INTRODUCTION

The interest towards the *XY*-model was aroused by the problem of ordering in Heisenberg antiferromagnets.[1] In the simplest models like an isotropic ferromagnet, the ground state energy level is already degenerate for a finite number of lattice sites and the corresponding states violate the symmetry of the system. The tendency towards ordering in the macroscopic system is manifested at the most elementary level, viz., in a pair of interacting sites. The situation is different in a Heisenberg antiferromagnet whose ground state is nondegenerate for any number of sites and any dimensionality of the system,[1] and the minimum excitation energy for a pair of sites is equal to the exchange interaction parameter. In this case, the ordering is basically associated with the macroscopic nature of the system. The same situation is also realized in some other quantum systems.

Such an effect can be studied in the model of an *XY*-chain in a transverse magnetic field H, which can lead to rigorous results. This model was analyzed by Lieb *et al.*[1] and Barouch *et al.*[2] who studied a chain of N spins ($S=1/2$) forming a closed circle with a Hamiltonian

$$H = -\sum_{n=1}^{N-1}(J_x S_n^x S_{n+1}^x + J_y S_n^y S_{n+1}^y) - H\sum_{n=1}^{N} S_n^2, \quad (1)$$

supplemented by interaction of boundary sites, where $J_x > J_y > 0$. Going over to Fermi operators and disregarding a certain ''boundary'' term, we can present the Hamiltonian as a noninteracting system of fermions with the dispersion relation

$$\varepsilon(k) = [(J_a \cos k - H)^2 + \Delta^2 \sin^2 k]^{1/2},$$

$$k = (2n/N)p, \quad p = 0,..., N-1,$$

$$J_a = \frac{1}{2}(J_x + J_y), \quad \Delta = \frac{1}{2}(J_x - J_y) \quad (2)$$

and with the vacuum state as the ground state. It follows hence that the ground state is not degenerate for $\Delta \neq 0$, $H \neq J_a$, and its energy for any N is separated from the rest of the spectrum by a gap δ:

$$\delta = \frac{1}{2}\Delta[1 - H^2/(J_x J_y)]^{1/2}, \quad H < J_x J_y/J_a;$$

$$\delta = |J_a - H|, \quad H > J_x J_y/J_a. \quad (3)$$

The information obtained in this way does not give any indication about the order for $N \to \infty$. In such a situation, the existence of the long-range order in the system in thermodynamic limit at $T=0$ and for nonzero anisotropy ($\Delta \neq 0$) is evidenced by the asymptotic behavior of the correlators of the type $\langle S_n^\alpha S_{n+1}^\alpha \rangle$ ($\alpha = x, y, z$) detected in Ref. 2 for $l \to \infty$.

Lieb *et al.*[1] also considered an open *XY*-chain in zero magnetic field for which a rigorous solution can be obtained without using the above-mentioned approximation. It was found that in this case there exists an eigenstate for $\Delta \neq 0$, whose energy separation from the ground level is $\sim (J_y/J_x)^{-N/2}$. A similar result was obtained by Pfeuty[3] for an open Ising chain in a transverse magnetic field. The authors of Refs. 1 and 3 believe that it is this quasidegeneracy that is responsible for the emergence of order for $N \to \infty$. Thus the assumption required for considering a chain closed into a ring does not affect the thermodynamic functions but complicates the physical interpretation of results and may also be manifested during structural analysis of the ordered states.

In view of all that has been stated above, it should be expedient to study the exact solutions of a finite ($N > 4$) open *XY*-chain in a transverse magnetic field over the entire range of variation of field and anisotropic parameters. In this work, we present the distribution of energy levels of single-fermion states as well as a classification of these states without any explicit details of their structure. Two categories of ''band'' type states and two types of states corresponding to quasidegeneracy are revealed. It is found that the specific quasidegeneracy is always associated with the emergence of long-range order. We shall discuss the critical size of the chains for which special solutions responsible for quasidegeneracy are obtained. We shall also present concepts from perturbation theory revealing the macroscopic nature of the quasidegeneracy and its particular role for a certain class of quantum systems. Since these simple concepts are supported by rigorous results obtained in the family of *XY*- models considered here, they can be used with confidence in other analogous situations also.

2. FORMULATION OF EQUATIONS

We shall use the methods described in Ref. 1 to consider the Hamiltonian (1) in which we assume, without any loss of generality, that $J_x > 0$, $|J_y| < J_x$, $H \geq 0$. Other versions can be reduced to this model through simple unitary transformations. The exact solution of model (1) is obtained by applying Jordan–Wigner transformation to the Fermi operators in terms of which the Hamiltonian assumes a quadratic form. It is diagonalized with the help of the uv-transformation which is defined by the following equations:

$$u = 1/\sqrt{2}(w+z), \quad v = 1/\sqrt{2}(w-z),$$

$$AA^+ w = \varepsilon^2 w, \quad A^+ w = \varepsilon z, \tag{4}$$

where u, v, w, z are N-dimensional columns, and matrix A is equal to

$$A_{n,m} = H\delta_{n,m} - \frac{1}{2}(J_a - \Delta)\delta_{n,m-1} - \frac{1}{2}(J_a + \Delta)\delta_{n,m+1}. \tag{5}$$

The fermion energy ε is chosen to be nonnegative so that the ground state does not contain fermions.

The problem is reduced to determining the eigenvalues and eigenvectors (there must be exactly N such functions and vectors) for the first of Eqs. (4):

$$AA^+ w = \varepsilon^2 w. \tag{6}$$

All the solutions of this equation have the form ($n = 1, 2, \ldots, N$; $N > 4$)

$$w_n = c_1 e^{ik_1 n} + c_1' e^{-ik_1 n} + c_2 e^{ik_2 n} + c_2' e^{-ik_2 n} \tag{7}$$

where k_1, k_2 are complex-valued and are connected with $\varepsilon > 0$ from Eq. (6) through the equations

$$\varepsilon = \varepsilon(k_p), \quad p = 1, 2. \tag{8}$$

The function $\varepsilon(k)$ is defined in (2). (We shall not consider rare cases of multiple roots and the corresponding types of solutions which, if required, can be obtained from (7) through the limiting transition $k_1 - k_2 \to 0$ or $k_{1,2} \to 0, \pi$.)

Relations (8) ensure for any values of $c_{1,2}$, $c_{1,2}'$ the solution of all equations (6) written in terms of the vector components w_n and matrix elements $(AA^+)_{n,m}$ except the first two ($n = 1, 2$) and the last two ($n = N, N-1$). These boundary conditions are satisfied through an appropriate choice of $c_{1,2}$, $c_{1,2}'$, which leads to a homogeneous system of four equations for them. The nontrivial solvability condition for this system gives another equation for determining the possible values of ε, $k_{1,2}$:

$$(1 + \gamma^2 \cot^2 \kappa_1)\sin^2[(N+1)\kappa_1]$$

$$= (1 + \gamma^2 \cot^2 \kappa_2)\sin^2[(N+1)\kappa_2],$$

$$\kappa_1 = \frac{1}{2}(k_1 - k_2), \quad \kappa_2 = \frac{1}{2}(k_1 + k_2),$$

$$\gamma \equiv \Delta/J_a = (J_x - J_y)/(J_x + J_y). \tag{9}$$

(Note that the condition $J_y > 0$ corresponds to $0 < \gamma < 1$, while the condition $J_y < 0$ corresponds to $\gamma > 1$.) Instead of one of the equations (8), we can take

$$\cos k_1 + \cos k_2 = 2h_m \quad \text{and} \quad \cos \kappa_1 \cos \kappa_2 = h_m,$$

$$h_m = H/J_m, \quad J_m = J_x J_y / J_a, \tag{10}$$

which describes the condition $\varepsilon(k_1) = \varepsilon(k_2)$. Then the second of Eqs. (8) will define the eigenvalues of ε. Formula (2) for $\varepsilon(k)$ is the same for open and closed chains, but possible values of k in our case are determined by the system of equations (9), (10).

In the absence of a magnetic field, formula (10) describes a simple relation between two ''momenta'' $k_1 \pm k_2 = \pi$, which reduces Eq. (9) to the form described in Ref. 1. The case of Ising's model in a transverse field is also reduced to an equation in a single momentum and the general solution of the system (6) in this case has the form $ce^{ikm} + c'e^{-ikm}$.[3]

In the general case described here, the two ''momenta'' involved in the formation of a state are connected through relation (10) which depends on the model parameters. This leads to various types of solutions and complicates their analysis.

3. CLASSIFICATION OF SOLUTIONS

Equations (9) and (10) have the following types of solutions depending on the position of numbers k_1, k_2 in the complex plane. In order to obtain a mutually unique parametrization of the families of functions (7), we impose certain constraints on k_1, k_2.

1. k_1, k_2 are real,

$$0 < k_2 < k_1 < \pi; \tag{11}$$

2. (a) k_1 is real, $k_2 = ip$; (b) k_1 is real, $k_2 = \pi + ip$;

$$0 < k_1 < \pi, \quad p > 0. \tag{12}$$

3. $k_{1,2}$ are complex, $k_1 = k_2^*$, $k_1 = k + ip$, $k_2 = k - ip$;

$$0 < k < \pi, \quad p > 0. \tag{13}$$

4. (a) $k_{1,2} = ip_{1,2}$, $0 < p_2 < p_1$; (b) $k_1 = \pi + ip_1$

$$k_2 = ip_2, \quad p_{1,2} > 0; \quad \text{(c)} \quad k_{1,2} = ip_{1,2} + \pi, \quad p_1 > p_2 > 0. \tag{14}$$

All the above relations are strict inequalities and this ensures that the vectors $\exp(ikm)$ appearing in (7) are linearly independent [see the remark following Eq. (8)].

Solutions of types 1 and 2 are called ''band'' solutions since the values of $\varepsilon(k_1)$ for them coincide with the corresponding values of $\varepsilon(k)$ for a ring-shaped closed chain to within quantities of the order of $1/N$.

Solutions of the first type are realized under the condition $H < |J_m|$ for the values of $k_{1,2}$ lying in the interval $(0, k_0)$, $\cos k_0 = 2|h_m| - 1$ for $J_y > 0$ and in the interval $(\pi - k_0, \pi)$ for $J_y < 0$. In these intervals, the function $\varepsilon(k)$ is nonmonotonic under the above condition and assumes each of its values twice. It has a minimum at the point $k_m = \arccos h_m$ if $J_y > 0$, and a maximum if $J_y < 0$. Thus, the possible values of $k_{1,2}$ for the first type of solutions satisfy the conditions

$$0 < k_2 < k_m < k_1 < k_0, \quad J_y > 0;$$

$$\pi - k_0 < k_2 < k_m < k_1 < \pi, \quad J_y < 0. \tag{15}$$

Solutions of type 2 correspond to values of k_1 lying in the interval (k_0, π) for magnetic fields $H < |J_m|$ if $J_y > 0$, and in the interval $(0, \pi - k_0)$ if $J_y < 0$. For $H < |J_m|$, the "band" solutions can be only of type 2.

Solutions of types 3 and 4 are realized in fields $H < J_a$, and correspond to quasidegeneracy in the system. As in Refs. 1, 4, we attribute this to the emergence of long-range order for $N \to \infty$. This will be supported by additional arguments.

4. "BAND" TYPE SOLUTIONS

For solutions of type 1 which are realized only in fields $|h_m| < 1$, Eq. (9) can be conveniently written in the form

$$\frac{1 + \gamma^2 \cot^2 \kappa_1}{1 + \gamma^2 \cot^2 \kappa_2} = \frac{\sin^2 (N+1) \kappa_2}{\sin^2 (N+1) \kappa_1},$$

$$0 < \kappa_1 < \pi/2, \quad \kappa_1 < \kappa_2, \quad \kappa_1 + \kappa_2 < \pi. \quad (16)$$

In the interval $[0, \kappa_0]$, where $\kappa_0 \equiv k_0/2$, Eq. (10) describes a monotonically decreasing function:

$$\kappa_2(\kappa_1) = \arccos(h_m / \cos \kappa_1). \quad (17)$$

Substituting this equation into Eq. (16), we obtain

$$f(\kappa_1) = F_N(\kappa_1), \quad 0 < \kappa_1 < \kappa_0, \quad (18)$$

where f and F_N are functions on the left and right-hand sides of Eq. (16) after such a substitution. The function $f(\kappa_1)$ decreases monotonically in the interval $[0, \kappa_0]$ from ∞ to 1. In a certain neighborhood of each point $\pi l / (N+1)$, $l = 0, 1, 2, \dots, m$, the function $F_N(\kappa_1)$ increases monotonically from 1 to ∞ to the left of this point and decreases monotonically to the right. Here m is defined by the condition

$$\frac{\pi m}{N+1} < \kappa_0 \leq \frac{\pi(m+1)}{N+1}. \quad (19)$$

At other points in the interval $(0, \kappa_0)$, the function $F_N(\kappa_1) < 1$ and $F_N(\kappa_0) = 1$. Thus, Eq. (18) has two solutions in each interval

$$P_l \equiv \left(\frac{\pi l}{N+1}, \frac{\pi(l+1)}{N+1} \right) \quad (20)$$

with $l = 1, 2, \dots, m-1$. In the interval P_0, Eq. (18) always has only one root. The absence of the second root (near $\kappa_1 = 0$) is equivalent to the condition

$$\frac{1}{\gamma^2} < \frac{(N+1)^2}{\sin^2 (N+1) k_m} - \frac{1}{\sin^2 k_m} + 1,$$

$$k_m = \arccos h_m. \quad (21)$$

The sufficient condition for this relation to be fulfilled (i.e., for the absence of the second root in the interval P_0) is the simpler relation

$$\frac{1}{\gamma^2} < \frac{1}{3} (N+1)^2 + \frac{2}{3}. \quad (22)$$

This relation shows that for an anisotropy $0 < \gamma < 1$, the absence of the second root in P_0 is ensured in a quite long chain, the choice of the length of the chain being indepen-

dent of how close the field H is to J_m. For $\gamma > 1 (J_y < 0)$, the second root does not appear in the interval P_0 for all $N > 4$.

It was assumed above that the numerator on the right hand side of Eq. (16) does not vanish together with the denominator. This, however, does not change in principle the above distribution of roots since we proceed in this case from Eq. (9) which is obviously satisfied. Turning directly to the system of equations for $c_{1,2}$, $c'_{1,2}$, we observe that its rank is equal to two and hence two independent solutions exist in this case also.

The fermion energy corresponding to the parameter κ_1 may be expressed as $\varepsilon[\kappa_1 + \kappa_2(\kappa_1)]$, where any point in the interval containing the given solution can be taken as κ_1 with an error not exceeding $\sim 1/N$.

Let us make a general remark. It is hard to prove directly the absence of the second root in P_0 under the condition (21) for any N and for arbitrary parameters. However, it can easily be shown that there must be at least two additional roots if such roots do exist at all. A count of the total number of irrefutably existing roots would lead to the conclusion that the corresponding algebraic eigenvalue problem has more than N linearly independent solutions, which leads to a contradiction. In the following analysis we shall always bear these arguments in mind so that no such roots are found whose existence has not been proved rigorously.

The solutions of type 2 can be parametrized by the numbers k, p:

$$k_1 = k, \quad k_2 = ip \quad \text{for } J > 0;$$

$$k_1 = \pi - k, \quad k_2 = ip + \pi \quad \text{for } J_y < 0,$$

$$0 < k < \pi, \quad p > 0. \quad (23)$$

In both cases ($J_y > 0$, $J_y < 0$), Eq. (10) assumes the form

$$\cos k + \cosh p = 2 |h_m| \quad \text{or} \quad |\cos \kappa|^2 = |h_m|,$$

$$\kappa = \frac{1}{2} (k - ip) \quad (24)$$

and defines uniquely the monotonically increasing function $p(k)$ with k varying in the interval (k_0, π) for $|h_m| < 1$, and in the interval $(0, \pi)$ for $|h_m| > 1$.

Denoting the arguments of complex numbers $\cos \kappa$ and $\sin[(N+1)\kappa]$ through 2Ψ and $-4\Phi_N$, respectively, we can represent Eq. (9) in the form

$$\exp(i\varphi) \equiv \frac{[1 - |h_m| \exp(-i\Psi)][1 \mp h_a \exp(i\Psi)]}{[1 - |h_m| \exp(i\Psi)][1 \mp h_a \exp(-i\Psi)]}$$

$$= \exp(i\Phi_N), \quad h_a \equiv \frac{H}{J_a}, \quad (25)$$

where the upper sign corresponds to the case $J_y > 0$, and the lower sign to the case $J_y < 0$. The quantities Ψ, Φ_N are connected with the parameters k, $p = p(k)$ through the relations

$$\tan(\Psi/2) = \tan(k/2) \tanh(p/2),$$

$$\tan(\Phi_N/4) = \cot[(N+1)k/2] \tanh[(N+1)p/2]. \quad (26)$$

An analysis of the functions $\Psi(k), \Phi_N(k)$ leads to the following conclusions concerning the solutions of Eq. (25).

For $|h_m|<1$ and for any sign of J_y, Eq. (25) must have a root in each interval P_l, $l=2m+1, \ldots, N-1$, where m is defined in (19). In addition, there exists one more solution which may be of type 1 and correspond to the value κ_1 in the interval P_m, or of type 2 and correspond to the value k in the interval P_{2m}.

For $|h_m|>1$ ($J_y>0$, $J_y<0$), Eq. (25) must also have a root in each interval P_l, $l=1,\ldots, N-1$. In the interval P_0, there is no solution for $J_y<0$. For $J_y>0$, a solution appears in the interval P_0 only if the following condition is satisfied:

$$1-h_a<\frac{\gamma^2}{(N+1)\coth[(N+1)p_0/2]}\left(\frac{h_m}{h_m-1}\right)^{1/2},$$

$$\coth p_0=2h_m-1. \tag{27}$$

An analysis of (27) leads to the following system of inequalities describing sufficient but simpler conditions under which a solution does not exist in the interval P_0:

$$\gamma^2>1-h_a>\gamma[\gamma+(1-\gamma^2)^{1/2}]/(N+1),$$

$$\gamma>[(N+1)^2+1]^{-1/2}. \tag{28}$$

It follows from these inequalities that no solution exists in P_0 for quite large N if the field $H<J_a$ and the anisotropy $\gamma \neq 0$. The value of N can be chosen so that it does not depend on the closeness of the field H to J_m. For $H>J_a$, it follows directly from (27) that a solution does exist in P_0.

Let us consider separately the possibility of the existence of a root in the interval P_N for various fields. For $J_y>0$, there are no roots in this interval for all values of the field and for all $N>4$. For $J_y<0$, a root appears in the interval P_N only if the following condition is satisfied:

$$1-h_a<\frac{\gamma^2}{(N+1)\tanh[(N+1)p(\pi)/2]}\left[\frac{|h_m|}{1+|h_m|}\right]^{1/2},$$

$$\cosh[p(\pi)]=2|h_m|+1. \tag{29}$$

A simpler sufficient condition for the absence of roots in P_N is

$$1-h_a>\gamma^2/(N+1). \tag{30}$$

It follows from (29) and (30) that for $H>J_a$, a root exists in P_N for all $N>4$, while for $H<J_a$ no such root exists for quite large N.

Let us summarize the results obtained on the number of "band" type solutions.

For $H<|J_m|<J_a(\gamma<\sqrt{2})$ or $H<J_a<|J_m|(\gamma>\sqrt{2})$, there are $2(m-1)+1$ solutions of type 1, $N-1-2m$ solutions of type 2, and one solution whose type (1 or 2) depends on the specific values of parameters. The total number of these roots is equal to $N-1$. For quite large N (the conditions for this are determined by the inequalities (21), (29)), there are no other "band" type solutions for the values of field indicated above.

If $|J_m|<H<J_a$, there exist $N-1$ solutions of type 2 only. For quite large values of N [conditions (27), (29)], there are no other "band" type solutions in this case also.

In fields $H>J_a$, there always exist exactly N "band" type solutions, some of which may be of type 1 only for $\gamma>\sqrt{2}$ since in this case $J_a<|J_m|$.

Thus, in fields $H<J_a$, one root is always missing for quite large N. This missing root corresponds to a solution of type 3 or 4, which we shall consider below.

5. QUASIDEGENERACY

At the beginning, we note that for solutions of type 3 and 4, it is convenient to present the fermion spectrum ε in (8) in terms of $\kappa_{1,2}$:

$$\varepsilon^2=\cos^{-2}(\kappa_{1,2})[J_g^2\cos^2(\kappa_{1,2})\mp H^2][J_{ag}^2\mp\cos^2(\kappa_{1,2})], \tag{31}$$

where the upper sign corresponds to the case $J_y>0$, and the lower one to the case $J_y<0$.

Solutions of type 3 are possible only for $J_y>0$ and "momenta" of type (13). Formula (10) uniquely defines in this case the monotonically increasing function $k(p)$ in terms of which Eq. (9) can be represented in the form

$$(\cosh^2 p-h_m^2)(J_{ag}^2-\cosh^2 p)$$

$$=J_{ag}^2(\cosh^2 p-h_g^2)\sinh^2 p\,\frac{\sin^2[(N+1)k(p)]}{\sinh^2[(N+1)p]},$$

$$J_{ag}\equiv J_a/J_g,\quad h_g\equiv H/J_g,\quad J_g\equiv(J_x|J_y|)^{1/2}. \tag{32}$$

An analysis of functions on the right and left sides of this relation shows that the condition for the existence of a root of this equation coincides for $H<J_m$ with the condition (21) for the absence of a solution of type 1 in the interval P_0, and for $J_m<H<J_g'$ with the condition (27) for the absence of a solution of type 2 in P_0. The field J_g' is determined from (32) by imposing the condition that the limiting relations $\cosh p\to J_g'/J_m$, $k_p\to0$ are satisfied for $H\to J_g'$ (for $H=J_g'$, the solution has a quasipolynomial form, see remark following formula (8)). Note that J_g' depends on N, but the difference J_g-J_g' is a rapidly decreasing function for $N\to\infty$:

$$J_g-J_g'\cong\Delta^4/(8J_a^2J_x)(N+1)(J_y/J_x)^N. \tag{33}$$

The solution of Eq. (32) can be presented in an explicit form only for large N. In the zeroth approximation $\cosh p=J_{ag}$, while the asymptotic formula for correction has the following form for $N\to\infty$ uniformly in the field interval $0<H<J_g'$:

$$J_{ag}^2-\cosh^2 p=4A\,\sin^2[(N+1)k_g](J_y/J_x)^{N+1}, \tag{34}$$

where

$$\cos k_g=H/J_g,\quad A=(J_a^2-H^2)\Delta J_g^{-2}|J_xJ_y-H^2|^{-1}.$$

To obtain the value of ε corresponding to the solution under consideration (we shall denote this value as ε_0), we should put $\kappa_1=ip$ in (31) and substitute (34) in it. Retaining only the principal nontrivial term of the asymptotic form in N, we obtain

$$\varepsilon_0\cong2B|\sin[(N+1)k_g]|(J_y/J_x)^{(N+1)/2}, \tag{35}$$

where $B=\Delta(J_a^2-H^2)J_a^{-1}|J_xJ_y-H^2|^{-1/2}$.

Note that in the limit $H\to J_g'$, formula (35) assumes the form

$$\varepsilon_0 \cong \frac{2\Delta^3(N+1)}{J_a J_g} (J_y/J_x)^{(N+1)/2}. \tag{36}$$

Putting $H=0$ in (35), we arrive at the result obtained in Ref. 1.

It can be seen from (35) and (36) that the energy corresponding to a type 3 solution for $N \to \infty$ is a rapidly decreasing function of N in the entire range of existence of this solution. Thus, the creation of a fermion with such an energy leads to a variation of the system energy that is exponentially small in comparison with N, i.e., to quasidegeneracy.

It is interesting to note that as can be seen from Eq. (35), the dependence of ε_0 on the field H displays characteristic oscillations. For each N, there exists a discrete set of fields (the set condenses as $N \to \infty$) in which the exact degeneracy $\varepsilon = 0$ takes place. The fields are defined by the equality $H_l = J_g \cos[\pi l/(N+1)]$, where $l=1,2,\dots, N/2$. These oscillations are a ''continuation'' of the same field oscillations in an isotropic XY-model obtained in Ref. 4 to the anisotropic case.

It should be observed once again that a type 3 solution exists in the field interval $0 < H < J'_g$. It will be shown that the solution changes to type 4 as the field crosses the upper boundary of this interval.

An analysis of Eqs. (9), (10) shows that for solutions of type 4, version (a) is realized in (14) for $J_y > 0$, while version (b) is realized for $J_y < 0$. The version (c) is usually not realized for type 4 solutions. For roots of type 4(a,b), it is convenient to represent Eqs. (9,10) in terms of the variables $p = (p_1 + p_2)/2$, $p' = (p_1 - p_2)/2$. In view of Eq. (10), p, p' satisfy the condition $0 < p' < p$. This equation uniquely defines monotonically decreasing functions $p'(p)$ (different for different signs of J_y) using which we can transform Eq. (9) into an equation in p. Let us consider successively the cases $J_y > 0$ and $J_y < 0$.

For $J_y > 0$, the equation in p is formally obtained from (32) by substituting $-\sinh^2[(N+1)p'(p)]$ for $\sin^2[(N+1)k(p)]$. An analysis of this equation leads to the conclusion that one root exists for $J'_g < H < J_a$, where J'_g has been defined above, if there is no ''band'' solution in the interval P_0, as expressed by an inequality inverse to (27). The asymptotic formula for this root for $N \to \infty$ has the form

$$J_{ag}^2 - \cosh^2 p \cong A Q_N^2 (J_x^{-1}[H + (H^2 - J_x J_y)^{1/2}])^{2(N+1)}, \tag{37}$$

where $Q_N = 1 - \exp[-2(N+1)p_g]$, $\cosh p_g = H/J_g$.

The corresponding value of $\varepsilon[\kappa_2 = ip$ in (31)] is given by

$$\varepsilon_0 \cong B Q_N (J_x^{-1}[H + (H^2 - J_x J_y)^{1/2}])^{N+1}, \tag{38}$$

where the base of the exponential function of N is less than unity in the interval of fields under consideration. For $H \to J'_g$ formula (38) is transformed into (36). Among other things, this is ensured by the factor Q_N in (37), (38). This factor can be disregarded for all fields except a small neighborhood of J'_g (determined by the smallness of N^{-1}). For $J_y \to 0$, Eq. (38) leads to the result obtained in Ref. 3.

For $J_y < 0$, Eq. (9) assumes the form

$$(\sinh^2 p + h_m^2)(J_{ag}^2 - \sinh^2 p) = J_{ag}^2(\sinh^2 p$$
$$- h_g^2)\cosh^2 p \, \frac{\cosh^2[(N+1)p'(p)]}{\cosh^2[(N+1)p]}. \tag{39}$$

An analysis of this equation leads to the conclusion that there exists just one root in the entire interval of fields $0 < H < J_a$ if the inequality opposite to (29) is satisfied. Asymptotic formulas for this root and the values of ε_0 are defined by the expressions (37) and (38) in which Q_N is assumed to be equal to unity.

Thus, for fields $H < J_a$ and $0 < \gamma < \infty$, a special solution is realized in the system in addition to the ''band'' solutions if N exceeds a certain critical value N_c. For given parameters of the model, this value can be determined from formulas (21), (27), and (29). It follows, among other things, from the rough sufficient conditions (22), (28), and (30) that for $J_y > 0$ the special solution exists for all $N > 4$, i.e. for $N_c = 4$, in the range of values of parameters satisfying the set of conditions

$$0 < \gamma < 1,$$
$$H/J_a < \min\{(1 - \gamma^2), \quad (1 - [\gamma^2 + \gamma(1 - \gamma^2)^{1/2}])\}.$$

6. PERTURBATION THEORY

In order to understand more clearly the nature of quasidegeneracy and its connection with the emergence of long-range order for $N \to \infty$, we study the XY-model under consideration from the point of view of the perturbation theory (PT). We proceed from Ising's model with $\hat{H}_0$, which corresponds to $J_y = 0$, $H = 0$ in (1) for a weak transverse field H or a small exchange J_y. The following obvious points, which will be quite significant in subsequent analysis, should be borne in mind. The quantity $\hat{H}_0$ has a doubly degenerate ground level energy E_0, the corresponding states $|+\rangle$ and $|-\rangle$ are (tensor) products of states of individual sites. All lattice sites of the vector $|+\rangle$ are orthogonal to the lattice sites of the vector $|-\rangle$ (for large N, this corresponds to the macroscopic difference between states $|+\rangle$ and $|-\rangle$). Besides, there exists a symmetry $\hat{H} = \hat{H}_0 + V$ (rotation around the z-axis by π) that transforms the states $|+\rangle, |-\rangle$ into each other and for which the degeneracy space $\{E_0\}$ of level E_0 splits into two one-dimensional spaces defined by the vectors $|+\rangle \pm |-\rangle$.

The introduction of a perturbation V causes a splitting of the level E_0 which is described by an equivalent operator in the perturbation theory. The general structure of its mth order term has the form

$$P_0 V (R_0 V)^{m-1} P_0,$$
$$R_0 \equiv (1 - P_0)(\hat{H}_0 - E_0)^{-1}(1 - P_0), \tag{40}$$

where P_0 is a projector on $\{E_0\}, V \propto H$ or J_y. It follows from the facts listed above that if $m < N$ for $V \propto H$ or $m < N/2$ for $V \propto J_y$, all terms in (40) can transform each of the states $|\pm\rangle$ into itself only, giving the same corrections to them, which cannot lead to a splitting of E_0. Only beginning from $m = N$ for $V \propto H$ and $m = N/2$ for $V \propto J_y$ does Eq. (40) acquire terms with a nonzero matrix element between $|+\rangle$ and

$|-\rangle$. This leads to the formation of eigenstates $|+\rangle \pm |-\rangle$ and to an exponentially small splitting $\sim (H/J_x)^N$ or $\sim (J_y/J_x)^{N/2}$ of the level E_0. In this case, the number of terms that can contribute to the first nonvanishing correction in the perturbation theory is not more than N, which does not change the rapidly decreasing nature of the dependence of splitting on N. For a larger dimension ν of the lattice, the rate of decrease increases on account of an increase in the excitation energy of intermediate states to quantities of the order of $J_x N^{(\nu-1)/\nu}$.

For large N, the splitting remains small right up to the value of perturbation closely approaching the gap J_x in the spectrum $\hat{H}_0$. However, the real applicability of perturbation theory may be hampered by corrections that do not undergo splitting and nonuniformly displace levels of energy $\hat{H}_0$ even in lowest orders of perturbation theory. This may lead to their intersection and thus render perturbation theory inapplicable. Exact results show that this does not happen in the case under consideration and perturbation theory really describes the true picture of splitting for all $H < J_x$ or $J_y < J_x$ for quite large N. However, if the above procedure is applied to an antiferromagnetic Ising chain with spin 1, including isotropic antiferromagnetic perturbation $z - y(J_y = J_z)$, the intersection of levels described above is realized for a certain value of the anisotropy if Haldane's hypothesis[7] is valid.

Thus, the analysis carried out in the framework of perturbation theory leads to the conclusion that the presence of quasidegeneracy in large systems (anomalously small splitting with a characteristic exponential dependence on N, $\sim \xi^N, \xi < 1$) indicates that each of the corresponding states is a superposition of the same macroscopically different states.

We shall now discuss in detail the mechanism behind the emergence of long-range order in the simplest case under consideration. As long as the number of sites is small, the ground state $\overline{2}^{1/2}(|+\rangle - |-\rangle)$ of the system is purely degenerate and separated from the remaining states by an observable energy gap. [In order to avoid confusion, we remark that we are dealing with the inverse images of real states in the subspace $\{E_0\}$ where the equivalent Hamiltonian in the perturbation theory is defined by (40).] For $N \to \infty$, this pure state is transformed into the limiting state $|\infty\rangle$, which is a mixture of limiting macroscopic distinguishable homogeneous states $|\infty, +\rangle$ and $|\infty, -\rangle$, since for any local observables (correlators) K, we can write

$$\langle \infty | K | \infty \rangle = 2^{-1}(\langle \infty, + | K | \infty, + \rangle + \langle \infty, - | K | \infty, - \rangle). \quad (41)$$

For $n \to \infty$, the nonzero limit of the correlator $\langle (S_0^x - \langle S_0^x \rangle) \times (S_n^x - \langle S_n^x \rangle) \rangle$ calculated in Ref. 2 for the state $|\infty\rangle$ is just the sufficient condition for its decomposition into a mixture of homogeneous states.[5] Apparently, the components $|\infty, \pm\rangle$ of the decomposition[41] cannot be decomposed further and are therefore really observable different thermodynamic states in which the ordering takes place ($\langle S_n^x \rangle \neq 0$).

Note that in the limit $N \to \infty$, the second state of the quasidegenerate doublet $|+\rangle + |-\rangle$ coincides with $|\infty\rangle$. This is manifested in single-fermion states of types 3 and 4, whose parameters are directly connected with the parameters

characterizing the behavior of correlators in the state $|\infty\rangle$, i.e., the parameters describing the spatially nonmonotonic part of the correlators $\sim \exp(-pn)\cos(kn)$ for large n in fields $H < J_g$.[2] Solutions of type 3 existing in the same regions of fields coincide exactly with the real and imaginary part of parameters $k_{1,2}$. In the field $J_g < H < J_a$ also, the parameters $p_{1,2}$ of the solution of type 4 define the parameter $p_1 - p_2$ of the exponentially decreasing part of the correlators.[2]

The analysis carried out in this section can be generalized, and hence we can speak about a certain class of quantum lattice systems existing in the vicinity of Ising-like models for which the above mechanism of quasidegeneracy and establishment of long-range order is realized for $N \to \infty$, in spite of the fact that the ground state is not degenerate for finite N.

7. CONCLUSION

Single-fermion states are classified for an open finite $(N > 4)$ anisotropic XY-chain with a transverse magnetic field, and the distribution of the corresponding energy levels is obtained for all values of the parameters J_x, J_y, and H. Two types of "band" type solutions (type 1 and type 2) are obtained for such a system. Their energy is defined by the formal dispersion relation $\varepsilon(k)$ for an infinite chain for real allowed values of k. In addition, there exists a special solution which can also be of two types (type 3 or type 4) and has an energy corresponding to complex values of k.

States of type 1 contain in their construction two real momenta $k_{1,2} > 0$ for which $\varepsilon(k)$ assumes identical values. In other words, there may exist solutions when the spectrum $\varepsilon(k)$ is nonmonotonic (for $k > 0$), and correspond to generalized standing waves. These solutions are realized in fields $H < |J_m|$ in which such a nonmonotonicity of $\varepsilon(k)$ exists.

States of type 2 exist for all fields and their construction contains one real "momentum" k_1. The boundary conditions are fulfilled on account of terms that decrease rapidly with increasing distance from the boundary and contain "momentum" k_2 of the type ip or $\pi + ip$.

In fields $H < J_a$, there are $N - 1$ solutions of "band" type and one special solution whose energy tends rapidly (exponentially in N) to zero with increasing length of the chain. For $N \to \infty$, the latter causes a degeneracy of the system, especially the degeneracy of the ground state. To be more precise, the region in which a special solution (of type 3 or 4) is realized for finite N is defined by the inequalities (21), (27), and (29). Among other things, it follows from these inequalities that if the model is nearly isotropic or the field approaches the critical value J_a from below, N must be quite large i,e., $N > N_c \gg 1$. At the same time, there exists a wide range of values of parameters for which a special solution exists for all $N > 4(N_c = 4)$.

In the entire range of parameters in which a special solution exists, the available results of calculations for correlators carried out in Ref. 2 for a ring indicate that the limiting ground state in it is a mixture of homogeneous macroscopically different states. These calculations were carried out for a model with identical signs of exchange parameters. However, using the characteristic quasidegeneracy as a true crite-

539   Low Temp. Phys. **23** (7), July 1997

A. A. Loginov and Yu. V. Pereverzev   539

rion for the existence of long-range order in the system, we can assume that it also exists for opposite signs of exchanges if $H < J_a$.

The informal analysis from the point of view of perturbation theory carried out in this work lends authenticity to the statement that quasidegeneracy is linked with long-range order. This analysis allows us to describe one of the possible mechanisms of the emergence of order in systems having a nondegenerate ground state in a finite volume. Such a state may be a superposition of two vectors which become macroscopically distinguishable with increasing number of sites, retaining in it nonzero weights for $N \to \infty$. In this limit, such a superposition is transformed into a mixture of macroscopically distinguishable states, whose individual components have the same energy density as the mixture. In fact this indicates that the thermodynamic limit for the ground state is not unique (first-order phase transition point), and the components of decomposition are purely thermodynamic phases

(if these, in turn, do not decompose into a similar mixture). These phases could be obtained directly by the method of quasimeans or by making a limiting transition under appropriate boundary conditions. In view of the fact that a symmetry element exists in such a case and transforms these components into each other, quasidegeneracy sets in during the transition $N \to \infty$.

*E-mail: pereverzev@ilt.kharkov.ua

[1] E. Lieb, T. Schultz, and D. Mattis, Ann. Phys. **16**, 406 (1961).
[2] E. Barouch and B. McCoy, Phys. Rev. **A3**, 786 (1971).
[3] P. Pfeuty, Ann. Phys. **57**, 79 (1970).
[4] V. M. Kontorovich and V. M. Tsukernik, Zh. Éksp. Teor. Fiz **62**, 355 (1972) [JETP **35**, 190 (1972)].
[5] D. Ruelle, *Statistical Mechanics. Rigorous Results*, Benjamin/Cummings, New York (1969).
[6] I. Affleck, J. Phys.: Condens. Matter **1**, 3047 (1989).

Translated by R. S. Wadhwa

Dynamic susceptibility of spin-1/2 Ising chain in transverse field

O. Derzhko and T. Krokhmalskii

Institute for Condensed Matter Physics, 1 Svientsitskii St., L'viv-11, 290011, Ukraine[1)]

Dynamic susceptibility of the one-dimensional spin-1/2 transverse Ising model is obtained by using the numerical approach suggested earlier [*Ferroelectrics* **153**, 55 (1996)]. The dependence of the susceptibility frequency shapes on the value of the transverse field at various temperatures is discussed. The way in which the frequency shape rebuilds as the transverse field increases is illustrated. © *1997 American Institute of Physics.* [S1063-777X(97)00607-5]

The one-dimensional spin-1/2 Ising model in a transverse field is an important subject of theoretical studies not only because of its usefulness in solid state physics, but also because many of its statistical mechanics properties can be examined exactly.[1–3] However, since the early 1970s it was known that calculation of some time-dependent spin correlation functions for this model encounter great difficulties and in spite of many papers dealing with this problem[4–7] (see also recent papers[8,9] dealing with such studies for the one-dimensional spin-1/2 *XX* model) the investigation of dynamic properties calls for more efforts. In the present paper our goal is to provide a fresh view on the analysis of spin dynamics. Specifically, we shall extend the earlier elaborated numerical approach for equilibrium statistical mechanics calculations for spin-1/2 *XY* chains[10,11] to the analysis of dynamic properties of transverse Ising model and we shall study, in particular, its dynamic susceptibility.

We consider spin-1/2 chain described by the Hamiltonian

$$H = \Omega \sum_{j=1}^{N} s_j^z + J \sum_{j=1}^{N-1} s_j^x s_{j+1}^x, \tag{1}$$

where Ω is the transverse field at the site, and J is the interaction between neighboring sites. Two distinctive cases corresponding to different signs of intersite interaction will be considered, i.e., $J < 0$ (ferromagnetic coupling) and $J > 0$ (antiferromagnetic coupling). We are interested in the time-dependent, two-spin correlation functions $\langle s_j^\alpha(t) s_{j+n}^\beta \rangle$, where the angle brackets denote thermodynamic average $\langle (\dots) \rangle \equiv \mathrm{Tr}[e^{-\beta H}(\dots)]/\mathrm{Tr}\, e^{-\beta H}$. The correlation function between the *z*-components was derived in Ref. 2. We shall restrict the analysis mainly to the correlation function between the *x*-components of two spins, noting that all other nonzero correlation functions can be found in principle by differentiation:

$$\langle s_j^x(t) s_{j+n}^y \rangle = -\langle s_j^y(t) s_{j+n}^x \rangle = \frac{1}{\Omega} \frac{d}{dt} \langle s_j^x(t) s_{j+n}^x \rangle,$$

$$\langle s_j^y(t) s_{j+n}^y \rangle = -\frac{1}{\Omega^2} \frac{d^2}{dt^2} \langle s_j^x(t) s_{j+n}^x \rangle. \tag{2}$$

In order to evaluate the quantity of interest, one should rewrite the Hamiltonian (1) in terms of Fermi operators with the help of the Jordan–Wigner transformation and then diagonalize the bilinear fermion form. Basic results may be summarized as follows: The relations between spin operators and Fermi operators are

$$s_j^x = \frac{1}{2} \varphi_1^+ \varphi_1^- \varphi_2^+ \varphi_2^- \cdots \varphi_{j-1}^+ \varphi_{j-1}^- \varphi_j^+,$$

$$s_j^y = \frac{1}{2i} \varphi_1^+ \varphi_1^- \varphi_2^+ \varphi_2^- \cdots \varphi_{j-1}^+ \varphi_{j-1}^- \varphi_j^-, \tag{3}$$

$$s_j^z = -\frac{1}{2} \varphi_j^+ \varphi_j^-,$$

where

$$\varphi_j^+ = \sum_{p=1}^{N} \Phi_{pj}(\eta_p^+ + \eta_p), \quad \varphi_j^- = \sum_{p=1}^{N} \Psi_{pj}(\eta_p^+ - \eta_p); \tag{4}$$

the transformed Hamiltonian (1) has the form

$$H = \sum_{k=1}^{N} \Lambda_k \left(\eta_k^+ \eta_k - \frac{1}{2} \right),$$

$$\{\eta_q, \eta_r^+\} = \delta_{qr}, \quad \{\eta_q, \eta_r\} = \{\eta_q^+, \eta_r^+\} = 0; \tag{5}$$

Λ_p, Φ_{pj}, and Ψ_{pj} are determined from the equations

$$\sum_{j=1}^{N} \Psi_{pj}(A_{jn} + B_{jn}) = \Lambda_p \Phi_{pn},$$

$$\sum_{j=1}^{N} \Phi_{pj}(A_{jn} - B_{jn}) = \Lambda_p \Psi_{pn},$$

$$\sum_{j=1}^{N} \Phi_{qj}\Phi_{rj} = \sum_{j=1}^{N} \Psi_{qj}\Psi_{rj} = \delta_{qr}, \tag{6}$$

$$\sum_{p=1}^{N} \Phi_{pi}\Phi_{pj} = \sum_{p=1}^{N} \Psi_{pi}\Psi_{pj} = \delta_{ij}$$

with

$$A_{ij} \equiv \Omega \delta_{ij} + \frac{J}{4} \delta_{j,i+1} + \frac{J}{4} \delta_{j,i-1},$$

$$B_{ij} \equiv \frac{J}{4} \delta_{j,i+1} - \frac{J}{4} \delta_{j,i-1}.$$

For further details see Refs. 1, 10, and 11. In view of (3)–(5), the calculation of $\langle s_j^x(t)s_{j+n}^x \rangle$ reduces to exploiting of the Wick–Bloch–de Dominicis theorem and the result can be expressed compactly in the form of the Pfaffian of $2(2j+n-1) \times 2(2j+n-1)$ antisymmetric matrix constructed from elementary contractions

$$
\begin{aligned}
4\langle s_j^x(t)s_{j+n}^x \rangle &= \langle \varphi_1^+(t)\varphi_1^-(t)\varphi_2^+(t)\varphi_2^-(t)\ldots\varphi_{j-1}^+(t) \\
&\quad \times \varphi_{j-1}^-(t)\varphi_j^+(t)\varphi_1^+\varphi_1^-\varphi_2^+\varphi_2^-\ldots\varphi_{j-1}^+\varphi_{j-1}^-\varphi_j^+\varphi_j^-\varphi_{j+1}^+\varphi_{j+1}^-\ldots\varphi_{j+n-1}^+\varphi_{j+n-1}^-\varphi_{j+n}^+ \rangle \\
&= \mathrm{Pf}
\begin{pmatrix}
0 & \langle \varphi_1^+\varphi_1^- \rangle & \langle \varphi_1^+\varphi_2^+ \rangle & \ldots & \langle \varphi_1^+(t)\varphi_{j+n}^+ \rangle \\
-\langle \varphi_1^+\varphi_1^- \rangle & 0 & \langle \varphi_1^-\varphi_2^+ \rangle & \cdots & \langle \varphi_1^-(t)\varphi_{j+n}^+ \rangle \\
\vdots & \vdots & \vdots & \cdots & \vdots \\
-\langle \varphi_1^+(t)\varphi_{j+n}^+ \rangle & -\langle \varphi_1^-(t)\varphi_{j+n}^+ \rangle & -\langle \varphi_2^+(t)\varphi_{j+n}^+ \rangle & \cdots & 0
\end{pmatrix},
\end{aligned}
\tag{7}
$$

where

$$
\langle \varphi_j^+(t)\varphi_m^+ \rangle = \sum_{p=1}^{N} \Phi_{pj}\Phi_{pm} \frac{\cosh[i\Lambda_p t - (\beta\Lambda_p/2)]}{\cosh(\beta\Lambda_p/2)},
$$

$$
\langle \varphi_j^+(t)\varphi_m^- \rangle = -\sum_{p=1}^{N} \Phi_{pj}\Psi_{pm} \frac{\sinh[i\Lambda_p t - (\beta\Lambda_p/2)]}{\cosh(\beta\Lambda_p/2)},
$$

$$
\langle \varphi_j^-(t)\varphi_m^+ \rangle = \sum_{p=1}^{N} \Psi_{pj}\Phi_{pm} \frac{\sinh[i\Lambda_p t - (\beta\Lambda_p/2)]}{\cosh(\beta\Lambda_p/2)},
$$

$$
\langle \varphi_j^-(t)\varphi_m^- \rangle = -\sum_{p=1}^{N} \Psi_{pj}\Psi_{pm} \frac{\cosh[i\Lambda_p t - (\beta\Lambda_p/2)]}{\cosh(\beta\Lambda_p/2)}.
\tag{8}
$$

Equations (6)–(8) form the starting point for further numerical calculations. Considering a chain of $N=280$ spins with $J=\pm 1$ and a certain value of the transverse field in the range $\Omega = 0.1 - 5$, we solved $N \times N$ standard problem (6) obtained in the result Λ_p, Φ_{pj}, Ψ_{pj}. Setting $j=32$ and certain n in the range from 0 to 30, we then computed elementary contractions (8) involved in (7) for a given temperature in the range $\beta = 10 - 0.1$ and time t up to 120 and evaluated the Pfaffian numerically obtaining in the result the quantity of interest, i.e., the correlation between the x-components of spins at the sites j and $j+n$ taken at times t and $t=0$, respectively. There are few practical limitations on this approach, i.e., finite chain size N, presence of boundaries $1 \leq j, j+n \leq N$, and finite time t. These effects lead to deviation from a time behavior inherent to an infinite chain, which is the case of interest in statistical mechanics. The value of this deviation depends on the values of the transverse field and the temperature. Nevertheless, since such effect is easy to recognize, one may derive in a wide range of parameters the results which are not subject to these influences, i.e., which refer to $N \to \infty$. The data produced in the calculations described above [as well as the results for $\chi_{xx}(\kappa,\omega)$ (9) obtained on their basis] pertain to infinite chains. The results of our numerical calculations were found to be in excellent agreement with the exact results obtained at $T=\infty$ (Ref. 6) and $T=0$, $\Omega = J/2$ (Ref. 7) and with the notorious exact result for the zz correlation function.[2] It should be emphasized

that the described approach allows one to study finite-size effects which, however, are beyond the scope of the present paper. Finally, we verified relations (2) which connect $\langle s_j^x(t)s_{j+n}^x \rangle$ with other correlation functions after these correlation functions are computed in a similar manner.

We shall discuss the dynamics of the transverse Ising model looking at the dynamic susceptibility

$$
\chi_{xx}(\kappa,\omega) \equiv \sum_{n=1}^{N} e^{i\kappa n} \int_0^\infty dt\, e^{i(\omega + i\varepsilon)t} \frac{1}{i} \langle [s_j^x(t), s_{j+n}^x] \rangle,
$$
$$
\varepsilon \to +0.
\tag{9}
$$

The frequency shapes of $\mathrm{Re}\,\chi_{xx}(0,\omega)$ and $\mathrm{Im}\,\chi_{xx}(0,\omega)$ at various transverse fields and temperatures are shown in Figs. 1 and 2. Small wiggles in the curves corresponding to $\beta = 5$ were introduced by the finite time cutoff in (9) because of rather slow decay of correlations versus time (especially for $\Omega = 0.2$, 1 and ferromagnetic intersite coupling). The wiggles can be removed either by increasing the time cutoff in (9), which requires computer resources, or by increasing the value of ε, which slightly smooths the frequency shapes and decreases, in particular, the heights of their peculiarities. Usually, we set $\varepsilon = 0.001 - 0.05$.

Let us now turn to the discussion of the results. Figure 1 shows the dependence of $\mathrm{Re}\,\chi_{xx}(0,\omega) - \omega$ and $\mathrm{Im}\,\chi_{xx}(0,\omega) - \omega$ curves on Ω various temperatures. From these plots we easily see that $\mathrm{Im}\,\chi_{xx}(0,\omega)$ exhibits two peaks for $\Omega = 0.2$ (the Ising-like case) and one peak for $\Omega = 1$ (the case of almost noninteracting spins in an external field). At low temperature $\beta = 5$ for $\Omega = 0.2$ $\mathrm{Im}\,\chi_{xx}(0,\omega)$ reveals a high sharp peak in the vicinity of zero frequency $\omega \approx 0.03$ and a low broad peak at $\omega \approx 0.76$ for ferromagnetic intersite coupling and two pronounced peaks at frequencies $\omega \approx 0.36$ and $\omega \approx 1.02$ for antiferromagnetic intersite coupling. In the case $\Omega = 1$ $\mathrm{Im}\,\chi_{xx}(0,\omega)$ reveals one high and broad peak at $\omega \approx 0.51$ and $\omega \approx 1.50$ for ferro- and antiferromagnetic coupling, respectively. As the temperature is raised to $\beta = 1$, the situation qualitatively remains the same. For $\Omega = 0.2$ $\mathrm{Im}\,\chi_{xx}(0,\omega)$ exhibits two lower and broader peaks compared with the preceding case, which are shifted to higher frequencies $\omega \approx 0.09$, $\omega \approx 0.94$ for ferromagnetic intersite interaction and to lower frequencies $\omega \approx 0.21$, ω

542   Low Temp. Phys. **23** (7), July 1997
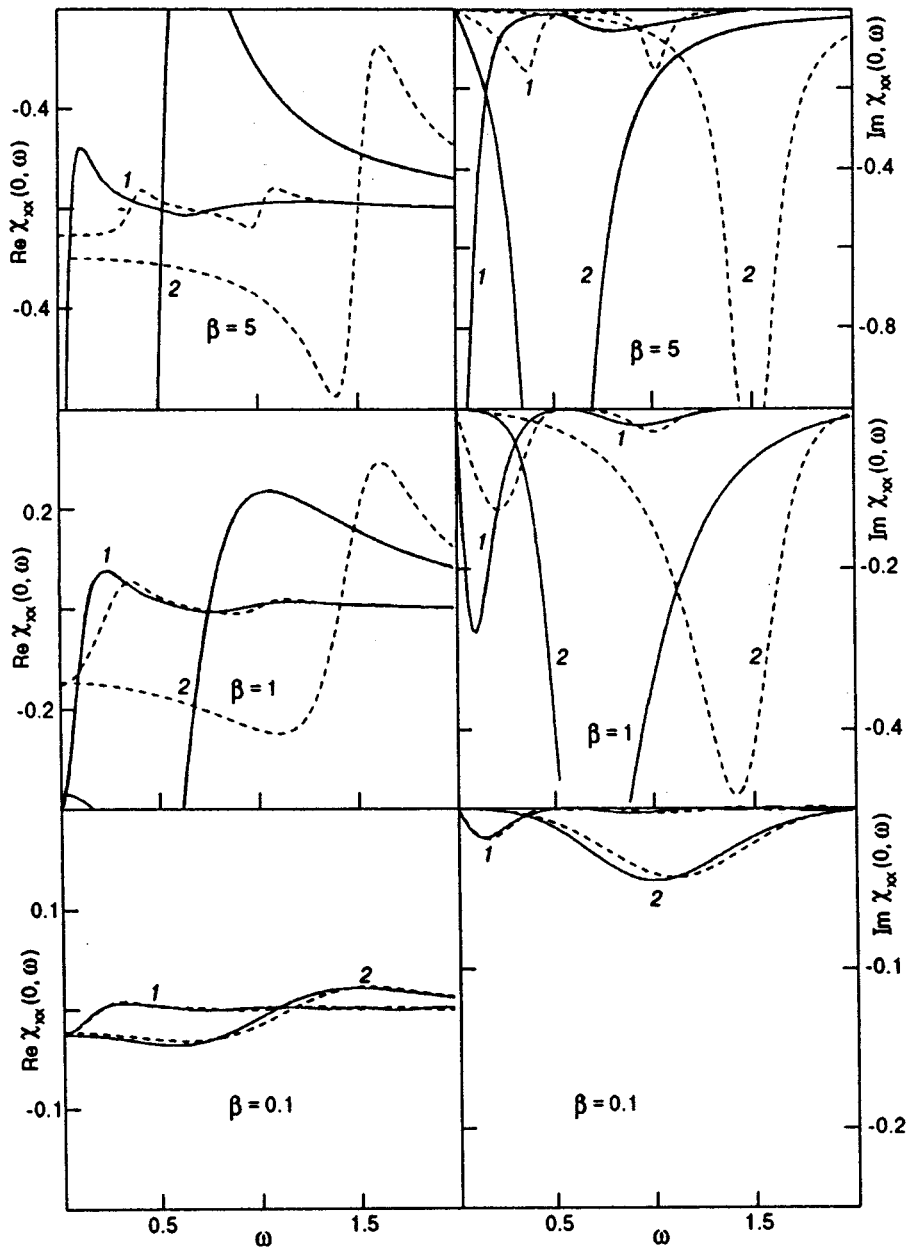
O. Derzhko and T. Krokhmalskii   542

FIG. 1. $\chi_{xx}(0,\omega)$ versus ω at various temperatures. The solid lines represent data for ferromagnetic intersite coupling $J=-1$, the dashed lines denote data for antiferromagnetic intersite coupling $J=1$; 1 corresponds to $\Omega=0.2$; 2 corresponds to $\Omega=1$.

≈ 1.00 for antiferromagnetic intersite interaction; in the latter case the low-frequency peak becomes higher than the high-frequency peak. For $\Omega=1$ Im $\chi_{xx}(0,\omega)$ exhibits only one lower and broader peak compared with the case $\beta=5$, which is shifted to higher frequency $\omega\approx 0.67$ for ferromagnetic coupling and to lower frequency $\omega\approx 1.42$ for antiferromagnetic coupling. At high temperature $\beta=0.1$ the frequency profiles of Im $\chi_{xx}(0,\omega)$ almost coincide for ferromagnetic and antiferromagnetic couplings, although it is still possible to recognize two peaks for $\Omega=0.2$ at $\omega\approx 0.13$, $\omega\approx 0.88$ and $\omega\approx 0.15$, $\omega\approx 1.03$ for ferro- and antiferromagnetic coupling, respectively, and one peak for $\Omega=1$ at $\omega\approx 1.00$ and $\omega\approx 1.10$ for ferro- and anti-ferromagnetic coupling, respectively.

In order to understand how two-peak shapes transform into one-peak shapes as the transverse field increases, we performed additional calculations of $\chi_{xx}(0,\omega)$ at $\beta=5$ for

$\Omega=0.3$, 0.4, 0.5, 0.6 (shown in Fig. 2). As can be seen from Fig. 2, the high-frequency peak on the curve Im $\chi_{xx}(0,\omega)$ $-\omega$ for $\beta=5$, $\Omega=0.2$ at $\omega\approx 0.76$ for ferromagnetic coupling and the low-frequency peak at $\omega\approx 0.36$ for antiferromagnetic coupling with increasing transverse field move toward the low-frequency peak at $\omega\approx 0.03$ for ferromagnetic coupling and toward high-frequency peak at $\omega\approx 1.02$ for antiferromagnetic coupling, which in turn become broader. The positions of the peaks are as follows: $\omega\approx 0.03$, $\omega\approx 0.57$ for $\Omega=0.3$, $\omega\approx 0.05$, $\omega\approx 0.28-0.36$ for $\Omega=0.4$ for ferromagnetic intersite interaction; $\omega\approx 0.56$, $\omega\approx 1.03$ for $\Omega=0.3$, $\omega\approx 0.75$, $\omega\approx 1.05$ for $\Omega=0.4$ for antiferromagnetic intersite interaction. For $\Omega=0.5$ two peaks have already coalesced: Im $\chi_{xx}(0,\omega)$ reveals one peak at $\omega\approx 0.10$ and $\omega\approx 1.00$ for ferro- and antiferromagnetic coupling, respectively. Further increase of the transverse field leads to the shift of one peak to higher frequencies, i.e., $\omega\approx 0.15$ if $\Omega=0.6$ and $\omega\approx 0.51$ if
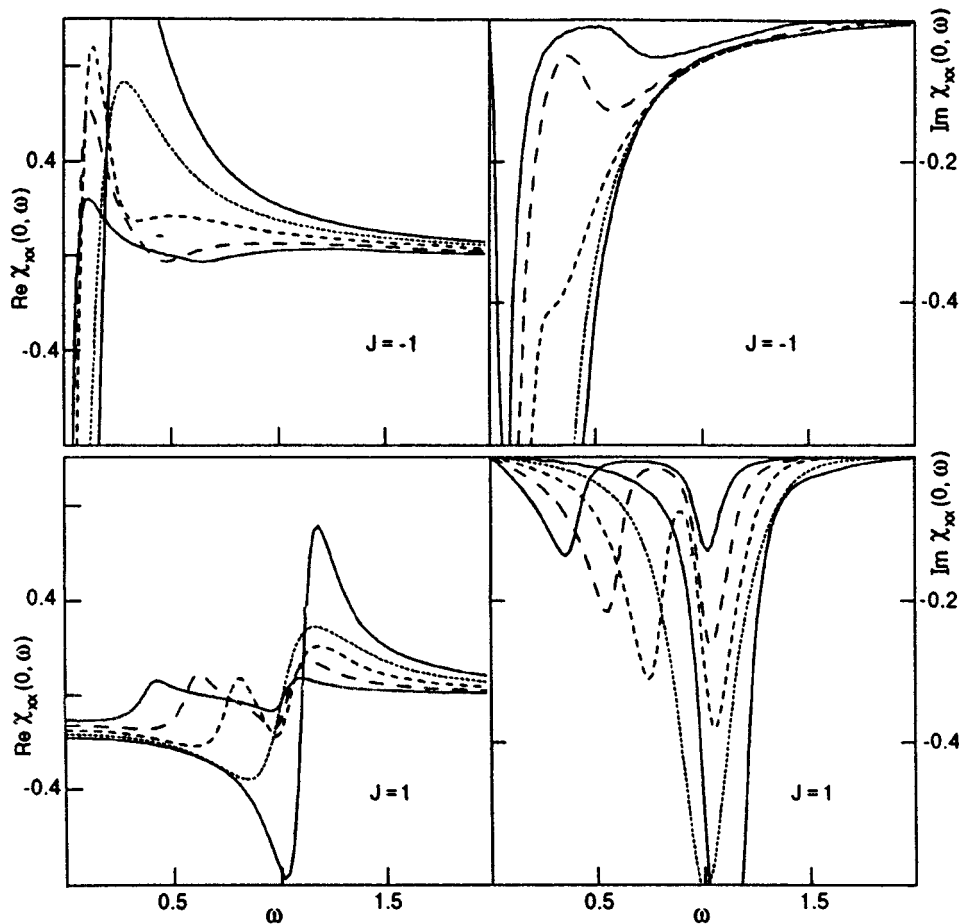
FIG. 2. $\chi_{xx}(0,\omega)$ versus ω for different values of transverse field at $\beta = 5$. The solid lines represent data for $\Omega = 0.2$ (these curves are also plotted in Fig. 1) and $\Omega = 0.6$; the long-dashed lines denote data for $\Omega = 0.3$; the short-dashed lines correspond to data for $\Omega = 0.4$; the dotted lines represent data for $\Omega = 0.5$.

$\Omega = 1$ for ferromagnetic coupling and $\omega \approx 1.10$ if $\Omega = 0.6$ and $\omega \approx 1.50$ if $\Omega = 1$ for antiferromagnetic coupling.

In summary, we were able to numerically examine the dynamic properties of one-dimensional spin-1/2 Ising model in a transverse field and to evaluate the frequency-dependent susceptibility. These results seem to be important since, to the best of our knowledge, they constitute the only exact numerical results available. In addition, we hope that the main features of the susceptibility in the given limiting cases of small and large transverse fields would be observable in the measurements of dynamic dielectric constant of quasi-one-dimensional, hydrogen-bonded ferroelectrics materials like CsH_2PO_4, $PbHPO_4$ (Ref. 12 and 13) ($\Omega < J/2$) and in the absorption spectrum measurements for J-aggregates[14,15] ($\Omega > J/2$). However, these problems and the reconsideration of some approximate approaches used earlier for analysis of experimental data require a separate study.

[1] E-mail: derzhko@icmp.lviv.ua, krokhm@icmp.lviv.ua

[1] E. Lieb, T. Schultz, and D. Mattis, Ann. Phys. **16**, 407 (1961).

[2] Th. Nijemeijer, Physica **36**, 377 (1967).

[3] P. Pfeuty, Ann. Phys. **57**, 79 (1970).

[4] B. M. McCoy, E. Barouch, and D. B. Abraham, Phys. Rev. **A4**, 2331 (1971).

[5] J. Lajzerowicz and P. Pfeuty, Phys. Rev. **B11**, 4560 (1975).

[6] J. H. H. Perk, H. W. Capel, G. R. W. Quispel, and F. W. Nijhoff, Physica **A123**, 1 (1984).

[7] G. Müller and R. E. Shrock, Phys. Rev. **B29**, 288 (1984).

[8] A. R. Its, A. G. Izergin, V. E. Korepin, and N. A. Slavnov, Phys. Rev. Lett. **70**, 1704 (1993).

[9] J. Stolze, A. Nöppert, and G. Müller, Phys. Rev. **B52**, 4319 (1995).

[10] O. Derzhko and T. Krokhmalskii, Ferroelectrics **153**, 55 (1996).

[11] O. Derzhko, T. Krokhmalskii, and T. Verkholyak, JMMM **157–158**, 421 (1996).

[12] J. A. Plascak, A. S. T. Pires, and F. C. Sá Barreto, Solid State Commun. **44**, 787 (1982).

[13] S. Wataral and T. Matsubara, J. Phys. Soc. Jpn. **53**, 3648 (1984).

[14] J. Knoster, J. Chem. Phys. **99**, 8466 (1993).

[15] H. Suzuura, T. Tokihiro, and Y. Ohta, Phys. Rev. **B49**, 4344 (1994).

Emission Mössbauer study of CMR manganite La$_{0.8}$Ca$_{0.2}$MnO$_3$. I. Anomalous ferromagnetism

V. Chechersky and A. Nath

Department of Chemistry, Drexel University, Philadelphia, PA 19104, U.S.A.

H. Ju and R. L. Greene

Center for Superconductivity Research, Department of Physics, University of Maryland, College Park, Maryland 20742, U.S.A.

Using ^{57}Co emission Mössbauer technique, we present clear evidence that in Ca-doped manganite, the magnetic and paramagnetic phases coexist below T_C, with the abundance of the latter increasing with temperature. In contrast with the regular ferromagnetic materials, the variation of the hyperfine internal magnetic field H_{int} with temperature deviates considerably from the Brillouin relation, and exhibits an abrupt drop at T_C. These features characterize the magnetic transition as a first-order transition. The non-Brillouin behavior of $H_{int}(T)$ and the temperature dependence of the shape of the magnetically split sextet indicate the presence of spin fluctuations in this material well below T_C. © *1997 American Institute of Physics.* [S1063-777X(97)00707-X]

Recent observations of colossal negative magnetoresistance (CMR) in thin films and bulk materials of doped manganites Ln$_{1-x}$M$_x$MnO$_3$ (Ln=La *et al.*, M=Ca *et al.*) have generated renewed interest in this system.[1–15] The double-exchange model accounts only qualitatively for ferromagnetic ordering and transport properties.[9,16–19] Ln$_{1-x}$M$_x$MnO$_3$ has a perovskite-type crystal structure, where Mn ions are surrounded by six oxygen anions which are shared by other Mn ions in a three-dimensional network, while the Ln/M ions occupy the spaces between these octahedra. The end members, $x = 0$ and $x = 1$, are antiferromagnetic insulators, but intermediate compositions ($0.2 < x < 0.5$) with mixed Mn^{3+}/Mn^{4+} are ferromagnetic metals. The electron hopping between Mn^{3+} and Mn^{4+} is believed to occur via O^{2-} by simultaneous electron jump from Mn^{3+} to O^{2-} and from the latter to Mn^{4+}. This "double exchange" event requires that the two hopping electrons have the same spin polarization: a requirement which is met when both Mn ions are ferromagnetically ordered.[16–19] Among the four $3d$ electrons of the Mn, t_{2g}^3 electrons are localized, while the e_g^{1-x} state which is strongly hybridized with O$_{2p}$ orbitals is itinerant below T_C in the ferromagnetic–metallic state and localized in the paramagnetic–insulating state above T_C. It is believed that the main function of the applied magnetic field is to increase T_C, which leads to a large decrease in resistivity, giving rise to a CMR. The basic features of this transition can be understood on the basis of the double exchange picture; however, several aspects are elusive.[9] Here we report on the unusual behavior of ferromagnetism in La$_{0.80}$Ca$_{0.20}$Mn(^{57}Co)O$_3$ as sensed by the Mössbauer effect probe involving substitution of a minuscule amount of Mn by ^{57}Co with minimal perturbation of the system.

The compound was synthesized by conventional solid state reactions and characterized by x-ray diffraction and magnetization measurements as a function of temperature. To obtain Mössbauer data, we substituted about 20 ppm of ^{57}Co for Mn in a compacted pellet of La$_{0.80}$Ca$_{0.20}$MnO$_3$, by diffusion at 950 °C for 4–5 h under O$_2$ flow (sample 1, T_C = 200 K). A few representative Mössbauer spectra of La$_{0.80}$Ca$_{0.20}$Mn(^{57}Co)O$_3$ at different temperatures are shown in Fig. 1. The observation of a single symmetrical sextet with fairly narrow line widths at 80 K indicates that the sample is homogeneous, and that the microprobe ^{57}Co occupies the unique crystallographic site of Mn. Even at 80 K, which is well below T_C = 200 K (T/T_C = 0.4), the magnetically ordered (MO) sixline component constitutes only 80%, the rest is paramagnetically relaxed (PR) species. The paramagnetic fraction grows at the expense of the magnetically ordered phase as the temperature increases until the MO component vanishes completely at T_C (Figs. 1 and 2). It is worthy of note that the temperature dependence of the amount of paramagnetic fraction in Fig. 2 perfectly mimics the resistivity behavior below T_C. These observations support the inferences drawn by Lynn *et al.* from their neutron scattering studies of La$_{0.67}$Ca$_{0.33}$MnO$_3$.[20] They observed a quasielastic component, which increases with temperature at the expense of the main spin-wave excitations. They assumed that this component can be attributed to a paramagnetic phase, where the electrons diffuse on a short length scale ($\sim$ 12 Å). However, this component was not observed for manganites with lower concentrations of Ca, e.g., 0.175.

The magnetic transition, as evidenced by the temperature dependence of the hyperfine internal magnetic field on the daughter ^{57}Fe nuclei, is quite sharp: the hyperfine splitting drops abruptly from about 50% of the maximum expected saturation value ($\leqslant$ 550 kOe) to zero at T_C = 200 K (Fig. 3). This feature and the coexistence of the paramagnetic and ferromagnetic species near T_C characterize this transition as a first-order phase transition.[21] The order of the transition is also supported by earlier reports of a significant change in volume at T_C.[22–25] It should be noted that a sharp transition is also expected in an ideal superparamagnetic material with
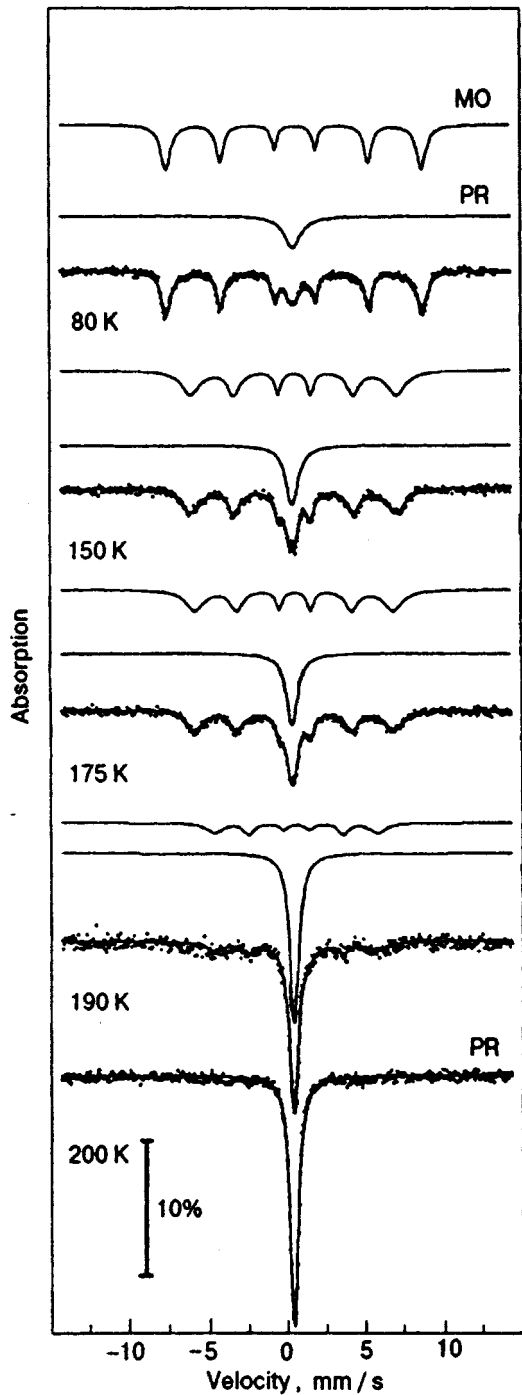
FIG. 1. Emission Mössbauer spectra of $La_{0.8}Ca_{0.2}Mn(^{57}Co)O_3$ at different temperatures: magnetically ordered (MO); paramagnetically relaxed (PR).
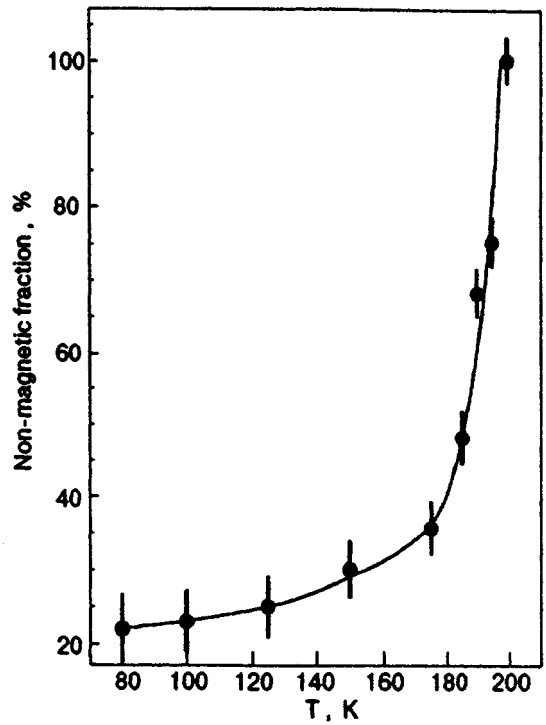

FIG. 2. The fraction of nonmagnetic component versus temperature. Line connecting experimental points with error bars is a guide for the eye.

1 reveal a temperature-dependent broadening of the line widths of the magnetic component. These two different observations presumably have the same origin. In a regular
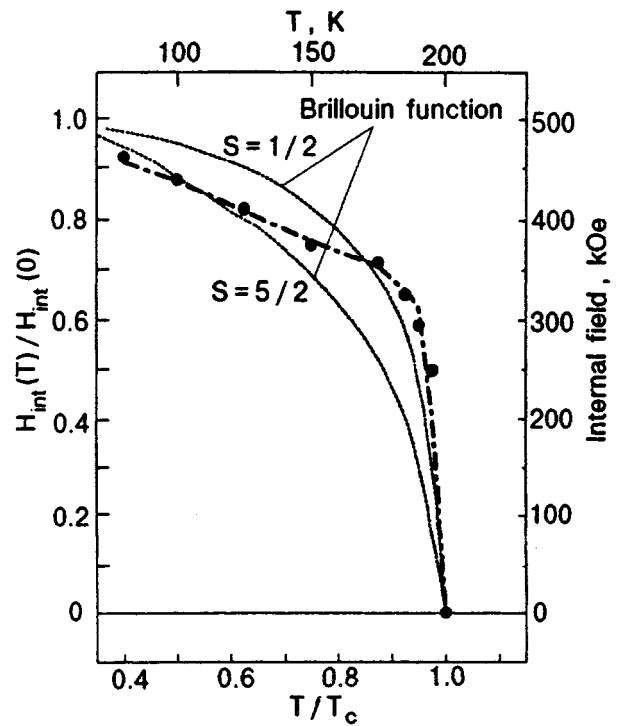
no spread in the sizes of magnetic clusters when it approaches its blocking temperature. However, we did not find any reliable evidence for superparamagnetism from our observations. Moreover, the value of T_C obtained from the magnetization and Mössbauer effect measurements agrees well.

The temperature dependence of the H_{int} on ^{57}Fe nuclei shows no saturation well below T_C and differs considerably from the Brillouin function typical of magnetic materials (Fig. 3). In addition, the experimental spectra shown in Fig.

FIG. 3. The normalized internal magnetic field versus normalized temperature. Solid line connecting experimental points is a guide for the eye; dotted lines are the Brillouin functions for the spin 1/2 and 5/2. The error bars are smaller than the dimension of the circles.

magnetically ordered material, the shape of the sextet is temperature-independent because the frequency of collective excitations is much higher than the Larmor frequency of the daughter ^{57}Fe ($\sim 10^8$ s^{-1}). Therefore, the Zeeman splitting (H_{int}) of the sextet is proportional to the time averaged z-component of the magnetic moment of an ion, $\langle S_z \rangle$, and mimics the temperature dependence of the spontaneous magnetization, i.e., the Brillouin function. In contrast, in the Ca-doped manganites, the heterogeneous distribution and the ionic radius mismatch of the substituent unavoidably introduce some disorder in the spin system. At any temperature below T_C, a certain fraction of the spin system is weakly ordered (and predestined to convert to paramagnetic component at a slightly higher temperature) and is likely to be surrounded by some paramagnetic ions in the vicinity. In these regions, due to dipole-dipole interactions, the weakly ferromagnetic spins fluctuate about the average value. Consequently, the z-component of the spins becomes time dependent, $S_z(t) = \langle S_z \rangle + \Delta S_z(t)$, where $\Delta S_z(t)$ is the instantaneous spin deviation from the mean value $\langle S_z \rangle$. This in turn induces a time-dependent hyperfine internal magnetic field $H_{int}(t) = \langle H_{int} \rangle (S_z(t)/S)$. The theory (Ref. 26 and the bibliography cited there) predicts two effects, inhomogeneous line broadening:

$$\Delta \gamma = (\nu_{eg} H_{int}/S)^2 \langle \Delta S_z \rangle^2 \tau; \qquad (1)$$

and line shifts relative to their positions in the absence of electronic spin fluctuations:

$$\Delta \delta = (\nu_{eg} H_{int}/S)^3 \langle \Delta S_z \rangle^3 \tau^2, \qquad (2)$$

where ν_{eg} is the magnetic hyperfine parameter; τ is the relaxation time, which is not exactly the same in (1) and (2), but assumed to be equal for the sake of simplicity. If the time of spin relaxation overlaps with the Mössbauer effect time scale ($\sim 10^{-7}$–10^{-11} s), we observe the temperature-dependent line shape. The temperature dependence of H_{int} does not reflect the true macroscopic magnetization as it arises mainly from the temperature-dependent value of $\langle \Delta S_z \rangle$.

Moreover, as the conversion of the ferromagnetic to paramagnetic species progresses with temperature, it is accompanied by a change in the Mn^{4+}/Mn^{3+} ratio (see the discussion in Part II) and thereby the internal magnetic field.

In sharp contrast with the paramagnetic spectra which consist of two unresolved doublets (Fig. 4a), the magnetically ordered component consists of only a single sextet (Figs. 1 and 4b) with an isomer shift (IS) intermediate between the values obtained for this temperature by extrapolating the IS vs. T plots for PR$_1$ and PR$_2$ species. It means that the transition into the magnetically ordered state is accompanied by a complete delocalization of holes in the band, which makes all the magnetically ordered iron atoms indistinguishable in the Mössbauer spectrum, regardless of their initial valence state in the lattice above T_C.

Preliminary results show that an external magnetic field of only 0.6 T applied at $T_C = 200$ K generates about 40% of the magnetically ordered phase with an internal magnetic

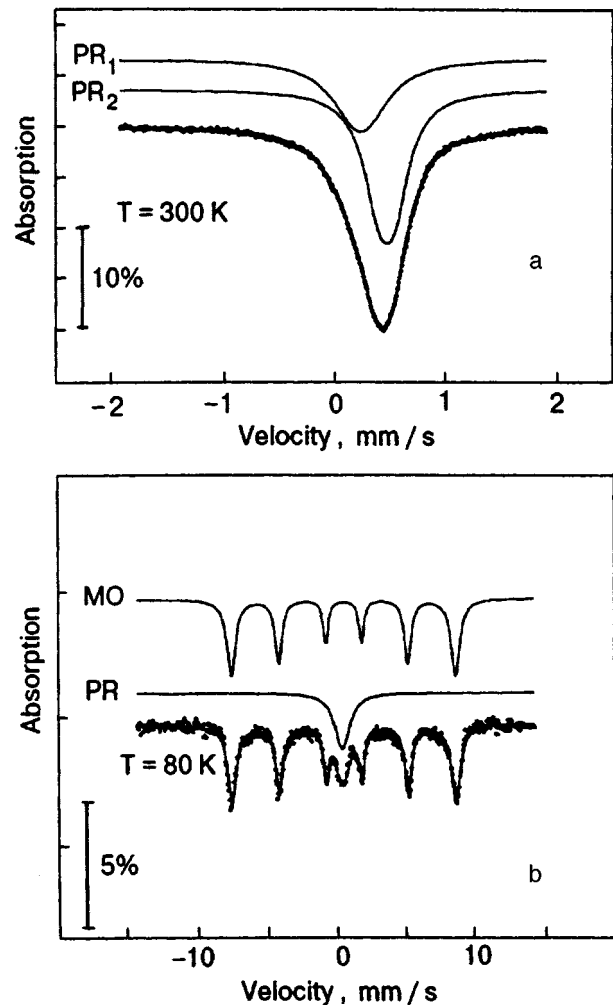FIG. 4. Computer fit of the Mössbauer spectra of La$_{0.8}$Ca$_{0.2}$Mn(^{57}Co)O$_3$ at $T = 300$ K (a); and 80 K (b). PR$_1$ and PR$_2$ are the two paramagnetic doublets; PR=PR$_1$+PR$_2$ (paramagnetic fraction in all the spectra collected in the wide velocity range was approximated by a single line without loss of the accuracy); MO is magnetically ordered component.

field of 64 kOe (Fig. 5). This ferromagnetic phase is metallic, as indicated by the isomer shift and by a decrease of about 25% in the resistivity of the sample.

The small magnitudes of quadrupole splittings even above T_C represent a relatively small degree of Jahn–Teller distortion of the oxygen octahedron in La$_{0.8}$Ca$_{0.2}$MnO$_3$. However, it is possible that we might be observing the mean value of the dynamic Jahn–Teller distortions.

In summary, we find that in contrast with normal ferromagnets, La$_{0.8}$Ca$_{0.2}$MnO$_3$ consists of a mixture of paramagnetic and ferromagnetic regions within the same matrix below T_C, and the fraction of the paramagnetic component increases with temperature. Also, the temperature dependence of the internal hyperfine field does not follow the Brillouin function. This circumstance, together with the temperature-dependent line widths of the magnetic component, is evidence of the presence of spin relaxation processes well below T_C. These two aspects directly bear on the magnetic and transport behavior and the CMR of doped manganites, and should be taken into account in any theoretical
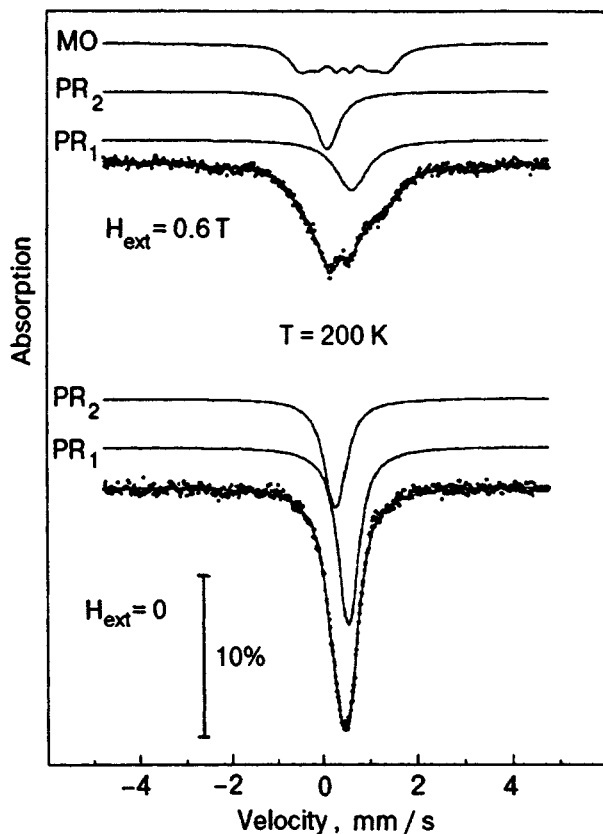
FIG. 5. Decomposition of Mössbauer spectrum of $La_{0.8}Ca_{0.2}Mn(^{57}Co)O_3$ at $T \approx T_C$ with and without external magnetic field. Abundance of magnetically ordered component (MO) is 40%. PR_1 and PR_2 are the two paramagnetic doublets.

model attempting to explain these effects. An abrupt fall of the hyperfine magnetic field at T_C and the coexistence of the paramagnetic and ferromagnetic regions characterize this transition as a first-order phase transition. We also present a microscopic evidence of the hole delocalization induced by ferromagnetic ordering.

ACKNOWLEDGMENTS

[1] R. M. Kusters, J. Singleton, D. A. Keen, R. McGreevy, and W. Hayes, Physica **B155**, 362 (1989).
[2] K. Chahara, T. Ohno, M. Kasal, and Y. Kozono, Appl. Phys. Lett. **63**, 1990 (1993).
[3] R. von Helmolt, J. Wecker, B. Holzapfel, L. Schultz, and K. Samwer, Phys. Rev. Lett. **71**, 2331 (1993).
[4] S. Jin, T. H. Tiefel, M. McCormack, R. A. Fastnacht, R. Ramesh, and L. H. Chen, Science **264**, 413 (1994).
[5] H. L. Ju, C. Kwon, Q. Li, R. L. Greene, and T. Venkatesan, Appl. Phys. Lett. **65**, 2108 (1994).
[6] R. Mahesh, R. Mahendiran, A. K. Raychaudhuri, and C. N. R. Rao, J. Solid State Chem. **114**, 297 (1995).
[7] B. Raveau, A. Maignan, and V. Caignaert, J. Solid State Chem. **117**, 424 (1995).
[8] H. Y. Hwang, S. W. Cheong, P. G. Radaelli, M. Marezio, and B. Batlogg, Phys. Rev. Lett. **75**, 914 (1995).
[9] A. J. Millis, P. B. Littlewood, and B. I. Shraiman, Phys. Rev. Lett. **74**, 5144 (1995).
[10] D. N. McIlroy, J. Zhang, S.-H. Liou, and P. A. Dowben, Phys. Lett. **A207**, 367 (1995).
[11] S. E. Lofland, S. M. Bhagat, H. L. Ju, G. C. Xiong, T. Venkatesan, and R. L. Greene, Phys. Rev. **B52**, 15058 (1995).
[12] H. Kuwahara, Y. Tomloka, Y. Morimoto, A. Asamitsu, M. Kasal, R. Kumal, and Y. Tokura, Science **272**, 80 (1996).
[13] K. Khazeni, Y. X. Jia, Li Lu, V. H. Crespi, M. L. Cohen, and A. Zettl, Phys. Rev. Lett. **76**, 295 (1996).
[14] A. Maignan, Ch. Simon, V. Caignaert, and B. Raveau, Z. Phys. **B99**, 305 (1996).
[15] C. N. R. Rao and A. K. Cheetham, Science **272**, 369 (1996).
[16] C. Zener, Phys. Rev. **82**, 403 (1951).
[17] P. W. Anderson and H. Hasegawa, Phys. Rev. **100**, 675 (1955).
[18] J. B. Goodenough, Phys. Rev. **100**, 564 (1955).
[19] P.-G. de Gennes, Phys. Rev. **118**, 141 (1960).
[20] J. W. Lynn, R. W. Erwin, J. A. Borchers, Q. Huang, A. Santoro, J.-L. Peng, and Z. Y. Li, Phys. Rev. Lett. **76**, 4046 (1996).
[21] R. Wäpling, Hyperfine Inter. **47**, 251 (1989).
[22] M. R. Ibarra, P. A. Algarabel, C. Marquina, J. Blasco, and J. Garcia, Phys. Rev. Lett. **75**, 3541 (1995).
[23] P. G. Radaelli, D. E. Cox, M. Marezio, S.-W. Cheong, P. E. Schiffer, and A. P. Ramirez, Phys. Rev. Lett. **75**, 4488 (1995).
[24] V. Caignaert, E. Suard, A. Maignan, C. Simon, and B. Raveau, C. R. Acad. Sci. Paris **321**, 515 (1995).
[25] P. Dai, J. Zhang, H. A. Mook, S.-H. Liou, P. A. Dowben, and E. W. Plummer, Phys. Rev. **B54**, R3694 (1996).
[26] H. Wegener, in Proc. Int. Conf. on Mössbauer Spectroscopy, Krakow, 1975, A. Z. Hrynkiewicz and J. A. Sawicki (Eds.), Povielarnia AGH, Krakow (1976), p. 257.

This article was published in English in the original Russian journal. It was edited by S. J. Amoretty.

Emission Mössbauer study of CMR manganite $La_{0.8}Ca_{0.2}MnO_3$. II. Step-by-step snapshots of the metal-insulator transition

V. Chechersky, K. Nomura,* and A. Nath

Department of Chemistry, Drexel University, Philadelphia, PA 19104, U.S.A.

H. Ju** and R. L. Greene

Center for Superconductivity Research, Department of Physics, University of Maryland, College Park, MD 20742, U.S.A.

We follow the step-by-step progression of events while approaching the Curie temperature T_C from below using ^{57}Co substituent as a microprobe in an emission Mössbauer study combined with resistivity measurements. In the temperature range $0.33 < T/T_C \leqslant 1$, the material consists of a mixture of ferromagnetic and paramagnetic regions within the same matrix. An increase of the amount of paramagnetic fraction is accompanied by a decrease in electron delocalization in the ferromagnetic regions. At $T \geqslant T_C$, the electrons are localized to neighboring Mn^{4+}/Mn^{3+} pairs only, in about 46% of the paramagnetic species. The strength with which Mn atoms are bound to the neighbors also decreases progressively and rather steeply in the range $0.65 \leqslant T/T_C = 1$. Zero field resistivity, ρ_0, follows linearly with the amount of the paramagnetic phase in the range $0.65 \leqslant T/T_C \leqslant 1$ and still shows metal-like behavior up to $T/T_C = 1.03$. © *1997 American Institute of Physics.* [S1063-777X(97)00807-4]

Substitution of La^{3+} by Ca^{2+} converts antiferromagnetic insulator $LaMnO_3$ into the mixed valence Mn^{3+}/Mn^{4+} ferromagnetic metal which undergoes a transition to the paramagnetic semiconducting state at T_C. According to the double-exchange model,[1] the probability of electron hopping between Mn^{3+} and Mn^{4+} via O^{2-} is controlled by the relative orientation of neighboring Mn spins and is at a maximum when Mn ions are ordered ferromagnetically. This accounts qualitatively for the correlation between magnetic and transport properties in doped manganites. The ''colossal magnetorersistance'' (CMR) recently observed in this system[2–9] is the focus of considerable attention, because of the potential applications for devices and the challenge to fully understand the basic nature of the transition and the associated CMR. The decrease by several orders of magnitude of the resistivity in a few-tesla magnetic field near T_C suggests that there is a healthy interplay between magnetic order, electronic behavior, lattice distortions, and elastic properties of the material. In a search for these correlations the simultaneous macro- and microscopic measurements performed on the same sample would be very valuable. Emission Mössbauer spectroscopy offers such a unique possibility.

Here we report the results of an emission Mössbauer effect study, where only a few tens of parts-per-million of Mn is substituted by ^{57}Co with minimal perturbation of the manganite system, in conjuction with simultaneous resistivity measurements. We follow the progressive enrichment of the ferromagnetic component in Mn^{4+} with decreasing electron delocalization as we approach the T_C from ferromagnetic component in Mn^{4+} with decreasing electron delocalization as we approach the T_C from below. This is accompanied by a sharp decrease in the binding of the Mn to its neighbors. To obtain Mössbauer data, we diffused a

couple of millicuries of carrier-free ^{57}Co into a compacted pellet of $La_{0.8}Ca_{0.2}MnO_3$ (sample 2, $T_C = 237$ K) measuring $2.5 \times 2.7 \times 12$ mm by a two-step thermal treatment, viz., at 950 °C for 4–5 h followed by 6 h at 900 °C, both under O_2 flow. A gas flow cryostat was modified to allow the four-probe resistivity measurements while collecting Mössbauer data.

The material was prepared by conventional solid state reaction and characterized by x-ray diffraction and magnetization measurements.

The temperature-dependent resistivity plot and Mössbauer spectra of $La_{0.8}Ca_{0.2}Mn(^{57}Co)O_3$ at corresponding temperatures are shown in Fig. 1. The six-line spectrum is characteristic of a magnetically ordered material, while a singlet or doublet (in the case of nonzero electric field gradient at the lattice site occupied by ^{57}Co) are an indication of a paramagnetic state. We found that even at $T/T_C = 0.33$ (not shown), the sample contains only 90% of magnetic fraction, the rest is paramagnetic. The presence of only a single symmetrical sextet with relatively narrow line widths (similar to the one shown in Part I of this paper for sample I Fig. 4b) shows that the sample consists of a single phase, and that the microprobe, ^{57}Co, occupies the unique crystallographic site of Mn. The ferromagnetic component converts into the paramagnetic state rather gradually up to $T/T_C \approx 0.85$. Thereafter, there is a rapid increase in the concentration of the paramagnetic component until it becomes 100% at $T_C = 237$ K. The coexistence of ferromagnetic and paramagnetic regions within the same matrix distinguishes it from conventional ferromagnetic materials[10] and could be responsible for its peculiar transport and magnetic properties. For instance, a plot of the resistivity as a function of the amount of ferromagnetic fraction in the temperature range $0.65 \leqslant T/T_C \leqslant 1$ is linear (Fig. 2). It means that the current flows exclusively
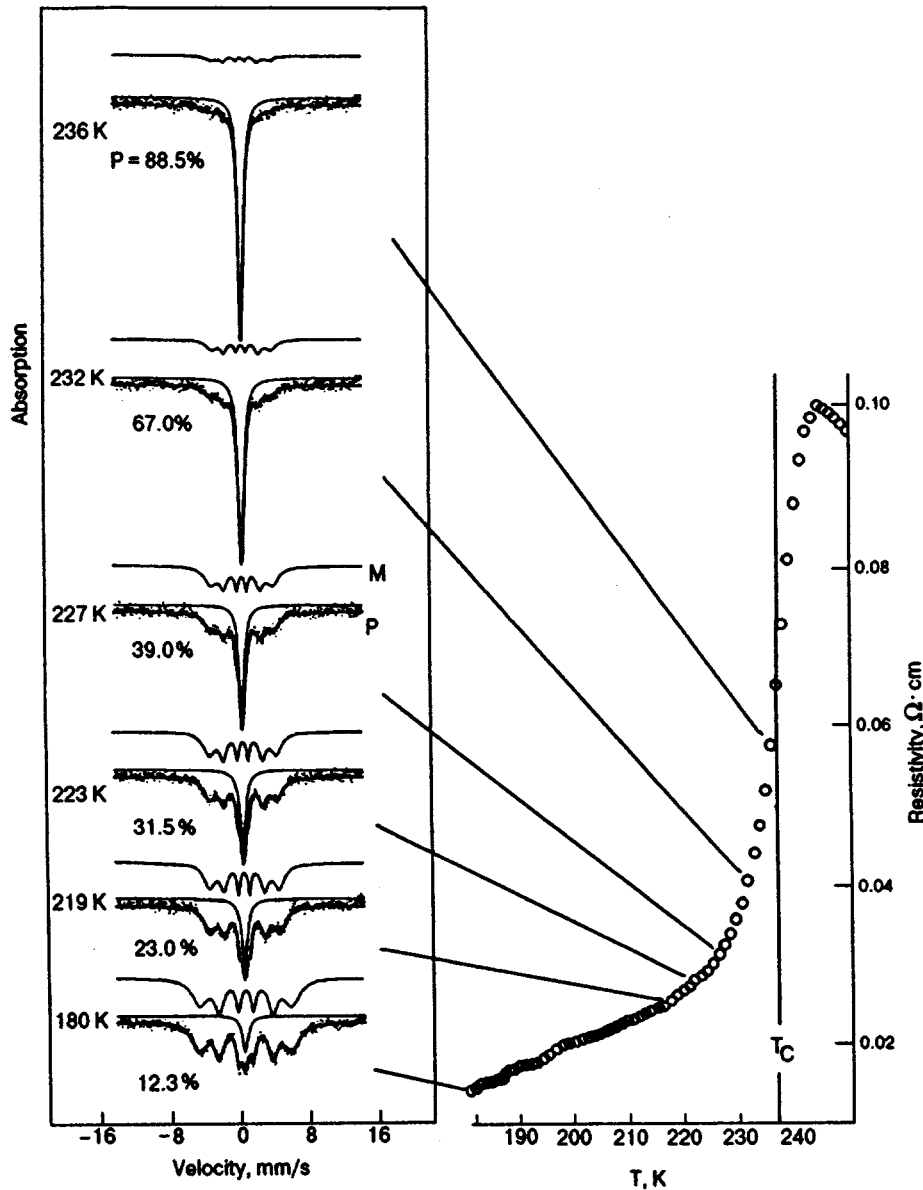
FIG. 1. The extent of ferromagnetic to paramagnetic state conversion and the change of resistivity in $La_{0.8}Ca_{0.2}Mn(^{57}Co)O_3$ as a function of temperature: P, paramagnetic component; M, ferromagnetic component. For simplicity, the two paramagnetic species (see text) have been approximated to a singlet without loss in accuracy in the computer analyses of Mössbauer spectra recorded in a wide velocity range.

through filamentary ferromagnetic regions surrounded by paramagnetic inclusions in accord with the recently proposed model.[11] The paramagnetic phase present below T_C may be a major source of carrier scattering from $T/T_C \approx 0.6$ to T_C.

The Curie temperature as determined by the Mössbauer effect, i.e., the temperature at which the sextet collapses completely, just corresponds to the maximum of the derivative $d\rho_0/dT$. It is noteworthy that the change from metal-like conductivity to the thermally activated behavior is above the transition into the paramagnetic state by 7 K (Fig. 1). One can perhaps rationalize this observation in the following fashion. At T_C, the static magnetic order as seen by Mössbauer effect measurements vanishes. However, the temperature-dependent line shapes (i.e., broadening) of the sextet below T_C (Fig. 1) are indicative of the presence of some dynamic magnetic correlations in quasistatic magnetic

regions. Correlation between these spin fluctuations could persist above T_C (with frequencies higher than about 10^{11} s^{-1}, which are above the limit of Mössbauer effect time scale), which would permit the probability of double exchange to be nonzero. This would account for the metallic behavior up to $T/T_C = 1.03$. The noncoincidence of T_C and maximum of the resistivity has been reported by several researchers.

We also observe a decrease in the magnitude of the chemical shift of the ferromagnetic species as a function of temperature (Fig. 3). The chemical shift is determined by the s-electron density on the daughter nucleus ^{57}Fe, which in turn is determined primarily by the shielding from $3d$-electron density—the higher the shielding the smaller will be the s-electron density and larger the magnitude of the chemical shift. Taking into account the expected negative
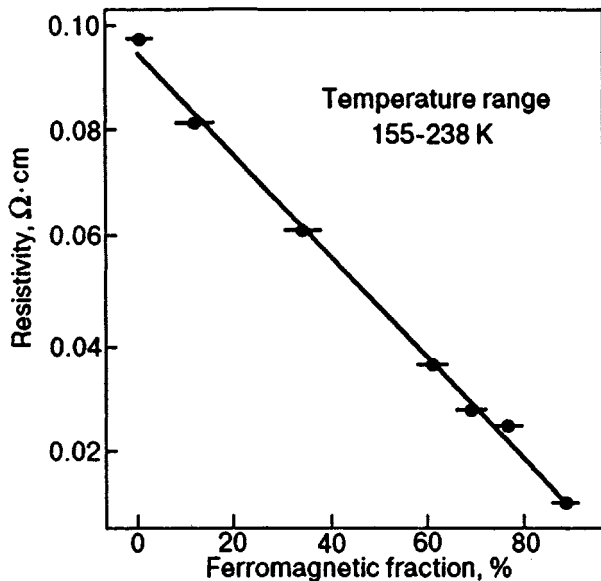
FIG. 2. A plot of resistivity versus ferromagnetic fraction in the temperature range $0.65 \leqslant T/T_C \leqslant 1$.

thermal shift with increasing temperature due to the second-order Doppler effect,[12] the chemical shift (δ) for the ferromagnetic component clearly undergoes a very sharp anomalous decrease in the range $0.65 \leqslant T/T_C = 1$ (Fig. 3). This observation is very insightful. The ferromagnetic species is progressively getting enriched in Mn^{4+} (Fe^{4+}). One can infer that the Mn^{4+} ions are sharing the delocalized electrons with progressively fewer Mn^{3+} as T_C is approached.

The paramagnetic component above T_C consists of two species (Fig. 4) with the following parameters at room tem-
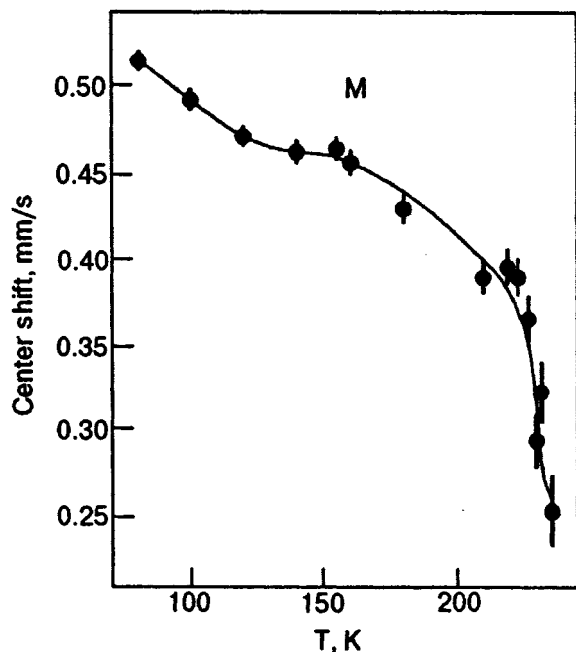
FIG. 3. A plot of the center (chemical) shift of ferromagnetic (M) species versus temperature for $La_{0.8}Ca_{0.2}Mn(^{57}Co)O_3$. The solid line is a guide for the eyes.

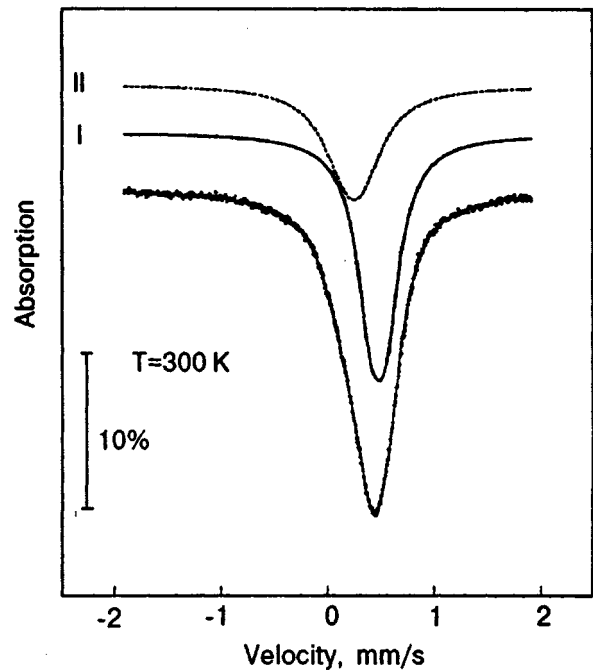
FIG. 4. Decomposition of Mössbauer spectrum of $La_{0.8}Ca_{0.2}Mn(^{57}Co)O_3$ in paramagnetic state. Species I and II correspond to two different valence states of the daughter ^{57}Fe (see text).

perature. Species I. $\delta = 0.44$ mm/s, Area $= 54\%$; Species II. $\delta = 0.21$ mm/s, Area $= 46\%$. The chemical shift for species I corresponds to the daughter $^{57}Fe^{3+}$ (at Mn^{3+}), while that for species II corresponds approximately half-way between that for $^{57}Fe^{3+}$ and $^{57}Fe^{4+}$, assuming $\delta \approx 0$ for $^{57}Fe^{4+}$ at 300 K.[13] Therefore, in the paramagnetic state, 46% of material consist of Mn^{3+}/Mn^{4+} pairs with the electron shuttling between a pair, while in the remaining 54% of the material there is no delocalization of electrons and the species contains only Mn^{3+}. The observation of 46% Mn^{4+}/Mn^{3+} pairs by emission Mössbauer spectroscopy translates to the presence of 23% of Mn^{4+} because $^{57}Co(^{57}Fe)$, which is situated in a Mn^{3+} site and shares an electron with a Mn^{4+} neighbor, cannot be distinguished from a $^{57}Co(^{57}Fe)$, which is situated in a Mn^{4+} site and shares an electron with a Mn^{3+} neighbor if the exchange rate is faster than the reciprocal lifetime of the excited state of the Mössbauer probe (10^7 s^{-1}). This also constitutes an elegant procedure for determining the concentration of holes in manganites. Since 20% units of Mn^{4+} arise from Ca substitution, the remaining presumably arise from cation vacancies created by thermal treatment in ambient O_2.[14] We attribute the localization of the electrons in Mn^{3+}/Mn^{4+} pairs to the distortions of the Mn–O octahedra with respect to each other, which introduces asymmetry. Our observations support the small polaron model[10,15–20] in the sense that the electrons are strictly localized between Mn^{4+}/Mn^{3+} pairs above T_C.

The normalized total area under the spectrum is plotted as a function of temperature in Fig 5. The area of the spectrum represents the recoil-free Mössbauer events and is thus a measure of the strength with which Mn is bound to its neighbors (i.e., the Debye–Waller factor). There is a dra-
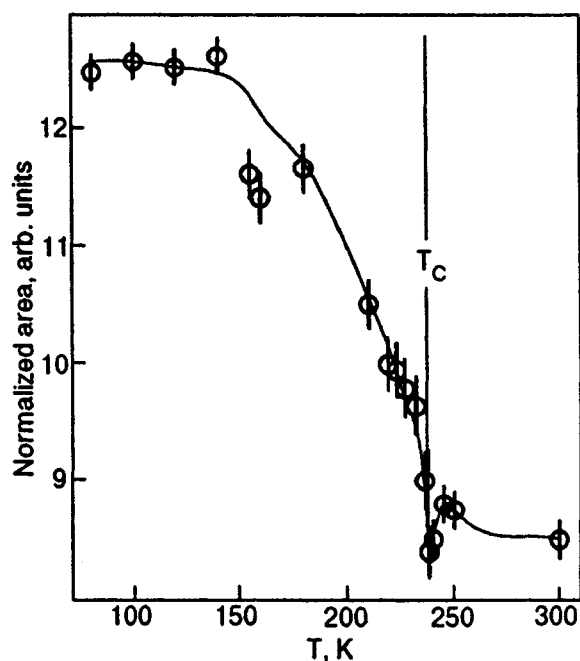
FIG. 5. A plot of normalized area under the Mössbauer spectrum as a function of temperature. The solid line is a guide for the eyes.

matic reduction of the area in the range $0.65 \leqslant T/T_C = 1$ and a minimum is attained at T_C. This clearly indicates that the amplitude of vibration for Mn is fairly large near T_C. This can again arise from torsional oscillations between Mn–O octahedra. The ferro-magnetic metal to paramagnetic insulator transition is accompanied by significant expansion ($\approx 13\%$) of the lattice.[21–24] An anomalously large amplitude of vibration for Mn (and O) atoms around T_C has been reported in Refs. 18, 24, and 25 which was predicted earlier elsewhere.[20]

The conversion to the paramagnetic state, anomalous changes in chemical shift of the ferromagnetic component, and a decrease in the total area of the spectrum, take place continuously in a wide temperature range and not precipitously at a well-defined transition temperature. The decrease in density of states as determined by photoemission studies[16,26] and density of holes by the Hall effect[27] for the La–Ca–Mn–O system also show a similar progressive change over a span of temperatures. Perhaps these observations are indicative of the first-order phase transition and/or the intrinsically heterogeneous nature of the doped oxide systems (a property shared by the high-temperature super-conductors).

We observe almost zero quadrupole splitting for the ferromagnetic state and small values ($\leqslant 0.15$ mm/s) for the two paramagnetic species. The magnitude of quadrupole splitting depends on the degree of deviation from spherical distribution of the electron cloud (viz., electric field gradient) around ^{57}Fe nucleus. Therefore, one would expect that the Mn–O bond lengths should be nearly equal in the ferromagnetic state. This rules out only the static Jahn–Teller distortions and not the dynamic ones.[19,28] On the other hand, the non-zero quadrupole splittings (about 0.15 mm/s) for both of the paramagnetic species are indicative of the fact that the

Mn–O bond lengths are unequal. It is presumably due to a small Jahn–Teller distortion, static or dynamic.[15,18,20,29] More importantly, the Mn–O bond lengths would differ for each of the paramagnetic species because of differing Mn valence. This was borne out by the powder neutron diffraction studies of Caignaert et al.[23] and Dai et al.[24] They observed that the Mn–O bond lengths are nearly equal below T_C, and that there is a distribution of bond lengths in the paramagnetic state. These observations are contrary to those made by Radaelli et al.[22]

In summary, moving along the $\rho_0(T)$ plot and collecting Mössbauer spectra at specified temperatures, we obtain an insight into the microscopic nature of some transport and magnetic properties of the La–Ca–Mn–O system. The presence of paramagnetic regions far below T_C is believed to be a major source of carrier scattering from $T/T_C \approx 0.6$ to T_C. Noncoincidence of T_C and the peak of $\rho_0(T)$ can be attributed to the spatial correlations of the spin fluctuations in a narrow temperature range above T_C. We also get a good measure of the different stages of the transition, starting with completely delocalized electrons in the ferromagnetic phase with Mn^{3+}/Mn^{4+} ratio of about 3.5. As T approaches T_C from below, the ferromagnetic phase is continually enriched in Mn^{4+} with decreasing extent of electron delocalization. Finally, at $T \gtrsim T_C$, the electrons are localized to neighboring Mn^{4+}/Mn^{3+} pairs only, in a considerable portion of the paramagnetic species. We also found a minimum of recoil-free fraction at T_C. The Mn atoms are undergoing larger mean-square displacements in the paramagnetic phase.

*Permanent address: Graduate School of Engineering, The University of Tokyo, Hongo 7-3-1, Bunkuo-ku, Tokyo 113.
**Present address: Lawrence Berkeley Laboratory, National Center for Electron Microscopy, Berkeley, CA 94720.

[1] C. Zener, Phys. Rev. **82**, 403 (1951); P. W. Anderson and H. Hasegawa, Phys. Rev. **100**, 675 (1955); J. B. Goodenough, Phys. Rev. **100**, 564 (1955); P.-G. de Gennes, Phys. Rev. **118**, 141 (1960).

[2] R. M. Kusters, J. Slagleton, D. A. Keen, R. McGreevy, and W. Hayes, Physica **B155**, 362 (1989).

[3] R. von Helmholt, J. Wecker, B. Holzapfel, L. Schultz, and K. Samwer, Phys. Rev. Lett. **71**, 2331 (1993).

[4] K. Chahara, T. Ohno, M. Kasai, and Y. Kozono, Appl. Phys. Lett. **63**, 1990 (1993).

[5] S. Jin, T. H. Tiefel, M. McCormack, R. A. Fastnacht, R. Ramesh, and L. H. Chen, Science **264**, 413 (1994).

[6] H. L. Ju, C. Kwon, Q. Li, R. L. Greene, and T. Venkatesan, Appl. Phys. Lett. **65**, 2108 (1994).

[7] R. Mahesh, R. Mahendiran, A. K. Raychaudhuri, and C. N. R. Rao, J. Solid State Chem. **114**, 297 (1995).

[8] B. Raveau, A. Maignan, and V. Caignaert, J. Solid State Chem. **117**, 424 (1995).

[9] C. N. R. Rao and A. K. Cheetham, Science **272**, 369 (1996).

[10] J. W. Lynn, R. W. Erwin, J. A. Borchers, Q. Huang, and A. Santoro, Phys. Rev. Lett. **76**, 4046 (1996).

[11] G. C. Xiong, Q. Li, H. L. Ju, S. M. Bhagat, S. E. Lofland, R. L. Greene, and T. Venkatesan, Appl. Phys. Lett. **67**, 3031 (1995).

[12] *Chemical Application of Mössbauer Spectroscopy* V. I. Goldanskii and R. H. Herber (eds.), Academic Press, New York (1968).

[13] Y. Takeda, S. Naka, M. Takano, T. Shinjo, T. Takada, and M. Shimada, Mat. Res. Bull. **13**, 61 (1978).

[14] J. A. M. Van Roosmalen and E. H. P. Cordfunke, J. Solid State Chem. **110**, 106 (1994).

[15] A. J. Millis, P. R. Littlewood, and B. I. Shraiman, Phys. Rev. Lett. **74**, 5144 (1995).

[16] J.-H. Park, C. T. Chen, S.-W. Cheong, W. Bao, G. Meigs, V. Chakarian, and Y. U. Idzerda, Phys. Rev. Lett. **76**, 4215 (1996).

[17] T. A. Tyson, J. Mustre de Leon, S. D. Conradson, A. R. Bishop, J. J. Neumeier, H. Röder, and J. Zang, Phys. Rev. **B53**, 13985 (1996).

[18] S. J. L. Billinge, R. G. Di Francesco, G. H. Kwei, J. J. Neumeier, and J. D. Thompson, Phys. Rev. Lett. **77**, 715 (1996).

[19] G.-M. Zhao, K. Conder, H. Keller, and K. A. Müller, Nature **381**, 676 (1996).

[20] A. J. Millis, B. I. Shraiman, and R. Mueller, Phys. Rev. Lett. **77**, 175 (1996).

[21] M. R. Ibarra, P. A. Algarabel, C. Marquina, J. Blasco, and J. Garcia, Phys. Rev. Lett. **75**, 3541 (1995).

[22] P. G. Radaelli, D. E. Cox, M. Marezio, S.-W. Cheong, P. E. Schiffer, and A. P. Ramirez, Phys. Rev. Lett. **75**, 4488 (1995).

[23] V. Caignaert, E. Suard, A. Maignan, C. Simon, and B. Raveau, C. R. Acad. Sci. **321**, 515 (1995).

[24] P. Dai, J. Zhang, H. A. Mook, S.-H. Liou, P. A. Dowben, and E. W. Plummer, Phys. Rev. **B54**, R3694 (1996).

[25] C. H. Booth, F. Bridges, G. J. Snyder, and T. H. Geballe, Phys. Rev. **B54**, R15606 (1996).

[26] D. N. McIlroy, J. Zhang, S.-H. Liou, and P. A. Dowben, Phys. Lett. **A207**, 367 (1995).

[27] J. E. Nunez-Regueiro, D. Gupta, and A. M. Kadin, J. Appl. Phys. **79**, 5179 (1996).

[28] J.-S. Zhou, W. Archibald, and J. B. Goodenough, Nature **381**, 770 (1996).

[29] R. P. Sharma, G. C. Xiong, C. Kwon, R. Ramesh, R. L. Greene, and T. Venkatesan, Phys. Rev. **B54**, 10014 (1996).

This article was published in English in the original Russian journal. It was edited by S. J. Amoretty.

Metallic point contacts formed by physical vapor deposition and chemical vapor deposition: microscopy study and point-contact spectroscopy

N. N. Gribov,[1,2] J. Caro,[1] T. G. M. Oosterlaken,[1] and S. Radelaar[1]

[1]*Delft Institute of Microelectronics and Submicron Technology (DIMES), Delft University of Technology, Lorentzweg 1, 2628 CJ Delft, The Netherlands**

[2]*B. I. Verkin Institute of Low Temperature Physics and Engineering, Academy of Sciences of Ukraine, 47 Lenin Ave., Kharkov 310164, Ukraine**

We have made an electron-microscopy study of nanoholes in membranes in successive stages of metal deposition using two different techniques: physical vapor deposition (PVD) and chemical vapor deposition (CVD). One-sided PVD (thermal evaporation) of gold and silver was used, as is relevant for heterocontacts. The key results in this case are: 1) the holes are not filled during deposition and 2) closing of the holes is accomplished by lateral growth of the film on the membrane. In the case of CVD of tungsten we found that nanoholes in membranes are filled at the beginning of the deposition, and that the process is capable of filling holes as small as 10 nm. Fabricated devices (α-tungsten) show good quality point-contact spectra which are characteristic of ballistic transport through the constriction. A very interesting stepwise current increase was observed for one amorphous tungsten point contact. © *1997 American Institute of Physics.* [S1063-777X(97)00907-9]

1. INTRODUCTION

Very stable metallic point contacts (PC) can be made with nanofabrication techniques.[1,2] the contacts are made by metal deposition on both sides of a thin silicon nitride membrane with a hole of diameter in the range 10–30 nm. In this way the nanohole is filled with metal and the electrodes are formed. By using nanofabricated contacts as microscopes of electronic transport, several new, subtle phenomena have been discovered, e.g., two-level resistance fluctuations due to defect motion in the constriction[3,4] and nonuniversal conductance fluctuations involving electron scattering at remote defects.[5,6]

Until a few years ago, nanofabricated point contacts were almost exclusively fabricated as homocontacts, i.e., contacts made of the same (very pure) metal. Recently, however, devices of a more complex structure have also been fabricated and studied. Examples are heterocontacts,[7,8] contacts including magnetic multilayers[9] and tunneling contacts.[10] To interpret the electrical transport measurements on these devices and to judge further capabilities of the nanofabrication technique of point contacts, it is crucial to know how the actual contact is formed. About this matter virtually nothing is known, so that one can only guess about the structure and morphology of the constriction region.

In this paper we report an electron-microscopy study of the closing and/or filling of nanoholes in membranes in successive stages of metal deposition and we present the point-contact spectra of the fabricated devices. The deposition techniques used are physical vapor deposition (PVD) and chemical vapor deposition (CVD). Physical vapor deposition, in this case thermal evaporation of Au and Ag from a boat, is the usual technique used to form lithographic point contacts. Chemical vapor deposition is intensively applied in integrated circuit fabrication to deposit semiconductors, insulators, and conductors. Here we use CVD of W, which is well known from the filling of vias (i.e., contact channels to devices or lower-level metallization) in integrated circuits,[11] but which so far was not used to produce metallic point contacts. We combine the results of scanning electron microscopy (SEM) and transmission electron microscopy (TEM) with point-contact spectra of fabricated contacts, thus presenting the complete picture of contact formation and the resulting electrical properties.

2. ELECTRON MICROSCOPY STUDY

Microscopy samples were prepared by patterning arrays of holes. Each hole forms from single-pixel exposure with an e-beam writer of e-beam sensitive resist on a silicon nitride layer. After the resist development holes in resist are transferred to the nitride by etching in an SF_6/He plasma. Etching is stopped when the resist is completely consumed and the nitride thickness is about 25 nm. Depending on whether a sample is prepared for SEM or for TEM, the nitride layer either is initially supported by silicon across the whole area or is a membrane as used for real point contacts,[2] respectively. In the case of SEM samples we used arrays of 750 $\times$750 holes placed on an 80-nm period square grid. The large extent of this array facilitates breaking of the chip through a ''line of holes.'' The supporting Si is very helpful here, since it is the Si chip that we break along a proper line. In the case of TEM samples we used a 200-nm period array of 7$\times$5 holes in the membrane.
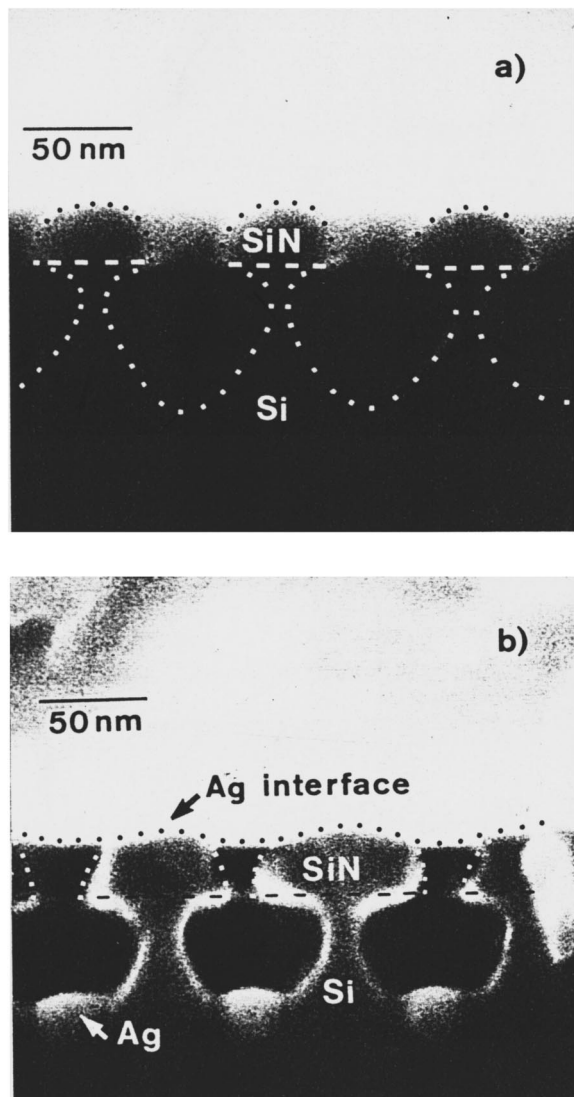
FIG. 1. SEM micrographs of the cross sections through a ''line of holes,'' before deposition (a) and after deposition of 200-nm Ag (b). The voids result from etching in the SF_6/He plasma. At the bottom of the voids in (b) some Ag is deposited. Small distrubances of the cross sections may exist as a result of breaking. Dots guide the eye in following interfaces/surfaces.

First, with the SEM inspection, we investigated how a hole is filled and/or covered during one-sided PVD of a 200-nm-thick Au or Ag layer, with the substrate oriented perpendicular to the evaporation beam. Before deposition, the substrate is cleaned *in situ* with an O_2 glow discharge. The chamber pressure, substrate temperature, and deposition rate are 5×10^{-7} Torr, 300 K, and 0.3–0.5 nm/s, respectively. The micrographs in Figs. 1a and 1b show the resulting cross sections. As can be seen, the nitride surrounding a hole is severely underetched. This results from the high isotropic etch rate of Si in the SF_6/He plasma. Effectively, each hole is in a (small) membrane, just like a hole of a real contact. The rounded profile of a hole arises from transferring the resist profile to the nitride and from subsequent over etching. The smallest diameter of a hole is 25 nm. The step coverage of the Ag film is very poor (see Fig. 1b: The film covers the hole, but does not fill it. This finding agrees with the fact that
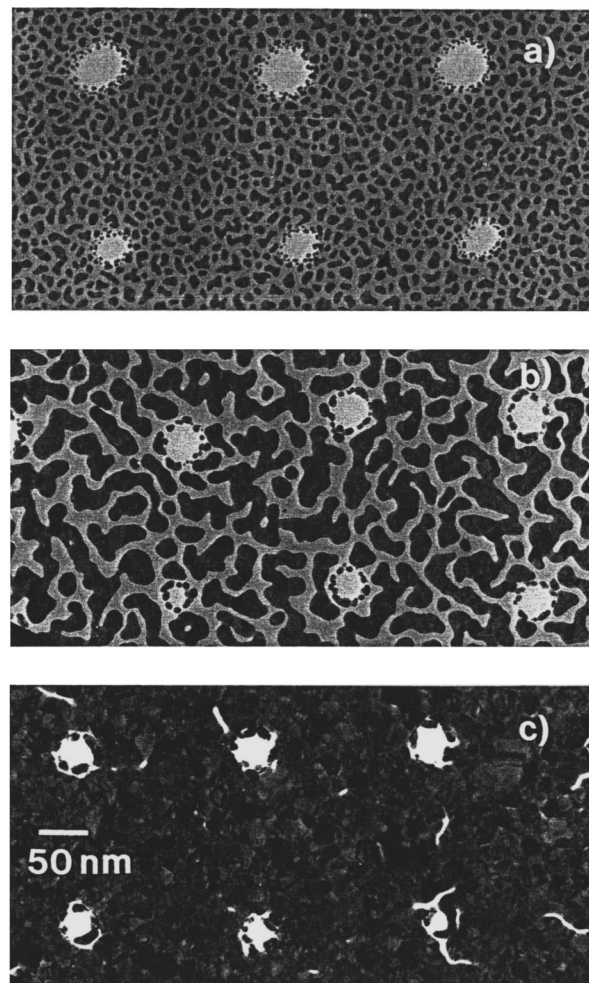

FIG. 2. TEM micrographs of membranes with holes after deposition of 2, 5, and 20-nm Au (a, b, and c, respectively). A necklace of small grains in the narrow part of the hole is discernible in (a) and (b). Closing of the hole is accomplished by lateral growth of the film. The bar marker in (c) is the same as in (a) and (b).

vias of microelectronic devices cannot be filled reliably with metal by PVD.[11] Inspection of the outer Ag surface revealed an array of shallow pits, which result from the missing material that has passed through the holes before closing. In the case of PVD of a 200-nm Au layer we made very similar observations.

As a further step we monitored with high-resolution TEM the growth of Au and Ag in successive stages of PVD on membranes with an array of holes of diameter in the range 30–70 nm. Figure 2 shows TEM micrographs in three stages of PVD of Au. From these micrographs and similar ones in other deposition stages we make the following observations.

1. In the initial stage of PVD ($\approx$2 nm on thickness monitor, i.e., 1.2×10^{16} atoms/cm^2; Fig. 2a grains on the unpatterned membrane parts and on the outer rounded wall of a hole have a certain density. However, a circular region close to the narrowest part of a hole is decorated with a necklace of smaller grains, which have a higher area density.

2. Grains on the membrane and on the rounded walls coalesce in a way characteristic of an amorphous substrate
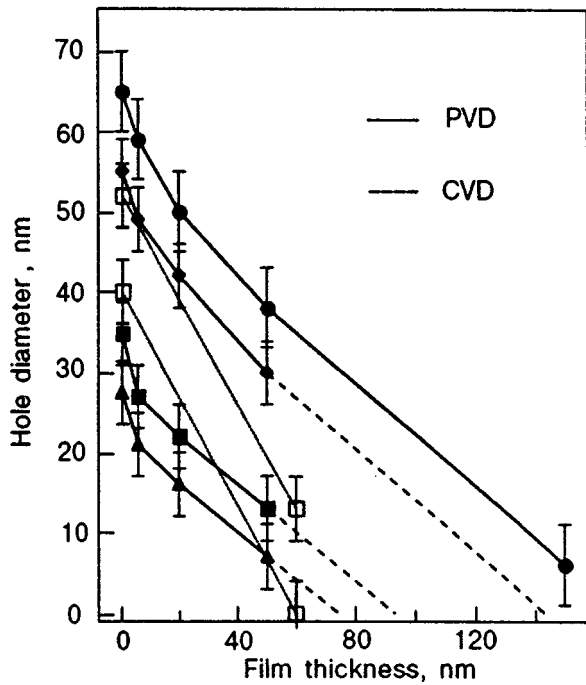
FIG. 3. Remaining hole size (average over membranes and directions) as a function of Au thickness deposited by PVD on one side of a membrane, for four initial hole diameters (filled symbols) and the corresponding dependences for CVD of W, for two initial hole diameters. Error bars result from differences between membranes and measurement directions. Dashed segments are extrapolations.
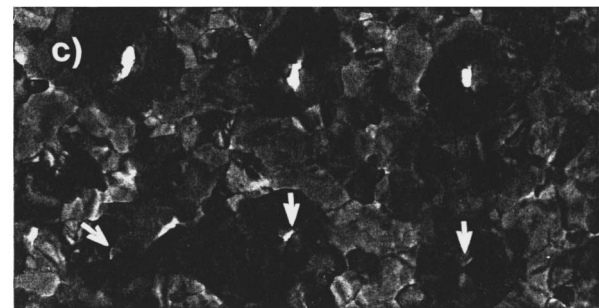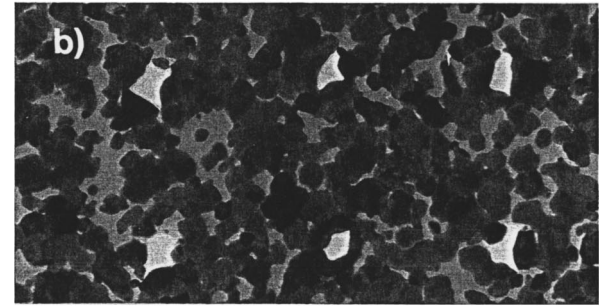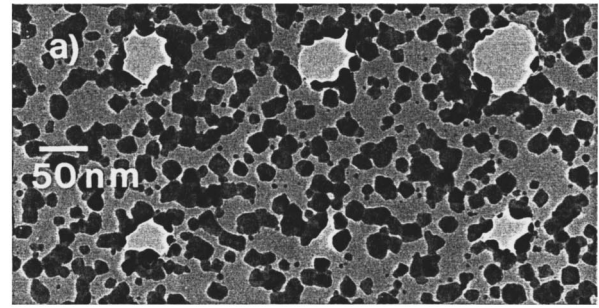

FIG. 4. TEM micrographs of membranes with holes after CVD of α-W during 30, 40, and 50 s (a, b, and c, respectively). The bar marker in (a) is the same as for (b) and (c). The arrows in (c) indicate the holes which are already closed.

(≈ 5 nm, i.e., 2.9×10^{16} atoms/cm^2; Fig. 2b. Since these grains grow faster than the necklace grains, they cannot coalesce with the regular grains in the broader area around a hole.

3. During the stage of formation of a closed polycrystalline film on the membrane (≈ 20 nm, i.e., 11.8×10^{16} atoms/cm^2; Fig. 2c closing of a hole occurs by lateral growth of the film. Also for these deposition experiments the observations for Au and Ag were very similar, even though the Ag exposures required to reach the stages of nucleus growth and grain coalescence are approximately twice those of Au.

On TEM micrographs we measured the remaining hole size after deposition of Au layers of different thicknesses. Figure 3 shows the resulting dependences. In the initial stage of deposition the size of the holes decreases very rapidly as a result of formation of the necklace. Further size decrease proceeds slowly. It can be seen that for an initial diameter of 30 nm one should deposit about 70-nm au to close the hole, i.e., a layer more than twice as thick as the hole diameter.

To investigate the capabilities of CVD to fill holes for point contacts, we also performed TEM analysis of membranes with holes onto which W was deposited by CVD. In particular, we deposited α-W (common bcc W), which we normally apply as interconnect material in microelectronic devices.[11] Depositions of α-W were carried out in a cold-wall, low-pressure CVD reactor by the reduction of WF$_6$ by H$_2$. Films deposited with this process have very good step coverage and a low resistivity. We used a 4″ quartz dummy wafer with slits to accommodate 6×9-mm^2 chips with eight

membranes. The slits were machined to leave open a 1-mm gap between the chips and the heater plate of the reactor, to give the reactants free access to the lower face of the membrane. A substrate cleaning step was not included, since we assumed that dry etching in SF$_6$/He plasma, which is stopped when the resist is consumed and the membranes are thinned to their final thickness, leaves a clean surface. The deposition parameters are $T = 500\,°C$ $p = 1$ Torr, 50 sccm WF$_6$, and 500 sccm H$_2$. The deposition times were 30, 40, 50, and 60 s (20 s appeared to be below the incubation time for nucleation).

In Fig. 4 we show TEM micrographs for deposition times 30, 40, and 50 s. In the initial stage [Fig. 4a] grains occur at the edge of and inside the holes. Holes are filled, therefore, at the outset of the deposition. This is in strong contrast with the above PVD results. Figure 4b shows the next stage, where filling of channels between regions of coalesced grains occurs and where grains and the smallest holes have approximately the same size. A substantial size decrease of some holes occurs already, although the film is not yet continuous. Again, this is in contrast with the results for PVD. The holes used here are much smaller than the struc-

556   Low Temp. Phys. **23** (7), July 1997
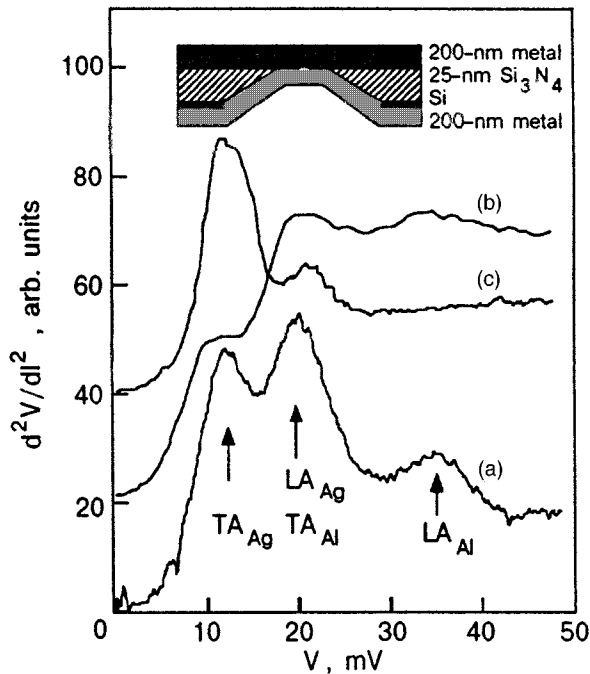
Gribov *et al.*   556

FIG. 5. PC spectra of the Ag/Al heterocontacts described in the text. For a 20-nm-thick Ag layer the phonon peaks from Al are absent. The contact diameters are in the range 10–25 nm. The inset shows a schematic cross section through a point contact.

tures presently filled with W in microelectronic industry.[12] Nevertheless, Figs. 4a and 4b indicate that very good step coverage develops. For a deposition time of 50 s [Fig. 4c, thickness ~60 nm, as measured with a surface profiler] the smallest holes are completely closed and the film seems continuous.

For the W depositions the film thickness was measured for a deposition time of 50 s. Nevertheless, this enables us to plot two more lines in Fig. 3, for two initial hole diameters. The considerably steeper slope of the lines for W beyond the range, where the necklace for PVD is formed, reflects the differences between PVD and CVD in the closing of a hole.

3. ELECTRICAL CHARACTERISTICS

Two different types of heterocontacts were made using PVD of Ag and Al as the final steps of our fabrication scheme.[2] Fabricated point contacts were characterized by measuring the point-contact spectrum $d^2V/dI^2(V)$ at the liquid-helium temperature. The spectra were nearly antisymmetric with respect to the bias-voltage polarity. It is known that in the case of ballistic electron transport through the contact (the elastic mean free path l_i of electrons is much larger than the contact size) $d^2V/dI^2(V)$ reflects the peculiarities of the phonon density of states of the metals that form the contact Figure 5 shows the PC spectra of PVD fabricated Ag/Al devices. For type-A heterocontacts (the cross section of the device is shown schematically in the inset in Fig. 5) after deposition of 200-nm Ag on side 1 of the membrane with a single nanohole, 200-nm Al was deposited on side 2. One can expect, taking into account the results in Fig. 1, that the Ag/Al interface for this type of heterocontacts is situated close to the center of the constric-

tion, and that the PC spectra should demonstrate the features of both metals. Indeed, as can be seen in Fig. 5a, the point-contact spectrum of a type-A device has clear phonon peaks of both Ag and Al. To move the interface Ag/Al away from the constriction, we fabricated type-B heterocontacts. For these contacts 200-nm Ag was deposited on side 1 of the membrane and a bilayer of 10-nm Ag/200-nm Al or 20-nm Ag/200-nm Al on side 2. In the case of 10-nm Ag the 35-mV peak of Al is still present in the spectrum (Fig. 5b), but is absent in case of 20-nm Ag. In the latter case the spectrum is that of pure Ag. Similar results were obtained for contacts with 200-nm, Al on side 1 and 20-nm Al/200-nm Ag on side 2. For these contacts the spectrum is that of pure Al. A possible explanation for this result is that geometry of our devices is between that of a clean orifice and a short channel. for the last geometry the spectral contribution from the regions outside the channel is reduced compared to that of the clean orifice model, most of the signal coming from the channel region. The results for the heterocontacts with a displaced interface seem to agree with this conclusion. However, the spectral intensities of our homogeneous contacts follow the theoretical relation for the clean orifice model,[4] which indicates that the degree of channel character is negligible. Therefore, since the thinner layer of the bilayer is comparable to the probing depth, this result remains unexplained.

From studies of metallization of vias in microelectronic devices it is known that the CVD method is capable of filling holes as small as 70 nm.[12] In order to further investigate the capabilities of W-CVD to fill much smaller holes we have fabricated α-W and amorphous W point contacts with a good yield of devices for electrical measurements. In the case of amorphous W we used the reduction of WF_6 by GeH_4 with the deposition parameters: $T = 300\ °C$, $p = 1$ Torr, 50 sccm WF_6, 50 sccm GeH_4, and 500 sccm H_2. In contrast to α-W, the films deposited by this process have a high resistivity as a result of relatively large concentration of incorporated germanium. The film thickness (per side) was about 350 nm for α-W and 175 nm for amorphous W.

Figure 6 shows a point-contact spectrum of an α-W device of resistance $R = 45.6\ \Omega$. The contact diameter is $d = 10$ nm (estimated from the Wexler formula), which is much smaller than the size of the contact plugs used now in microelectronics. The spectrum shows a sharp TA-phonon peak at 20 mV and a weaker and broader feature at 40 mV, which is a double-phonon peak. The background is relatively low and there is a weak zero-bias anomaly. Finally, the LA-phonon peak is not resolved, which is not unusual of α-W contacts.[13,14] The W spectrum in Fig. 6 is comparable to the best spectra of ballistic mechanical point contacts made from a high-purity W base material.[13,14] This indicates that the CVD deposited α-W is of high quality. Indeed, an estimate of the elastic mean free path from the ratio $R_{300K}/R_{4.2K}$ of the film (in the free electron approximation) gives $l_i = 95$ nm, confirming the ballistic transport through the contact.

Bulk layers of amorphous W deposited with CVD are superconducting below 4.3 K, which makes it possible to study the superconducting properties of contacts of this ma-
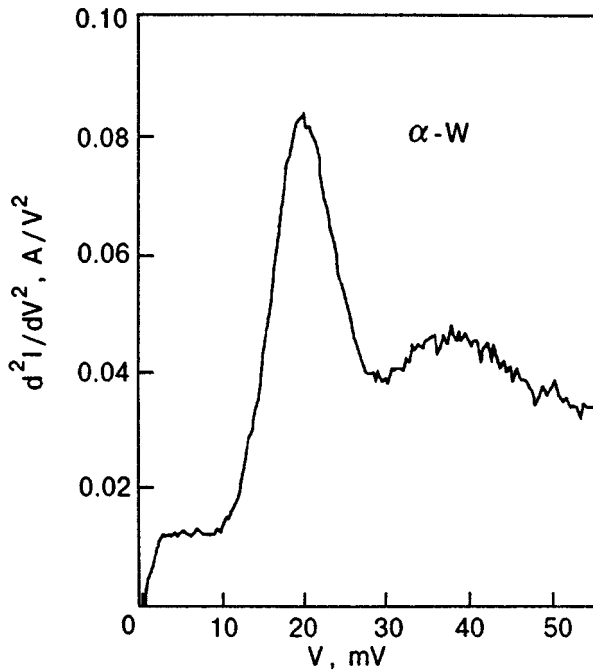
FIG. 6. Point-contact spectrum of an α-W device formed by chemical vapor deposition. $T = 1.5$ K and $R = 45.6$ Ω.

FIG. 7. The $I-V$ characteristics of an amorphous W point contact of $R_N = 12.2\Omega$, measured at different temperatures. The estimated contact diameter is 125 nm. Below 4.3 K the curves display a supercurrent.

terial. To characterize the amorphous W point contacts, we measure the $I-V$ curve and its second derivative $d^2V/dI^2(V)$ above and below the superconducting transition temperature for several devices. Above T_c the amorphous W contacts appears to be not very interesting, because the point-contact spectra are virtually structureless. This is a result of the high resistivity of the material (150–200 mΩ·cm at 4.2 K) and the related very short elastic mean free path ($l_i \approx 1$ nm). Below T_c the curves show a rich variety of features which are related to the superconducting state (since they are absent above T_c), which could not be classified in a systematic way. We attribute this circumstance to device-dependent compositional inhomogeneities on the scale of the constriction, which arise from the incorporated Ge atoms.

Figure 7 shows examples of $I-V$ curves of an amorphous W point contact with normal state resistance $R_N = 12.2$ Ω and a diameter of 125 nm in the range 1.5–5 K. The contact is characterized by $\xi = 15$ nm and $\lambda \approx 500$ nm. These values were estimated from Gor'kov's relations for dirty superconductors[15] (ξ is the coherence length and λ is the penetration depth). Consequently, the device operates in the dirty transport limit, where $\xi, l_i \ll d \ll \lambda$. Below 4.3 K the contact is in the superconducting state and the curves have some structures, in particular, instabilities and a stepwise current increase at low currents. A significant hysteresis was observed when sweeping the current in the opposite direction (see the 1.5-K curve). The sign of the hysteresis was found to be random. From more accurate measurements we found that in the range of a steep current increase the voltage may switch rapidly between two discrete levels, indicative of a transition between two metastable states.

The stepwise behavior is reminiscent of similar behavior in narrow ($\xi, \lambda \ll$ width) superconducting channels.[16,17] This behavior was, among other things, explained in terms of
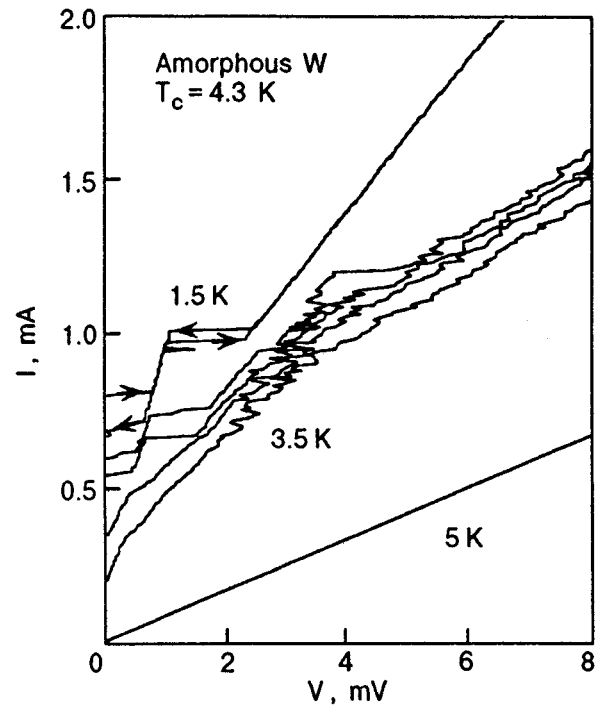
phase-slip centers (PSC). Our amorphous W point contacts, however, operate in a different limit than those channels, so that the PSC model does not apply. The origin of the steps in Fig. 7 is probably of mesoscopic nature. To the best of our knowledge, this would be a new aspect of this type of $I-V$ curves, which we will discuss further.

We assume that the stepwise behavior may be related to the motion of vortices created near the entrance of the constriction by the magnetic field generated by the transport current. Although $\lambda \gg d$, the formation of such vortices is possible, since $\xi \ll d$ (ξ is a measure of the vortex core, whose characteristics in this case may be slightly different from those of the Abrikosov vortices). At large enough currents the device resistance would arise from the motion of the vortices. It is known that vortex motion can be blocked by pinning centers, which are expected to be readily available in amorphous CVD-W with built-in germanium. Vortex motion, therefore, is possible only at large enough currents, where the current-induced force overcomes the pinning force. Since the vortex core size (and thus the spatial scale of the pining relief) is not much smaller than the contact size, one expects a sample-specific percolation-like character of the vortex motion. Increasing the current, therefore, would first lead to the formation of one ''path'' of vortex motion, which corresponds to a chain of weak enough pinning centers. Then, with an increase of the current, a second percolation path would appear. Accordingly, switching-on of paths would correspond to the steps on the $I-V$ curve, as observed. Of course, this tentative explanation needs further checking.

558   Low Temp. Phys. 23 (7), July 1997

Gribov et al.   558

4. DISCUSSION

The TEM observations for PVD of Au and Ag films on unpatterned parts of the membranes and on the rounded edges of the holes can be explained by applying the growth mechanisms of a metallic film on amorphous substrates[18] and need no further discussion. The main point to be addressed is that, aside from the inner edge region, where the necklace is formed, the holes do not become filled with metal. This can be explained in the following way. The edge of the hole is a part of the substrate with positive curvature (rounded profile; see Fig. 1) and negative curvature (due to the circular shape, as seen in top view). From studies of the metallization of vias in microelectronic integrated circuits it is known[19] that areas of dominating negative curvature are preferential sites for nucleation and growth. In our case this leads to nuclei close to the narrowest part of the hole and subsequently to the necklace of small grains. Since, the hole is a missing area, the atoms emitted from the melt are lost. This reduces the number of adatoms collected by nuclei near the hole, so that these nuclei grow slower than other nuclei. This effect is even enhanced because of the inclination of the wall of the hole with respect to the incoming atomic beam (increase of area). We believe that the absence of coalesced grains at the inner edge of the hole (see Fig. 2b) and the slower growth of necklace grains are attributable to this mechanism.

After deposition on one side, the metal that covers the hole acts as a microsubstrate during deposition on the other side. TEM inspection after deposition of 20-nm Ag on side 2 (200-nm Ag was deposited on side 1) showed a dark region inside the hole, surrounded by a light halo, while it was not clear that growth had started on the side wall. This suggests preferential growth on the metal inside the contact hole, which after prolonged deposition on side 2 might lead to a (poly) crystal that bulges out of a hole. A 200-nm Al is deposited on the surface of this bulging crystal. This means that the distance of the Ag/Al interface on side 2 to the constriction is equal to the height of the crystal, which can be larger than 20 nm and larger than the expected depth to which the electron-phonon interaction can be probed. If this is true, it may explain the absence of the LA peak in Fig. 5c for the Ag/Al heterocontact with the 20-nm Ag interlayer.

The results for one-sided PVD tempt us to speculate about the fabrication of homocontacts, which are usually formed while rotating the substrate in the beam emerging from the melt. We expect that such a two-sided deposition will not noticeably suppress the tendency of the hole's wall to remain uncovered. However, when a hole starts to close from two sides, edges may continue to grow (as seen from the inside), so that filling starts. Simultaneously, the interior of the hole becomes less accessible, so that filling becomes harder and may not be completed in some cases (void formation). Clearly, this would limit the yield of the fabrication process.

Our electrical measurements on heterocontacts indicate that, in principle, very good devices of this type can be fabricated with PVD. It turns out, however, that deposition of a bilayer on one side of the membrane does not give enough control over the position of the heterointerface. In additions, control over the degree of flatness of the interface, a require-ment for detailed studies of interface scattering, is not guaranteed. These findings suggest modifications of the fabrication process. For example, we are considering to form point contacts by first depositing metal 1 (or a bilayer or multilayer of metals) on side 1 of the membrane, followed by a highly selective etch of type hole and finally by depositing metal 2 in the hole and on the reverse side of the membrane.

In the case of CVD the TEM observations can be understood from the properties of this process. First, because the reactive sticking coefficient is small, most of the impinging molecules are reemitted. This circumstance and also the random velocity distribution of the reactants provide a supply of the material to all surface areas, irrespective of the local surface orientation. Thus, the walls of the hole are covered from the beginning of deposition. In turn, for the PVD process the sticking probability is close to unity (no reemission) and, by geometry, the velocity of impinging atoms is mainly directed along the axis of the hole, promoting preferential growth at its entrance.

The electrical data for W contacts indicate that CVD, by nature, is very suitable to fabricate metallic point contacts. A limitation is that CVD processes are available for a limited number of metals. Stimulated by the results on the W contacts, we have recently started the fabrication with CVD of Si point contacts. In this case CVD makes it possible to fabricate completely single-crystalline devices.[20]

5. CONCLUSIONS

We have made an electron-microscopy study of the closing of nanoholes in membranes at the successive stages of one-sided physical vapor deposition of Au and Ag, as it occurs in heterocontact formation. We is found that the holes do not become filled with metal in a one-sided deposition. The holes are closed by lateral growth of the film on the membrane when its thickness is more than twice the hole diameter. Metal closing of one side of a hole serves as a microsubstrate for growth of metal deposited from the other side. Growth from the other side seems to occur preferentially on the metal and not on the side walls.

We have also applied chemical vapor deposition of α-W and amorphous W to the formation of point contacts. From TEM inspections we find that the W-CVD process is capable of filling holes as small as 10 nm from the beginning of the deposition, in contrast to physical vapor deposition. Fabricated devices show good quality point-contact spectra of electron-phonon interaction, conforming that PVD and CVD processes yield ballistic point contacts. For one amorphous W device we have observed a very interesting stepwise current increase which may arise from switching-on of percolation paths for vortex motion.

tre of High Resolution Electron Microscopy of Technical University of Delft for TEM analyses.

*E-mail: gribov@dimes.tudelft.nl

[1] K. S. Ralls, R . A. Buhrman, and R. C. Tiberio, Appl. Phys. Lett. **55**, 2459 (1989).

[2] P. A. M. Holweg, J. Caro, A. H. Verbruggen, and S. Radelaar, Microelectronic Engineering **11**, 27 (1990).

[3] K. S. Ralls and R . A. Buhrman, Phys. Rev. Lett. **60**, 2443 (1988).

[4] P. A. M. Holweg, J. Caro, A. H. Verbruggen, and S. Radelaar, Phys. Rev. B **45**, 9311 (1992).

[5] P. A. M. Holweg, J. A. Kokkedee, J. Caro, A. H. Verbruggen, S. Radelaar, A. G. M. Jansen, and P. Wyder, Phys. Rev. Lett. **67**, 2549 (1991).

[6] P. A. M. Holweg, J. Caro, A. H. Verbruggen, and S. Radelaar, Phys. Rev. B **48**, 2479 (1993).

[7] N. N. Gribov, J. Caro, and S. Radelaar, Physica B **218**, 97 (1996).

[8] D. C. Ralph, Ph.D. Thesis, Cornell University (1994).

[9] R. Louie, S. Upadhyay, and R. A. Buhrman, Bull. Am. Phys. Soc. **41**, 304 (1996).

[10] D. C. Ralph, C. T. Black, and M. Tinkham, Phys. Rev. Lett. **74**, 3241 (1995).

[11] E. H. A. Granneman, Thin Solid Films **228**, 1 (1993).

[12] T. Ohba, MRS Bull. **20**, 46 (1995).

[13] J. Caro, R. Goehoorn, and D. G. de Groot, Solid State Commun. **39**, 267 (1981).

[14] L. F. Rybal'chenko, I. K. Yanson, N. L. Bobrov and V. V. Fisun, Sov. J. Low Temp. Phys. **7**, 82 (1981).

[15] L. P. Gor'kov, S ov. Phys. JETP **9**, 1364 (1959).

[16] A. Barone and G. Paterno, Physics and Applications of the Josephson effect, Wiley, New York, (1982).

[17] T. M. Klapwijk, M. Sepers, and J. E. Mooij, J. Low Tem. Phys. **27**, 801 (1977).

[18] D. W. Pashley, M. J. Stowell, M. H. Jacobs, and T. J. Law, Philos. Mag. **10**, 127 (1964).

[19] T. Smy, S. K. Dew, and M. J. Brett, presented at a course in conjunction with the Advanced Metalization Conference in Texas (1994).

[20] J. W. H. Maes, J. Caro, C. C. G. Visser, T. Zijlstra, E. W. J. M. van der Drift, S. Radelaar, F. D. Tichelaar, and E. J. M. Fakkeldij, Appl. Phys. Lett. **70**, 973 (1997).

560   Low Temp. Phys. **23** (7), July 1997

Gribov *et al.*   560

LOW-DIMENSIONAL AND DISORDERED SYSTEMS

Peculiarities in the effect of hydrogen on CDW transition in NbSe₃

Kh. B. Chashka, V. A. Bychko, M. A. Obolenskii, Raid Hasan, and V. I. Beletskii

*Kharkov State University, 310077 Kharkov, Ukraine**

A. V. Basteev and A. N. Prognimak

Kharkov Institute of Machine Building Problems, 310046 Kharkov, Ukraine

The influence of intercalated hydrogen concentration on the physical properties of NbSe₃ is investigated. The mass-spectrometric analysis reveals a nonlinear dependence of hydrogen extraction from the crystal structure on the saturated pressure. Resistive measurements make it possible to study the concentration dependence of the temperature T_{CDW} corresponding to a phase transition accompanied with the formation of a charge density wave (CDW) and temperature dependence of CDW pinning threshold fields. A metal-semiconductor phase transition is observed for certain concentrations of intercalated hydrogen. All the measurements are made in the temperature range of the first CDW transition (90–300 K). © *1997 American Institute of Physics.* [S1063-777X(97)01007-4]

Phase transitions accompanied with the formation of a charge density wave (CDW) are observed in many layered and straight-chain metallic compounds including NbSe₂ and NbSe₃ with a strong anisotropy of physical parameters.

The CDW instability was predicted by Peierls[1] who proved that the minimum free energy for a one-dimensional atomic chain is attained during the formation of a CDW. In this case, the electron density in the given direction is described by the relation

$$\rho(x) = \rho_0 [1 + \alpha \cos(\mathbf{Q}x + \varphi)], \tag{1}$$

where ρ_0 is the homogeneous electron density, $\alpha\rho_0$ the charge modulation amplitude, $\mathbf{Q} = 2\mathbf{k}_F$ the modulation wave vector, and the phase φ characterizes the position of the CDW relative to the ionic lattice.

The existence of CDW transition is associated with the formation of Fermi surface regions coinciding as a result of parallel transfer by the vector $\mathbf{Q} = 2\mathbf{k}_F$ (nesting). Under these conditions, the polarizability of the electron system in the periodic electric field of the lattice is large, and the lattice becomes unstable to a periodic distortion with the wave vector $\mathbf{Q}$. A gap formed in the energy spectrum in coinciding regions of the Fermi surface reduces the value of electron energy. A CDW is generated if the gain in the electron energy is larger than the increment of elastic energy due to crystal lattice distortion.

In perfect systems, a lattice distortion can be displaced without dissipation in the form of a propagating wave as a result of translational invariance. The CDW energy does not depend on the phase φ. In real systems, such a translational invariance is violated due to phase pinning at defects or in the lattice itself.

If the CDW energy in an applied electric field exceeds the pinning energy, the CDW starts sliding over the lattice and makes an additional contribution to conductivity.

The quantum model of CDW propagation developed by Bardeen[2] presumes that the CDW can tunnel through potential barriers in the region $E > E_{th}$ (where E_{th} is the threshold field for CDW depinning).

In this model, the following expression was obtained for conductivity:

$$\sigma(E) = \sigma_a + \sigma_b (1 - E_{th}/E) \exp(-E_0/E), \tag{2}$$

where σ_a is the ohmic conductivity and E_0 the activation field connected with the pinning energy ε_g through the expression

$$E_0 = \pi \varepsilon_g^2 / 4\hbar e^* v_F. \tag{3}$$

Here $e^* = e m^* / M_F$ is the effective charge, m^* the effective mass, and M_F the Froehlich mass of charge carriers, characterizing transport in the CDW state. Expression (2) is in good agreement with experimental data for pure samples of trichalcogenides.

A large number of experimental publications have been devoted to the study of the effect of impurities on the CDW state in NbSe₃. These publications are mainly aimed at the investigation of the effect of doping. The latter can be carried out by replacing Nb atoms by the atoms of another transition metal, but it is difficult to determine exactly the concentration of impurities obtained during the single crystal growth as a result of doping. It is difficult to obtain high concentrations of impurity atoms as a result of doping, and these atoms are distributed nonuniformly over the crystal.[3]

For low-dimensional structures such as chalcogenides of transition metals, impurities can be introduced not only by doping, but also by intercalation.

As a result of intercalation, two effects are observed irrespective of the type of intercalate and the position of impurity in the lattice: a change in the parameters of the initial lattice and a change in the charge carrier concentration as a

result of charge transfer from the intercalate to the matrix. For this reason, intercalation with hydrogen is especially interesting. In view of the small size of the hydrogen atom, hydrogen can be intercalated to high concentrations without a noticeable lattice distortion, and the simplicity of its electron structure simplifies the interpretation of experimental data.

At the present time, the information on complex experimental analysis of the effect of band structure variation of quasi-one-dimensional trichalcogenides on the thermodynamic characteristics of the CDW transition, including the temperature T_{CDW} of the CDW transition, as well as on the propagation of CDW in electric fields exceeding E_{th} is scarce. Moreover, the effect of a mobile impurity (such as hydrogen) on the mechanisms of CDW pinning remains unclear.

For this reason, we shall investigate here the effect of hydrogen impurity on the CDW transition in NbSe₃.

EXPERIMENTAL TECHNIQUE

Niobium triselenide single crystals were grown by the method of chemical gas-transport reactions.

The saturation of samples with hydrogen was carried out from the gaseous phase at a constant temperature 350 °C under various pressures. The saturated pressure varied from 2 to 10 bar.

The hydrogen concentration in the samples was determined by using mass spectrometry. The small mass of the single crystals did not allow us to determine the hydrogen concentration in a single crystal, and hence we used the following method. Pellets of diameter 5 mm and thickness 1 mm were pressed from NbSe₃ single crystals under a pressure not exceeding $5 \cdot 10^2$ bar. The central part of the pellet was cut in the form of a block of the size $1 \times 1 \times 5$ mm and used for subsequent resistive measurements. All the three parts of the pellet and an individual NbSe₃ single crystal were placed into a cell for saturating with hydrogen. Segment-shaped parts of the tablets were used in mass-spectrometric analysis. The samples were placed on glass ceramic substrates on which currents and potential leads were fixed. Electric contacts were created with the help of conducting silver paste (Fig. 1).

We studied the influence of hydrogen concentration on the temperature dependence of the resistance R of pressed samples. The results of measurements are shown in Fig. 2. It should be noted that according to Monceau,[3] all the main peculiarities in the behavior of the resistance are clearly manifested in resistive measurements on the samples prepared in this way. For example, this method can be used to determine the CDW transition temperature reliably. At the same time, a monocrystalline sample of NbSe₃ was saturated under a pressure of 10 bar, after which the hydrogen concentration in it could be reduced by gradual cooling in a vacuum $\sim 10^{-9}$ bar. The temperature of heating in such experiments did not exceed 200 °C, and according to the results of mass spectrometry, hydrogen is liberated under such conditions without a loss in the stoichiometry of the compound NbSe₃. Such a technique allowed us to trace the variation of T_{CDW}, E_{th}, I_{th}, and other parameters of the compound for a
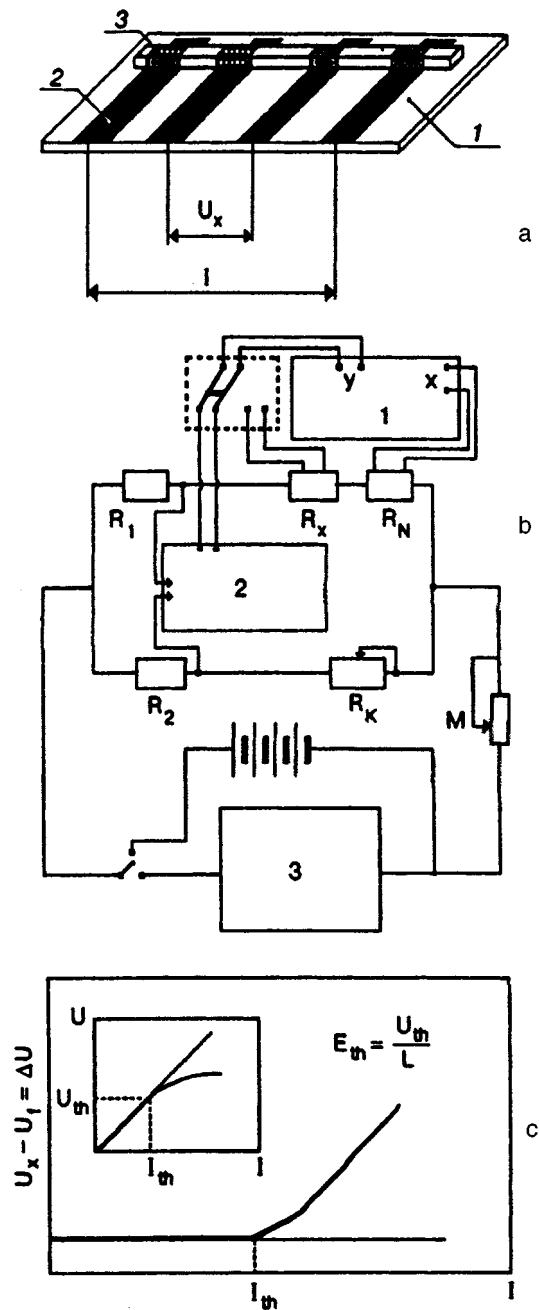

FIG. 1. (a) Location of the sample on the substrate: substrate (1), contact pads (2), and sample (3). (b) Measuring circuit: $x-y$ recorder (1), photoamplifier (2) dc scanning generator (3). (c) Method of determining CDW threshold field by using the dc bridge circuit. The inset shows an example of standard IVC recording.

constant size of the sample. Thus, all the peculiarities observed in our experiments can be attributed mainly to the change in hydrogen concentration. The results of these measurements are presented in Fig. 3.

The measurements of R were made in the temperature range 90–300 K. In this region, the first CDW transition takes place in NbSe₃.

In order to observe nonlinear conductivity and to determine the threshold values of the electric field strength E_{th} and current I_{th}, we measured the current–voltage characteristics (IVC). The measuring circuit allowed us to record the
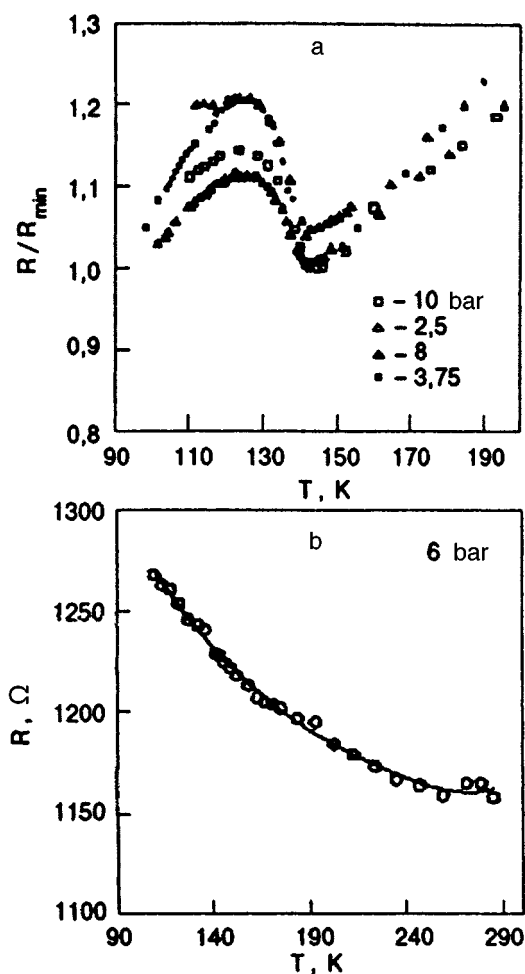
FIG. 2. Temperature dependence of resistance for several hydrogen saturation pressures for pellet samples with a metallic (a) and semiconducting (b) behavior of resistance.

$U(I)$ dependence directly and to measure the dependence of $(U_x - U_f)$ on I by using the bridge circuit (U_x is the voltage across the sample in the state with pinned CDW and U_f is the voltage across the sample in the state with a slipping CDW). This method made it possible to increase the sensitivity of the measuring circuit for measuring I_{th} by three orders of magnitude. The threshold field of depinning, E_{th}, was defined as $(I_{th}R_x)/L$, where I_{th} is the threshold value of transport current, which was determined from bridge circuit measurements, R_x the sample resistance in the pinned state, which was determined on the linear segment of the $U(I)$ dependence and was equal to U_x/I for $I < I_{th}$, and L the distance between the potential contacts. The methods of determining I_{th}, R_x, and U_{th} are illustrated in Fig. 1.

DISCUSSION OF EXPERIMENTAL RESULTS

The results of mass-spectrometric measurements of the amount of hydrogen liberated from the pellets are shown in Fig. 4. The peculiar nonmonotonic dependence of the amount of hydrogen released from the sample on the saturated pressure can apparently be associated with our experimental conditions. Since the liberation of hydrogen from the sample occurred at $T = 500\ ^\circ C$, we took into account in our

analysis only the hydrogen whose binding energy was less than kT. The remaining hydrogen can remain in the bound state in the matrix lattice at this temperature. This assumption leads to the conclusion about the existence of at least two nonequivalent positions of hydrogen in the NbSe$_3$ lattice, which can be associated with the presence in this lattice of nonequivalent chains differing both in the atomic separation of Nb–Se, Se–Se, and Nb–Nb, and with the binding energy in the chains.[3] Also, this is in accord with the results of analysis of the NbSe$_2$–hydrogen system, in which we discovered two nonequivalent states of hydrogen with different binding energies.[4] It should be borne in mind that the unit cell of NbSe$_2$ has a configuration close to that of NbSe$_3$, but they differ in the way of packing into layers or chains respectively. Thus, the amount of hydrogen was apparently determined inaccurately in mass-spectrometric measurements, but, on the other hand, the results of measurements indicate that an increase in saturation pressure leads to a redistribution of hydrogen in the lattice and to an increase in the relative amount of strongly bound hydrogen.

The results of measurements of resistance of polycrystalline of pressed samples are shown in Fig. 2. In Fig. 2a, the values of resistance are normalized to R_{min}, viz., the minimum value in the region of the CDW transition. In Fig. 2b, the values of R are given in absolute units. It should be noted that the metallic type of resistance is observed under pressures 8 bar $> P > 3.75$ bar. An increase in saturation pressure leads to an overall increase in R. It can be seen from the figure, however, that all the peculiarities typical of a CDW transition are preserved. In samples saturated under pressures of 6 bar, the semiconductor behavior of the resistance was observed. The estimate of the forbidden gap width from resistive measurements gives $\Delta/k_B = 17$ K (where Δ is the energy gap and k_B the Boltzmann's constant). Balseiro and Falicov[5] proved that the CDW transition temperature can be described by the relation

$$T_{CDW} = 1{,}14\hbar\omega_0 \exp[-1/(\lambda_{eff} N(\varepsilon))], \qquad (4)$$

where $N(\varepsilon)$ is the density of electron states at the Fermi level and λ_{eff} the effective constant of the electron–phonon interaction. Thus, the CDW transition temperature is a function of the density of states. In the rigid-band approximation, intercalation with hydrogen should displace the Fermi level. It should be noted that saturation with hydrogen in this model can be an effective tool for influencing the band structure. Usually, hydrogen intercalated in the lattice of low-dimensional structures is a donor that facilitates the conduction band filling and shifts the Fermi level so that the conductance of the samples increases. Bullett[6] carried out detailed analysis of the band structure and proved that the conduction band is quite narrow, and the Fermi level lies in the smooth segment to the left of the peak on the $N(\varepsilon)$ dependence. In this case, saturation with hydrogen must lead to a sharp increase in the density of states, when ε_F approaches the peak on the $N(\varepsilon)$ curve, which in turn must be reflected in the behavior of T_{CDW}. The dependence of T_{CDW} on saturation pressure shown in Fig. 5 is in quantitative agreement with the proposed mechanism. Complete filling of the conduction band must lead to the emergence of the
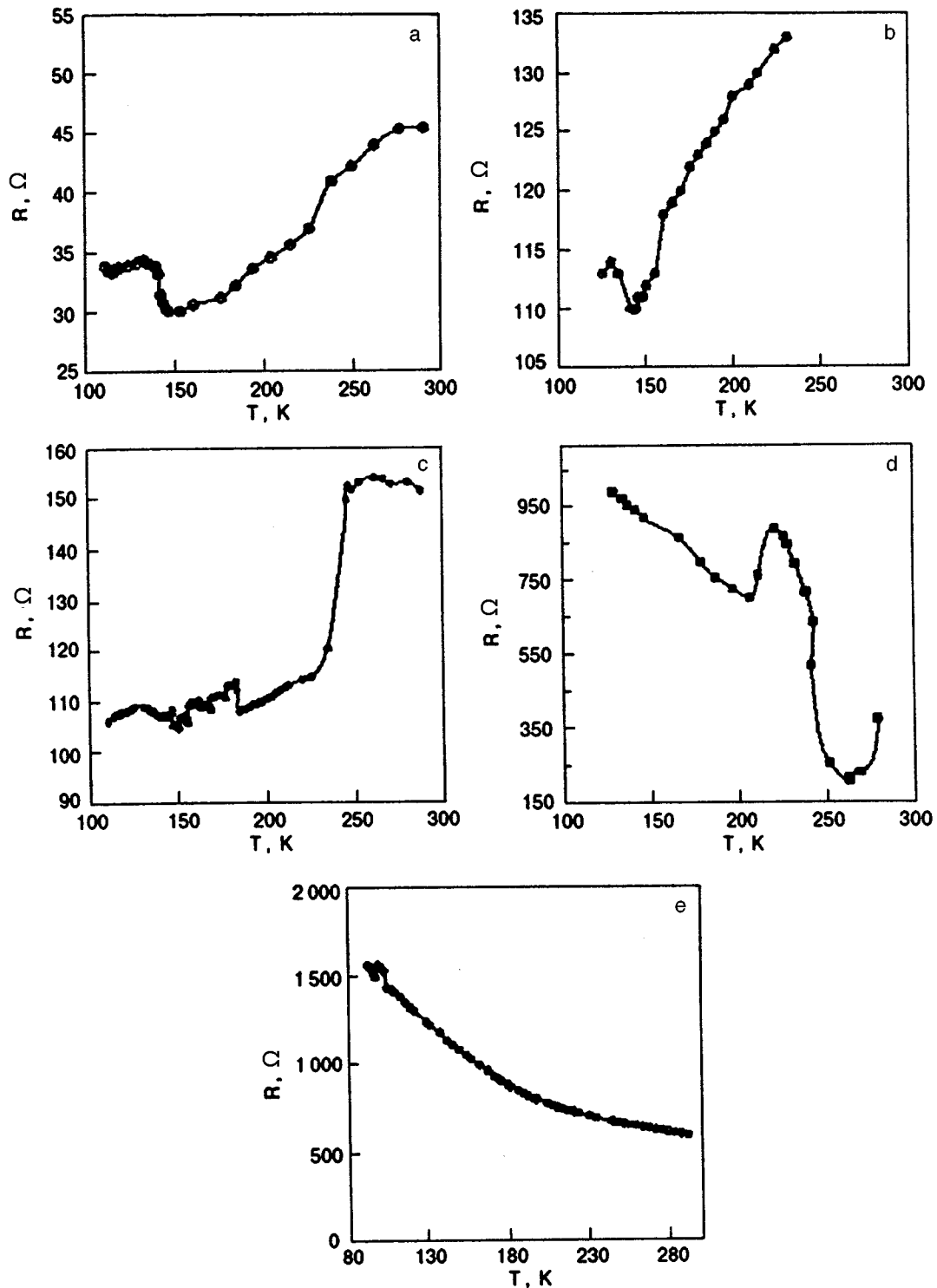
FIG. 3. Variation of the temperature dependence of the resistance of a single crystal as a result of gradual hydrogen extraction: after first heating in vacuum (a), after second heating in vacuum (b), and after 48 (c), 96 (d), and 144 hours (e).

semiconducting state, which is actually observed in experiments. The origin of the metallic state at higher saturation pressures and accordingly at higher hydrogen concentrations remains unclear. In order to study this state, we investigated the resistance of monocrystalline samples saturated with hydrogen under the pressure $P \sim 10$ bar, in which the hydrogen content decreases gradually with time. The evolution of the temperature dependence of the resistance R of the sample

under investigation is illustrated in Fig. 3. As in the pressed samples, the behavior of the resistance R of this sample is initially of the metallic type. Gradual removal of hydrogen from the sample leads to an overall increase in the resistance and ultimately to the emergence of the semiconducting state. The estimate of the energy gap in this case gives $\Delta/k_B \sim 180$ K, which is close in order of magnitude to the results obtained by Bullett.[6] We can assume that the increase
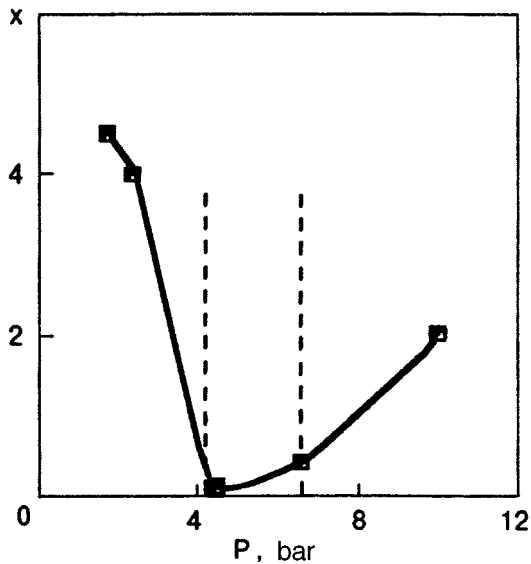
FIG. 4. Amount of liberated hydrogen as a function of saturation pressure (x is the number of atoms per unit cell).

in saturation pressure leads to partial filling of the next energy band. It is surprising, however, that the value of T_{CDW} changes only slightly in this case. Unfortunately, we did not obtain in our experiments the concentration dependence $T_{CDW}(x)$ for low hydrogen concentrations, but such measurements are planned in the nearest future.

The results of investigation of threshold fields on a monocrystalline sample saturated with hydrogen at 10 bar are presented in Fig. 6a. It can be seen that the values of E_{th} differ considerably from those obtained for pure samples both in the absolute value of the threshold fields (which is in accord with the results obtained by Thorne *et al.*),[7] and in the presence of descending regions on the $E_{th}(T)$ curve at $T > 140$ K and $T < 104$ K, which are absent for pure samples.[3] The temperature dependence of pinning energy calculated by using relation (3) is shown in Fig. 6b. It also

FIG. 6. Temperature dependence of the threshold fields E_{th} for pure (■) and saturated under a pressure of 10 bar (◉) samples (a) and of the pinning energy ε_g calculated by formula (3) for a single crystal saturated with hydrogen at 10 bar (b).

has a clearly manifested peak at $T \sim 140$ K. In our opinion, such singularities in the behavior of E_{th} indicate that hydrogen atoms are effective pinning centers, and the presence of a peak on the $\varepsilon_g(T)$ curve signifies an increase in the mobility of hydrogen upon heating in an electric field. The intensity of pinning remains unclear and requires further investigations. As the sample approached the semiconducting state in our experiments, we observed the emergence of low-frequency voltage oscillations in the electric field range $E > E_{th}$, an example of such a recording is given in Fig. 7. A detailed discussion of the results of these experiments will be given in the following communication.

CONCLUSIONS

(1) It has been established that the temperature corresponding to the first CDW transition weakly depends on the concentration of intercalated hydrogen.

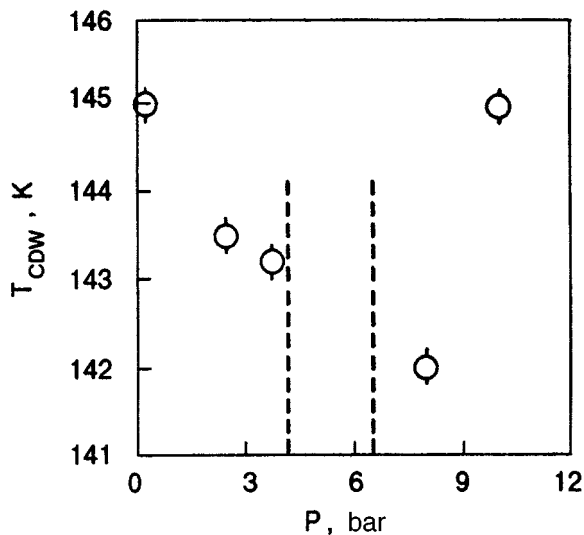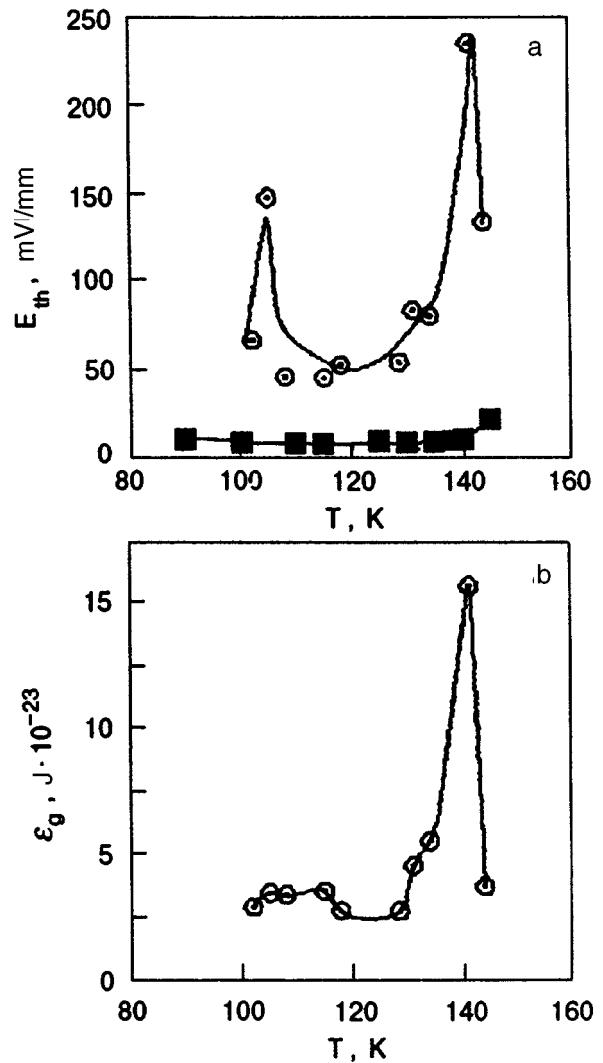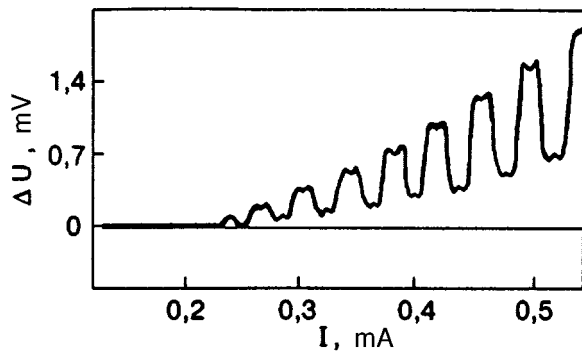(2) The values of the threshold field of CDW depinning for hydrogen-saturated samples is higher than for

FIG. 5. Dependence of the CDW transition temperature on the hydrogen saturation pressure, measured for pellet samples.

565   Low Temp. Phys. **23** (7), July 1997

Chashka *et al.*   565

FIG. 7. Example of recording of voltage oscillations in the sample in the state corresponding to Fig. 3b.

tures. Further investigations are undoubtedly required in order to determine more exactly the position of hydrogen atoms in the lattice, the binding energy and the charge state of hydrogen atoms occupying various positions. Intercalation with hydrogen can become an informative method for analyzing the shape of the $N(\varepsilon)$ curve. If, in addition, hydrogen is a mobile impurity, it must noticeably affect the nonlinear behavior of the resistance in the CDW state for both transitions in $NbSe_3$ in an external magnetic field.

[*]E-mail: mikhail.a. obolenskii@univer.kharkov.ua

pure samples. The shape of the temperature dependence of the threshold fields of CDW depinning changes qualitatively.

(3) The results of mass spectrometry give a nonmonotonic dependence of the amount of liberated hydrogen on saturation pressure with a minimum at $P \sim 6$ bar.

(4) The samples saturated at $P \sim 6$ bar exhibit the semiconducting behavior of the resistance.

It should be noted in conclusion that the $NbSe_3$–hydrogen system exhibits a number of peculiar fea-

[1] R. Peierls, *Quantum Theory of Solids*, Oxford (1955).
[2] J. Bardeen, Phys. Rev. Lett. **42**, 1498 (1979); Phys. Rev. Lett. **45**, 1978 (1980); Physica **B14**, 143 (1986).
[3] P. Monceau (ed.), *Electronic Properties of Inorganic Quasi-One- Dimensional Materials*, vol. II, Reidel Publ. Company, Dordreht–Boston–Lancaster (1986).
[4] M. A. Obolenskii, Kh. B. Chashka, V. I. Beletskii, and A. V. Basteev, Preprint-227 IP. Mash. (1988).
[5] C. A. Balseiro and L. M. Falicov, Phys. Rev. **B20**, 4457 (1979).
[6] D. W. Bullett, J. Phys. **C15**, 3069 (1982).
[7] R. E. Thorne, T. L. Adelman, J. Mc. Carten *et al.*, Phys. Rev. **B40**, 6 (1989).

Translated by R. S. Wadhwa

PHYSICAL PROPERTIES OF CRYOCRYSTALS

Analysis of decomposition of impurity–helium solid phase

R. E. Boltnev, E. B. Gordon, I. N. Krushinskaya, M. V. Martynenko, A. A. Pelmenev,
E. A. Popov, V. V. Khmelenko

*Branch of the Institute of Energy Problems in Chemical Physics, Russian Academy of Sciences, 142432
Chernogolovka, Moscow distr., Russia**

A. F. Shestakov

*Chernogolovka Institute of Chemical Physics, Russian Academy of Sciences, 142432 Chernogolovka,
Moscow distr., Russia*

The elemental composition of the impurity–helium solid phase (IHSP) grown by injecting of a
gas jet containing Ne, Ar, Kr, and Xe atoms and N_2 molecules into superfluid HeII is
studied. The measured stoichiometric ratios $S = N_{He}/N_{Im}$ are much larger than the values predicted
by the model of frozen together monolayer helium clusters. The theoretical possibility of
freezing together of two-layered clusters is justified in the continual model of the helium subsystem
of IHSP which fills the space between rigid impurity centers. Regularities of decomposition
of ''dry'' samples (extracted from liquid helium) are analyzed in the temperature range 1.5–12 K
under pressures from 10 to 500 torr. Two stages of sample decomposition are discovered: a
slow stage accompanied by cooling and a rapid stage accompanied by heat release. These results
suggest the presence of two types of helium in IHSP, viz., weakly bound and strongly
bound helium which can be attributed respectively to the second and first coordination spheres of
helium formed around heavy impurity particles. A tendency to elevation of the thermal
stability of impurity–helium (IH) samples upon an increase in the mass of impurity center has
been observed. An increase in the helium vapor pressure above the samples also increases
their stability. It is found that the decomposition of IH samples containing nitrogen atoms in the
temperature range 3–4.5 K is accompanied with luminescence induced by recombination
of atoms. This indicates the possibility of a wide range of chemical reactions in solidified helium.
© *1997 American Institute of Physics.* [S1063-777X(97)01107-9]

1. INTRODUCTION

The observation of solidification of solid helium upon
the introduction of heavy impurity particles to superconduct-
ing helium resulting in the formation of a new metastable
impurity–helium solid phase (IHSP)[1,2] opens new prospects
for investigation of the properties of particles separated by
helium atoms. On the other hand, the impurity–helium solid
phase itself is a new object in the low-temperature physics,
whose properties have been studied insufficiently.

The formation of IHSP was demonstrated for various
impurity (Im) particles: Ne, Ar, Kr, Xe, and N atoms and
N_2 molecules. The IHSP was obtained by introducing into
superfluid helium of a gas jet of impurity particles diluted
with helium after its passage though the rf discharge region.
It was found that this phase prepared in superfluid helium
can exist outside the liquid also. It is decomposed completely
at temperatures 6.5–8.5 K.[3,4]

A theoretical analysis based on the cluster approach[4,5]
confirmed that the physical foundation for the formation
of the IH phase is the decrease in the amplitude of radial
vibrations of helium atoms in the field of dispersion forces of
aheavy impurity center resulting in the formation of rigid

van der Waals impurity–helium complexes and in their
freezing together in IHSP.

A direct experimental evidence of partial loss of
quantum-mechanical properties of helium around impurity
particles has been obtained recently.[6] The rotational structure
of vibrational spectra of SF_6 molecules implanted in He_n
helium clusters ($n \sim 10^4 - 10^5$) was recorded, and the mo-
ment of inertia of the emitting complex was determined. The
obtained value is much larger than the moment of inertia of
a free SF_6 molecule and corresponds to the complex formed
by an SF_6 molecule surrounded by eight helium atoms rig-
idly coupled with the shell.

Experiments on the determination of the elemental com-
position of the impurity–helium solid phase revealed that it
consists mainly of solidified helium; the stoichiometric coef-
ficients $S = N_{He}/N_{Im}$ for various impurity particles vary from
12–17 for Ne and N atoms to 60 for Ar atoms.[4] However,
the form of decomposition of IHSP has not been investigated
in detail, and it remains unclear whether the elemental com-
position of IHSP samples is preserved right up to their de-
struction or can be changed during heating. The aspects of
stability and decomposition mechanism are very important

for understanding the nature of the impurity–helium phase: it either preserves its metastable state up to the temperature of decomposition which is of the form of a phase transition, or its properties change during heating from 1.5 to 7 K which leads to its complete decomposition at $T \sim 7–8$ K. It was noted earlier that the shape of a ''dry'' sample changes at temperatures which are much lower than 7 K. Moreover, an analysis of thermoluminescence of N atoms stabilized in IHSP samples demonstrated the merging of impurity particles in IHSP even at $T \sim 1.5$ K in samples immersed in He II.[7] However, it remained unclear whether these processes were of bulk nature or a manifestation of an insignificant number of defects in IHSP responsible for luminescence was detected.

In this paper, we report on the study of decomposition of impurity–helium samples under various conditions: holding outside liquid helium at constant temperature, heating from 1.5 to $T \sim 10–12$ K in helium under various pressures.

We used the methods developed for studying the elemental composition of IH samples, including the independent determination of the true volume of the samples and the number of impurity particles in them.[3,4] In earlier experiments, the samples were evaporated immediately after the measuring the true volume for determining the number and type of impurity particles on the basis of an analysis of the formed gas, while in our cycle of experiments we made long-term measurements of their true and apparent volumes during heating from 1.5 to 10–12 K, and only then the samples were evaporated to carry out the analysis of the formed gas. Moreover, we modified the measuring technique in order to improve the stability of measuring conditions and to elevate their accuracy.

As in Refs. 3 and 4, we used atoms of inert gases Ne, Ar, Kr, Xe and N_2 molecules as impurity particles. Most experiments were made on the samples obtained by injecting into He II gas flows which were not subjected to the action of rf discharge since this leads to additional thermal effects of recombination of chemically active particles formed in the rf discharge region. This method makes it possible to study thermal effects accompanying the transition from the metastable impurity–helium phase to the stable (impurity–helium) state. In order to determine the possibility of partial ''evaporation'' of helium from the samples, we measured temperature in the bulk of the sample and near its surface.

In order to obtain additional information on the nature of decomposition of impurity–helium samples, the latter were obtained in some experiments by introducing into He II a gas jet after its passage through the rf discharge region, while allowed us to detect synchronously the luminescence of nitrogen impurity atoms. The effect of external pressure on the stability of the samples was studied on the same samples.

In addition, we carried out a theoretical analysis of the stoichiometric composition of IHSP based on the approaches used for describing optical properties of impurity atoms in liquid helium.[8–10]

TABLE I. Experimental conditions for obtaining impurity-helium samples (for the gas mixture composition $[N_{Im}^0]/[N_{He}^0] = 0.01$).

No. of experiment	Impurity Atom (molecule) Im	Gas jet, $dN/dt \cdot 10^{-19}$, particles/s	Sample accumulation time τ, s	Degree of condensation α, %
1		11.0	2750	9
2	Ne	7.2	770	36
3		6.06	1470	9
4		9.0	637	23
1		8.6	3060	13
2	Ar	8.67	2480	7
3		7.4	2500	9
4		6.92	1750	15
1		5.7	1490	35
2	Kr	6.13	820	40
3		5.4	2345	9
1	Xe	7.24	890	30
1	N_2	5.82	1672	14

2. EXPERIMENTAL TECHNIQUE AND SETUP

2.1. Method of obtaining and investigating the samples prepared by introducing in HeII the gas jets not subjected to rf discharge

The experimental technique used for obtaining IHSP samples is described in detail in Refs. 3. The schematic diagram of the low-temperature setup is shown in Fig. 1. In this series of experiments, most of IHSP samples were obtained by introducing ''cold'' gas mixtures (not subjected to the action of rf discharge) in the bulk of superfluid helium filling a specially shaped cup 5. In order to prevent joint freezing of impurity particles in the gas, we used gas mixtures strongly diluted with helium ($[N_{Im}]/[N_{He}] = 1:100$) and heated the end of the pipe through which the gas was introduced by an annular heater 15 ($R = 10\ \Omega$) to $T \sim 80$ K. The temperature of the lower part of the pipe was measured by a copper–constantan thermocouple 3.

Under typical experimental conditions ($P_{He} \sim 10–15$ torr and gas flux $dN/dt \sim (7–9) \times 10^{19}$ particles/s), we obtained the samples with Ne, Ar, Kr atoms and nitrogen molecules as impurity centers. In the case when the Xe impurity was used, impurity–helium samples could not be obtained with the help of ''cold'' jets since virtually all of xenon was frozen out at the walls of the quartz tube of the source (the equilibrium pressure of saturated xenon vapor at $T \sim 80$ K is $4 \cdot 10^{-3}$ torr, while $P_{Xe} = 10^{-1}$ torr in the gas mixture passing through the source of atoms). For this reason, xenon–helium samples were obtained only as a result of action of a rf discharge on the gas mixture being condensed. Table I gives experimental conditions for various impurity–helium samples.

Sample accumulation was terminated after the sample filled the cylindrical part of the cup to a height of 0.5–2 cm. The samples were in the form of jelly-like semitransparent cylinders which did not differ in appearance from the samples obtained earlier as a result of passage of a gas jet undergoing condensation through the region of a rf discharge.[1] Such cylinders preserved their shape in helium and exhibited elastic properties: the upper free surface of the

sample vibrated in the presence of mechanical vibrations of the helium Dewar, being displaced by a distance up to 0.1 cm from the equilibrium position.

Taking into account the high porosity of the obtained IHSP samples,[3] we investigated experimentally the behavior of the apparent and true volume of the sample as functions of time and temperature. In the course of experiments, the following operations were made with IHSP samples:

(1) visual observation of the volume and shape of the sample with the help of a video camera;
(2) measurements of the true and apparent volumes in consecutive cycles ''removal–immersion'' in the HeII volume with a short-term holding ($t \sim 150$ s) above the helium surface at $T = 4 - 6$ K;
(3) analysis of variation of the apparent volume during the removal of liquid helium from the cup and heating from 1.5 K to $T > 8$ K;
(4) evaporation of impurity particles of the sample and their accumulation in the measuring volume outside the helium Dewar flask for determining their amount.

In order to ensure the stability of the conditions during the determination of the true sample volume in the given measuring cycle, a side cylinder 4 (see Fig. 1) of a much larger volume (100 cm^3) was placed at the level of the working quartz cup (10 cm^3) and filled with helium with the help of a second thermomechanical pump 11. The special shape of the cylinder made it possible for mobile parts of the construction to move freely and permitted the visual control of processes occurring in the Dewar flask. The presence of the side cylinder filled with helium allowed us to stabilize and maintain experimental condition during the measurements of the volumes of the samples, the background rate of decrease in the liquid helium level being $\sim 10^{-3}$ cm/s, which increases the accuracy in determining the volume. Moreover, in the computational procedure described above,[3] the change in the background rate of helium extraction from the cylinder after the removal of the sample from the helium volume was additionally taken into account. Accordingly, the sample volume was determined from the relation

$$V_0 = \{h_1 - h_2 + v_1(t_1^0 - t_1) - v_2(t_2 - t_1^0)\}\pi d^2/4 - V_d,$$

where d is the inner diameter of the cylinder, h_1 and t_1 are the position of the helium level in the cylinder and the time of its measurement, h_2 and t_2 are the position of the helium level in the cylinder after the extraction of helium from the sample and the time of its measurement. t_1^0 is the instant of time corresponding to the extraction of helium from the sample, v_1 and v_2 are the background rates of decrease in the level of liquid helium in the cylinder upon the immersion of the sample in helium and its removal from helium respectively, and V_d is the volume of the metallic container in which the sample is kept.

The stoichiometric ratio $S = N_{He}/N_{Im}$ was determined from independent measurements of the true volume of the samples and of the absolute number of impurity particles in them.[3,4] The number of impurity particles in the sample was calculated after evaporation of the sample and the accumu-
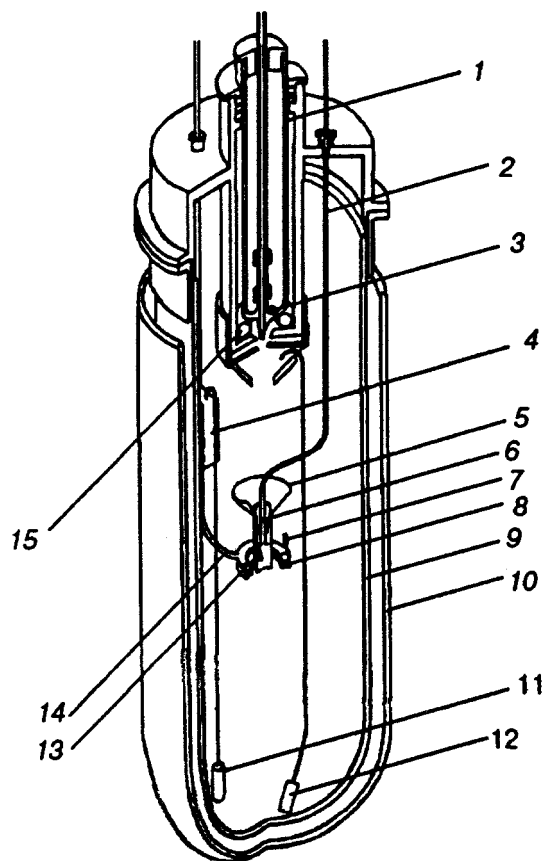

FIG. 1. Schematic diagram of the low-temperature part of the setup: source of atoms (1), gas accumulating tube (2), thermocouple junction controlling liquid nitrogen temperature in the source (3), side cylinder for liquid helium (4), quartz cup for accumulating sample (5), throttle seal on the collecting tube (6), side tube thermometer (7), annular permanent magnet (8), helium Dewar flask (9), nitrogen Dewar flask (10), thermomechanical pump for liquid helium supply to the side cylinder (11), thermomechanical pump for liquid helium supply to the cup for sample accumulation (12), thermometer of collecting tube (13), side tube (14), and annular heater (15).

lation of the formed gas in the measuring volume outside the helium Dewar flask by measuring the gas pressure and using the mass-spectrometric analysis.[3]

Since we investigated impurity–helium samples in which atoms of heavy inert gases (Ar, Kr, Xe) with relatively high boiling points play the role of impurity centers, special experiments were required for determining the efficiency of their accumulation in the volume outside the helium Dewar flask after sample evaporation. Such experiments for Kr atoms revealed that the efficiency of accumulation under the conditions described earlier[3] is high and amounts to $(98 \pm 2)\%$.

In experiments on temporal stability of ''dry'' impurity–helium samples (extracted from liquid helium), the container with the sample was removed from helium with the help of an annular magnet 8 (see Fig. 1) fixed on the side tube and was held $1 - 3$ cm above the helium surface, where the temperature was $4 - 6$ K. After this, the image of the sample was recorded simultaneously with the measurement of temperature. The pressure of helium vapor in the Dewar flask in this case was ~ 10 torr.

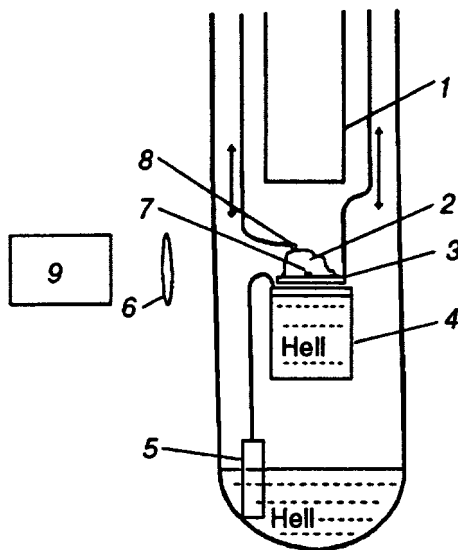In experiments on temperature stability of the samples,

FIG. 2. Schematic diagram of experimental setup on thermoluminescence recording in an impurity–helium solid phase: source of atoms (1), impurity–helium solid sample (2), mesh disk (3), quarts cup for accumulating sample (4), thermomechanical pump for supplying liquid helium to the cylinder (5), condenser lens (6), thermometer in the sample (7), thermometer above the sample (8), and system of optical radiation recording (9).
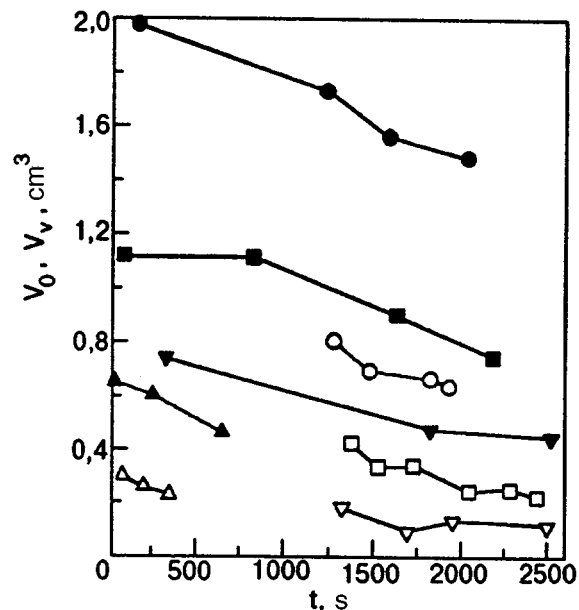

FIG. 3. Time dependences of true V_0 (light symbols) and visible V_v (dark symbols) volumes of impurity–helium samples with different impurity centers: Ne (squares), N_2 (nablas), Ar (triangles), and Kr (circles) in a series of ''removal–immersion'' cycles in the bulk of He II.

the accumulating tube with thermometer *13* (see Fig. 1) fixed to it was introduced in the cup with the sample located at the bottom so that the thermometer was immersed in the sample completely. The changes in the shape and the apparent volume of the sample were recorded by a video camera through observation slits in the Dewar flask. The recording of temperature and sample image was started when the cylinder was filled with helium. After the helium supply to the cylinder with the help of the thermomechanical pump *12* was terminated, the level of helium in the cylinder lowered. The visible volume of the sample decreases considerably as the level of helium passed through the sample, but the temperature in the sample remained constant.

After the removal of liquid helium from the cup, the sample was heated. As a rule, the samples under investigation were cylindrical and preserved their shape, decreasing in size. By the end of heating, the shape of the samples changed to spherical. The visible volume of the sample was determined according to the sample image in video recording.

2.2. Methods of investigation of samples obtained by introducing gas jets passed through the rf discharge region into HeII

Figure 2 shows schematically the setup for the experiment on the stability of IH samples obtained by introducing into He II the gas mixtures after their passage through the rf discharge region. Samples were accumulated in a cylinder of diameter 3.5 cm. A mesh disk of diameter 3 cm fixed on a special tie-rod was located at the bottom of the cylinder during accumulation and made it possible to extract the sample from the He II volume when the accumulation was completed. A semiconducting thermometer fixed at the center of the disk remained inside the sample after its growth. A second semiconducting thermometer was fixed to another tie-

rod and measured the temperature above the sample surface. Its position could be changed in the course of the experiment.

Thermoluminescence of IH samples containing stabilized active particles was detected by a monochromator MDR-1 supplied with a photomultiplier FEU-136 operating in the photon counting mode.

The systems of temperature and luminescence recording were automated on the basis of a DVK-3 computer and a set of KAMAK standard blocks.

3. EXPERIMENTAL RESULTS

3.1. Temporal stability

Visual observation of the shape and visible volume of IHSP samples placed in the cylinder with HeII revealed the absence of any visible change after prolonged holding (up to 10^4 s). On the contrary, the removal of the samples from liquid helium and their holding at $T = 4–6$ K and $P = 10$ torr during ~ 150 s resulted in their decomposition manifested in a decrease in the visible and true volumes. After each sample ''removal–immersion'' cycle, the visible V_v and the true V_0 volumes were determined. The results of these measurements for impurity–helium samples with different impurity centers are shown in Fig. 3. The initial ratio V_v/V_0 was 2.6 for Ne and 2.2 for Kr and Xe. It can be seen that the visible and true volumes decrease almost linearly with time. Table II gives the initial values of true and visible volumes of the samples and their relative change after 4–6 ''removal–immersion'' cycles in He II. The relative decrease in true volumes $(\Delta V_0/V_0) \cdot 100\%)$ varied from 16–23% for Ar, Kr, Xe, and to 34–38% for N_2 and Ne.

TABLE II. Values of true and visible volumes of impurity-helium samples (Im = Ne, Ar, Kr, Xe, N_2) immediately after accumulation and their relative decrease after 4–6 ''removal-immersion'' cycles in He II.

Impurity particle	Initial volume, cm³		Relative decrease in volume	
	true V_0	apparent V_v^0	true V_0/V_0^1	visible V_v^0/V_v^1
Ne	0.425	1.16	1.6	1.5
Ar	0.378	1.63	1.2	1.8
Kr	0.79	2.0	1.3	1.4
Xe	0.30	0.66	1.3	1.42
N_2	0.17	0.75	2.1	1.8

3.2. Stability during heating

After measuring the true and visible volumes, the samples were placed on the bottom of the cylinder filled with liquid helium. An accumulation tube with a thermometer fixed to it was introduced in the cylinder. Usually, the thermometer was immersed in the sample, reaching the bottom of the container. After the helium supply to the cylinder was terminated, the level of helium decreased; the visible sample volume decreased considerably as the level of helium passed through the sample. In this case, the thermometer detected the constant temperature ~ 1.7 K. The sample temperature started increasing only after evaporation of the entire amount of liquid helium from the cylinder, and the sample volume decreased further.

Figure 4 shows typical thermograms of heating and time dependences of visible volumes for impurity–helium samples with various compositions. It can be seen that the sample volume changes most noticeably at temperatures 3–5 K for Ne–He samples and 5–6 K for Kr–He samples. A strong heat release accompanied with instantaneous decomposition was observed only for Ne–He samples (see Fig. 4a); in remaining cases, a decrease in volume to a certain stationary value was observed. Table III contains the values of relative decrease in visible volume during heating and in the entire course of the experiment. It should be noted that as the level of helium passed through the sample, the visible volume changed from the value V_v^1 observed after 4–6 ''removal–immersion'' cycles (see Table II) to the value V_v^2 (see Table III) observed immediately before the sample heating, i.e., by a factor of 1.12 (for Xe) or 2.2 (for Ne).

3.3. Determination of elemental composition

After the completion of the stability test for the samples, impurity particles were accumulated, and their number was measured. Under the assumption made in Ref. 3, this allowed us to determine the following parameters of impurity–helium samples: volumes of IH clusters $V_c = V_0/N_{Im}$, their diameters $D = 2[3V_c/(4\pi)]^{1/3}$, and the stoichiometric ratio $S = V_c/V_f - 1$ for IH samples (where $V_f = 46$ Å³ is the volume occupied by helium atoms in the liquid at $T = 1.7$ K).

Table IV contains the measured number of impurity particles immediately after their accumulation as well as after short-term sample holding above the He II surface. In order to illustrate the decrease in the true volume of the samples
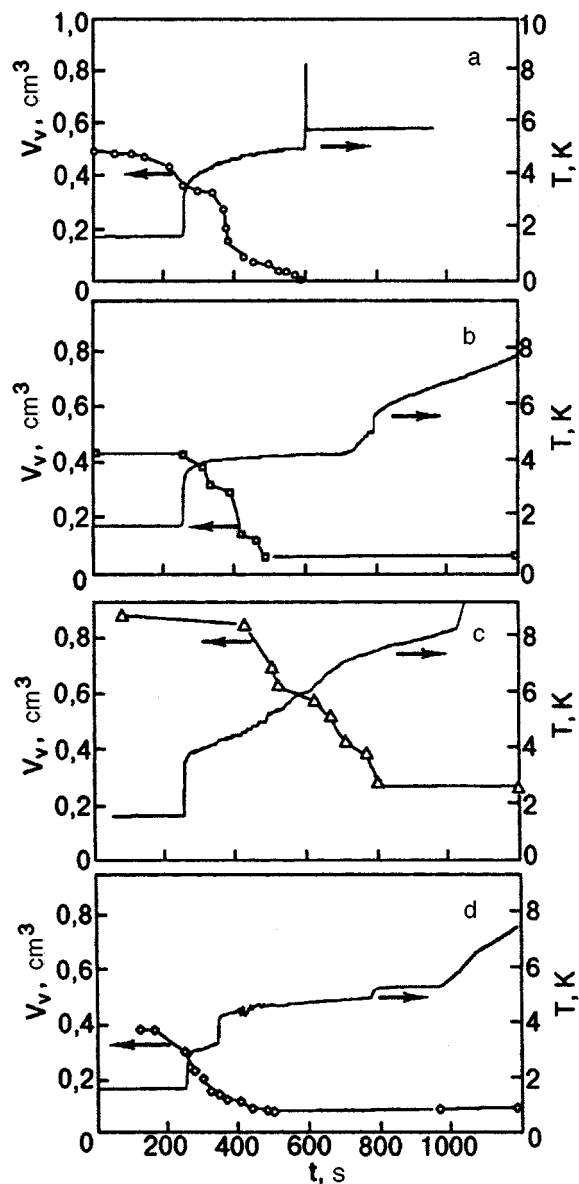

FIG. 4. Time dependences of visible V_v volumes of impurity–helium samples (Im=Ne (a), N_2 (b), Kr (c), and Xe (d)) for heating and corresponding thermograms of heating. The samples are obtained by introducing gas flows not subjected to the action of a rf discharge into He II.

(as a result of ''removal–immersion cycles required for their determination; see Fig. 3), Table IV also shows the ranges of volume variation and the corresponding variation of stoichiometric ratio. The parameters of the samples which were evaporated (as in Ref. 3) immediately after the determination

TABLE III. Relative change in visible volumes of impurity-helium samples during heating of dry samples (V_v^2/V_v^k) and in the course of entire experiment (V_v^0/V_v^k).

Impurity particle	V_v^2/V_v^k	V_v^0/V_v^k
Ne	3	10
Ar	4	12
Kr	4	8.5
Xe	5	8
N_2	6	15

TABLE IV. Determination of elemental composition of impurity-helium samples.

Impurity atom (molecule) Im	No. of experiment	Sample volume, cm^3		Number of particles in sample $N_{Im} \cdot 10^{-20}$	IH cluster volume V_c, Å^3	Initial diameter of IH cluster D, Å	Stoichiometric coefficient S
		initial V_0	after annealing V_t				
Ne	1*	0.20	-	2.64	757	11.3	16
	2	0.425–0.266	-	2.0	2125–1330	16.0	45–28
	3	0.174–0.133	-	0.813	2140–1635	16.0	45–34
	4*	0.346	-	1.33	2601	17.06	55
Ar	1*	0.43	-	3.77	1140	12.96	24
	2*	0.403	-	1.44	2799	17.5	60
	3*	0.465	-	1.65	2818	17.52	60
	4	0.378–0.32	0.028	1.74	2172–1839	16.0	46–39
Kr	1	0.79–0.60	-	2.92	2705–2054	17.2	58–44
	2	0.36–0.25	0.07	2.0	1800–1250	15.09	38–26
	3*	0.23	-	1.07	2150	16.01	46
Xe	1	0.30–0.203	-	1.96	1530–1036	14.3	32–22
N$_2$	1	0.17–0.08	-	1.26	1349–635	13.7	28–13

Note: Asterisk marks experiments in which samples were evaporated immediately after the measurement of their volume.

of true volumes for evaluating the number of impurity particles in them are also given in the table for comparison.

In some experiments, the true volumes V_t of the ''dry'' impurity–helium samples were measured after the completion of heating cycles; these values are also given in Table IV. The true volumes measured in this case were close to the values of visible volumes.

3.4. Heating of samples containing active particles

Figure 5a shows thermograms for a ''dry'' Kr–helium sample recorded in the experimental geometry shown in Fig. 2. The first thermometer was inside the sample, while the second was 1 mm above the sample; the helium pressure in the Dewar flask was 10 torr. The supply of HeII to the cylinder was terminated, and the sample was heated as the level of helium in the cylinder decreased. It can be seen from Fig. 5a that the temperature in the sample at the initial stage was considerably lower than the temperature outside the sample, and the temperature detected by the inner thermometer increased abruptly and becomes close to the temperature outside the sample only after the instantaneous decomposition of the sample occurring at the temperature registered by the outer thermometer which is close to the temperature ~ 7–8 K of the decomposition of IH sample reported earlier.[2,4]

Figure 5b shows the time dependence of the thermoluminescence intensity for a sample at a wavelength $\lambda \sim 525$ nm. The glow is due to luminescence of nitrogen impurity atoms stabilized in the sample. In the temperature range 2.5–4.5 K, thermoluminescence has a high intensity and is accompanied by a considerable decrease in the sample volume. A further heating quenches the glow, and the sample volume remains unchanged up to instantaneous decomposition. The decomposition is accompanied by a high-intensity luminescence glow and a temperature jump up to 8.3 K. A similar decomposition is observed for all IH samples containing active particles.

3.5. Effect of external pressure on sample stability

Experiments on the effect of external pressure on the sample stability were made according to the scheme presented in Fig. 2. Thermogram of sample heating (with the thermometer inside the sample) and the intensity of its luminescence were recorded under a pressure increasing after the pumping of helium vapor from the Dewar flask was terminated.

Figure 6 shows a thermogram of heating and the temperature dependence of thermoluminescence of the sample for a Kr–helium sample. The pressure in the Dewar flask increased as a result of heating and amounted to 100 torr at the moment of instantaneous decomposition. It can be seen that the decomposition of the sample in this case takes place at a higher temperature $T \sim 10$ K; the temperature jump is also much stronger (up to ~ 18 K).

At a slower heating, Ar–He and Kr–He samples could be heated up to 13 K, the pressure in the Dewar flask being ~ 500 torr. The drop of helium pressure due to evacuation of helium vapor from the Dewar flask at this temperature led to instantaneous decomposition of the sample accompanied by a luminous glow.

Thus, it has been established that the stability of IH samples is higher under a higher pressure of the helium medium.

4. DISCUSSION OF RESULTS

The obtained results make it possible to analyze the composition of impurity–helium samples and lead to the conclusion that the composition changes as a result of holding outside helium.

4.1. Analysis of initial stoichiometric ratios

Initial stoichiometric ratios for impurity–helium samples obtained by injecting gas jets which were not subjected to the action of an rf discharge (see Table IV) amount to 16–55
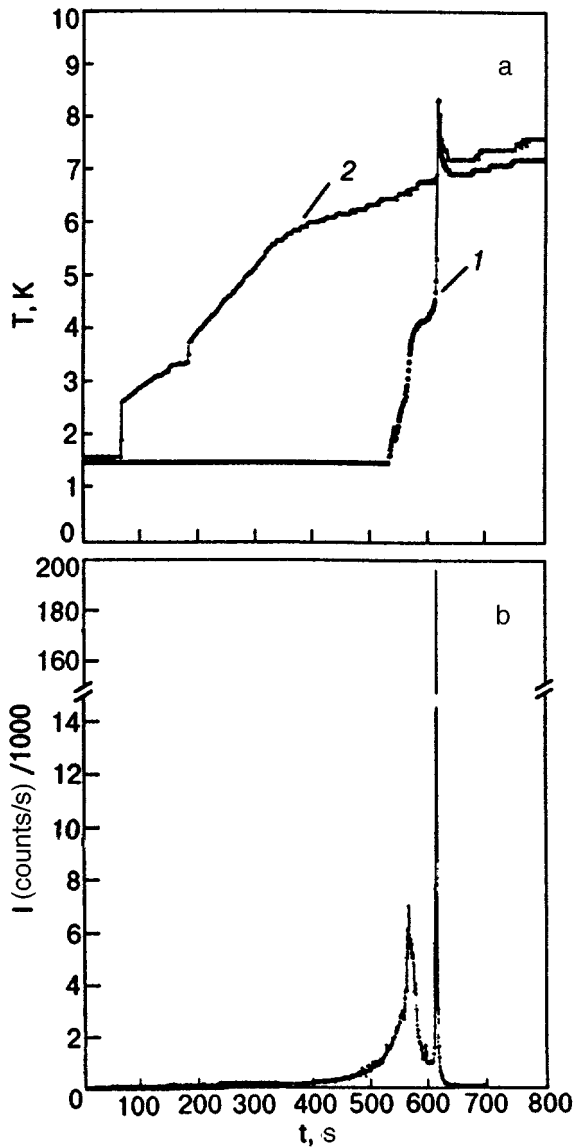
FIG. 5. (a) Thermograms of heating for Kr–He sample obtained by introducing of a gaseous mixture [Kr]:[He] = 1:200 after its passage through the rf discharge region into He II: curve *1* was plotted according to the readings of the thermometer in the sample (see Fig. 2), and curve *2* corresponds to the readings of the thermometer above the sample. (b) Thermoluminescence kinetics of a Kr–He sample at $\lambda = 525$ nm under the helium pressure in the Dewar flask of 10 torr.

FIG. 6. (a) Thermograms of two consecutive heating of the mesh with the sample (curve *1*) and without sample (curve *2*) upon an increase in pressure in the Dewar flask from 10 to 100 torr. (b) Thermoluminescence kinetics of a Kr–He sample at $\lambda = 525$ nm under increasing helium pressure.

for Ne–He, 24–60 for Ar–He, 26–58 for Kr–He, and 13–28 for N_2–He samples. In the model of IHSP as a phase of impurity–helium clusters frozen together, we can conclude that clusters have one or two filled helium shells surrounding heavy impurity particles.

Before analyzing the obtained results, it is expedient to consider theoretically the possibility of existence of IHSP with a varying stoichiometric composition.

Phenomenological Model of IHSP

We developed a simplified phenomenological approach based on the assumptions normally used for studying the optical properties of atoms in liquid helium.[8–10] The main fundamental assumption concerns the additivity of the contributions of the energy of helium with a cavity of a certain shape and the energy of an 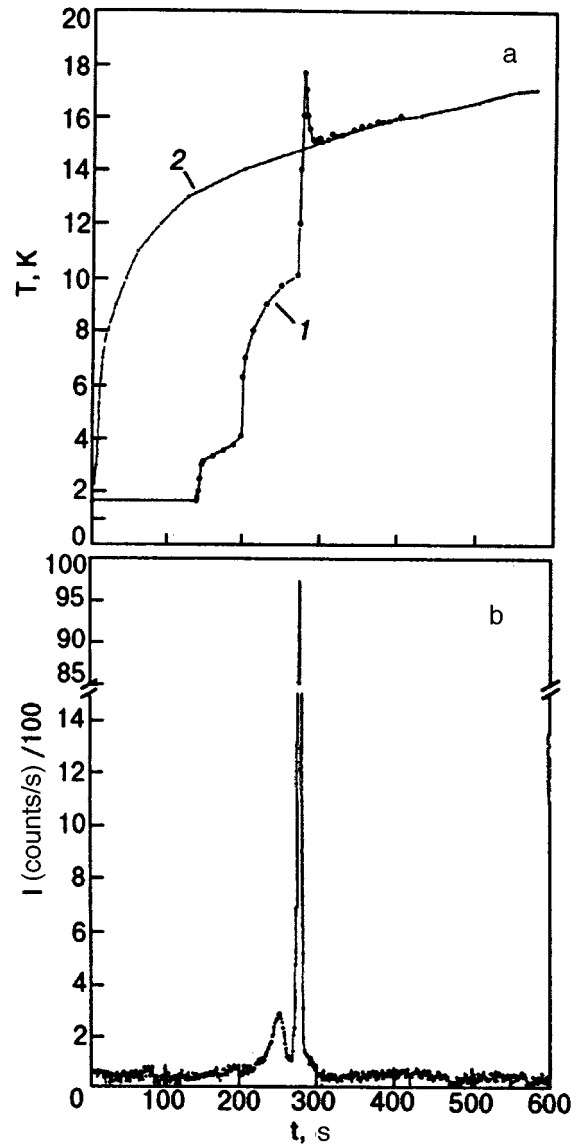atom perturbed by the ambient to the total energy of the system.[9] This assumption makes it possible to obtain a satisfactory description of the pressure dependence of displacement and width of spectral lines for atoms in helium.[8–10]

In the first approximation, we can neglect the form of mutual arrangement of impurity centers in the IHSP lattice in view of fast damping of the van der Waals interaction of impurity particles with helium atoms. In this case, the contribution from the interaction of impurity atoms to the energy of the system can be neglected the more so in view of the large separation between impurities. According to calculations, this contribution is small even for a transient state of merging of two one-layer impurity–helium clusters.

Thus, an analysis of the impurity–helium phase on the whole boils down to an analysis of one of its cells having the composition Im He_n. The expression for the system energy normalized to a cell has the form

$$E = n\varepsilon_{He} + E_{cav} + E_{int},$$

where ε_{He} is the average energy per atom of the He- subsystem, E_{cav} the energy of cavity formation, and E_{int} the energy of interaction of an impurity center with the ambient. The dependence of ε_{He} on the average density ρ of the helium subsystem is defined, as usual, by the formula

$$\varepsilon_{He} = \rho b/2 + \rho^{(1+\gamma)} c/2,$$

where the constants $b = -888.81$ K·Å^3, $\gamma = 2.8$, and $c = 1.045537 \cdot 10^7$ K·Å$^{3+3\gamma}$, given in Ref. 11 ensure the correct description of the properties of liquid helium at $T=0$, viz., the atomic volume $V = [-(1+\gamma)c/b]^{1/\gamma} = 45.8$ Å^3, the energy per atom $\varepsilon = (\gamma/(\gamma+1))(b/2V) = -7.15$ K, and the isothermal compressibility $k = -2V^2/\gamma b = 1.20 \times 10^{-2}$ atm^{-1}. The energy of a spherical cavity of radius R, i.e.,

$$E_{cav} = \sigma 4\pi R^2 + P \frac{4\pi}{3} R^3 + \frac{4\pi\hbar}{8m} \int_0^\infty \frac{(\nabla\widetilde{\rho})^2}{\widetilde{\rho}} r^2 dr$$

is the sum of the surface energy proportional to the surface tension $\sigma = 0.274$ K/Å^2,[12] the work done to create the cavity, which is proportional to the external pressure P, and the term representing the kinetic energy E_k associated with the existence of a helium density gradient at the edges of the cavity. The contribution to this term comes from the spherical layer in which the helium density $\widetilde{\rho}$ changes significantly from 0 at the center to a constant value ρ. The energy

$$E_{int} = 4\pi \int_0^\infty \widetilde{\rho}(r) V_{int}(r) r^2 dr$$

of interaction of an impurity center with the helium surroundings is determined by the interaction potential $V_{int}(r)$.

We introduce the following simplifying assumptions: the distribution of helium around an impurity center is spherical, an impurity atom is incompressible, i.e., the cavity radius $R = const$, and possible changes in the distribution of helium density $\widetilde{\rho}$ in the vicinity of an impurity center upon a change in the IHSP composition are reduced to its multiplication by a constant. These assumptions are based on the fact that the separation between atoms in liquid helium is much larger than the distance corresponding to the minimum of the He–He pair interaction. The analysis of solitary impurity–helium clusters by the density functional method[13] led to the conclusion that the He density distribution in the first coordinate sphere around an impurity center (for the KrHe$_n$ cluster) does not change starting from $n = 20$: this is in accord with the approximation of a rigid impurity atom.

Bearing in mind that the energy of interaction E_{int} as well as the kinetic energy E_k under these approximations are linear functions of density, i.e.,

$$E_{int} + E_k = \rho 2\Delta b,$$

we can write the energy of IHSP in the form

$$E = \frac{(nb + \Delta b)}{2} \rho + \frac{nc}{2} \rho^{(1+\gamma)} + \sigma 4\pi R^2 + \frac{4\pi}{3} R^3 P. \quad (1)$$

Since $P = \rho^2 \partial E / \partial\rho$, we can treat the obtained expression as an equation of state of IHSP. We will use this expression for

an analysis of Rg–helium systems (Rg=Ne, Ar, Kr, Xe) of an arbitrary composition RgHe$_n$. For zero pressure, the helium density can be determined from the formula

$$\rho = [-(1+\gamma)nc/(nb+\Delta b)]^{1/\gamma}.$$

This leads to the following expression for the binding energy of an impurity atom:

$$E_b = E(RgHe_n) - \varepsilon n. \quad (2)$$

For $n \to \infty$, we have $E_b = \Delta b/2V + \sigma 4\pi R^2$. We equate this quantity to the binding energy for a solitary atom obtained by Dalfovo[13] and then find Δb on the basis of the estimate $R \cong r_e - 0.2$ Å following from an analysis of graphical data[13] obtained for the helium density in the vicinity of an impurity, where r_e is the equilibrium distance for diatomic Rg–He molecules (borrowed from Ref. 14). The results of calculations based on formulas (1) and (2) and valid for a rigid impurity atom are presented in Fig. 7. All systems exhibit a monotonic increase in the binding energy and in the helium density upon a decrease in the stoichiometric ratio. It should be noted that for large densities comparable with the density of liquid helium, our arguments are not quite correct. However, we do not aim at deriving the equation of state at the moment (which is a complicated and interesting problem). It would be reasonable to assume that the "solidification" of helium in the entire IHSP cell is just the condition of its existence. For this reason, the criterion of existence of IHSP can be established on the basis of the equation of state of the liquid:

$$\rho \geq \rho_c,$$

where ρ_c os a certain critical density corresponding to solidification of helium. This criterion determines implicitly the maximum stoichiometric ratio in IHSP. Naturally, this ratio is exactly observed when an IHSP sample is grown in excess of liquid helium as in our experiments. A reliable estimate of the number n can be obtained from the ratio of atomic volumes of solid and liquid helium during freezing, which is equal to 0.88,[15] extrapolated to $T=0$, which gives $1/\rho_c = 0.88V = 40.3$ Å^3. The corresponding values are given in Fig. 7. Since the only effect of external pressure for pure helium is just the attainment of critical density, helium in peripheral regions of an IHSP cell is a quantum-mechanical object just like ordinary solid helium. On the other hand, the earlier quantum-mechanical analysis of a one-layered helium cluster[4,5] revealed that the number of quantum degrees of freedom for helium in the latter case decreases in view of rigid nature of radial vibrations of the helium shell. The corresponding solid state naturally has a high density. It can be determined by extrapolating the density of solid helium to the value at $T=0$ along the melting phase-transition curve and amounts to $1/\rho_c = 34.41$ Å^3.[15] This result can be used for calculating the values of the stoichiometric coefficient ν for strongly bound "classical" helium. Figure 7 presenting the values of ν shows that these values are quite close to the occupation numbers for the first coordination sphere calculated by Dalfovo.[13]

Thus, the above analysis shows that according to simple physical considerations concerning the short range of the
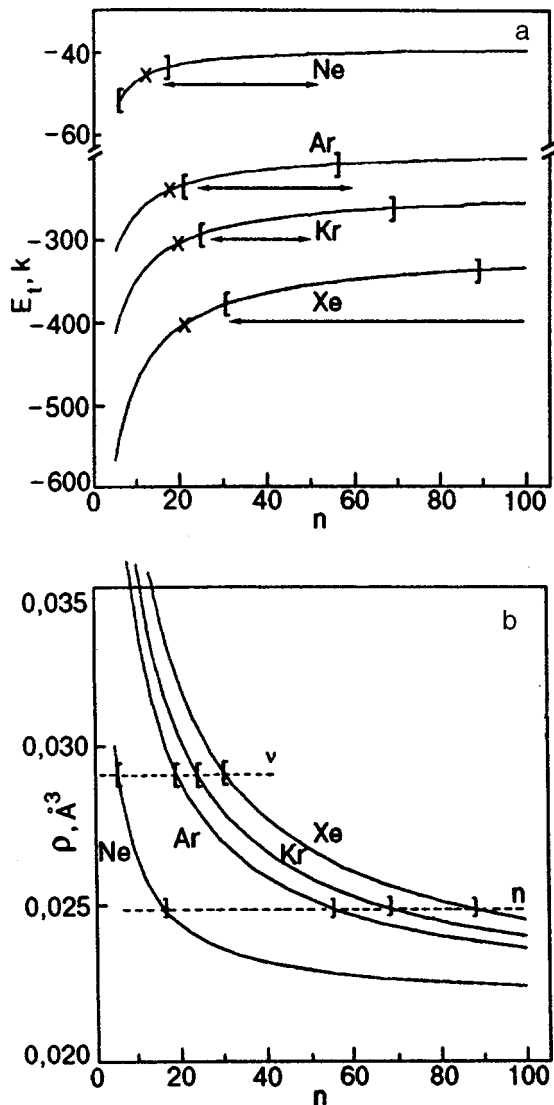
574   Low Temp. Phys. 23 (7), July 1997

Boltnev et al.   574

FIG. 8. Theoretical diagram of IHSP stability for the compositions $NeHe_\nu$ (curve *1*) and $XeHe_\nu$ (curve *2*). The phase diagrams for helium (curve *3*), classical helium (curve *4*), and IHSP as a system of clusters $NeHe_{12}$ (curve *5*) are shown for comparison.

FIG. 7. Dependence of the binding energy (a) and the average helium density (b) on n in the impurity–helium solid phase $RgHe_n$ (Rg=Ne, Ar, Kr, Xe); theoretical estimates of the number ν of rigidly bound helium atoms and of the total number n of helium atoms per impurity center (square brackets) and the range of experimental values of stoichiometric coefficients ($\leftrightarrow$), $\times$ marks the number of helium atoms in the first coordination sphere, obtained by Dalfovo.[13]

strongly. This allows us to assume that the IHSP stability is ultimately determine d by the conditions under which helium of the first coordination sphere starts evaporating. Estimating the helium vapor pressure under these conditions, i.e.,

$$p_{He} = p_0(T)\exp(-(D_{HeA} - D_{HeHe})/T)),$$

where $D_{HeA} - D_{HeHe}$ is the difference in the energies of interaction between He and an impurity center and between He–He atoms, $p_0(T)$ being the vapor pressure over classical solid helium calculated by us earlier,[5] we obtained Rg–IHSP stability diagrams presented in Fig. 8.

4.2. Analysis of decomposition of IH samples

The analysis carried out above explains why the stoichiometric ratio for freshly prepared samples is much higher than that in Ref. 3. Moreover, the kinetics of decomposition which includes two stages, i.e., the initial smooth stage and subsequent fast stage (see above) becomes qualitatively clear.

The first stage of gradual decomposition of the samples is manifested during consecutive removals of IH samples from the bulk of HeII and their holding at $T \approx 4-6$ K. Sample decomposition was detected from the decrease in true and visible volumes (see Fig. 3). Formally, a decrease in the sample volume with a constant number of impurity particles in the sample indicates a decrease in the stoichiometric ratio, Such a decrease was observed for all the samples under investigation (see Table IV).

The experimentally obtained rates of decrease in the true volumes of impurity–helium samples make it possible to estimate the characteristic time of the first stage of decomposition (Table V). This time varies from $2 \cdot 10^3$ s for a Kr–He sample to $8.5 \cdot 10^3$ s for a N_2–He sample. We assume that the sample consists mainly of solidified helium, and a decrease in the volume is due to evaporation of He atoms from its branched surface.

Van der Waals interaction, the stoichiometric ratios for a stable "classical" IHSP must be close to the occupation numbers for the fist coordination sphere of an impurity particle. However, helium atoms in the first coordination sphere have small amplitudes of zero-point vibrations, and the corresponding decrease in the zero-point vibrational energy is sufficient for solidification of a certain number of neighboring helium atoms due to effects of short-range correlations between them. However, helium atoms belonging to a remote (far) coordination sphere are bound by energies typical of the He–He interaction, i.e., much more weakly than the atoms from the first coordination sphere which interact with the impurity atom.

Consequently, an IHSP with a composition AHe_n can be regarded as a system $(AHe_\nu)He_{n-\nu}$ if we single out helium from the first coordination sphere which is bound more
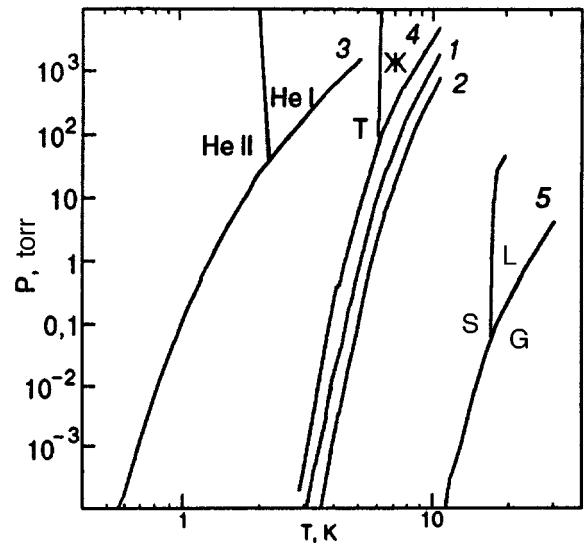
TABLE V. Analysis of decomposition of ''dry'' impurity-helium samples at external temperature $T \sim 4-6$ K.

Impurity particle in sample	Sample volume V_0, cm^3	Time of holding sample of $T \sim 4-6$ K t_T, s	Change in sample volume ΔV_0, cm^3	Sample decomposition rate dN/dt, particle/s	Lifetime of sample with $V_0 = 1$ cm^3 at $T \sim 4-6$ K t_c, s
Ne	0.425	540	0.19	$9.6 \cdot 10^{18}$	2842
Ar	0.378	312	0.07	$6.3 \cdot 10^{18}$	4457
Kr	0.78	385	0.19	$1.4 \cdot 10^{19}$	2026
Xe	0.30	150	0.08	$1.44 \cdot 10^{19}$	1875
N$_2$	0.17	600	0.07	$3.3 \cdot 10^{18}$	8571

The first stage accompanied with intense evaporation of helium in the absence of merging of heavy centers naturally leads to sample cooling. This follows not only from the fact that the temperature in the sample at this stage is lower than in the absence of helium (which can be explained by a high heat capacity of IHSP and liquid helium), but also from the presence of ''steps'' on the thermogram for attenuating temperature-dependent luminescence of nitrogen impurity atoms (See below and Fig. 5). The fact that the temperature in the sample at this stage is considerably lower than near the sample explains why this stage was not detected in the first experiments: the change in the sample volume occurred at the temperature 7–8 K indicated by the outer thermometer, i.e., near the temperature at which the second stage of decomposition begins.

At the second stage, energy is liberated as a result of merging of heavy particles, and the temperature in the bulk of the sample becomes higher than in the background measurements.

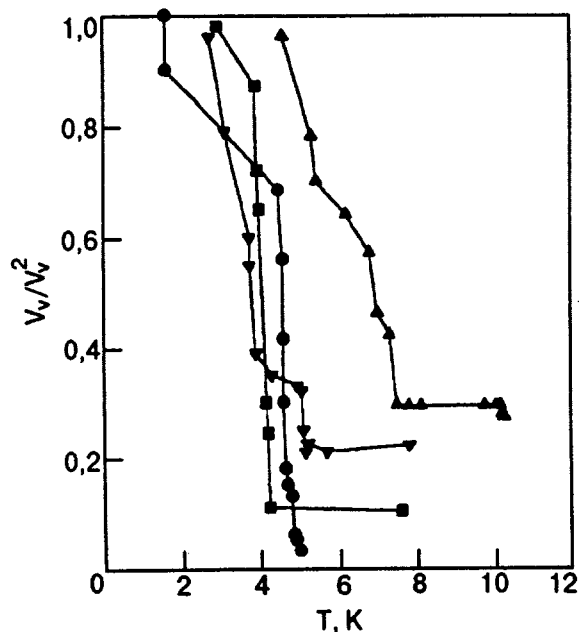Figure 4 characterizes the second stage of decomposition. The temperature range in which the volume decreases abruptly depends on the type of impurity particles. Figure 9 shows the temperature dependences of the relative volumes of the samples, which indicate that the second stage occurs in the temperature range 3–4 K for the Ne–He sample and 5–7 K for the Kr–He sample.

If, however, the Kr–He sample was obtained by introducing a gas jet after its passage through the rf discharge region onto He II, the stage of merging of impurity particles is manifested in the luminescence of nitrogen impurity atoms (see Fig. 5b). Since nitrogen impurity ($10^{-3}\%$) is always present in a real gas mixture, the passage of the gas jet through the discharge region leads to the formation of metastable atoms N(^2D) which are stabilized in the helium medium for long periods of time $\sim 10^4$ s. The prohibition on the $^2D - ^4S$ transition of the nitrogen atoms is removed and the lifetime is reduced to 15–30 s only as a result of merging of such an atom with another heavy particle, viz., a Kr atom.[7,16]

It should be noted that all the samples containing ''active particles,'' i.e., obtained by condensation of gas jets having passed through the rf discharge region, suffered instantaneous decomposition. In the case when the samples were obtained without the action of the rf discharge on the jet, instantaneous decomposition was observed only for the Ne–He sample, while the remaining samples retained their volume upon further heating up to 12 K after its strong reduction by a factor of 8–12 (see Table IV).

An increase in pressure stabilizes IHSP, and its ultimate decomposition occurs in the higher-temperature region. The temperature interval of decomposition for heavy impurity centers is wider than for Ne impurity centers.

The breakdown of the helium–impurity phase can be used for carrying out chemical reactions at ultralow temperatures. The addition of a small amount of chemically active particles to the inert mixture [Rg]/[He] undergoing condensation leads to the formation of an impurity–helium solid phase with stabilized chemical reagents in superfluid helium. If we then remove the sample from He II and heat it, association of impurity particles leading to a reaction between chemical reagents will take place. The sample stability and the temperature region of the chemical reaction can be varied by choosing appropriate main impurity ([Rg]=Ne, Ar, Kr, etc.). This opens new prospects for studying reactions with matrix-isolated particles, and the parameters of the matrix (impurity–helium phase) can be varied over a wide range.

FIG. 9. Experimental temperature dependences of relative variations of visible volumes for various impurity–helium samples (Im = Ne (●), N$_2$ (■), Kr (▲) (dark triangles) and Xe (dark nablas ▼).

CONCLUSIONS

(1) The composition of impurity–helium samples obtained by injecting impurity particles from a gas jet which has not been subjected to the action of a rf discharge into HeII is determined experimentally. The stoichiometric ratios for all the particles under investigation (Ne, Ar, Kr, Xe, and N_2) are much larger than the values predicted by the model of one-layered clusters frozen together. The theoretical possibility of freezing together two-layered clusters is substantiated in the framework of the continual model of the helium subsystem of the IHSP filling the space between rigid impurity centers.

(2) The breakdown of impurity–helium samples removed from He II under low pressures is investigated. It is shown that the failure occurs in two stages. At the first stage, ''weakly bound'' helium from the second coordination helium spheres surrounding impurity particles evaporates, leading to sample cooling. The second stage begins at temperatures 3–6 K and is characterized by the breakdown of the first coordination spheres, the association of heavy impurity particles, a considerable decrease in volume, and sample heating. It is found that the temperature ranges in which the failure of IH samples takes place are determined by the type of the impurity particle: the lighter the particle, the lower the temperature at which the decomposition processes begin (3 K for N_2 and Ne and 5 K for Kr). The type of the impurity particle also determines the nature of decomposition: instantaneous decomposition of IHSP is observed for Ne, while samples with Ar, Kr, Xe and N_2 are characterized by a steady-state value of the volume at the end of decomposition. A considerable decrease in volume during decomposition is recorded when the temperature increases to 7 K: by a factor of 8 for Kr– and Xe–He samples and by a factor of 12–15 for Ar– and N_2–He samples.

The presence of even a small fraction of active impurity particles ($[N] \sim 10^{-3}\%$) in impurity–helium samples leads to their instantaneous decomposition as a result of heating.

(3) Thermoluminescence of IHSP accompanying the decrease in the volume of IH samples at temperatures 3–4.5 K has been observed for the first time. Luminescence is associated with merging of impurity particles as well as with the recombination of N atoms during IHSP decomposition.

(4) It is found that $T = 7$ K is the temperature of ultimate decomposition of IHSP during its heating under a helium vapor pressure $P = 10$ torr. All processes in IHSP such as a decrease in volume, luminescence, and heat release occur up to this temperature.

(5) The effect of external pressure on the stability of IH samples is investigated It is found that an increase in pressure improves the stability of the sample, and their decomposition occurs at a higher temperature, its nature remaining unchanged.

(6) Insulation of chemically active particles by solidified helium in IHSP at $T = 1.5$ K allows us to analyze their properties on one hand and makes it possible to carry out chemical reactions at low temperatures during the IHSP decomposition on the other hand.

It should be interesting to apply the methods of x-ray diffraction analysis for determining the IHSP structure and for investigating the rearrangement of impurity particles during its decomposition.

* E-mail: khmel@binep.ac.ru

[1] E. B. Gordon, A. A. Pel'menev, E. A. Popov et al., Fiz. Nizk. Temp. **15**, 86 (1989) [Sov. J. Low Temp. Phys. **15**, 48 (1989)].

[2] E. B. Gordon, V. V. Khmelenko, A. A. Pel'menev et al., Chem. Phys. Lett. **155**, 301 (1989).

[3] R. E. Boltnev, E. B. Gordon, I. N. Krushinskaya et al., Fiz. Nizk. Temp. **18**, 819 (1992) [Sov. J. Low Temp. Phys. **18**, 576 (1992)].

[4] E. B. Gordon, V. V. Khmelenko, A. A. Pel'menev et al., Chem. Phys. **170**, 411 (1993).

[5] E. B. Gordon, A. A. Pel'menev, E. A. Popov et al., Fiz. Nizk. Temp. **18**. 1365 (1992) [Sov. J. Low Temp. Phys. **18**, 952 (1992)].

[6] M. Hartmann et al., Phys. Rev. Lett. **75**, 1566 (1995).

[7] R. E. Boltnev, E. B. Gordon, V. V. Khmelenko et al., Chem. Phys. **189**, 367 (1994).

[8] T. Kinoshita, K. Fukuda, Y. Takahashi, and T. Yabuzaki, Z. Phys. **B98**, 387 (1995).

[9] A. P. Hickman, W. Steet, and N. F. Lane, Phys. Rev. **B12**, 3705 (1975).

[10] S. Kanorsky, A. Weis, M. Arndt et al., Z. Phys. **B98**, 371 (1995).

[11] S. Stringari and J. Treiner, J. Chem. Phys. **87**, 5021 (1987).

[12] D. O. Edwards and W. W. Saam, in Progress in Low Temperature Physics VIIIA, North Holland, Amsterdam (1978).

[13] F. Dalfovo, Z. Phys. **D29**, 61 (1994).

[14] R. Cambi, D. Cappeletti, G. Luiti, and F. Pirani, J. Chem. Phys. **95**, 1852 (1991).

[15] Handbook on Physicochemical Foundations of Cryogenics [in Russian] (ed. by N. P. Malkov), Energoatomizdat, Moscow (1987).

[16] R. E. Boltnev, E. B. Gordon, V. V. Khmelenko et al., J. Chim. Phys. **92**, 362 (1995).

Translated by R. S. Wadhwa

Free and self-trapped excitons in rare-gas cryocrystals: coexistence and mixing of states

I. Ya. Fugol' and E. I. Tarasova

B. Verkin Institute for Low Temperature and Engineering, National Academy of Sciences of the Ukraine, 310164 Kharkov, Ukraine*

The absorption spectra for rare-gas cryocrystals are calculated taking into account one-phonon scattering and multiphonon interaction of free excitons with local lattice vibrations. The possibility of coexistence of free and self-trapped excitons in nonequilibrium states above the bottom of the exciton band is discussed on the basis of a comparison of the free exciton energy with exciton damping in the one-phonon scattering and during transitions to exciton-vibron states. It is found that free exciton damping at low temperatures is mainly determined by one-phonon scattering in the entire exciton band only for xenon. In argon and krypton crystals, both types of damping make comparable contributions. The probability of transition of an exciton to self-trapped states in neon is so high that the existence of band excitations is unlikely. © *1997 American Institute of Physics.* [S1063-777X(97)01207-3]

INTRODUCTION

The lowermost exciton states in rare-gas solids (RGS) are genetically related to a Rydberg-type atomic state and are characterized by an intermediate excitation radius which is much larger than the radius of the ground state, but does not exceed the distance to nearest neighbors in the lattice. As a result (and also due to high deformability of the cryocrystal lattice), excitons in RGS possess a number of peculiar properties. According to the type of the exciton–phonon interaction, the situation in RGS can be treated as an intermediate case, which leads to a nontrivial phenomenon of existence of free (F) and self-trapped (ST) excitons. On one hand, the strong resonant coupling (the exciton band half-width $B \sim 0.5$ eV) leads to a considerable decrease in the energy of band quasiparticles relative to the local crystal excitation level E_M in the nondeformed lattice (see the diagram in Fig. 1). On the other hand, an exciton can form a potential well due to local lattice deformation in view of the strong exciton-phonon coupling and can be trapped at one or two nearest atoms.[1–6] The depth E_{LR} of the potential of the self-trapped state depends on the exciton-phonon interaction parameter $D = \sqrt{\omega E_{LR}^{1/2}}$ (ω is the characteristic phonon energy) which determines the slope of the potential at the point $E = E_M$, where E_M corresponds to the middle of the band. The quantity D characterizes the electron energy fluctuation during the lattice vibration time $\hbar/\omega$ and determines the width of the absorption spectrum for a local center.[6] A band exciton stays at a lattice site for a short time $\hbar/B \ll \hbar/\omega$ (the adiabaticity condition), and the intensity of its scattering at the local potential is determined by the nonadiabaticity parameter

$$\lambda = D^2/B^2 \ll 1. \tag{1}$$

Weak scattering corresponds to the coherent motion of a band exciton, which is manifested in dynamic narrowing of the absorption line (as compared to a local center) and in its displacement towards the bottom of the band (the wave number $k = 0$). In this case, for $E_{LR} > B$ (the strong coupling condition; see Fig. 1), the population of self-trapped exciton states locally deforming the lattice and their manifestation in the spectrum also become possible. Thus, a weak exciton–phonon scattering and a strong coupling with a local deformation

$$\omega \ll D \ll B < E_{LR}. \tag{2}$$

are observed in RGS.

Table I contains the parameters of exciton–phonon interaction taking into account the existence of two types of self-trapped states: one-center quasi-atomic states (a-STE) and two-center quasi-molecular states (m-STE). All RGS are characterized by very large values of E_{LR} and B as compared to low phonon frequencies.[3] This peculiarity is responsible for considerable difficulties in the calculation of exciton dynamics. We outline here the main problems involving an analysis of various aspects of the exciton-phonon interaction in RGS.

Relatively narrow absorption peaks typical of band quasiparticles are characterized in RGS by a considerable asymmetric region corresponding to higher energies and having a width much larger than the phonon frequency.[1–4] The shape of the bands does not correspond to the model of weak exciton–phonon scattering (especially for Ne and Ar). In spite of the importance of the problem, the origin of the short-wave wing has not been interpreted unambiguously yet. The excited states of the wing with small coefficients of absorption and reflection are used in experiments for effective excitation of the crystals.

The conditions for simultaneous manifestations of band and self-trapped states in absorption spectra were first considered theoretically for a strong exciton–phonon coupling in molecular crystals,[5,6] and then analyzed for a large set of relations between B and E_{LR} also.[7–11] However, the possibility of manifestation of the dual nature of exciton absorption specifically for RGS has not been estimated in view of complexity of the situation (2).
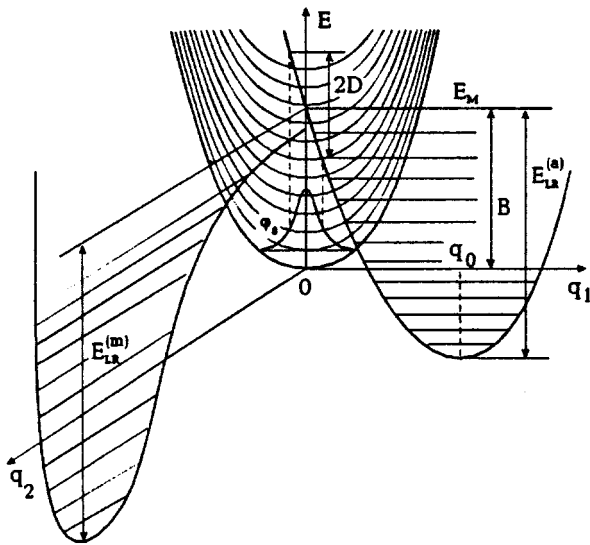
FIG. 1. Formation of band and self-trapped exciton states in the configuration coordinates model: quasi-molecular state (left), quasi-atomic state (right), and band states of excitons (center); φ_0 is the distribution function for the motion of an atom at a lattice site in the ground state.

The peaks of free excitons observed in luminescence of Xe, Kr, and Ar crystals as well as high-intensity exciton emission bands of the a-STE type in Ne and Ar and of the m-STE type in Ne, Ar, Kr, and Xe were considered in terms of coexistence of band and self-trapped states.[1–4] A finite lowermost excitation state which is usually observed in luminescence is attained as a result of long-term multistage relaxation that takes place during the optical lifetime $\tau_0 \sim 10^{-9}$ s, where $\tau_0 \gg \hbar/\omega \sim 10^{-13}$ s. Naturally, it is important to analyze the possibility of coexistence of band and localized excitons at various stages of their energy relaxation in nonstationary states.

Exciton self-trapping is the most important factor determining the dynamics of excited states, distribution of relaxation channels, and transport of excitation energy in RGS. Nevertheless, peculiarities of exciton dynamics and separation of the mechanisms of self- trapping (in a perfect crystal) and localization of excitons at defects as well as separation of energy intervals in the exciton band in which self-trapping is most intense remain disputable.

The peculiar structural and temperature sensitivity of the spectra for free and self-trapped excitons as well as emission of impurity centers populated from the exciton states of the matrix also remain unclear. These dependences cannot be explained without taking into account the intraband relaxation and energy transport by nonthermalized excitons.

The development of the theory for intermediate-radius excitons turned out to be historically connected with the adiabatic approach in the theory of deformation interaction of excitons with the lattice. For this reason, experimental data were interpreted as the coexistence of free and self-trapped excitons separated by a barrier at the adiabatic potential, and the population of ST states was associated with overcoming of a self- trapped barrier by free excitons near the bottom of the band.[1–4] The application of the adiabatic approach to RGS is justified by formulas (1) and (2) and has formed the basis for considerable advances in understanding of self-trapping in wide-band insulators.[1] However, it was pointed out long ago by Rashba[5] in his pioneering work devoted to light absorption in the case of a strong coupling between an exciton and phonons that the disregard of the motion of nuclei does not permit an analysis of the effect taking into account vibrational excitations of ST states near and above the adiabatic barrier state. The difficulties were explained by the mixing of states of free and self-trapped excitons in large-amplitude vibrationally excited states due to an increase in the transparency of the barrier. Subsequently, Joselevich and Rashba[12,13] considered self-trapping of excitons with kinetic energies ε_k at the level of the self-trapping barrier ($\varepsilon_k < 0.1$ eV). The process was induced by a transition to the adiabatic potential in the barrier region. Such a channel is associated with the necessity of a certain initial local deformation as well as a fast transformation of the kinetic energy into the energy of local deformation of the lattice. The estimates obtained for perfect crystals led to values of self-trapping probability which were too low to explain high-intensity ST-luminescence peaks. However, the very important qualitative conclusion that this probability is considerably higher than for thermalized excitons and has a peak at the level of the adiabatic barrier height was obtained.[12] This result served as a strong impetus for subsequent intense studies of possible self-trapping mechanisms for high-energy excitons, including those taking into account nonadiabatic mixing of band excitons and vibrationally excited ST states.

The idea of configuration mixing is based on the quantum-mechanical analysis od the motion of atoms in a lattice. The states of free excitons and vibrationally excited self- trapped states (see Fig. 1) which differ in the configuration of nuclear wave functions the more strongly, the larger the lattice deformation around a local excitation lie above the bottom of the band. Self-trapping can be considered by using a nonadiabatic approach as a transformation of the kinetic energy of a band exciton into the kinetic energy of a local

TABLE I. Parameters of exciton-phonon interaction (energy in eV).

Cryocrystal	Type of state	E_{LR}	B	ω	D	λ	G_0	$\tau_{ST'}$, s	E_b
Xe	m-STE	0.85	0.45	0.0063	0.073	0.03	$4 \cdot 10^{-8}$	$2 \cdot 10^{-8}$	0.16
Kr	m-STE	1.38	0.45	0.0071	0.1	0.05	$1.7 \cdot 10^{-4}$	$4 \cdot 10^{-12}$	0.115
Ar	a-STE	0.77	0.35	0.0091	0.084	0.06	$5.9 \cdot 10^{-4}$	$1.1 \cdot 10^{-12}$	0.08
	m-STE	1.6			0.12	0.12	$3.8 \cdot 10^{-2}$	$1.7 \cdot 10^{-14}$	
Ne	a-STE	0.85	0.2	0.0075	0.08	0.16	$5.5 \cdot 10^{-2}$	$1.2 \cdot 10^{-14}$	0.02

vibrational motion of atoms during tunneling of the nuclear subsystem.

The problems listed above stimulate an analysis of all the approaches proposed earlier for describing the exciton–phonon interaction in order to develop the ideas on the structure and dynamics of intermediate-radius excitons in RGS.

The main aim of this research is the discussion of a more complete concept of coexistence of free and self-trapped excitations in RGS including the range of exciton kinetic energies up to the middle of the band for time intervals starting from absorption ($\tau_a \sim 10^{-15}$ s).

In this publication, we analyze absorption spectra for RGS taking into account one-phonon damping and the coupling between free and self-trapped excitons (Sec. 1), the dispersion range for band excitons which corresponds to the formation of branches of mixed exciton- -vibron states predicted in the model[7,14] (Sec. 2), and consider in detail the problem of coexistence of free and self-trapped excitons in nonequilibrium states above the bottom of the band by comparing the probabilities of exciton scattering by phonons and of damping at local exciton-vibrational states (Sec. 3).

1. MANIFESTATION OF FREE AND SELF-TRAPPED EXCITONS IN ABSORPTION (WEAK DAMPING APPROXIMATION)

The difficulties in the analysis of coexistence of free and self-trapped excitons in the intermediate case of exciton coupling with phonons are associated with the description of delocalized free excitons (F) as well as excitons localized virtually on a lattice site (ST) by using a unified approach. It was shown in publications on the effect of exciton-phonon interaction on the exciton absorption spectra[6–11,15] that the high-energy tail and the main part of the absorption band have the form of a Lorentzian constricted due to the high mobility of a free exciton. It should be recalled that the absorption spectrum for a local center can be described by a wide Gaussian curve. The low-energy of the absorption band in the exciton resonant region decreases exponentially (according to the Urbach law) and is associated with optical transitions to ST states. In order to take into account the F–ST dualism in exciton absorption, two approaches to the problem of excitation eigenstates in the lattice have been developed: (a) the states of an F exciton are used as the basis, and the exciton-phonon interaction with one, two, etc. phonons is taken into consideration consecutively (in order to obtain a local state, the sum of an infinite series should be determined), or (b) the complete set of ST states is used as the basis, to which the operator of resonant transfer of excitation is applied. As a rule, both approaches involve considerable difficulties when attempts are made to obtain a general solution in the case of intermediate coupling.

The application of approach (b) by Cho and Toyazawa[7] resulted in a renormalization on one-site exciton-vibron levels of the ST state (corresponding to a linear exciton–phonon interaction) to a set of narrow bands with a specific energy–momentum relation. As a result, the change in the form of the absorption spectrum from a Gaussian to a narrow resonant peak for an almost free exciton upon an increase in the parameter B of resonant transfer of excitation was demon-

strated graphically. It was shown that the formation of the free exciton peak near the bottom of the band occurs when condition (1) is satisfied. These authors managed to describe the Urbach of the absorption band near resonance associated with transitions to quasi-local ST states below the bottom of the band. The inclusion of only local phonons at sites nearest to an excitation did not allow the authors of Ref. 7 to obtain the Lorentzian shape of the high-energy wing of the band since the scattering at lattice phonons was not envisage by the model. It was shown, however, that a weak (in view of nonadiabaticity) band of absorption by quasi-local exciton-vibron states can be observed in the high- energy region of the band.

The next advancement in the analysis of the problem was made by Sumi[9] who took into account quantum effects of motion in the lattice by using a nonadiabatic approach. The proposed method of approximation of multiphonon processes made it possible to realize successfully approach (a) and to obtain polaron-like narrow-band states below the exciton resonance as well as the phonon structure of the absorption spectrum on the high-energy side of the fundamental exciton peak.

Sherman[10] described a method of exact solution of the problem by using approach (a) and confirmed Sumi's results on calculation of absorption spectra to a considerable extent. Coupled exciton states were constructed on the local basis in the form of orthogonal wave functions constructed by consecutive broadening of the exciton-phonon localization region so that scattering at delocalized phonons was also taken into account. Sherman[10] calculated the absorption spectra numerically for a crystal with a fixed frequency ω of optical phonons and with the set of values of E_{LR} and B with maximum values 7ω and 20ω, respectively. For RGS crystals, $E_{LR} \sim 100\omega$ and $B \sim 50\omega$ (see Table I), and the effect of mixing of the states has a high sensitivity to the magnitude and to the ratio of these parameters. For this reason, the results obtained in Ref. 10 cannot be interpolated to RES easily, and the proposed algorithm of using recurrent relations for obtaining the complete set of states in extremely cumbersome.

The next stage in overcoming the difficulties in calculating the systems with $E_{LR} > B \gg \omega$ was the publication by A. Sumi[11] who made an attempt to combine phenomenologically approaches (a) and (b) each of which was applied in the first approximation in the relevant perturbation. It is important that Sumi[11] analyzed the interaction with acoustic phonons, which is typical of RGS. Since he calculated optical spectra, the analysis was carried out near the bottom of the exciton band ($k=0$), where configuration mixing of free and self-trapped excitons is known to be weak. In order to calculate Green's function $G(k,E)$ of the exciton–phonon system, the imaginary component of the mass operator $S(E)$ was formally written as the sum of two dampings: the one-phonon damping $\Gamma(E)$ of free excitons, and the damping $G_{ST}(E)$ associated with the probability of transition of an exciton with energy E to a self-trapped state. The spectral distribution of the probability of excitation absorption by a local center is proportional to the Frank–Kondon factor and has the form of a Gaussian with the half-width D:

$$J_{ST}(E) = \frac{1}{(2\pi)^{1/2}D} \exp\left[-\frac{(E-E_M)^2}{2D^2} \right]. \tag{3}$$

According to Refs. 8, 11, and 14 that attenuation of the exciton state due to transitions to a self-trapped state far away from the middle of the band E_M can be approximated by the formula

$$G_{ST}(E) = \sqrt{2\pi}\, \frac{(E-E_M)^2}{D} \exp\left[-\frac{(E-E_M)^2}{2D^2} \right]. \tag{4}$$

A. Sumi noted that, according to this formula, the value of $G_{ST}(E)$ near the bottom of the band is exponentially small in the parameter $E^2/D^2 \sim B^2/D^2 \gg 1$, and $\Gamma(E) \gg G_{ST}(E)$ above the bottom of the band. For this reason, the attenuation $G_{ST}(E)$ is manifested significantly only below the bottom of the band, where $\Gamma(E) = 0$, and hence contributes only to the formation of the low-energy edge of exciton band absorption. Sumi[11] carried out self-consistent calculations of Green's function, scattering $\Gamma(E)$, as well as the absorption band for $E_{LR} = 50\omega$ and $B = 40\omega$, which is far from the parameters typical of RGS (see Table I). Thus, the analysis of the problem for the range of parameters typical of RGS has not yet been carried out.

In this section, we describe the results of calculations of exciton absorption curves for RGS made according to the following algorithm. The absorption spectrum is defined in terms of Green's function in the form

$$A(E) = -1/\pi\ \mathrm{Im}\ G(k=0, E), \tag{5}$$

and Green's function is defined through the mass operator $S(E)$:

$$G(k,E) = \frac{1}{E - \varepsilon(k) - S(E)}. \tag{6}$$

Here $\varepsilon(k)$ is the energy-momentum relation for an exciton in a rigid lattice, and

$$\mathrm{Im}\ S(E) = \Gamma(E) + G_{ST}(E). \tag{7}$$

Such an approach presumes that the perturbation is small and does not lead to a significant rearrangement of the eigenstates of the band exciton. We used formula (4) for $G_{ST}(E)$ and the well-known approximation for the probability $\Gamma(E)$ of exciton scattering at acoustic phonons at $T = 0$:[1,16]

$$\Gamma(E) = \lambda E. \tag{8}$$

We did not calculate the band peak width since it is known that absorption bands in RGS are very wide and can be described by the transverse-longitudinal exciton splitting $\Delta E \sim \Delta\omega_{LT} \sim 0.1$ eV in the polariton model.[1] However, real spectra are characterized, in addition to an anomalous width of the resonant peak, by a noticeable background in the high- and low-energy regions.[1,2,4] The peculiarities of the absorption band are manifested most clearly for Xe since other resonances are far away. The calculations based on this algorithm resulted in an integral-small blue side-band in the absorption band (solid curve in Fig. 2a), which corresponds to the prevailing concepts on weak exciton scattering in this crystal. The integral intensity of the spectrum is equal to
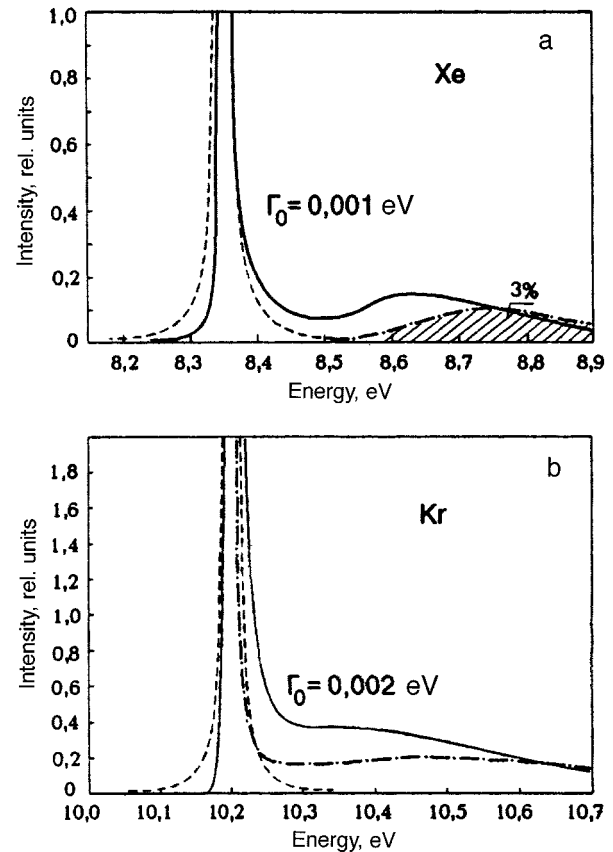

FIG. 2. Calculated absorption spectra for excitons in Xe (a) and Kr (b). The solid curve is calculated by formulas (4)–(8); the dashed curve corresponds to the Lorentzian with the half-width Γ_0 characteristic of one-phonon damping; the dot-and-dash curve is calculated according to the energy-momentum relation (10). The integral intensity of the high-energy band relative to the total intensity is $\lambda < 3\%$ for Xe.

unity. The parameters used in the calculations are given in Table I. The asymmetry of the curve is emphasized by a comparison with the Lorentzian curve with the width $\Gamma_0 = \mathrm{const}(E)$, which is typical of one-phonon scattering near resonance (dashed curve). The solid curve in Fig. 2b corresponds to the absorption spectrum for Kr obtained by using the same algorithm. Although the band asymmetry is manifested clearly, the maximum height of the main exciton peak is much larger than the contribution from the phonon wing (the height of the peak is two orders of magnitude larger than the scale of the figure and is naturally not presented), and its integral intensity amounts to more than 90%. The exciton absorption spectrum obtained for Kr is close to that calculated by us for Ar if we take into account only one-center, self-trapped states.

Experimental absorption spectra for Ne and Ar are still broader than for Xe and Kr. This corresponds to prevailing concepts concerning higher intensity of exciton-phonon interaction in light RGS. However, partial superposition of singlet and triplet resonances, transverse-longitudinal band splitting, and coexistence of two types of self-trapped states complicate considerably the interpretation of experimental results for these crystals. For this reason, it is important to obtain additional theoretical information on possible proper-
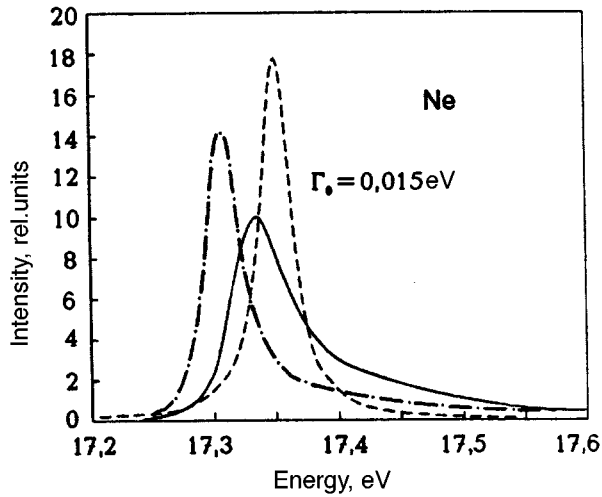
FIG. 3. Calculated absorption spectra for excitons in Ne. Notation is the same as in Fig. 2.

ties of excitons, even if we confine ourselves to the simplest quantitative estimates.

Let us consider the theoretical absorption spectrum for Ne taking into account only one-center self-trapped states, which dominate in this crystal. Calculations based on formula (5) give a considerable blue side-band (up to 25% of the integral intensity) and general asymmetry of the band (solid curve in Fig. 3). The dashed curve corresponds to the Lorentzian describing the absorption of free excitons with the characteristic one-phonon damping. The obtained pattern indicates a considerable contribution of self-trapped states to exciton absorption in Ne and casts a shadow of doubt on the correctness of calculations carried out in the approximation of weak damping of exciton states, which does not change the band structure of quasiparticles. Naturally, it was considered expedient to analyze additionally the possible contribution of self-trapped states to absorption and to the energy-momentum relation for excitons, taking into account the renormalization of band states. Further analysis aims at determining the influence of nonadiabatic effects in the exciton-phonon interaction on the states of excitons near and above the bottom of the band in RGS.

2. BAND EXCITON STATES TAKING INTO ACCOUNT NONADIABATIC EXCITON-VIBRON MIXING

In this section, we discuss briefly the mixing of states of free excitons and vibrational excitations of self-trapped states on the basis of an approach using the basis of self-trapped states [of type (b); see Introduction] which was proposed earlier.[7,14] The analysis will be based on the model of non-dispersive phonons. Degeneracy of all normal coordinates of the lattice makes it possible to introduce their linear forms q_n, each of which interacts with an electron excitation located at the nth lattice site. The Hamiltonian of an electron-excited crystal can be written in the traditional form:

$$H = H_{exc} + H_{lat} + H_{int}. \qquad (9)$$

The expressions for individual terms actually coincide with their form in Refs. 9 and 10. The electron component of the

Hamiltonian H_{exc} can be diagonalized, as usual, with the help of the Fourier transform. The lattice term H_{lat} corresponds to the lattice in the absence of an electron excitation and contains the kinetic energy operator for nuclei. The interaction term H_{int} corresponds to a linear approximation in phonon operators and is not regarded as small. We choose for the orthonormal basis the vibrationally excited states of an exciton localized at the same site with the deformation. We assume that these states are a solution for a self-trapped exciton (the problem with Hamiltonian (9) without a resonant transfer term in H_{exc}) and have equidistant vibrational levels for all energy values up to the top of the exciton band (harmonic approximation for H_{lat}). Figure 1 shows the dependence of the lattice potential on the normal coordinate q of the lattice site at which the excitation is localized (we assume that $H_{lat} + H_{int} = E_M - \omega q_0 q + \omega q^2/2$). The dimensionless parameter q_0 (the displacement of the potential minimum in a self-trapped state) is a measure of the exciton-phonon coupling and determines the parameter $D = \omega q_0/\sqrt{2}$ and $E_{LR} = \omega q_0^2/2$. We confine our analysis to the approach called the consideration of "internal subspace,"[7] in which the processes of exchange of a local excitation between phonons and the ambient lattice are disregarded. For this case, an exact solution of the Schrödinger equation for the total Hamiltonian (9) was obtained,[7,14] and the energy-momentum relation $E(k)$ for mixed exciton-vibron states was determined in the form

$$\sum_s \frac{j_s}{E(k) - e_s} = \frac{1}{\varepsilon(k)}. \qquad (10)$$

Here e_s is the energy of the s-th vibrational level of the ST state, $\varepsilon(k)$ corresponds to the dispersion branch of an exciton in a rigid lattice, measured from the lattice-site level E_M, and j_s is the Frank–Condon factor for a local center. In the absence of exciton-phonon coupling ($q_0 \to 0$), $j_s = \delta_{M0}$, and we obtain, in accordance with (10), the energy momentum relation for free excitons in a rigid lattice: $E(k) = E_M + \varepsilon(k)$. In the case of a strong exciton–phonon coupling ($D \gg \omega$), the expression for j_s has the asymptotic form

$$j_s = \frac{\omega}{(2\pi)^{1/2} D} \exp\left(-\frac{(e_s - E_M)^2}{2D^2}\right). \qquad (11)$$

In this paper, we calculate the energy spectra corresponding to Eq. (10) by using the parameters for RGS from Table I. The result obtained for a-STE in Ar is shown schematically in Fig. 4a, while the results of numerical calculations for branches at the center of the band are presented in Fig. 4b. Peculiarities of the spectrum are completely determined by the form of variation of j_s, i.e., the overlap integral for nuclear wave functions of a free exciton and the vibrational s-state of a self-trapped exciton. The parameter j_s has the maximum value $j_M \sim \omega/D$ at the middle of the band (for $E = E_M$). According to Eq. (10), the states of the free and self-trapped excitons are mixed, and the width of the energy region in the band with a relatively strong mixing of states is of the order of D (see Fig. 4).
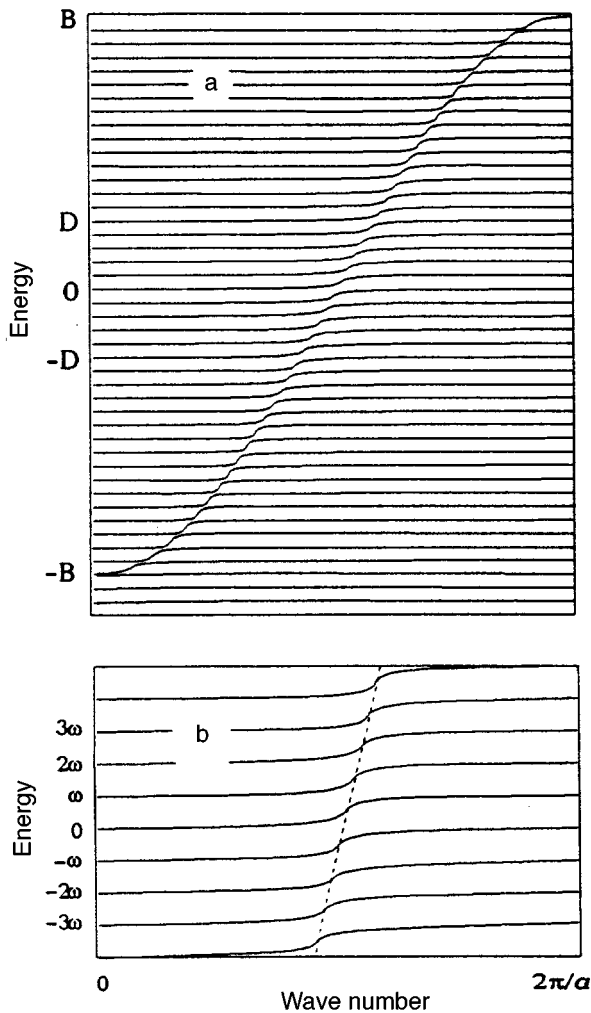
FIG. 4. Energy-momentum relation for exciton-vibron states calculated by formula (10) for Ar taking into account the quasi-atomic self-trapped state (the parameters of calculation are given in Table I): general view (a), numerical calculations for the middle of the band (b); the dashed line corresponds to the energy- momentum relation $\varepsilon(k)$ for excitons in a rigid lattice.

Let us now consider a fairly large peripheral region of the energy-momentum relation where $|e_s - E_M| \gg D$, and the nuclear wave functions of free and self-trapped states overlap to a considerably smaller extent. In Xe, Kr, and Ar cryocrystals, exciton states near the bottom of the band are virtually not mixed with exciton-vibron states in view of the smallness of the Frank–Condon factor $\exp(-B^2/2D^2)$ determining a very low transparency of the self-trapping barrier at the adiabatic potential. Thus, the traditional application of the adiabatic approximation for an analysis of self-trapping near the bottom of the exciton band for heavier cryocrystals is in accord with the obtained result. Nevertheless, according to the theory, the energy range $|E - E_M| \lesssim D$ for each branch with the number s contains regions corresponding to noticeably mixed exciton- vibron states. However, band states are not destroyed completely even in the case of a strong exciton-phonon interaction in the Ar cryocrystal. Figure 4 shows that considerable changes are observed only in a certain range of wave vectors, whose relative width at the center of the band is approximately equal to D/B. The blurring of

the exciton energy-momentum relation is determined by the damping $G_{ST}(E)$.

The absorption spectra for the obtained exciton-vibron states for cryocrystals with a weak exciton–phonon damping (Xe, Kr) and a strong damping (Ne) differ significantly (the dot-and-dash curve in Figs. 2 and 3). In the Xe spectrum, the contributions from two bands, viz., a very narrow (since this model disregards scattering at acoustic phonons) purely exciton peak near the bottom of the band and a broad ($\Delta E \sim D$) band of the Gaussian type at the middle of the band, can be separated easily. The ratio of integral intensities of these bands is equal to $(1-\lambda)/\lambda$, where λ is a small parameter (see formula (1) and Table I). This fact can be interpreted as a manifestation of the effect of coexistence of free and self- trapped excitons in absorption. The small contribution ($\sim 3\%$) to absorption from self-trapped states in Xe indicates the suitability of the model described in the previous section.

An increase in the nonadiabaticity parameter λ in the series from Xe to Ne is accompanied not only by an increase in the intensity of the second band, but also by a shift of its peak towards the bottom of the band. The value of E_{LR} for Kr for which the exciton band width is the same as for Xe is much larger, and hence the contribution from ST states to absorption is manifested in the form of a gently sloping sideband with a weakly manifested peak extended far into the blue edge (all the spectra are orthonormalized to unit integral intensity).

The contributions of the two types of absorption in the Ne spectra cannot be separated in practice, and the spectrum has the shape of an asymmetric wide band (dot-and-dash curve in Fig. 3) shifted to the red edge relative to the position of the bottom of the band for a nondeformed lattice (''pure'' exciton corresponds to the Lorentzian in Fig. 3). This shift, distinguishing the result from that obtained in the previous section (solid curve in Fig. 2), is a manifestation of mixed exciton-vibron narrow-band states below a purely exciton resonance. According to Refs. 7 and 10, it is difficult to single out a phonon-free peak in the absorption band in this case in view of the effect of mixing of states. Nevertheless, the shapes of these bands are close, which can also indicate the qualitative applicability of the model considered in the previous section, presuming that the states of free excitons are characterized by weak damping. In order to clarify the origin of exciton states in Ne as well as possible changes in the band properties of excitons in other cryocrystals, we must analyze in detail the total damping of excitons, which determines the stability of band states of quasiparticles, as well as the relation between $\Gamma(E)$ and $G_{ST}(E)$, which is of fundamental importance for determining the kinetic parameters of free excitons.

3. CRITERIA FOR COEXISTENCE OF FREE AND SELF-TRAPPED EXCITONS ABOVE THE BOTTOM OF THE BAND

The smallness of the quasiparticle damping as compared to its kinetic energy is a criterion for preserving the free (coherent) type of motion of an exciton. One-phonon damping for the intraband exciton scattering ($\mathbf{k}-\mathbf{k}'$ transitions) was analyzed by us in detail earlier.[16] We proved that free
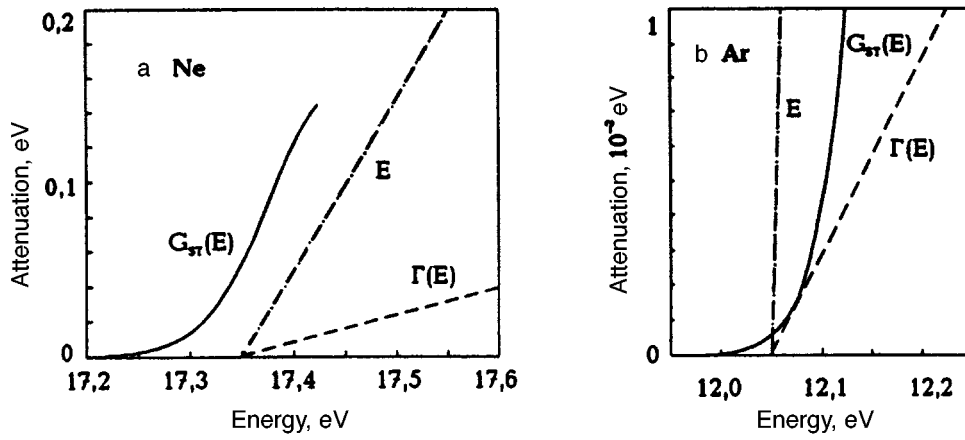
FIG. 5. Relation between the exciton kinetic energy E (dot-and dash line) and the contributions of transitions $G_{ST}(E)$ to a quasi-atomic self-trapped states (solid curve) and one-phonon scattering $\Gamma(E)$ (dashed line) to damping: for Ne (a) and for Ar (b).

states can serve as a good approximation for excitons scattered by acoustic phonons virtually for all exciton states in the temperature interval corresponding to the existence of cryocrystals. A similar analysis should be carried out taking into account the damping associated with transitions to a self-trapped state. Figures 5 and 6 show the $G_{ST}(E)$ and $\Gamma(E)$ dependences calculated by formulas (4) and (8) respectively for all RGS Let us first consider the relation between the quantities $G_{ST}(E)$ and $\Gamma(E)$.

One-phonon relaxation processes following the excitation dispersion curve dominate over the probability of transitions to self-trapped states in the energy range where

$$G_{ST}(E) \ll \Gamma(E). \tag{12}$$

It can be seen from Figs. 5 and 6 that this region is significant only in Xe and is not observed in Ar and Ne. This means that the coexistence of nonthermalized states of free and self-trapped excitons in a certain energy range can be confirmed only for a Xe cryocrystal (and near the bottom of the band in Kr to a certain approximation), and the quantity $G_{ST}(E)$ can be regarded as the probability of self-trapping. In this case, the natural assumption is made that after a transition to a self-trapped state, the probability of relaxation of an excitation in vibrational levels is much higher than the

probability of a reverse transition to the band state. In this case, the excitation energy transfer should be considered by taking into account only the mean free path of free excitons relative to scattering $\Gamma(E)$ at phonons.

In the region where $G_{ST}(E) \sim \Gamma(E)$, which has the maximum width for Xe, Kr, and Ar, we cannot judge about self-trapping probability in terms of $G_{ST}(E)$ since multiple transitions from the states of free excitons to self-trapped states and back are possible during the relaxation time. In order to determine the self-trapping probability, detailed analysis of relaxation processes in a self-trapped state taking into account multiphonon processes which are beyond the scope of this paper is required. Nevertheless, we can state with confidence that the kinetics of free excitons in this energy range will be determined by two types of damping with comparable contributions.

It should be recalled that expression (4) for $G_{ST}(E)$ is valid only for the energy range far away from the center of the band, where $|E - E_M| \gg D$. For this reason, we are not in a position to analyze the condition $G_{ST}(E) \gg \Gamma(E)$ on the basis of the results presented in Figs. 5 and 6 for Ar, Kr, and Xe in the range of high kinetic energies of excitons. However, it is obvious that processes of transition to a self-
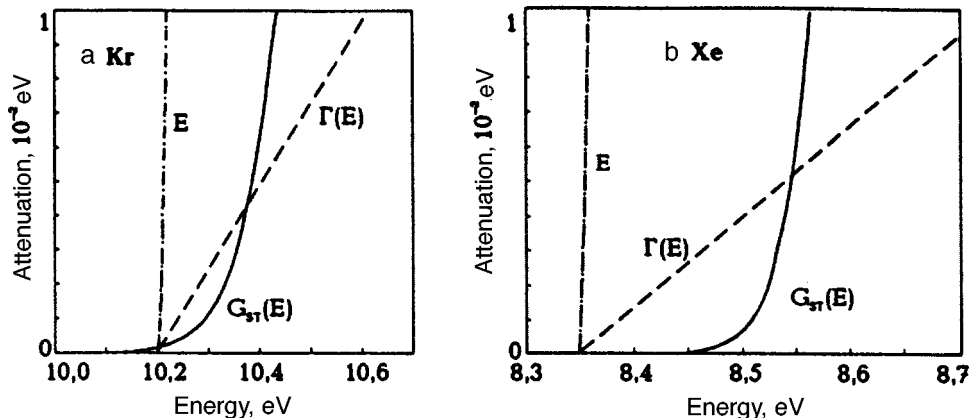

FIG. 6. The same as in Fig. 5, but taking into account transitions to a quasi-molecular self-trapped state: for Kr (a) and for Xe (b).

trapped state in Ne dominate over intraband scattering for all exciton states in the band of this crystal.

Let us now consider the stability of the band state to self-trapping process. The criterion for the conservation of coherence is the small value of the total damping for a quasiparticle relative to the value of its kinetic energy. On the scale of Figs. 5 and 6, the energy–momentum relation (the dot-and-dash line denoted by E) appears as a nearly vertical line, and the relation

$$G_{ST}(E)/E \ll 1 \qquad (13)$$

is satisfied to a high degree of accuracy for excitons above the bottom of the band in Xe, Kr, and Ar crystals. It was mentioned in the previous sections that exciton-vibron narrow-band states (see Fig. 4a), which make a specific contribution to absorption on the low-energy side of the exciton peak, must be manifested in these crystals near the bottom of the band in the given theory. However, the change in the energy–momentum relation for excitons in the resonance region, which is associated with a considerable phonon–exciton mixing, must introduce considerable corrections to the problem of existence of such branches. This aspect must be investigated in greater detail.According to Fig. 5a, the situation in Ne is opposite to condition (13) for the entire band, and this leads to the following important conclusion. A nonadiabatic exciton- phonon interaction in Ne induces considerable mixing of states of free and vibrationally excited self-trapped excitons, which must be manifested in a violation of the energy– momentum relation for band excitations in the limit of a rigid lattice. The state of free excitons in this case cannot be treated as a good zeroth approximation in an analysis of relaxation of excitations and energy transport in the lattice. The presence of a large contribution of resonant transfer in the exciton energy in Ne along with a very strong deformational interaction with the lattice is responsible for unique peculiarities of this crystal. A further analysis of the properties of excitons in Ne should be carried out in terms of nonstationary states.

In conclusion, let us consider the relation between the formal estimates of nonadiabatic effects, viz., energy-momentum relation (10) and self-trapping probability (4), obtained here with the actual peculiarities of the structure of lowermost self-trapped electron excitations in RGS in the form of quasi-atomic and quasi-molecular centers. It is known that the luminescence spectra of Ne and Ar crystals exhibit both types of self- trapped states, while the spectra of Kr and Xe crystals display only quasi-molecular centers. The states of quasi-molecular type are characterized by a considerable nonlinearity and nonisotropy in the deformational coordinate. The interaction of a one- center state with the RGS lattice is symmetric and has the form of a strong repulsion of nearest neighbors. In our calculations, we used the one-coordinate model of the exciton- phonon interaction, which formally corresponds to a one-center self-trapped state. The parameters of self-trapped and band states as well as the lattice parameters are given in Table I.

It should be noted above all that binding energies E_b of the lattices are small, especially for light cryocrystals. This means that the system of local vibrational levels in a one-center (repulsive surroundings) state with energies $e_s \sim E_{LR}$ in RGS is unstable in view of the fact that stresses are considerably higher than the tensile strength of the lattice for large strains. The theory of mixing of exciton-vibron states in this case can be used either in terms of the damping of states of free excitons, or for considering fast processes, e.g., absorption of light. The presence of a wide region of energies and coordinates in which the lattice potentials corresponding to the ground and a self-trapped state overlap indicates the instability of the basis state in an analysis of a polaron-like energy-momentum relation of type (10) (an exciton plus a high-energy vibron at the same site) in the range of small strains (see Fig. 1). Polaron-type states (as in Fig. 4b) must obviously decay into a free exciton and vibrational excitations of the lattice. Such processes were not taken into account in the model corresponding to the energy-momentum relation (10). Moreover, even a qualitative description of transformation of a high energy of local deformation of the lattice associated with electron excitation into independent local or band excitations of the lattice subsystem does not exist.

One more decay channel is also possible for quasi-atomic self-trapped states. This channel is associated with a transition of an excitation from quasi-atomic to quasi-molecular local vibrations since the lattice surrounding the region of expansion around the excitation is compressed,[17] which increases the resonant coupling between the atoms of the ambient and can induce two-center self-trapping.

The energy range corresponding to quasi-molecular vibrational levels lies below E_M. In this region, we can expect an additional an additional effect, viz., the mixing of states of quasi-atomic and quasi-molecular types, along with the change in the disperse structure of excitons, if the binding forces between an excitation and corresponding localized states are strong enough (e.g., as in Ne and Ar). It should be emphasized that in spite of the large value of $E_{LR}^{(m)}$ as compared to $E_{LR}^{(a)}$ (see Fig. 1), the coupling between excitons and low-symmetry quasi-molecular vibrations is weaker than their coupling with completely symmetric mode of one-center states. The considerable nonlinearity of the molecular potential near the middle of the band also plays a significant role. Quasi-atomic excitation with a smaller value of E_{LR} indeed dominates in the radiation emitted by Ne and Ar crystals in which both types of self-trapped states are observed. This fact indicates above all that the estimates of the probability $G_{ST}(E)$ obtained here for two-center states on the basis the quantities E_{LR} can be too high. In addition, the strong repulsive interaction of an excitation with the surrounding particles can lead to a considerable contribution from the one-center self-trapping channel to the population of quasi-molecular states (see above). For this reason, we confined our analysis of $G_{ST}(E)$ in these crystals only to one-center self-trapping.

The exaggerated values of $G_{ST}(E)$ for Xe and Kr must be reflected qualitatively in the expansion of the energy range (12) in which nonthermalized states of free and self-trapped excitons can coexist. In spite of the fact that one-center self-trapping in Xe and Kr cryocrystals is disadvantageous from the energy point of view (judging from the large

deformational potential (1.3 eV for Xe) observed in experiments on the temperature shift of absorption bands),[1] the term corresponding to one-center excited state in this crystals is also essentially repulsive at a distance separating nearest neighbors in the lattice. This means that a one-center metastable quasi-local state can play the role of an intermediate stage in absorption and in transitions of an excitation between the band and a quasi-molecule. This can ultimately increase the probability of self-trapping to a two-center state in the region above the bottom of the band, compensating the above-mentioned effect of nonlinearity of molecular potential to a certain extent.

It should be emphasized that the self-trapping probabilities and the existence of new polaron-like dispersion branches are problematic in the case of quasimolecular excitation rather than the zeroth approximation itself in the form of local exciton-vibron highly excited levels since the vibrational structure of the self-trapped state is formed within a molecule due to a resonant bond between two atoms (as they approach each other) and is stable in the lattice in the zeroth approximation.

An analysis of optical properties including polariton effects in the region of photon- exciton mixing involves the determination of the self-trapping probability for excitons at the bottom of the band, where $k=0$. Table I contains the values of $G_{ST}(E=-B)\equiv G_0$ as well as corresponding life times τ_{ST} for free excitons relative to self-trapping. Comparing the values of this time for Xe with the latest estimates obtained from optical experiments on damping of free excitons in especially perfect crystals taking polariton effects into consideration ($\tau_{ST}\gtrsim 2\cdot 10^{-8}$ s),[18] we see that results coincide wonderfully. The two opposite effects (the contribution of one-center states and the nonlinearity of the quasi-

molecular potential) probably compensate each other during the formation of the probability of exciton self-trapping in Xe. In any case, the mutual influence and coexistence of two self- trapping channels in RGS require further detailed investigations.

*E-mail: fugol@ilt.kharkov.ua

[1] I. Ya. Fugol', Adv. Phys. **27**, 1 (1978), *ibid* **37**, 1 (1988).

[2] N. Schwentner, E. E. Koch, and J. Jortner, *Electronic Excitation in Condensed Rare Gases*, Springer Verlag, Berlin (1985).

[3] A. F. Prikhot'ko, V. G. Manzhelii, I. Ya. Fugol' *et al.*, *Cryocrystals* [in Russian], Naukova Dumka, Kiev (1986).

[4] G. Zimmerer, in *Excited State Spectroscopy in Solids*, North Holland, Amsterdam (1987).

[5] È. I. Rashba, Optika i Spektroskopiya **3**, 568 (1957).

[6] Y. Toyozawa, Progr. Teor. Phys. **20**, 53 (1958).

[7] K. Cho and Y. Toyozawa, J. Phys. Soc. Jpn. **30**, 1555 (1971).

[8] H. Sumi and Y. Toyozawa, J. Phys. Soc. Jpn. **31**, 342 (1971).

[9] H. Sumi, J. Phys. Soc. Jpn. **36**, 770 (1974), *ibid* **38**, 825 (1975).

[10] A. V. Sherman, Phys. Stat. Sol. b**131**, 225 (1985); *ibid* **135**, 697 (1986), *ibid* **145**, 319 (1988).

[11] A. Sumi, J. Phys. Soc. Jpn. **47**, 1538 (1979).

[12] A. S. Joselevich and E. I. Rashba, J. Lumin. **34**, 223 (1986).

[13] E. I. Rashba and A. S. Joselevich, in *Quantum Tunneling in Condensed Matter* (ed. by Ju. Kagan and A. Leggett), Elsevier Science Publ., Amsterdam (1992).

[14] A. M. Ratner, Solid State Commun. **53**, 311 (1985).

[15] M. Schreiber and Yu. Toyozawa, J. Phys. Soc. Jpn. **51**, 1528, 1544 (1982).

[16] I. Ya. Fugol' and E. I. Tarasova, Fiz. Nizk. Temp. **7**, 1326 (1981) [Sov. J. Low Temp. Phys. **7**, 6441 (1981)].

[17] A. Kongeter and M. Wagner, J. Chem. Phys. **92**, 4003 (1989).

[18] D. Varding, I. Reimand, and G. Zimmerer, Phys. Stat. Sol. **B185**, 301 (1994).

Translated by R. S. Wadhwa

Molecular adsorption states and sticking probability of D$_2$ molecules on the W(110) surface at liquid helium temperatures

V. D. Osovskii, Yu. G. Ptushinskii, V. G. Sukretnyi, and B. A. Chuikov

*Institute of Physics, National Academy of Sciences of the Ukraine, 252022 Kiev, Ukraine**

The dependence of the sticking probability of D$_2$ molecules on the W(110) surface of tungsten on the degree of coverage $S(\theta)$ at the substrate temperature $T_s \sim 5$ K is measured under different conditions of adlayer formation. The effect of significant increase in the sticking probability for D$_2$ in the course of population of weakly bound absorption states observed earlier (V. D. Osovskii *et al.*, Pis'ma Zh. Eksp. Teor. Phys. **60**, 569 (1994) [JETP Lett. **60**, 586 (1994)]) increases considerably on the surface precovered with an ordered monolayer of deuterium atoms and even more strongly for a surface covered with atomic and physisorbed molecular monolayers. The peculiarities in the $S(\theta)$ dependence observed at $T_s \sim 5$ K are explained, taking into account the island mechanism of adlayer growth as well as the precursor mediated process of its formation. The $S(\theta)$ dependences are also obtained for $T_s = 78$ and 300 K and indicate the Langmuir mechanism of adsorption during the population of the 550 K atomic state as well as the precursor mediated mechanism of formation of the 410 K atomic state. © *1997 American Institute of Physics.* [S1063-777X(97)01307-8]

INTRODUCTION

Adsorption of hydrogen on metal surfaces is of considerable interest in connection with the problems of its dissolution and storage in metals as an ecologically pure fuel, hydrogen embrittlement of metals, and so on. The small size and mass of hydrogen atoms and molecules as well as the double mass of the hydrogen isotope (if we disregard tritium) can ensure manifestations of special effects in the course of interaction of hydrogen with the surface, which are not observed for larger molecules. Low-temperature studies are of special importance since in this case weakly bound physical adsorption states can be populated and analyzed under steady-state conditions, and quantum effects can be manifested. Weakly bound molecular adsorption states often play the role of precursors in the mechanism of dissociative adsorption which is the main stage in the above-listed processes. For this reason, an analysis of low-temperature adsorption of hydrogen isotopes is a very interesting problem.

Hydrogen adsorption at metal surfaces is studied in detail,[1] except for low temperatures of the substrate. In few publications devoted to low-temperature adsorption of hydrogen, the symmetry of the adlayer, the mobility of adsorbed particles, and phase transitions at temperatures close to the liquid helium temperature were mainly studied.[2–8] In our earlier publications, the data on the spectra and kinetics of population of weakly bound hydrogen adsorption states are reported.[9–13] Among other things, the effect of a strong increase in the sticking probability for D$_2$ molecules on the W(110) surface was observed for the substrate temperature $T_s \sim 5$ K during the population of weakly bound molecular adsorption states.[13] This effect was interpreted as a consequence of elevated efficiency of kinetic energy scattering for an incident molecule impinging on a weakly bound molecule adsorbed earlier as compared to its collision with the pure surface or the surface covered with rigidly bound adsorbed

atoms. In the present research, we carried out experiments on multiple population and depletion of weakly bound molecular adsorption states and observed a considerable enhancement of this effect. The data of sticking probability of D$_2$ molecules at $T_s = 78$ and 300 K are also obtained for comparison.

EXPERIMENTAL TECHNIQUE

The experiments were made on a ultrahigh-vacuum setup of the ''camera obscura'' type by the methods of molecular beam and thermodesorption spectroscopy. The experimental technique is described in detail in Refs. 12 and 14. The sticking probability S was determined from the dependence of the flux of molecules scattered or desorbed from the sample surface on the adsorption time:[15]

$$S(t) = 1 - I(t)/I_m, \tag{1}$$

where $I(t)$ and I_m are the ionic currents of the detector of scattered molecules at the instant t and after the total reflection of molecules from the saturated sample surface.

The coverage degree $\theta = n/n_0$ (n is the surface concentration of adsorbed particles and $n_0 \sim 1.4 \cdot 10^{15}$ cm^{-2} is the concentration of the surface atoms of the substrate) was determined from the time dependence of S from the formula

$$\theta = \nu/n_0 \int_0^t S(t)dt, \tag{2}$$

where ν is the gas-kinetic molecular flux on the sample surface. In our previous publications,[9–13] the value of the quantity θ is given in relative units since we did not measure the flux ν. However, we can use the results obtained in Refs. 2 and 16, according to which $\theta = 1$ in the case of saturation of atomic phase of hydrogen adsorption on the W(110) surface, and determine the proportionality factor between the quantity θ and the area bounded by the curve $S(t)$. Such a method of
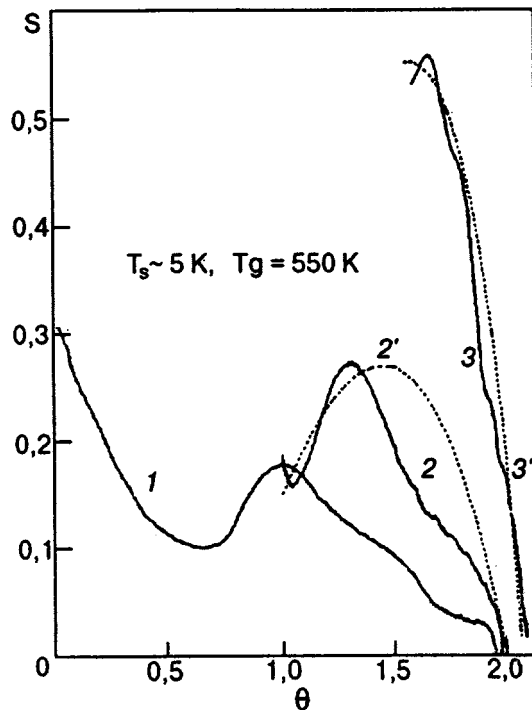
FIG. 1. Dependence of the sticking probability for D_2 molecules on the degree of coverage of the initially pure surface (curve *1*), the surface initially covered with an atomic deuterium monolayer (curve *2*), and the surface covered additionally with a molecular deuterium monolayer (curve *3*); curves *2'* and *3'* represent calculated dependences.

FIG. 2. Thermodesorption spectrum for D_2. The temperature T_d corresponds to the desorption peak, K: 5 (*1*), 8 (*2*), 15 (*3*). 60 (*4*), 150 (*5*), 410 (*6*), and 550 (*7*).

evaluating θ is approximate and does not take into account the possible error in recording molecules scattered by the cold surface or desorbed thermally.

DISCUSSION OF EXPERIMENTAL RESULTS

Figure 1 shows the $S(\theta)$ dependences for three different processes at $T_s \sim 5$ K. The first process (curve *1*) corresponds to adsorption of D_2 at the initially pure W(110) surface. In this experiment, the gas temperature $T_g = 550$ K, and the value $S_0 \sim 0.3$ of the initial sticking probability ($\theta = 0$) corresponds approximately to the dependence $S_0(T_g)$ from Ref. 13. The most typical peculiarity of the $S(\theta)$ dependence, i.e., an increase in S upon the onset of the population of weakly bound physical adsorption states, is observed at $T_g = 550$ K as well as at lower values of T_g.[13] For convenience, Fig. 2 reproduces the spectrum of thermodesorption of the D_2 adlayer from Ref. 13, saturated at $T_s \sim 5$ K. In Ref. 13, we assumed that weakly bound 15 K and 8 K molecular adsorption states correspond to the second and third monolayers,[1] but the peak at 15 K in the thermodesorption spectrum is much smaller than that at 8 K, and we believe that these states correspond to the second monolayer. The emergence of two peaks as a result of thermodesorption of molecules from the same monolayer is probably due to the presence of defects in the surface structure or with the fact that the adlayer has two phases: two-dimensional condensed islands and a two-dimensional gas. For this reason, we shall not mention the 15 K state in further analysis since it does not contain an appreciable amount of D_2 molecules.
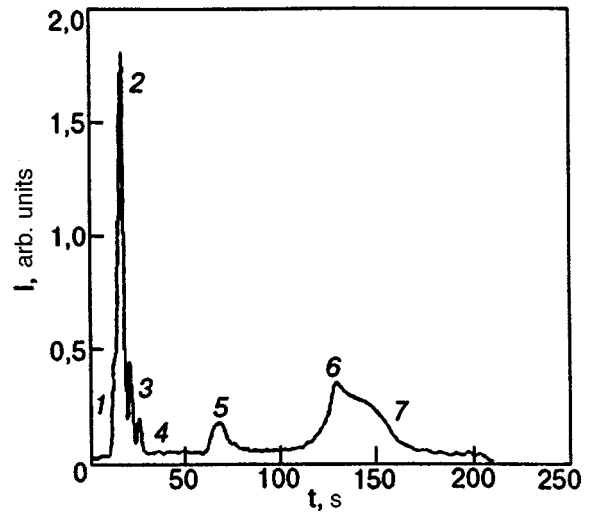
The second process (curve *2*) is the desorption of D_2 at $T_s \sim 5$ K following sample annealing at 300 K after the completion of the first process. It was shown in Ref. 2 that the W(110) surface remains covered by an ordered monatomic deuterium layer as a result of such an annealing.[2] It can be seen that the region of strong increase in S is displaced towards larger θ, and the maximum value of S increased considerably.

In our opinion, the reason behind the observed difference in the curves *1* and *2* lies in the fact that, in view of the island mechanism of growth of the atomic layer, weakly bound D_2 adsorption states in the first process are populated even before the entire surface is covered by the atomic layer. For this reason, the conditions required for an increase in the sticking probability are created for lower values of the total coverage degree θ than in the second process, when weakly bound adsorption states are formed above the monatomic coating that has already been formed. The form of the $S(\theta)$ dependence for this process indicates that the precursor state whose role is most probably played by the 5 K state participates in the population of the second monolayer.

The third process (curve *3*) is the adsorption of D_2 following isothermal desorption from the 5 K state occurring after interception of the molecular beam. The D_2 molecules cannot be stationary in the 5 K state, and a certain number of molecules is present at the surface for an open molecular beam as a result of dynamic equilibrium between adsorption and desorption. A decrease in the coverage after interception of the molecular beam was determined by the time dependence of the detector current after the interception.

Figure 1 shows that, as a result of actuation of the molecular beam after such an interception, the sticking probability becomes much higher than for the pure surface. We believe that the large value of S at the beginning of the third process is determined, first, by the fact that before the actuation of the molecular beam, the surface is covered by weakly coupled molecules in the 8 K state, which ensure effective loss of kinetic energy of incident molecules, and hence a

high trapping probability. Second, molecules in the 5 K state are still absent at the beginning of the third process, and their evaporation rate reducing the sticking probability, is equal to zero. In the second process, the 5 K absorption state is populated even before the formation of the complete monolayer at 8 K, probably due to the island mechanism of the growth of the second monolayer (the 8 K) state, and D_2 molecules evaporate intensely at this stage.

A phenomenological analysis of adsorption involving precursor state and characterized by different values of sticking probability above empty and filled regions was carried out by Zhdanov.[17] Under certain simplifying assumptions, he obtained the following equation for sticking probability:

$$S = (1 - \theta_2)S_e + \theta_2 S_f K_{fe}(1 - \theta_2)/[K_{fe}(1 - \theta_2) + K_{fd}], \quad (3)$$

where S_e and S_f are the sticking probabilities above empty and filled regions, K_{fe} the rate constant for transitions of molecules from the precursor state above the filled region to the precursor above an empty region, K_{fd} is the rate constant for desorption from the precursor state above a filled region, and θ_2 is the coverage degree in the second monolayer.

The dashed curve $2'$ in Fig. 1 shows the $S(\theta)$ dependence for the second process obtained from Eq. (3) for the values $S_e = 0.15$ and $S_f = 0.55$, which are approximately equal to the experimental values of sticking probability at the beginning of the second process (the surface is covered by a monolayer of deuterium atoms) and at the beginning of the third process (the surface is also covered with a monolayer of D_2 molecules in the 8 K state). The theoretical and experimental curves were matched with the help of the fitting parameter K_{fe}/K_{fd}.

In simulating the third process, we must supplement the right-hand side of Eq. (3) (we denote it by $f(\theta_3)$) with the term taking into account evaporation of molecules from the 5 K state:

$$S = f(\theta_3) - K_d n_0 \theta_3/\nu, \quad (4)$$

where K_d is the desorption rate constant, $n_0 \sim 10^{15}$ cm^{-2} the surface concentration of substrate atoms, $\nu \sim 10^{13}$ cm$^{-2} \cdot$s^{-1} the gas-kinetic molecular flux in our experiments, and θ_3 the coverage degree in the third monolayer.

Curve $3'$ in Fig. 1 shows the $S(\theta)$ dependence calculated by using Eq. (4) for $S_e = 0.55$ (which is equal to the experimental value of S at the beginning of the third process), $S_f = 0.95$, and $K_d = (kT/h)\exp(-q/kT)$ (k and h are the Boltzmann and Planck constants respectively, and q the desorption activation energy). On basis of Eq. (4), we assume that the filling of the third monolayer (the 5 K state) also involves the precursor state.

It can be seen from Fig. 1 that the experimental and theoretical curve are in qualitative agreement, which makes more reliable the explanation of peculiarities in the $S(\theta)$ dependence at $T_s \sim 5$ K under various experimental conditions, which was proposed in Ref. 13 and here. Moreover, a comparison of the experimental and theoretical dependences $S(\theta)$ for the third process led to the value $S_f = 0.95$ for the sticking probability for the incidence of a D_2 molecule on a site occupied by a molecule adsorbed earlier in the 5 K state.
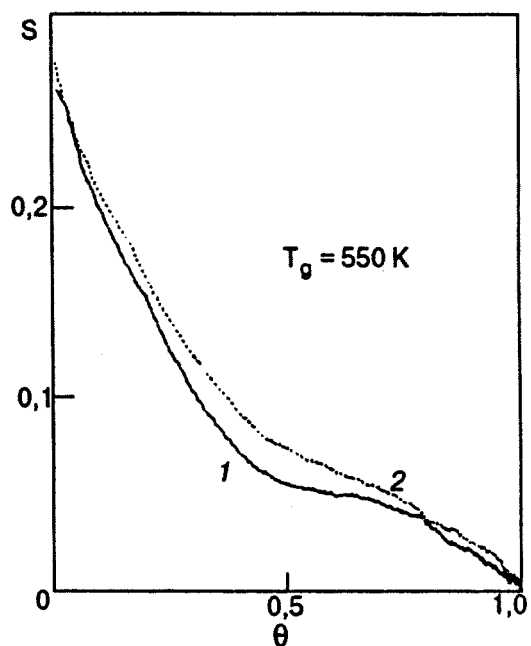

FIG. 3. Dependence of the sticking probability for D_2 on the degree of coverage at $T_s = 78$ (curve 1) and 300 K (curve 2).

The $S(\theta)$ dependences measured at higher substrate temperatures (78 and 300 K) are shown in Fig. 3. Naturally, the maximum degree of coverage at these temperatures can only be as high as unity since weakly bound adsorption phases are unstable at these temperatures. The sharp decrease in the value of S with increasing θ in the interval of coverage degree $0 < \theta < 0.5$ corresponds to the Langmuir mechanism of adsorption in the case of population of the 550 K atomic adsorption state. The second atomic state 410 K is obviously filled with the participation of a precursor (in all probability, this is the 8 K state), which is manifested in slowing down of the decrease in the sticking probability upon an increase in θ. As expected,[15] this slowing down is manifested most clearly for $T_s = 78$ K than for $T_s = 300$ K. A similar enhancement of the role of the precursor upon a decrease in the substrate temperature was encountered by us during investigation of oxygen adsorption on tungsten.[14]

CONCLUSION

We observed new manifestations of the positive effect of weakly bound physical adsorption states on the sticking probability of D_2 molecules at the W(110) surface at low temperatures. Depending on the conditions of adlayer, formation, the difference in the manifestations of this effect can be explained under the assumption on the island mechanism, of its growth. The values of sticking probability for a D_2 molecule incident on a pure surface (~ 0.3), on the surface covered by a monolayer of adsorbed deuterium atoms (~ 0.15), and on the surface covered additionally with physisorbed molecular monolayer (~ 0.55) were calculated directly from experiments and by comparing of experimental and theoretical $S(\theta)$ dependences. The sticking probability (~ 0.95) for a D_2 molecule impinging on a molecule ad-

sorbed earlier in the 5 K state was also determined. The $S(\theta)$ dependences at higher temperatures ($T_s > 78$ K) indicate that two different mechanisms of formation of the atomic phase of deuterium absorption (Langmuir mechanism and through an extrinsic precursor) are realized.

---

*E-mail: osov@marion.iop.kiev.ua

[1])As in Ref. 13, the adsorption states are identified according to the temperature corresponding to the peak in the thermodesorption spectrum.

[2])In Ref. 2, experiments were made with hydrogen, but in all probability, the situation with deuterium will be the same.

[1] K. Christman, Surface Sci. Rep. **9**, 1 (1988).

[2] P. P. Lutsishin, T. N. Nakhodkin, O. G. Panchenko, and Yu. G. Ptushinskii, Zh. Éksp. Teor. Fiz. **82**, 1306 (1982) [Sov. Phys. JETP **55**, 259 (1982)].

[3] V. V. Gonchar, Yu. M. Kagan, O. V. Kanash et al., Zh. Éksp. Teor. Fiz. **84**, 249 (1983) [Sov. Phys. JETP **57**, 142 (1983)].

[4] V. V. Gonchar, O. V. Kanash, and A. G. Fedorus, Pis'ma Zh. Éksp. Teor. Fiz. **38**, 162 (1983) [JETP Lett. **38**, 189 (1983)].

[5] P. P. Lutsishin, O. A. Panchenko, and S. V. Sologub, Pis'ma Zh. Éksp. Teor. Fiz. **41**, 31 (1985) [JETP Lett. **41**, 37 (1985)].

[6] V. V. Gonchar, O. V. Kanash, I. A. Kotlyarova et al., Zh. Éksp. Teor. Fiz. **95**, 1773 (1989) [Sov. Phys. JETP **68**, 1023 (1989)].

[7] P. P. Lutsishin, O. A. Panchenko, and V. F. Shpagin, Surface Sci. **278**, 218 (1992).

[8] V. F. Koval, P. P. Lutsishin, O. A. Panchenko, and S. V. Sologub, Surface Sci. **331–333**, 1317 (1995).

[9] V. V. Dvurechenskikh, V. D. Osovskii, Yu. G. Ptushinskii et al., Pis'ma Zh. Éksp. Teor. Fiz. **54**, 41 (1991) [JETP Lett. **54**, 40 (1991)].

[10] V. V. Dvurechenskikh, V. D. Osovskii, Yu. G. Ptushinskii et al., Ukr. Fiz. Zh. **37**, 716 (1992).

[11] B. A. Chuikov, V. V. Dvurechenskikh, V. D. Osovskii et al., Surface Sci. **285**, 75 (1993).

[12] V. D. Osovskii, Yu. G. Ptushinskii, V. G. Sukretnyi, and B. A. Chuikov, Fiz. Nizk. Temp. **19**, 570 (1993) [Low Temp. Phys. **19**, 406 (1993)].

[13] V. D. Osovskii, Yu. G. Ptushinskii, V. G. Sukretnyi, and B. A. Chuikov, Pis'ma Zh. Éksp. Teor. Fiz. **60**, 569 (1994) [JETP Lett. **60**, 586 (1994)].

[14] B. A. Chuikov, V. D. Osovskii, Yu. G. Ptushinskii, and V. G. Sukretnyi, Surface Sci. **213**, 359 (1989).

[15] Yu. G. Ptushinskii and B. A. Chuikov, Poverkhnost' No. 9, 5 (1992).

[16] P. W. Tamm and L. D. Schmidt, J. Chem. Phys. **54**, 4775 (1971).

[17] V. P. Zhdanov, *Elementary Physicochemical Processes on Surface* [in Russian], Nauka, Novosibirsk (1988).

Translated by R. S. Wadhwa

SHORT NOTES

Weakly damping waves in quasi-two-dimensional conductors

V. G. Peschansky and D. A. Torjanik

*B. Verkin Institute for Low Temperature Physics and Engineering, National Academy of Sciences of the Ukraine, 310164 Kharkov, Ukraine**

J. A. Roldan Lopez

Universidad Nacional de Trujillo, Facultad de Ciencias Fisicas y Matematicas, Ciudad Universitaria, Trujillo, Peru

The transfer of electromagnetic field to the bulk of a layered conductor by charge carriers with a quasi-2D energy spectrum is most effective when the electric field of the wave is polarized along the normal to the layers. © *1997 American Institute of Physics.* [S1063-777X(97)01407-2]

Layered conductors of organic origin possess a quasi-two-dimensional electron energy spectrum, and their kinetic parameters are essentially anisotropic.

Peculiarities of quasi-2D energy spectrum of charge carriers, i.e.,

$$\varepsilon(\mathbf{p}) = \sum_{n=0}^{\infty} \varepsilon_n(p_x, p_y)\cos(anp_z/h) \qquad (1)$$

leads to a number of peculiar effects in a magnetic field.

As a rule, the coefficients of the cosines in the dependence of the energy ε of charge carriers on their quasi-momentum $\mathbf{p}$ in formula (1) decrease rapidly with increasing number n, and the maximum value of the function $\varepsilon_1(p_x, p_y)$ on the Fermi surface $\varepsilon(\mathbf{p}) = \varepsilon_F$ is equal to $\eta\varepsilon_F \ll \varepsilon_F$ (η is the parameter characterizing the quasi-two-dimensional electron energy spectrum) so that the velocity component for charge carriers along the normal to the layers, i.e.,

$$v_z = -\sum_{n=1}^{\infty} (an/h)\varepsilon_n(p_x, p_y)\sin(anp_z/h) \qquad (2)$$

is much smaller than the velocity component along the layers.

Layered conductors in a constant external magnetic field $\mathbf{H}$ turn out to be more transparent than in zero field. In a strong magnetic field, when the radius of curvature r of the trajectory of conduction electrons is much smaller than not only their mean free path l, but also the wavelength $1/k$, the orientational effect, i.e., a strong dependence of kinetic parameters of a conductor on the magnetic field orientation relative to the layers, is observed. For certain values of the angle θ between the magnetic field vector and the normal $\mathbf{n}$ to the layers, the asymptotic behavior of high-frequency electrical conductivity and acoustoelectronic coefficients changes significantly, leading to a considerable increase in the damping length for electromagnetic[1–4] and acoustic[5] waves. However, the magnetic field also stimulates the acoustic transparency of layered conductors for

$$1 \ll kr \ll kl \qquad (3)$$

also.[6–9]

In contrast to acoustic transparency in magnetic fields satisfying condition (3), weak damping at the skin depth δ for electromagnetic waves propagating along the x-axis for values of θ differing noticeably from $\pi/2$ is possible only for selected values of magnetic field

$$H_n = kcD_p/2\pi e(n + 1/4), \qquad (4)$$

where c is the velocity of light, e the electron charge, D_p the diameter of the Fermi surface in the direction orthogonal to the magnetic field and to the wave vector $\mathbf{k}$, and the integer n is large, but still much smaller than $1/\eta$. In this case, the magnetic field $\mathbf{H} = (0, H\sin\theta, H\cos\theta)$ must be strong enough for the period $T = 2\pi/\Omega$ of electron motion in the orbit $\varepsilon = \mathrm{const}$ and $p_H = \mathbf{p} \cdot \mathbf{H}/H = \mathrm{const}$ to be much smaller than its mean free time τ. For an experimental geometry in which the magnetic field is orthogonal to the wave vector of an electromagnetic wave incident on the surface $x_s = 0$ of the conductor, conduction electrons can transfer information on the field and skin layer to the bulk of the conductor over a distance of the order of their mean free path in the form of narrow spikes predicted by Azbel.[10] For $\eta \ll \delta/r$, the field in a spike coincides in order of magnitude with the field in the skin layer over a wide frequency range.[11]

For a considerable deviation of the magnetic field from the normal to the layers, electron orbits become strongly elongated in the direction of "openness" of the Fermi surface, and the condition $T \ll \tau$ can become inadequate for an infinitely large value of H. For values of θ close to $\pi/2$, the effect of magnetic field on the charge carrier dynamics becomes weak in view of the smallness of quasi-2D parameter η, and the Azbel spike mechanism is replaced by the transfer of the varying field by electrons moving rapidly to the bulk of the sample in the form of the Reuter–Sondheimer quasi-waves.[12]

For $\theta = \pi/2$, a considerable fraction of conduction electrons move in open orbits in the momentum space $p_y = \mathrm{const}$, and the fan of all possible directions of their drift

fills the entire xy-plane. In this case, the relation between the Fourier transforms of the current density $\mathbf{j}(k)$ and electric field $\mathbf{E}(k)$, i.e.,

$$j_i(k) = \sigma_{ij}(k)E_j(k) + \int dk' Q_{ij}(k,k')E_j(k') \qquad (5)$$

is nonlocal even in a strong magnetic field, the kernel $Q_{zz}(k,k')$ differs from zero even for purely specular reflection of charge carriers from the sample surface $x_s = 0$, and $\sigma_{ij}(k)$ has the form

$$\sigma_{ij}(k) = \frac{2e^3 H}{c(2\pi h)^3} \int dp_z \int_0^T dt \int_{-\infty}^t dt' v_i(t)v_j(t')$$

$$\times \exp(\nu(t'-t))\cos ik[x(t')-x(t)]. \qquad (6)$$

Here $\nu = 1/\tau - i\omega$, and t and t' are the times of charge motion in a magnetic field according to the equations

$$\frac{\partial p_x}{\partial t} = -\frac{eHv_z}{c}; \quad \frac{\partial p_z}{\partial t} = \frac{eHv_x}{c}. \qquad (7)$$

For $\eta \ll 1$, the time variation of the electron velocity v_x does not exceed $v\eta^{1/2}$, where v is the characteristic Fermi velocity, so that we can assume that away from the saddle points on the Fermi surface, an electron moves without an acceleration in the momentum space along the p_z axis over a distance equal to the unit cell period during the time

$$T = \frac{2\pi hc}{aeHv_x} = \frac{2\pi v}{\Omega_0 v_x}. \qquad (8)$$

It can be easily verified that the components of the tensor $\sigma_{ij}(k)$ for infinitely small values of η have a root singularity of the form

$$\sigma_{zz}(k) = \left(\frac{\omega_0^2 \eta^2}{\nu}\right)\{(\alpha_+^2 - 1)^{-1/2} + (\alpha_-^2 - 1)^{-1/2}\}; \qquad (9)$$

$$\Delta\sigma_{yy}(k) = \nu(\omega_0/kv)^2\{(kv/\nu)^2 + 1\}^{1/2}; \qquad (10)$$

where ω_0 is the frequency of plasma oscillations of charge carriers, insignificant numerical factors of the order of unity are omitted, and $\alpha_\pm = i(kv \pm \Omega_0)/\nu$.

The kernel of the integral operator $Q_{ij}(k,k')$ as a function of k also possesses this property.

At distance from the sample surface which are much larger than the characteristic radius of curvature $r = v/\Omega_0$ of an electron trajectory in a magnetic field or the displacement of an electron over a wave period $2\pi v/\omega$, the electromagnetic field decreases in proportion to $x^{-3/2}\exp(-x/l)$. A slowly decreasing varying electric field $E_z(x)$ for $\Omega_0 \gg \omega$ oscillates with H over large distances x:

$$E_z(x) = E_z(0)\eta^{-4/3}\left(\frac{\omega_0}{c}\right)^{-4/3}\left(\frac{v}{\omega}\right)^{2/3}r^{-1/2}x^{-3/2}$$

$$\exp\left(\frac{ix}{r} - \frac{x}{l}\right),$$

$$r \ll x \ll r/\eta. \qquad (11)$$

The damping of electric field $E_y(x)$ over the mean free path of charge carriers for $\eta \ll 1$ has the form

$$E_y(x) = E_y(0)\left(\frac{\omega_0}{c}\right)^{-4/3}\left(\frac{v}{\omega}\right)^{2/3}l^{-1/2}x^{-3/2}$$

$$\times \exp\left(-\frac{x}{l} + \frac{i\omega x}{v}\right); \quad v/\omega \ll x \ll v/\omega\eta \qquad (12)$$

and does not contain the magnetic field.

The oscillatory dependence of $E_y(x)$ on magnetic field is manifested only in small corrections proportional to η^2. Numerical factors of the order of unity, which are determined by the form of the energy–momentum relation for conduction electrons, are omitted in formulas (11) and (12).

Such a strong polarization dependence of the intensity of a wave penetrating in the bulk of the sample makes it possible to use even thin plates of a layered conductor, whose thickness is considerably larger than the skin depth, but smaller than or of the order of the mean free path of charge carriers, as filters transmitting a wave of a certain polarization.

*E-mail: peschansky@ilt.kharkov.ua

[1] V. G. Peschansky, S. N. Savel'eva, and H. Kheir Bek, Fiz. Tverd. Tela (St. Petersburg) **34**, 1630 (1992) [Sov. Phys. Solid State **34**, 864 (1992)].
[2] V. G. Peschansky, H. Kheir Bek, and S. N. Savel'eva, Fiz. Nizk. Temp. **18**, 1012 (1992) [Sov. J. Low Temp. Phys. **18**, 711 (1992)].
[3] V. G. Peschansky, H. Kheir Bek, S. N. Savel'eva, and D. A. Torjanik, Phys. Low-Dim. Struct. **8**, 81 (1994).
[4] V. G. Peschansky, G. Espeho, and T. Bedassa, Fiz. Nizk. Temp. **21**, 971 (1995) [Low Temp. Phys. **21**, 748 (1995)].
[5] V. M. Gokhfeld, O. V. Kirichenko, and V. G. Peschansky, Zh. Éksp. Teor. Fiz. **108**, 2147 (1995) [JETP **81**, 1171 (1995)].
[6] O. V. Kirichenko and V. G. Peschansky, J. Phys. (France) **4**, 823 (1994).
[7] O. Galbova, G. Ivanovski, O. V. Kirichenko, and V. G. Peschansky, Fiz. Nizk. Temp. **22**, 425 (1996) [Low Temp. Phys. **22**, 331 (1996)].
[8] O. V. Kirichenko and V. G. Peschansky, Pis'ma Zh. Éksp. Teor. Fiz. **64**, 845 (1996) [JETP Lett. **64**, 903 (1996)].
[9] O. Galbova, G. Ivanovski, O. V. Kirichenko, and V. G. Peschansky, Fiz. Nizk. Temp. **23**, 173 (1997) [Low Temp. Phys. **23**, 127 (1997)].
[10] M. Ya. Azbel', Zh. Eksp. Teor. Fiz. **38**, 553 (1960) [Sov. Phys. JETP **11**, 400 (1960)].
[11] M. A. Lur'e, V. G. Peschansky, and K. Jiasemides, J. Low Temp. Phys. **56**, 277 (1984).
[12] G. E. H. Reuter and E. H. Sondheimer, Proc. Roy. Soc. London **195**, 336 (1948).

Translated by R. S. Wadhwa

Bloch−Siegert type shift and indirect interaction between nuclear spins

L. L. Buishvili

Institute of Physics, Georgian Academy of Sciences, 380077 Tbilisi, Georgia

T. L. Buishvili

Department of Physics, Tbilisi State University, 380028 Tbilisi, Georgia

The Bloch−Siegert-type shift of resonant frequency associated with cross-relaxation interaction is investigated. It is shown that indirect interaction between spins with a low concentration is determined by the polarization of spins with a higher concentration at low temperatures. © *1997 American Institute of Physics.* [S1063-777X(97)01507-7]

The dynamics of a spin system consisting of two spins with close Zeeman splittings at ultralow temperatures has been recently studied experimentally. These spins can be the nuclear spins of different isotopes, e.g.,[1] ^{203}TL (with a 30% concentration) and ^{205}TL (with a 70% concentration) having the spin 1/2. Typically, the concentration of one type of spins is much higher than the concentration of the other type of spins. We denote by S the spins with a higher concentration and by I the spins with a lower concentration. Direct interaction between the spins with the lower concentration will be neglected. The Hamiltonian of such a system has the form

$$\mathcal{H} = \omega_S S^z + \omega_I I^z + H_{SS}^z + \sum_{n,i} A_{in} S_n^z I_i^z + \sum_{n,i} (B_{in} S_n^+ I_i + B_{in}^* S_n I_i^+),$$

where $S^z = \Sigma_n S_n^z$; $I^z = \Sigma_i I_i^z$; ω_S and ω_I are the Zeeman frequencies of the S and I spins, respectively, H_{SS}^z is the secular component of interaction between S spins, the forth term corresponds to the secular component of interaction between the S and I spins, and the last term is responsible for cross-relaxation. We assume that $\omega_S - \omega_I$ is much higher than the frequencies characterizing the dipole−dipole interaction between nuclear spins. In this case, following the universal method,[3] and transforming the density matrix

$$\widetilde{\rho} = \exp(i(\omega_S S^z + \omega_I I^z)t)\rho \, \exp(-i(\omega_S S^z + \omega_I I^z)t),$$

we obtain the equation $d\widetilde{\rho}/dt = [\mathcal{H}', \widetilde{\rho}]$, where

$$\mathcal{H}'(t) = H_{SS}^z + \sum_{n,i} A_{in} S_n^z I_i^z + \sum_{n,i} (B_{in} S_n^+ I_i^- e^{i(\omega_S - \omega_I)t} + B_{in}^* S_n^- I_i^+ e^{-i(\omega_S - \omega_I)t}). \quad (1)$$

This expression contains rapidly oscillating terms responsible for small parameters: $H_{SS}^z/(\omega_S - \omega_I)$, $A_{in}/(\omega_S - \omega_I)$, $B_{in}/(\omega_S - \omega_I)$. Consequently, we can apply the method of averaging[2,3] which gives

$$\mathcal{H}'_{av} = H_{SS}^z + \sum_{n,i} A_{in} S_n^z I_i^z + \frac{1}{\omega_S - \omega_I}[H_+, H_-], \quad (2)$$

where

$$H_+ = \sum_{n,i} B_{in} S_n^+ I_i^-; \quad H_- = \sum_{n,i} B_{in}^* S_n^- I_i^+,$$

and the commutator is given by

$$[H_+, H_-]$$
$$= 2\left(\sum_{nii'} B_{in} B_{i'n}^* S_n^z I_i I_{i'}^+ + \sum_{nn'i} B_{in} B_{in'}^* I_i^z S_n^+ S_{n'} \right). \quad (3)$$

Since the spins of the S type in the system interact, the third term in formula (2) for $n \neq n'$ can be combined with the first term, and the averaged Hamiltonian assumes the form

$$\mathcal{H}'_{av} = H_{SS}^z + \sum_{n,i} A_{in} S_n^z I_i^z + \frac{2}{\omega_S - \omega_I}\left(\sum_{nii'} B_{in} B_{i'n}^* S_n^z I_i^- I_{i'}^+ + \sum_{n,i} |B_{in}|^2 I_i^z S_n^+ S_n^- \right). \quad (4)$$

The second term and the component of the third term with $i = i'$ cause a frequency shift for the I spins (for $I = 1/2$ and $S = 1/2$), the shift caused by the third term $\Sigma_{i,n}|B_{in}|^2/(\omega_S - \omega_I)$, being similar to the Bloch−Siegert frequency shift.[4] However, the Bloch−Siegert shift is induced by a varying field, while in our case the shift is due to cross-relaxation terms. A similar shift is also observed for S spins.

The third term (for $i \neq i'$) corresponds to indirect interaction between I spins. By lowering temperature, we can attain a magnetically ordered state for I spins, and the sign reversal for $\langle S_n^z \rangle$ can lead to the ferromagnetic−antiferromagnetic transition or the reverse transition depending on the initial conditions.

It should be noted in conclusion that the above arguments remain also valid in the case of two-level systems with different frequencies, which are mutually coupled through the electric dipole−dipole interaction. However, in this case the term $\Sigma_{i,n} A_{in} S_n^z I_i^z$ is absent, and hence the frequency shift is determined only by Bloch−Siegert-type terms.

[1]G. Eska and E. Schveberth, Jpn. J. Appl. Phys. (Suppl.) **26**, 435 (1987).

[2]N. N. Bogoliubov and Yu. A. Mitropol'skii, *Asymptotic Methods in the Theory of Nonlinear Oscillations*, Gordon and Breach, NY (1962).

[3]L. L. Buishvili and M. G. Menabde, Zh. Éksp. Teor. Fiz. **77**, 2435 (1979)

[Sov. Phys. JETP **50**, 1176 (1979); L. L. Buishvili, E. B. Volzhan, and M. G. Menabde, Teor. Mekh. Fiz. **46**, 251 (1981); L. L. Buishvili and M. G. Menabde, *Radiospectroscopy* [in Russian], Perm' (1983).

[4]F. Bloch and A. Siegert, Phys. Rev. **57**, 522 (1940).

Translated by R. S. Wadhwa

LETTERS TO THE EDITOR

New modes of coupled electron−ripplon oscillations in a Wigner crystal in strong driving electric fields

V. E. Sivokon', V. V. Dotsenko, Yu. Z. Kovdrya, and V. N. Grigor'ev

B. Verkin Institute for Low Temperature Physics and Engineering, National Academy of Sciences of the Ukraine, 310164 Kharkov, Ukraine*

Resonant peculiarities in the conductivity of a Wigner crystal with a surface charge density $6\times10^8 \text{cm}^{-2}$ as functions of the amplitude of an exciting signal are investigated at temperature 75 mK in the frequency range 1–20 MHz. It is found that an increase in the signal amplitude induces new resonances which probably are due to coupling of phonon modes of the electron crystal with the modes of capillary waves excited under nonlinear conditions. © *1997 American Institute of Physics.* [S1063-777X(97)01607-1]

Surface electrons localized over liquid helium form a quasi-two-dimensional classical system with Coulomb interaction. This system has been studied intensely both theoretically and experimentally.[1] The formation of an electron crystal discovered for the first time by Grimes and Adams[2] in 1979 is one of the most striking effects manifested by such a system.

A specific property of a Wigner crystal (WC) in a system of surface electrons is the formation of coupled electron–ripplon resonances. The observation of such resonances was the first experimental evidence of the formation of a WC.[2] Experimental study of the electron–ripplon resonant spectrum in weak driving electric fields[3] confirmed the correctness of the theoretical concepts concerning the origin of these resonances.[4,5] It would be interesting to study the spectrum of these resonances in strong driving fields, in which nonlinear effects can be observed, the more so that a number of new fascinating phenomena in the nonlinear region of WC were detected recently.

The nonlinear behavior of a Wigner crystal in a magnetic field was studied in Refs. 6–9, where it was found that the behavior of longitudinal magnetoconductivity changes abruptly starting from certain values of the driving electric field.

Nonlinear properties of a WC manifested in an essentially nonmonotonic dependence of the longitudinal conductivity on the driving field amplitude were also observed in zero magnetic field.[10] All the above-mentioned effects have not received a reliable theoretical explanation.

The change in the electron–ripplon vibrational spectrum of WC in the nonlinear region has been studied insufficiently. In strong fields, overheating of electrons and WC melting can in general take place. In all probability, this was observed by Yusel *et al.*[11] who discovered the transformation of the optical mode of coupled electron–ripplon vibrations into the plasma mode typical of the liquid phase. In the only theoretical publication we are aware of, in which the nonlinear effect on WC is considered,[12] the emergence of additional (so-called demultiplicative resonances) whose frequencies are connected with the resonant frequencies of capillary waves on the helium surface deformed by electrons in strong driving fields is predicted.

Here we analyze the variation of the electron–ripplon resonant spectrum with the magnitude of the driving field. We investigated a Wigner crystal with the surface charge density $6\times10^8 \text{ cm}^{-2}$ (the melting point 0.54 K) at a helium bath temperature of 75 mK. Measurements were made in the frequency range 1–20 MHz for measuring signal amplitudes from 0.3 to 10 mV. The measuring cell was in thermal contact with the dilution chamber of the refrigerator and had the form of a parallel-plate capacitor of diameter 27 mm with a layer of liquid helium of the height ~ 1 mm in the capacitor gap. Electrons were sputtered on the liquid helium surface during short-term actuation of a filament and were confined with the help of a positive potential applied to the lower capacitor plate. The upper plate separated by 2 mm from the lower plate consisted of three annular measuring electrodes. A signal from the high-frequency generator was supplied to the outer annular electrode, and the response was recorded from the inner electrode, the intermediate electrode being earthed. The cell and the measuring circuit are described and analyzed in detail and Ref. 13.

The results of measurements are shown in Fig. 1 in the form of frequency dependences of the amplitude of the response of the measuring cell to rf signals with different amplitudes of the generator voltage. The amplitude of the driving electric field acting in the plane of the layer is proportional to the amplitude of the input signal, but is also a function of the conductivity of the electron layer and frequency and varies along the radius of the electron ''spot.'' The frequency dependences of the amplitude of the output signal are of resonant type and can be approximated by the sum of the resonant curves. The resonance curves were assumed to be of Lorentzian shape in the course of the analysis.

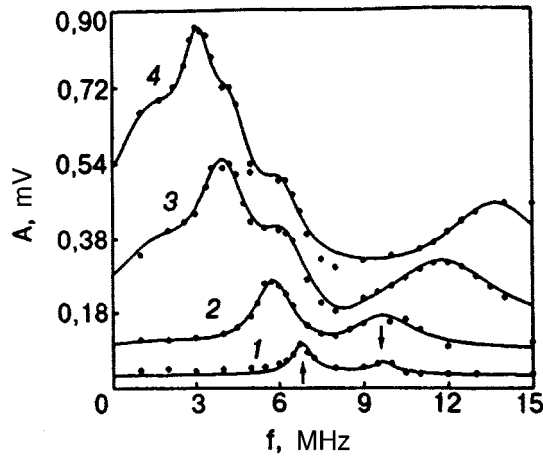We selected the resonant frequencies, amplitudes, and widths so that the total calculated signal corresponded to

FIG. 1. Frequency dependences of the resonance signal amplitudes (in mV) for different amplitudes of excitation: 0.3 (curve *1*), 1 (curve *2*), 5 (curve *3*) and 10 mV (curve *4*). For the sake of visualizations, the curves are displaced along the amplitude axis by $+$ 0.05 mV (curve *2*), $+$ 0.1 mV (curve *3*) and $+0.2$ mV (curve *4*). The points correspond to experimental data and the curves are the result of approximation by the sum of Lorentzian curves.
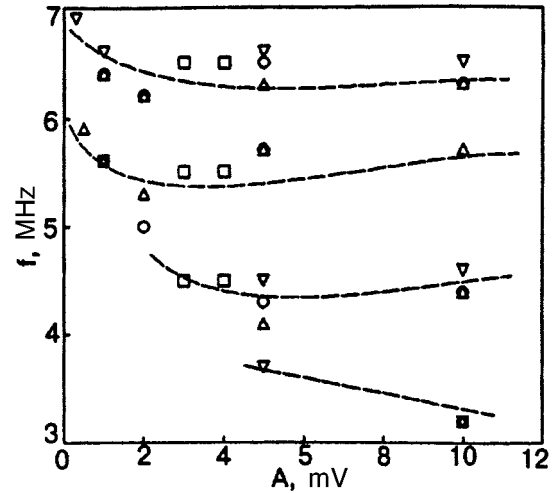
FIG. 2. Dependences of the frequencies of resonances appearing in the low-temperature region on the amplitude of the exciting signal. Different symbols corresponds to different series of measurements. Dashed curves are plotted for a more visual illustration of the observed dependences.

experimental data. The results of analysis are presented by solid curves in Fig. 1.

For the lowest amplitudes of the signal (driving field), the frequency dependence of the response amplitude can be presented as the sum of two resonant curves. As the amplitude of the measuring signal increases, the resonant pattern changes. The resonance at a frequency ~9 MHz is broadened considerably and shifted towards higher frequencies.

In the low-frequency region, the resonance corresponding to the first harmonic of standing waves in the cell is slightly displaced, and additional low-frequency resonances whose number increases with the signal amplitude appear: an additional resonance appears near the initial resonance starting from the amplitude 0.5 mV, the third resonance appears when the signal reaches 2 mV, and the fourth at 5 mV. The frequency of each new resonance differs from that of the previous resonance by approximately 1 MHz. Figure 2 shows the dependences of the positions of these resonances on the amplitude of excitation (driving field). Several series of measurements were made in order to verify the reproducibility of the results.

A theoretical analysis of the resonant properties of a WC over liquid helium was carried out in Refs. 4, 12, 14. In the absence of coupling between electrons and ripplons, the spectrum of longitudinal plasma oscillations in the electron layer (taking into account the screening effect of electrodes) has the form

$$\omega_l^2 = \frac{4\pi n_s e^2 k \ \sinh kd \ \sinh k(H-d)}{m \ \sinh kH}, \qquad (1)$$

where n_s is the surface electron density, m and e are the electron mass and charge, H is the gap between the measuring and confining electrodes, d the height of the liquid helium level with respect to the confining electrode, and k the wave vector determined from the condition of zero current at the boundary of the electron layer.

The presence of the electron crystal leads to electron localization and to the emergence of static deformation of the liquid helium surface. The conditions are created for resonant excitation of capillary waves[15,16] with frequencies

$$\omega_n = (\alpha/\rho)^{1/2} g_n^{3/2}, \qquad (2)$$

where α and ρ are the surface tension and density of liquid helium and g_n the vector of the reciprocal crystal lattice. When the electron–ripplon interaction is taken into account, coupled electron–ripplon vibrations appear. The frequencies of these vibrations for the first resonance are defined as

$$\omega^2(k) = \frac{\omega_1^2 \omega_l^2(k)}{C_1\omega_1^2 + \omega_l^2(k)}, \qquad (3)$$

where ω_1 is the first mode from the set (2) and C_1 the coefficient of coupling between electrons and ripplons, corresponding to the first mode. The arrows in Fig. 1 indicate the positions of two harmonics of standing waves predicted by (3) if we use for C_1 the value calculated on the basis of the self-consistent theory[5] and also take into account of the ^{3}He impurity on the surface tension. It can be seen that the experimental and theoretical results are in good agreement for very small values of the driving field.

Monarkha[12] predicted the emergence of so-called demultiplicative resonances (or partition resonances) in vibrational spectra at frequencies $\omega_2/3$, $\omega_3/3$,... . in strong driving fields. It is still unclear how such resonances will be manifested during measurements in a specific measuring cell, but the fact that the inclusion of nonlinearity leads to the emergence of additional low-frequency resonances correlates with the experimental results described above. The low-frequency nonlinear resonances observed by us probably correspond to coupling of the phonon modes of the electron crystal with additional low-frequency modes described by Monarkha.[12]

Thus, we have studied electron–ripplon resonances in a Wigner crystal for high values of the amplitude of an exciting signal. New vibrational modes for the Wigner crystal on

the surface of superfluid helium were observed in strong driving electric fields for the first time. The frequencies of these modes are lower than the frequencies of linear resonances. The experiments will be continued in the range of high concentrations and temperatures close to the melting point of the Wigner crystal.

*E-mail: sivokon@ilt.kharkov.ua

[1] V. B. Shikin and Yu. P. Monarkha, *Two-Dimensional Charged Systems in Helium* [in Russian], Nauka, Moscow (1989).

[2] C. C. Grimes and G. Adams, Phys. Rev. Lett. **42**, 795 (1979).

[3] V. E. Sivokon', V. V. Dotsenko, Yu. Z. Kovdrya, and V. N. Grigor'ev, Fiz. Nizk. Temp. **22**, 1107 (1996) [Low Temp. Phys. **22**, 845 (1996)].

[4] D. S. Fisher, B. L. Halperin, and P. M. Platzman, Phys. Rev. Lett. **42**, 798 (1979).

[5] Yu. P. Monarkha and V. B. Shikin, Fiz. Nizk. Temp. **9**, 913 (1983) [Sov. J. Low Temp. Phys. **9**, 471 (1983)].

[6] I. Wilen and R. Gianetta, Jpn. J. Appl. Phys. **26** Suppl. 26-3, 2105 (1987).

[7] K. Shirahama and K. Kono, Techn. Rep. ISSP, ser. A, No. 2852 (1994).

[8] K. Shirahama and K. Kono, JLTP **104**, 237 (1996).

[9] A. Blackburn, K. Djerfi, M. I. Dykman *et al.*, Czech. J. Phys. **46**, S6, 3056 (1996).

[10] V. E. Sivokon', V. V. Dotsenko, Yu. Z. Kovdrya, and V. N. Grigor'ev, Fiz. Nizk. Temp. **21**, 1020 (1995) [Low Temp. Phys. **21**, 782 (1995)].

[11] S. Yusel, L. Menna, and E. Y. Andrei, Phys. Rev. **B47**, 12672 (1993).

[12] Yu. P. Monarkha, Fiz. Nizk. Temp. **6**, 685 (1980) [Sov. J. Low Temp. Phys. **6**, 331 (1980)].

[13] V. E. Sivokon', V. V. Dotsenko, S. S. Sokolov *et al.*, Fiz. Nizk. Temp. **22**, 715 (1996) [Low Temp. Phys. **22**, 549 (1996)].

[14] Yu. P. Monarkha, Fiz. Nizk. Temp. **7**, 692 (1981) [Sov. J. Low Temp. Phys. **6**, 338 (1981)].

[15] V. B. Shikin, Pis'ma Zh. Éksp. Teor. Fiz. **19**, 647 (1974) [JETP. Lett. **19**, 335 (1974)].

[16] Yu. P. Monarkha and V. B. Shikin, Zh. Éksp. Teor. Fiz. **68**, 1423 (1975) [Sov. Phys. JETP **41**, 710 (1975)].

Translated by R. S. Wadhwa

597   Low Temp. Phys. 23 (7), July 1997

Sivokon' *et al.*   597

Victor Moiseevich Tsukernik: On His 70th Birthday

Victor Moiseevich Tsukernik, a leading theoretical physicist, turned 70 on May 28, 1997. We congratulate him on this occasion and wish him sound health, great achievements in his scientific activity and personal life.

Editorial Board